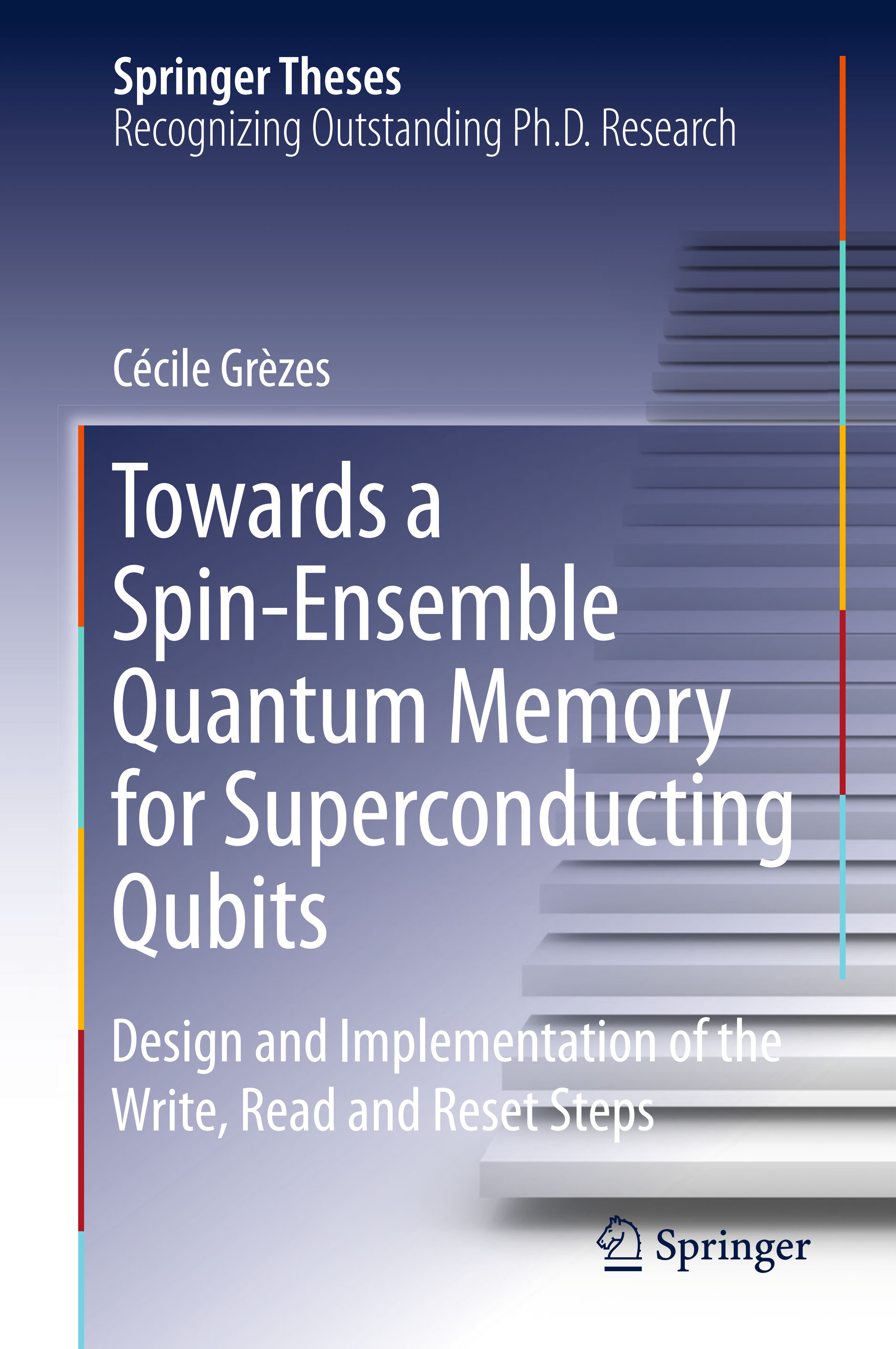

Springer Theses
Recognizing Outstanding Ph.D. Research

Cécile Grèzes

Towards a Spin-Ensemble Quantum Memory for Superconducting Qubits

Design and Implementation of the Write, Read and Reset Steps

Springer

Springer Theses

Recognizing Outstanding Ph.D. Research

Aims and Scope

The series “Springer Theses” brings together a selection of the very best Ph.D. theses from around the world and across the physical sciences. Nominated and endorsed by two recognized specialists, each published volume has been selected for its scientific excellence and the high impact of its contents for the pertinent field of research. For greater accessibility to non-specialists, the published versions include an extended introduction, as well as a foreword by the student’s supervisor explaining the special relevance of the work for the field. As a whole, the series will provide a valuable resource both for newcomers to the research fields described, and for other scientists seeking detailed background information on special questions. Finally, it provides an accredited documentation of the valuable contributions made by today’s younger generation of scientists.

Theses are accepted into the series by invited nomination only and must fulfill all of the following criteria

- They must be written in good English.
- The topic should fall within the confines of Chemistry, Physics, Earth Sciences, Engineering and related interdisciplinary fields such as Materials, Nanoscience, Chemical Engineering, Complex Systems and Biophysics.
- The work reported in the thesis must represent a significant scientific advance.
- If the thesis includes previously published material, permission to reproduce this must be gained from the respective copyright holder.
- They must have been examined and passed during the 12 months prior to nomination.
- Each thesis should include a foreword by the supervisor outlining the significance of its content.
- The theses should have a clearly defined structure including an introduction accessible to scientists not expert in that particular field.

More information about this series at http://www.springer.com/series/8790

Cécile Grèzes

Towards a Spin-Ensemble Quantum Memory for Superconducting Qubits

Design and Implementation of the Write, Read and Reset Steps

Doctoral Thesis accepted by
the University of Paris VI, France

Springer

Author
Dr. Cécile Grèzes
Quantronics Group
CEA Saclay
Gif-sur-Yvette
France

Supervisor
Prof. Patrice Bertet
Quantronics Group
CEA Saclay
Gif-sur-Yvette
France

ISSN 2190-5053 ISSN 2190-5061 (electronic)
Springer Theses
ISBN 978-3-319-21571-6 ISBN 978-3-319-21572-3 (eBook)
DOI 10.1007/978-3-319-21572-3

Library of Congress Control Number: 2015944717

Springer Cham Heidelberg New York Dordrecht London
© Springer International Publishing Switzerland 2016
This work is subject to copyright. All rights are reserved by the Publisher, whether the whole or part of the material is concerned, specifically the rights of translation, reprinting, reuse of illustrations, recitation, broadcasting, reproduction on microfilms or in any other physical way, and transmission or information storage and retrieval, electronic adaptation, computer software, or by similar or dissimilar methodology now known or hereafter developed.
The use of general descriptive names, registered names, trademarks, service marks, etc. in this publication does not imply, even in the absence of a specific statement, that such names are exempt from the relevant protective laws and regulations and therefore free for general use.
The publisher, the authors and the editors are safe to assume that the advice and information in this book are believed to be true and accurate at the date of publication. Neither the publisher nor the authors or the editors give a warranty, express or implied, with respect to the material contained herein or for any errors or omissions that may have been made.

Printed on acid-free paper

Springer International Publishing AG Switzerland is part of Springer Science+Business Media
(www.springer.com)

Supervisor's Foreword

The research project described in Cécile Grezes's Ph.D. thesis takes place within a large effort worldwide to build a new type of machine called a quantum computer. A quantum computer relies on registers of quantum two-level systems called qubits, which obey the laws of quantum physics. By placing the qubit registers in complex superpositions of quantum states according to the rules of a quantum algorithm, a quantum computer can implement certain tasks more efficiently than a classical machine, such as factorizing large numbers or simulating interacting quantum systems. Because of their coupling to a fluctuating environment, qubits placed in superpositions of states retain their quantum coherence only during a finite time; this coherence time defines the longest calculation that can be performed with the computer. Electrical circuits made in superconducting metallic electrodes and incorporating tunnel junctions, cooled at millikelvin temperatures in a dilution refrigerator, are among the most promising qubit candidates nowadays, with demonstrations of elementary processors including up to 10 qubits. However, the coherence time of superconducting qubits is presently too short (few tens of microseconds) to hope building a truly operational large-scale quantum computer.

A new research direction emerged in 2008 to solve this issue, when several theorists proposed to combine superconducting qubits with other quantum systems having much longer coherence times which would serve as quantum memory and could thus extend the time allowed for a quantum computation. It rapidly appeared that ensembles of electronic spins in a solid could be well suited for this idea. When embedded in ultra-pure crystals, spins can have coherence times reaching seconds or hours. In our group, we started an experimental effort to build a quantum memory using an ensemble of nitrogen-vacancy (NV) centers in diamond. NV centers consist of a substitutional nitrogen atom sitting next to a vacancy of the diamond lattice; their ground state has a spin degree of freedom with a demonstrated coherence time up to 1 second, which is thus promising to store quantum information.

When Cécile arrived in the group to work on this project for her Ph.D., early initial steps had been taken by postdoc Yuimaru Kubo, who had demonstrated spectroscopically the coherent coupling of an ensemble of NV centers to microwave photons in a superconducting resonator. However, the design and realization of an operational quantum memory remained very far from reach, and this was precisely the Ph.D. subject of Cécile. As a first step of her thesis work, Cécile was involved in a collaboration with theorists from Aarhus University in Danemark. This made possible to devise a complete quantum memory protocol and to calculate its fidelity for realistic parameters. The protocol includes a "write" step during which the quantum state is transferred from a superconducting qubit into the spin-ensemble memory, and a subsequent "read" step triggered by complex sequences of microwave pulses to recover the state after storage.

The first experiment demonstrating the "write" step was a success, in which Cécile was actively involved at the beginning of her Ph.D. But the most experimentally challenging part was the implementation of the "read" step of the protocol. Indeed, it required the combination of spin-echo techniques borrowed from magnetic resonance, with optical irradiation to actively reset the spins in their ground state between experimental sequences, all the experiment being cooled at millikelvin temperatures. Cécile took the lead in this experimental effort. Thanks to her dedicated work, insight, and talent, she obtained several remarkable results, which culminated with the first demonstration of the storage of a microwave pulse at the single-photon level into the NV ensemble memory, and its retrieval 100 microseconds later by a spin-echo sequence. This is a landmark result for this field, which opens the way to realistic quantum memory implementations in a near future. As a recognition of the significance of her work, Cécile was asked to give an invited talk at the Americal Physical Society 2015 March meeting, and she received the Madeleine Lecoq prize from the French Academy of Sciences.

Cécile's Ph.D. manuscript contains a detailed account of this work, from the description of the quantum memory protocol up to the experimental implementation of most of its building blocks. It also includes a chapter which summarizes all the theoretical aspects needed to understand this complex system involving superconducting qubits, resonators, ensembles of spins, microwave and optical photons. I believe this manuscript will constitute a reference for people interested in the field, and I am very glad to see it published.

Paris, France
May 2015

Prof. Patrice Bertet

Acknowledgments

First of all, I would like to thank my supervisor Patrice Bertet without whom none of the work presented here would have been possible. I am very grateful for the opportunity he gave me to be involved in his research, as well as for his invaluable scientific advice and availability for discussions. Thanks also to:

Daniel Esteve for the opportunity he gave me to join the unique working environment of the Quantronics group.

Yuimaru Kubo for accompanying me the first months of this thesis and helping me to get started with this project.

Denis Vion, **Andreas Dewes**, and **Vivien Schmitt** for sharing with me their experience on superconducting qubits manipulation and readout on numerous occasions.

Patrick Pari, **Philippe Forget**, **Mathieu Combarieu**, and the low temperature laboratory at the CEA Saclay for continuous help on the cryogenic part.

Pascal Sénat, **Pierre-Francois Orfila**, and the technical staff of the "Grand Atelier" whose expertise is so valuable. The technical challenges of this project could not have been overcome without your skill and creativity for building so many various pieces of equipment.

This work is the result of many theory-experiment collaborations, and my thanks intrinsically go well beyond the Quantronics group to all who contributed to this project.

Last, thank you to my father Yannick for encouraging me through all of my studies, Nabiha—although constantly travelling through the most remote parts of the planet—and Parichat for your unconditional support during the writing of this thesis.

Abstract

Processing quantum information requires quantum-mechanical systems with long coherence times and that can be easily coupled together to perform logic operations. Superconducting qubits are well suited to perform the rapid logic gates since they couple very strongly to microwave fields, but have coherence times limited so far to tens of microseconds. This limitation has motivated proposals to combine them to a physical system better protected against decoherence. In this hybrid architecture, a memory provides the long-lived register of N quantum states and a few-superconducting qubit processor performs qubit gates to create multi-qubit entanglement. The implementation comes however with new challenges. The multi-qubit register must be able to store N quantum states (*write*), retrieve each of them on-demand (*read*), and be re-initialized between successive experimental sequences (*reset*).

This thesis work discusses the development of these three memory operations in a hybrid quantum circuit, in which collective degrees of freedom of an ensemble of NV center spins in diamond are used as a multimode quantum memory for superconducting qubits. In the first part of the thesis, I present the details of our quantum memory protocol. It relies on the coupling of the NV ensemble to a resonator with tunable frequency and quality factor. Incoming quantum states are written by resonant absorption of a microwave photon in the spin ensemble, and then read out of the memory by applying a sequence of control pulses to the spins and to the resonator. The second part of the thesis reports our experimental efforts towards the implementation of this protocol, which requires a combination of the most advanced techniques of superconducting quantum circuits and pulsed electron spin resonance.

The *write step* of the protocol is demonstrated in a first experiment by integrating on the same chip a superconducting qubit, a resonator with tunable frequency, and the NV ensemble. Arbitrary qubit states are stored into the spin ensemble via the resonator. After storage, the resulting collective quantum state is rapidly dephased due to inhomogeneous broadening of the ensemble and a refocusing sequence must be applied on the spins to bring them to return in phase and to re-emit collectively the quantum state initially absorbed as an echo. In a second experiment, we demonstrate an important building block of this read-out operation, which consists in retrieving multiple classical microwave pulses down to the single photon level using Hahn echo refocusing techniques. Finally, optical repumping of the spin ensemble is implemented in order to reset the memory in-between two successive sequences.

Contents

1 **Introduction** . . . 1
- 1.1 Rationale for the Hybrid Way . . . 1
- 1.2 Spin Ensemble Quantum Memory Principle . . . 4
- 1.3 Storing a Qubit State in a Spin Ensemble (Write) . . . 6
- 1.4 Retrieving Few-Photon Fields Stored in a Spin Ensemble (Read) . . . 10
- 1.5 NV Clock Transitions for Long Coherent Storage . . . 13
- 1.6 Towards an Operational Quantum Memory . . . 14
- References . . . 16

2 **Background** . . . 19
- 2.1 Superconducting Circuits and Microwave Engineering . . . 19
  - 2.1.1 Superconducting Resonators . . . 19
  - 2.1.2 Josephson Junction Based Circuits . . . 29
  - 2.1.3 Circuit Quantum Electrodynamics . . . 39
- 2.2 NV Center Spins in Diamond . . . 45
  - 2.2.1 Structure . . . 45
  - 2.2.2 The NV Center Spin Qubit . . . 46
  - 2.2.3 Coherence Times . . . 51
- 2.3 Coupling Ensembles of NV Center Spins to Superconducting Circuits . . . 53
  - 2.3.1 Single Spin-Resonator Coupling . . . 53
  - 2.3.2 Spin Ensemble-Resonator Coupling: Collective Effects . . . 54
  - 2.3.3 The Resonator-Spins System in the Low-Excitation Regime . . . 65
  - 2.3.4 The Resonator-Spins System Under Strong Drive Powers . . . 74
- References . . . 75

3 Proposal: A Spin Ensemble Quantum Memory for Superconducting Qubits 79
3.1 Spin-Based Quantum Memory 79
  3.1.1 Motivations 79
  3.1.2 Spin Ensemble Quantum Memory: Principles 80
3.2 Spin Ensemble Quantum Memory Protocol 82
  3.2.1 The Write Step: Storage of N Quantum States $|\psi_1\rangle \ldots |\psi_n\rangle$ 82
  3.2.2 The Read Step: On-Demand Retrieval of $|\psi_i\rangle$ 83
  3.2.3 The Full Quantum Memory Protocol 86
3.3 Simulations 87
References 89

4 Experiment 1 (Write): Coherent Storage of Qubit States into a Spin Ensemble 93
4.1 State of the Art and Principle of the Experiment 93
  4.1.1 State of the Art 93
  4.1.2 Strong Coupling of NVs to a Superconducting Resonator 94
  4.1.3 Principle of the Experiment 96
4.2 Experimental Realization 98
  4.2.1 The Hybrid Quantum Circuit 98
  4.2.2 Measurement Setup 104
4.3 Operating the Hybrid Quantum Circuit 110
  4.3.1 Superconducting Circuit Characterization 110
  4.3.2 Transferring Qubit States to the Bus Resonator 118
  4.3.3 Coupling the NV Spin Ensemble to the Bus Resonator 120
4.4 Storage of Qubit States into a NV Spin Ensemble 122
  4.4.1 Storing a Single Photon from the Qubit into the Spin Ensemble 122
  4.4.2 Storing a Coherent Superposition from the Qubit to the Spin Ensemble 126
  4.4.3 Entanglement Between the Spin Ensemble and the Resonator 129
4.5 Conclusions on Experiment 1: The Write Step 131
References 132

5 Experiment 2 (Read): Multimode Retrieval of Few Photon Fields from a Spin Ensemble 133
5.1 Principle of the Experiment 133
5.2 Experimental Realization 135
  5.2.1 The Hybrid Quantum Circuit 135
  5.2.2 Measurement Setup 139

5.3 Spectroscopy of the Resonator-Spins System 145
  5.3.1 Characterization of the Resonator 146
  5.3.2 System Spectroscopy at Zero-Magnetic Field 147
5.4 Active Reset of the Spins 150
  5.4.1 Effect of Light Irradiation on the Superconducting Resonator 150
  5.4.2 Continuous Irradiation: Dependence of the Spin Polarization on the Optical Power 156
  5.4.3 Pulsed Irradiation: Active Spin Polarization 160
  5.4.4 Spin Relaxation Time Measurement 165
5.5 Multimode Retrieval of Few Photon Fields Stored in a Spin Ensemble 166
  5.5.1 Applying Hahn Echoes to the Spin Ensemble 166
  5.5.2 Retrieval of Few-Photon Pulses Stored in the Spin Ensemble 174
5.6 NV Clock Transitions for Long Coherent Storage 181
  5.6.1 Atomic Clock Transitions in NV Centers in Diamond . . . 181
  5.6.2 Full System Spectroscopy 182
  5.6.3 Dependence of the Echo Coherence Time on the Magnetic Field 185
  5.6.4 Advanced Analysis: Spin Classes Contributions to the Echo Decay 189
5.7 Conclusion on Experiment 2: The Read Step 195
References 197

6 Towards an Operational Quantum Memory 199
6.1 Reaching Efficient Memory Operations 199
  6.1.1 Storage and Retrieval of Photon Fields at the Single Photon Level with Improved Efficiencies 199
  6.1.2 Reaching the Operational Level 205
6.2 Running the Full Quantum Memory Protocol 207
  6.2.1 Step 1/2: Realization of a Frequency Tunable Resonator Compatible with Refocusing Pulse Applications 207
  6.2.2 Realizing a Hybrid Circuit Able to Run the Full Memory Protocol 215
References 218

7 Conclusions and Perspectives 219
References 221

Appendix A: Fabrication 223

Appendix B: NV Center Distribution 225

Curriculum Vitae 229

Chapter 1
Introduction

1.1 Rationale for the Hybrid Way

Research in quantum physics has undergone a major breakthrough over the last few decades with the advent of experimental techniques able to manipulate the state of individual quantum systems. This progress has triggered a large effort worldwide to use non-classical phenomena to carry out information processing tasks more efficiently than allowed by classical physics. One of these applications, the quantum computer, takes advantage of entanglement and massive parallelism enabled by the superposition principle to solve problems intractable by classical computers. In quantum information processing (QIP), information is encoded in the quantum state of quantum bits (or qubits) with basis states $|0\rangle$ and $|1\rangle$. As classical information, it can be materialized in different physical forms and converted from one to another without changing its content. The choice of the physical implementation is left to the “quantum engineer”: either natural microscopic systems such as atoms, ions, photons, electron and nuclear spins, or more artificial systems such as superconducting qubits, nanomechanicals resonators, or semiconducting heterostructures. Each physical system has specific advantages from the point of view of QIP. Microscopic systems benefit from a natural decoupling from their environment which results in long coherence times, mechanical resonators can be functionalized to measure various forces, photons are interesting for communications while superconducting circuits are electrically addressable and well suited for rapid logic gates. It is then natural to imagine that integrating different physical resources will lead to new quantum devices with new functionalities. This is the framework of the emerging field of hybrid quantum systems that aims to couple different quantum systems with complementary properties to benefit from their respective advantages [1, 2].

The birth of this field is linked to the development of circuit quantum electrodynamics (cQED), in which superconducting qubits interact with microwave photons in a resonator [3, 4]. Indeed, in cQED, the quantum systems are purposely designed electrical circuits offering a large flexibility that can be exploited for coupling to other

© Springer International Publishing Switzerland 2016

C. Grèzes, *Towards a Spin-Ensemble Quantum Memory for Superconducting Qubits*, Springer Theses,
DOI 10.1007/978-3-319-21572-3_1

systems. Superconducting qubits are promising candidates for building a quantum computer since they couple very strongly to microwave fields, which enables rapid single- and multi-qubit gates, but have coherence times limited so far to tens of microseconds [5, 6], allowing only a short time window to perform quantum calculations before the whole system decoheres. This time limitation has motivated early hybrid quantum system proposals of increasing the coherence time of superconducting qubits by combining them to other quantum systems better protected against decoherence. It was thus proposed to couple superconducting qubits, via a superconducting resonator, to ions [7], atoms [8–10], polar molecules [11], electrons on helium [12], or impurity spins [13–15]. Here, the microscopic systems are magnetic or electrical dipoles that couple to the electromagnetic field substained by the superconducting resonator. The prerequisite for such a hybrid scheme to be operational is to reach the regime of strong coupling between the quantum system and the resonator, in which they can coherently exchange a photon. Whereas the coupling of one individual microscopic system to a superconducting circuit is usually too weak, the coupling constant of an ensemble of N such systems is enhanced by $\sqrt{N}$, allowing to satisfy this requirement. Our research project focuses on the use of ensembles of spins in solids to build a quantum memory for superconducting qubits.

The spin species considered in this thesis work is the negatively charged nitrogen-vacancy center in diamond [16] (NV center). Depicted in Fig. 1.1, it consists of a substitutional nitrogen atom with a neighboring vacancy. Its electronic spin, a triplet with transition between states $m_S = 0$ and $m_S = \pm 1$ in the microwave domain, is particularly attractive for the implementation of a microwave quantum memory as it has coherence times that can reach seconds [17] and can be actively reset in the spin ground state by optical pumping [18]. In our experiments, we use one of the two microwave transitions so that the NV center spin can be described as a two-level system.

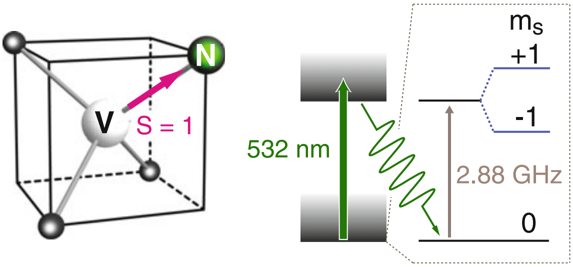

Fig. 1.1 **The nitrogen-vacancy center.** Sketch of a NV center with its vacancy (V) and nitrogen atom (N), as well as three neighboring carbon atoms. Its electronic ground state has a spin $S = 1$ with transition between states $m_S = 0$ and $m_S = \pm 1$ at 2.88 GHz in zero magnetic field. It can be repumped optically into the $|m_S = 0\rangle$ state

A multimode quantum memory Beyond the strong coupling requirement, the use of an ensemble of spins rather than a single one in our research towards a quantum memory has an important interest: an ensemble of N spins provides several collective degrees of freedom to store qubit states in parallel. From the quantum computation point of view, such a multi-qubit register associated to a few(2)-qubits processor would work like a genuine quantum Turing machine that promotes the few-qubits processor to N-qubits operations with good coherence properties. Experimental progress has been slow, because combining different quantum systems requires developing new experimental techniques to make them compatible. The first step in this direction, the strong coupling of a resonator to the ensemble of spins, was demonstrated in the group shortly before the beginning of this thesis work [19].

This thesis goes one step further and presents the development of building blocks of memory operations in a hybrid circuit, in which an ensemble of NV center spins is used as a multimode quantum memory for superconducting qubits. The qubit is of Transmon type, with which a two-qubit processor has been developed in 2012 in the group [20]. The microwave photon exchange between the two systems is implemented by a superconducting resonator used as a quantum bus, which is electrically coupled to superconducting qubits, and magnetically coupled to the ensemble of NV spins, as schematically shown in Fig. 1.2.

In Chap. 2, we introduce the theoretical background needed to understand the work that follows, with a particular emphasis on the modeling of the spin ensemble-resonator coupled system. We then present the spin ensemble quantum memory protocol in which building blocks of *write*, *read* and *reset* memory operations can be isolated [21]. The experimental demonstration of coherent storage of quantum information from a superconducting qubit to the NV spin ensemble (*write operation*) is reported in Chap. 4 [22]. The active polarization of the spins (*reset operation*) and retrieval of multiple few photon field initially stored (building block of the *read*

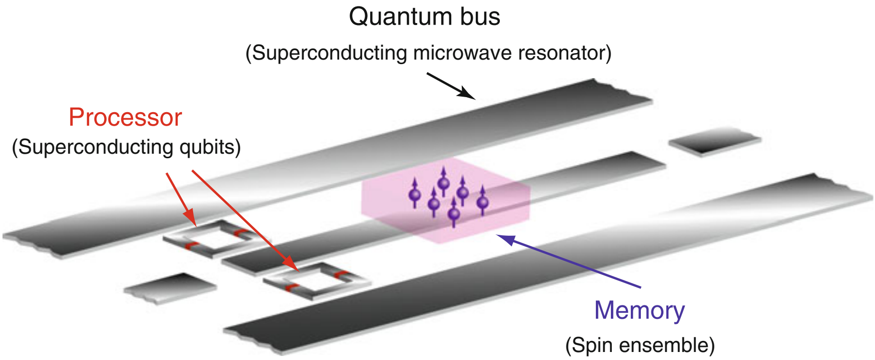

Fig. 1.2 Concept of the hybrid quantum processor combining a few(2)-qubits processor and a spin ensemble multimode quantum memory. The microwave photon exchange between both is implemented by a superconducting resonator used as a quantum bus, which is coupled electrically to the qubits and magnetically to the spins

operation) are presented in Chap. 5 [23]. Finally, solutions for reaching the level of an operational quantum memory are discussed in Chap. 6, illustrated by a selection of experimental results going in this direction.

1.2 Spin Ensemble Quantum Memory Principle

In the goal of realizing a spin-based quantum memory for superconducting qubits, the first step is to design a suitable protocol, and to estimate theoretically the efficiency with which an incoming quantum state can be restored after its storage. We took inspiration from related experiments on optical quantum memories based on atom and ion ensembles [24], for which storage and retrieval procedures have been developed. These protocols proceed along the following principles. First, the optical pulse carrying the quantum state of interest is collectively absorbed by the ensemble of ions (this is the *write step*). Due to inhomogeneous broadening that causes each ion in the ensemble to have a slightly different Larmor frequency, the resulting collective quantum state is rapidly dephased. In order to retrieve this state on-demand (the *read step*), an operation is performed on the ions that brings them to return in phase at a later time in the sequence and to re-emit collectively the quantum state initially absorbed as an echo. Several experiments have already successfully implemented this refocusing [25, 26], which is the most challenging part of the quantum memory protocol. The microwave quantum memory protocol builds on these same ideas, adapted to the requirements of a cQED setup working at millikelvin temperatures, and taking advantage of the new possibilities offered by Josephson quantum circuits. Indeed, efficient absorption of microwave photons by the spin ensemble requires to insert them inside a resonator, which is straightforwardly achieved by planar superconducting resonators used in cQED. Our proposed protocol, described in detail in Chap. 3 [21], uses the physical system depicted in Fig. 1.3 to implement

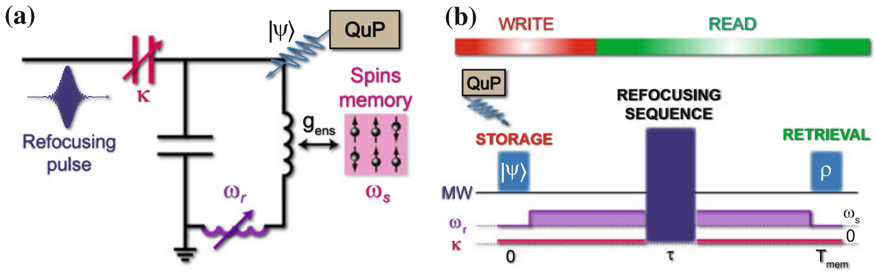

Fig. 1.3 Spin ensemble quantum memory principle. a Quantum memory circuit. The resonator, with frequency ω_r and damping rate κ tunable at the nanosecond scale, is coupled to the spin ensemble (frequency ω_s) with coupling strength g_{ens}. An external processor (QuP) delivers a quantum state $|\psi\rangle$ to the bus resonator, to be stored into the spin-based memory. Refocusing pulses are applied to the spins via the resonator. **b** Schematic timing of pulses and cavity parameters ω_r and κ. The quantum state delivered by QuP is stored in the spin ensemble (write operation). A refocusing sequence acts as time-reversal for the spins and triggers the retrieval of the stored quantum state as an echo (read operation)

write and *read* operations in the spins memory. The bus resonator, with frequency ω_r and damping rate κ both tunable, is coupled to the spin ensemble with frequency ω_s and spin linewidth Γ, with an ensemble coupling constant g_{ens}. Such a resonator with tunable parameters can be realized using SQUIDs, as described in Chaps. 2 and 4.

Write operation The resonator receives $|\psi\rangle$ from the external superconducting qubit processor (QuP), which initializes the cavity-field state. The cavity is tuned to the spin frequency and a high quality factor so that the spin ensemble and the resonator are in the **strong coupling regime** ($g_{ens} \gg \kappa, \Gamma$). The microwave photon carrying out the state $|\psi\rangle$ is collectively absorbed by the spin ensemble and is transferred to collective spin modes decoupled to the cavity. This transfer takes place in a time $T_2^* = 2/\Gamma$, the free induction decay time of the spins.

Read operation The stored quantum state is coherently retrieved by applying a refocusing sequence that combines the application of π-pulses with dynamical tuning of the resonator frequency and quality factor to act as a time reversal for the spins. The echo, described by the density matrix ρ, restores the initial state $|\psi\rangle\langle\psi|$. The maximum storage time after which the quantum state can be retrieved is of order the echo coherence time T_2 of the spin ensemble.

Extension to multimode storage and on-demand retrieval As is the case for optical quantum memories [27], collective excitations of the ensemble can be used to simultaneously encode a large number of qubits. As seen from the collective spin mode coupled to the cavity, the other spin modes behave as a conveyor belt with loading time the free induction decay time (T_2^*), and life time the Hahn-echo decay time (T_2), as illustrated in Fig. 1.4a. Once absorbed by the spin ensemble, the quantum state is transferred into one of these collective spin modes in a characteristic time T_2^*, after which the collective spin mode coupled to the cavity is accessible again for storage. Hence, consecutive *write steps* separated by time of order T_2^* can be performed to store various quantum states. The lifetime of the memory is approximately the Hahn-echo decay time T_2, so that the maximal number of stored quantum states

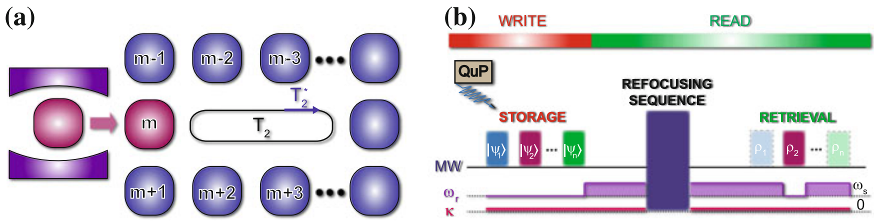

Fig. 1.4 Multimode storage and on-demand retrieval. a Collective excitations of the spins can be used to simultaneously encode a large number of qubits. As seen from the collective spin mode coupled to the cavity, the other modes behave as a conveyor belt, with loading time the free induction decay time (T_2^*) and life time the Hahn-echo decay time (T_2). **b** Extension of the quantum memory protocol to multimode storage and on-demand retrieval

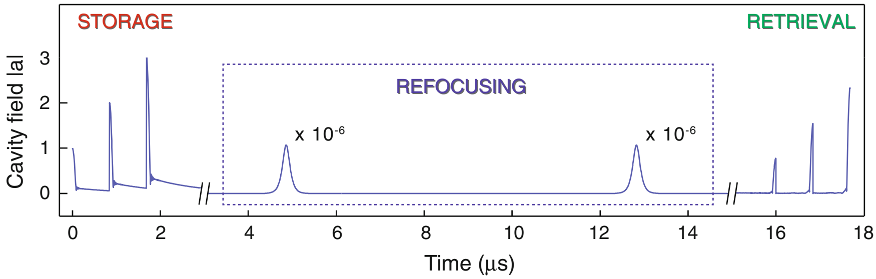

Fig. 1.5 Results of numerical simulations, showing that successive cavity field states can be stored and retrieved with 80 % efficiency with our memory protocol

is of order T_2/T_2^*. On-demand retrieval is obtained by extending the *read* protocol to multiple states with dynamical detuning of the cavity to retrieve selectively the state $|\psi_i\rangle$, while keeping the others in the memory (see Fig. 1.4b).

Numerical simulations performed by Brian Julsgaard at Aarhus University [21, 28] show that the NV memory can store and retrieve multiple quantum states of the field with 80% efficiency with realistic experimental parameters (see Fig. 1.5), and higher using spin species with better coherence times. The core of this thesis is the description of two experiments going in the direction of implementing this protocol with NV centers in diamond. The first one demonstrates the coherent storage of a qubit state into the NV ensemble, bringing a proof-of-concept of the *write operation*. The second shows the retrieval of multiple few photon microwave pulses initially stored, a first step towards the *read operation*.

1.3 Storing a Qubit State in a Spin Ensemble (Write)

As mentioned above, the coupling strength of an individual spin for typical parameters of superconducting resonator is too small to achieve strong coupling and subsequent transfer of quantum information (Fig. 1.6). For NV centers coupled to

Fig. 1.6 The write step

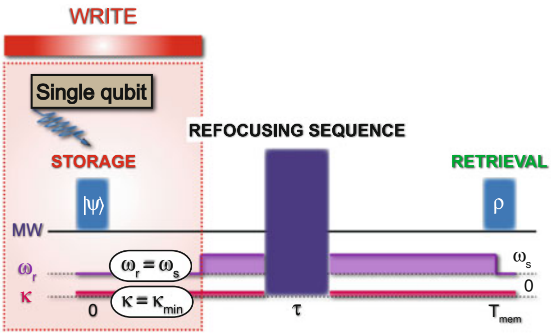

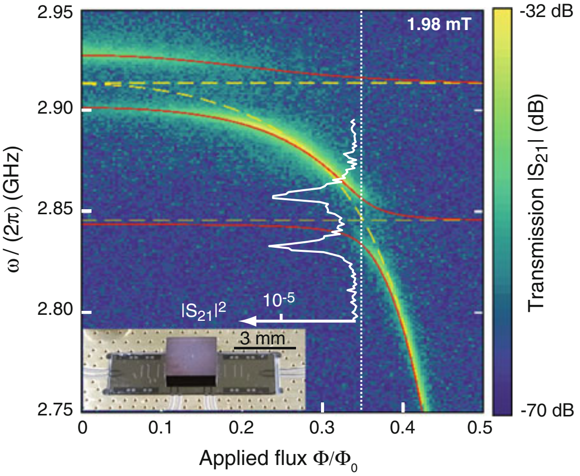

Fig. 1.7 Spectroscopic evidence for spin ensemble-resonator strong coupling [19]. The resonator transmission spectrum shows two avoided level crossings whenever the tunable resonator frequency crosses the NV resonance frequencies

a planar microwave resonator, the coupling constant is $g/2\pi \sim 10\,\mathrm{Hz}$, which is four orders of magnitude smaller than resonator linewidth κ reachable in cQED. The strong coupling between superconducting resonators and collective spin modes was evidenced by the experiment performed in the group in 2010 with a collection of 10^{12} NV center spins [19]. It is manifested by the appearance of a vacuum Rabi splitting inthe transmission spectrum of the resonator (shown in Fig. 1.7) when its frequency is tuned through the NV center electron spin resonance. Later, experimental evidences for the coherent coupling to a superconducting circuit were obtained with other types of electronic spins [29–32], and the storage of hundreds of photons microwave fields into collective excitations of a spin ensemble was demonstrated [33]. These experiments were carried out in the classical regime since the resonator and spin ensemble behave as two coupled harmonic oscillators driven by classical microwave fields. In the perspective of building a quantum memory, it is instead necessary to perform experiments at the level of a single quantum of excitation. For that purpose, in the first part of this thesis work, we integrate on the same chip three different quantum systems: an ensemble of NV center spins, a superconducting qubit, and a resonator acting as a quantum bus between the qubit and the spins, in the goal of demonstrating the storage of a qubit state into the ensemble.

A sketch of our hybrid quantum circuit [22] is shown in Fig. 1.8. The diamond single-crystal that contains the spins is placed on top of the superconducting circuit. The quantum bus, a coplanar waveguide resonator, is electrostatically coupled to the qubit and magnetically coupled to the spins. It is made frequency-tunable by inserting a SQUID in the resonator central line [34, 35] making it possible to transfer quantum information from one system to the other.

The storage of the qubit state $|\psi\rangle$ into the spin ensemble proceeds by pulsed control of the bus resonator frequency (see Fig. 1.9a). The state is retrieved without using refocusing before complete transfer into the collective spin modes decoupled

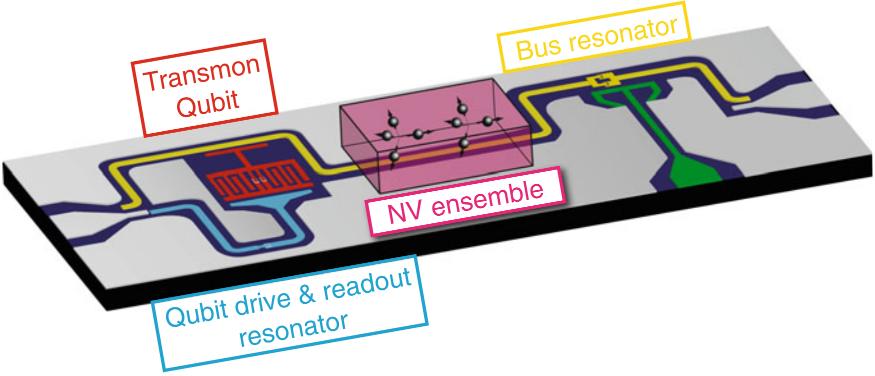

Fig. 1.8 Write experiment: schematic of the hybrid quantum circuit. A transmon qubit (*red*) is coupled to an ensemble of NV centers electron spins (*pink*) via a frequency tunable bus resonator (*yellow*)

to the cavity, in order to demonstrate that the qubit state is not altered during the storage. The qubit is used as a readout apparatus for the comparison with the initially encoded state.

Figure 1.9b shows the storage and retrieval of the qubit state initially prepared in $|e\rangle$. The quantum of excitation is exchanged coherently between the quantum bus and the spin ensemble. This exchange is damped by the transfer into the other collective modes of the spins with characteristic time $T_2^* \sim 200\,\text{ns}$, as requested for the *write step* of the protocol. To demonstrate that the phase information is preserved during the storage, the experiment is repeated with a superposition state $(|g\rangle + |e\rangle)/\sqrt{(}2)$ and the density matrix of the retrieved state reconstructed by quantum state tomography [22] (see Fig. 1.9c).

The combination of the results of Fig. 1.9 demonstrates that an arbitrary qubit state ψ can be stored into the spin ensemble. The leakage of the quantum state into the other collective spin modes being a part of the *write step* of our memory protocol, the only loss of quantum information during the storage comes from energy damping in the resonator and non-static spin dephasing, that reduce the efficiency of *write step* to $3T_2^*$ as seen in Fig. 1.9. The detailed description of this experiment can be found in Chap. 4.

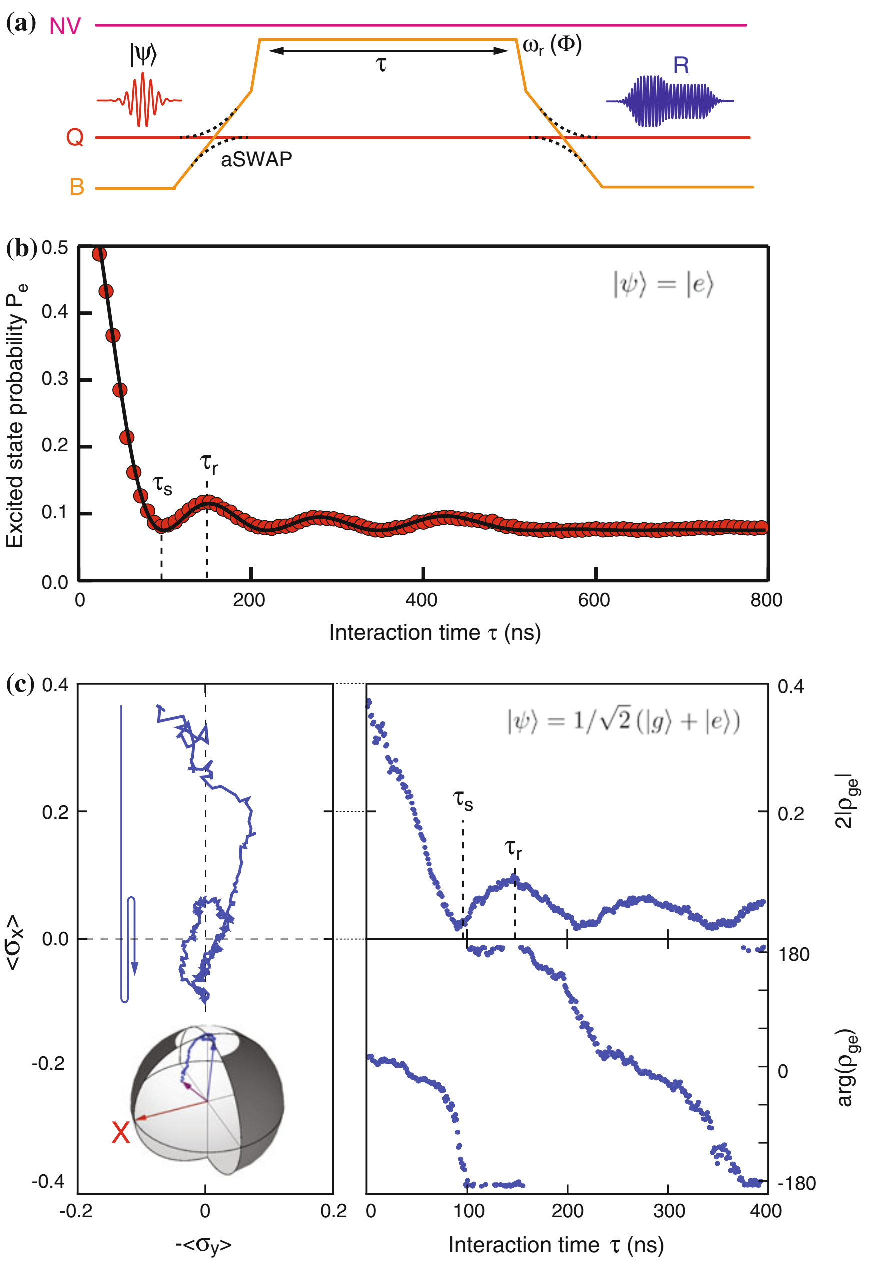

Fig. 1.9 Write experiment. a Protocol for storing a qubit state into the spin ensemble. **b** Swap oscillations of an excitation $|e\rangle$ and **c** of a coherent superposition of quantum states $(|g\rangle + |e\rangle)/\sqrt{2}$, initially prepared in the qubit. The transfer to the spin ensemble is complete at τ_s

1.4 Retrieving Few-Photon Fields Stored in a Spin Ensemble (Read)

After storage, spins dephase due to the spread of resonance frequencies in the ensemble, and the quantum information is no longer directly accessible from the resonator. To retrieve the quantum states initially stored, our goal is to apply Hahn-echo refocusing techniques inspired by magnetic-resonance methods [36]. These techniques are based on the application of π-pulses that act as a time reversal for the spins, producing a dipole rephasing and the subsequent emission of an echo of the initially stored states. For our quantum memory purpose, this *read operation* has to be implemented at the quantum level, with retrieval efficiency close to 1, and in a setup compatible with superconducting qubit technology. The object of the second part of this thesis work is precisely to identify the challenges posed by this task and to demonstrate experimentally that they can be solved. In this aim, in Chap. 5 we test a protocol simpler than the full *read operation* but which constitutes an essential building block (Fig. 1.10): the retrieval with a single refocusing pulse of weak microwave pulses initially stored [37]. The hybrid quantum circuit developed for this experiment [23] is shown in Fig. 1.11. It consists of a diamond single-crystal placed on top of the inductance of a planar superconducting LC resonator. A fiber is attached to the circuit, in which green light can be injected for active reset of the spin ensemble.

A prerequisite: active reset of the spins Prior to memory operation, the spin ensemble must be initialized in its ground state, or close enough. NV center spins have spin transition frequencies in the GHz range and thus, without external excitation, are mainly polarized in the spin ground state at millikelvin temperature. Once excited however, they relax extremely slowly in the spin ground state [23, 38]. To test the *write step* of the protocol, we operated at the single-photon level such that the amount of excited spins was always negligible compared to the total number of spins. In the second part of the protocol however, strong refocusing pulses are applied and subsequently a large amount of excited spins is left at the end of each experimental sequence. To repeat at a reasonable rate, there is thus a need for an active reset of the NV spins. In this aim, the usual optical pumping used at room-temperature (see Fig. 1.1) is adapted to the low-temperature environment [23].

Fig. 1.10 **The read step**

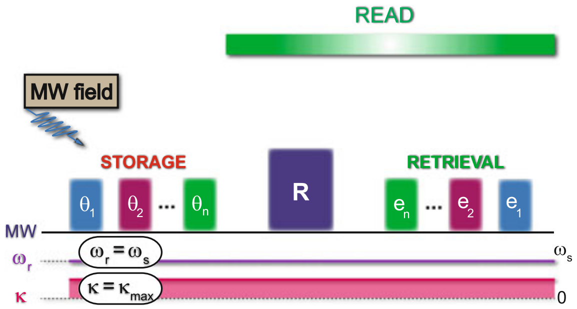

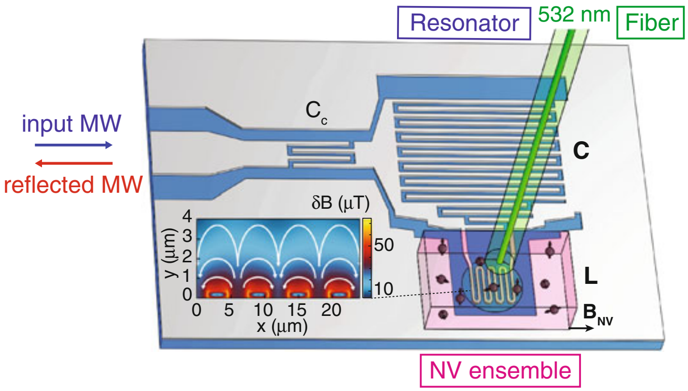

Fig. 1.11 Read experiment: schematic of the circuit. An ensemble of NV electronic spins (*pink*) is coupled to a planar superconducting LC resonator. Laser pulses are shone on the diamond through an optical fiber glued to its top face, to reset the spins in their ground states between successive operation

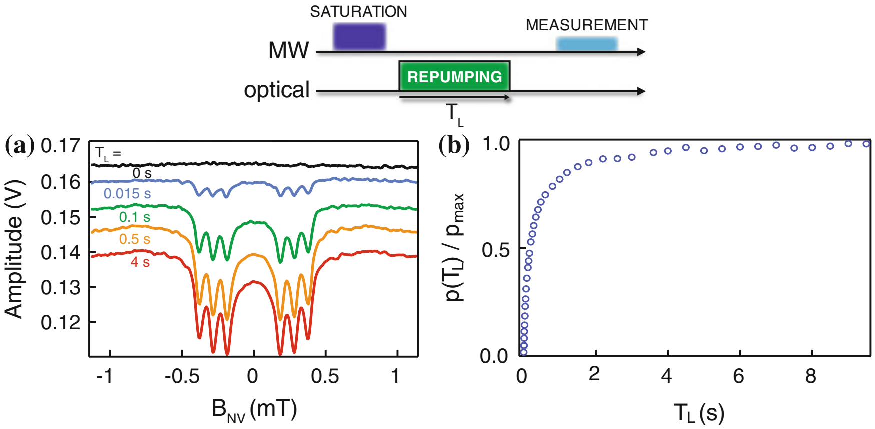

Fig. 1.12 Read experiment: active reset of the spins. a Reflected amplitude for 1.5 mW laser power and different duration T_L. The curves show the spectroscopic signatures of the spins, with an amplitude that increases with T_L because of increasing spin polarisation. **b** Relative spin polarisation dependence on T_L

Typical pulsed polarization experiments are shown in Fig. 1.12 with 1.5 mW optical power. The spin polarization increases with the optical pulse duration and then saturates, which indicates that the spins reach the maximum polarization allowed by optical pumping at this wavelength. In this circuit a large polarization of the spins is obtained in a few seconds, sufficiently fast to make it possible to implement the *read step* of the protocol. The detailed description of the active reset of the spins can be found in Sect. 5.4.

Storage and retrieval of multiple few photon field Fig. 1.13 shows an example of multimode storage and retrieval of weak microwave pulses with refocusing

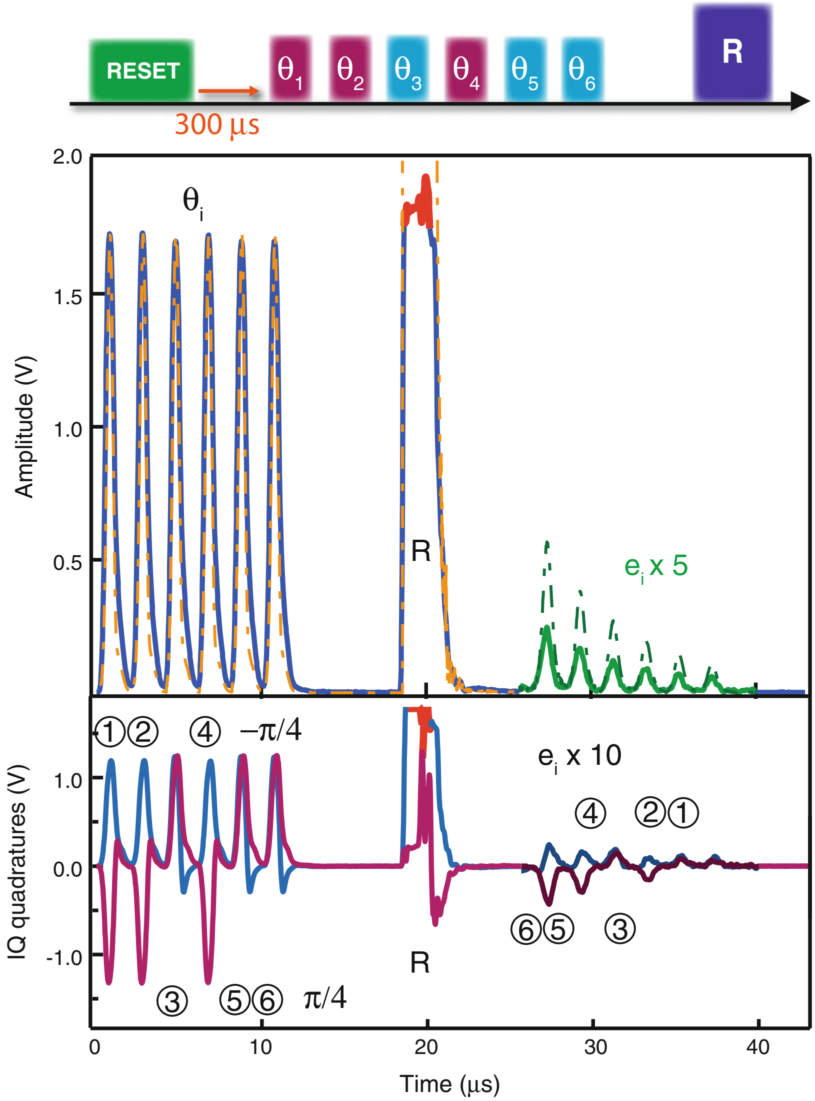

Fig. 1.13 **Read experiment.** Six consecutive microwave pulses θ_i with a varying phase and identical amplitude corresponding to $\approx 10^4$ photons in the resonator are absorbed by the spin ensemble, followed 10 μs later by a strong refocusing pulse R applied to trigger their retrieval. The six pulses are recovered up to 35 μs after their storage with an amplitude reduced by $\sim 10^2$ compared to the incoming pulses

techniques. Six consecutive microwave pulses are first absorbed by the spin ensemble and a single refocusing pulse is applied. The six pulses are retrieved up to 35 μs after their storage [23]. This result demonstrates that complex dynamical control of spin ensembles is compatible with hybrid quantum circuits, as requested for our quantum memory protocol. The efficiency of the process is $\sim 2 \cdot 10^{-4}$, limited by the short echo coherence time of the spin ensemble used for the experiment. In Chap. 5, we discuss this experiment in greater details together with the factors that limit the efficiency, for the purpose of developing efficient *read* memory operation.

1.5 NV Clock Transitions for Long Coherent Storage

A quantum memory is only interesting if it has long coherence times. For NV centers, Hahn-echo coherence times T_2 up to 5 ms have been obtained with single spins at room temperature [39], and up to 1 s in ensembles of NV centers at 100 K using dynamical decoupling [17]. So far, most of these echo coherence time measurements on NV centers have been performed at finite magnetic fields. Indeed the NV spectrum around zero magnetic field is complicated by terms in the Hamiltonian describing the effect of strain or electric fields, which induce a mixing between the spin states $m_S = \pm 1$ due to spin orbit interaction.

We point out in our experiments that this spin mixing has an interesting consequence: the NV eigenstates present a sweet spot and become insensitive to first order to magnetic field fluctuations. In such case, the coherence time is expected to show an enhancement, a situation known as a clock transition (CT) [40]. The hybrid quantum circuit that we developed for the second experiment makes it possible to unveil several aspects of the NV low-field properties. Three CTs exist at finite magnetic field due to the hyperfine interaction of the NV center electronic spin with the nitrogen (^{14}N) nuclear spin. At these CTs, the Hahn-echo time T_2 shows an enhancement (see Fig. 1.14). Put back in the perspective of the development of a quantum memory

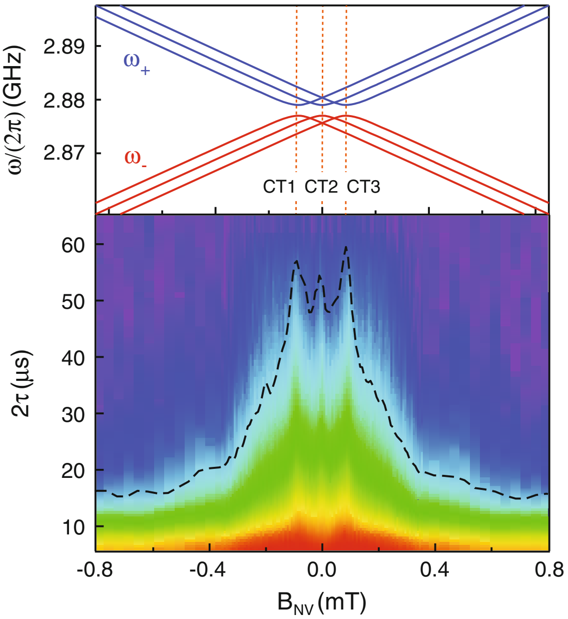

Fig. 1.14 Decay of the spin-echo amplitude as a function of the external magnetic field. The coherence time is enhanced at the three clock transitions

for superconducting qubits, those points have potential interest for memory operation. A more detailed analysis of the coherence times around these clock transitions is presented in Sect. 5.6.

1.6 Towards an Operational Quantum Memory

The two experiments outlined in this thesis work constitute proofs-of-concept of *write* and *read* memory operations in a spin ensemble. In order to reach an operational quantum memory for superconducting qubits, further developments are however required: (i) the fidelity of the memory operations must come closer to 1, which calls for a quantitative understanding of our experiments imperfections, and (ii) the complete memory protocol of Fig. 1.3 must be implemented, which requires the development of new engineering solutions for tuning the cavity parameters.

Reaching efficient memory operations The experiment reported in Chap. 4 demonstrates complete storage of arbitrary qubit states in the spin ensemble with ∼95 % efficiency which validates the *write step* of the protocol. Its retrieval however is challenging, as shown by the experiment described in Chap. 5: with refocusing sequence, we obtain a retrieval efficiency of order 10^{-4}. We analyze this low retrieval efficiency as due to three factors: the finite echo coherence time of the ensemble, the finite spin coupling to the resonator and the refocusing pulse imperfections. Numerical simulations, in good agreement with the data (see Fig. 1.13), show that, in this experiment, the main limitation of the retrieval efficiency is the short echo coherence time of the spins, which yields a reduction by a factor 10^3.

Longer coherence times can be achieved [17] with samples having a reduced concentration of nitrogen impurities as well as isotopic enrichment in ^{12}C. Such a sample was provided to us by Junichi Isoya after the experiments reported in Chaps. 4 and 5. Figure 1.15 shows a storage and retrieval experiment performed in a hybrid

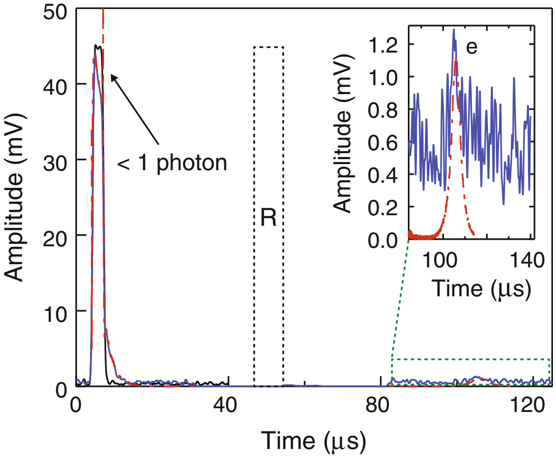

Fig. 1.15 Storage and retrieval at the single photon level in an isotopically enriched sample having long coherence times. Less than 1 photon is absorbed by the spins and retrieved after 100 μs storage with 0.5 % efficiency

quantum circuit similar to Fig. 1.11 with this new sample for which we measured $T_2 = 84\,\mu\text{s}$. The retrieval is achieved with much larger efficiency: $5 \cdot 10^{-3}$ instead of 10^{-4} despite a longer storage time (100 µs). The storage pulse contains < 1 photon, demonstrating that when the retrieval efficiency is sufficient, we can go down to the single photon level, as required for the memory protocol. Besides coherence times, better refocusing pulses can be obtained either by rapid adiabatic passage [21, 41], or by tailoring the spin spatial distribution [42, 43]. These combined advances should make possible to reach the figures of merit requested for the *read step* to be in the quantum regime, and therefore to implement the full quantum memory protocol of Fig. 1.3 at the single photon level. Preliminary measurements in this direction and solutions for development up to the operational level are discussed in Sect. 6.1 of this thesis.

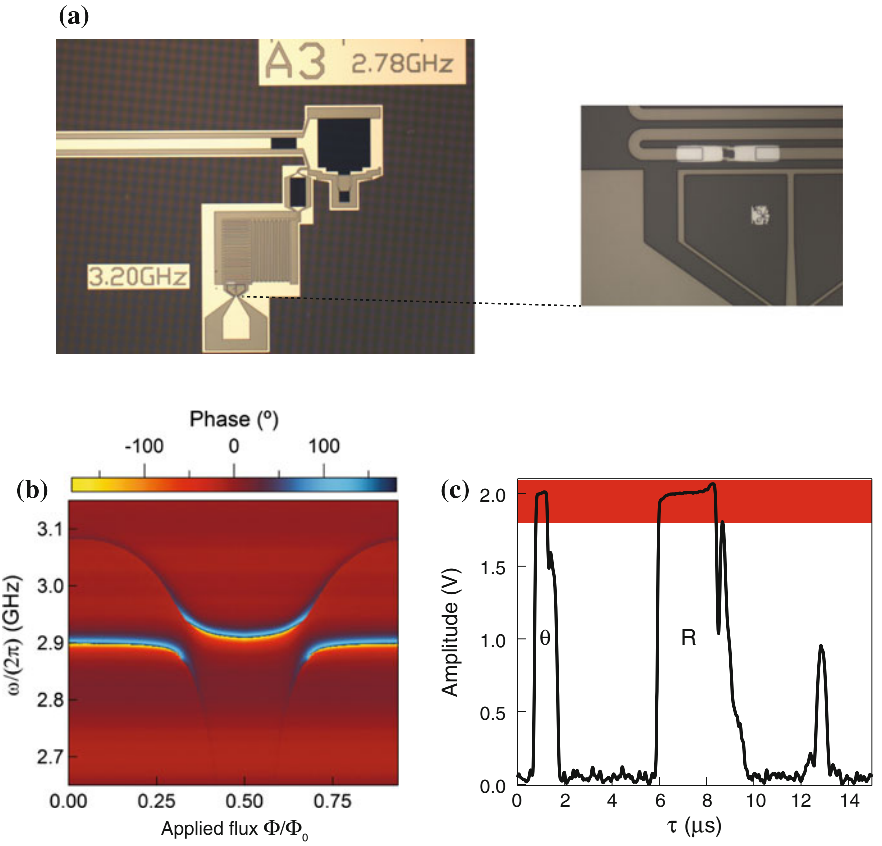

Fig. 1.16 Tuning the cavity ON and OFF resonance during the refocusing sequence. a The quantum bus is coupled to a second resonator made tunable in frequency by inserting a SQUID loop. **b** Spectroscopy of the circuit as a function of the local magnetic field applied to the SQUID loop of the tunable resonator. The frequency of the quantum bus is displaced due to the coupling with the tunable resonator. **c** Storage and retrieval of a weak microwave pulse, demonstrating the compatibility of the circuit with the application of refocusing pulses

Running the full quantum memory protocol The echo protocol that was tested in the experiment reported in Chap. 5 is not suitable by itself for a quantum memory. As mentioned above and further explained in Chap. 3, there is a need in our protocol to dynamically tune the cavity frequency and quality factor during the refocusing sequence. This task is challenging compared to what we achieved for the *write* experiment: when strong refocusing pulses are applied, the usual way of tuning the resonator parameters by inserting a SQUID is not allowed because of the high intra-cavity field in the resonator. We worked on the development of alternative solutions, especially on the frequency tunability. The approach we followed is to couple the quantum bus to a second resonator, itself made tunable in frequency by inserting a SQUID. We show in Fig. 1.16 the spectroscopy of this circuit showing a detuning up to 40 MHz, and spin echo signal obtained using refocusing pulses. This experiment demonstrates the operation of a frequency tunable resonator compatible with the applications of refocusing pulses. We discuss in details this experiment in Sect. 6.2 of this manuscript, together with engineering solutions to realize a circuit able to run the full memory protocol.

References

1. N. Daniilidis, H. Häffner, Quantum interfaces between atomic and solid-state systems. Ann. Rev. Condens. Matter Phys. **4**, 83–112 (2013)
2. Z. Xiang, S. Ashhab, J.Q. You, F. Nori, Hybrid quantum circuits: Superconducting circuits interacting with other quantum systems. Rev. Mod. Phys. **85**, 623 (2013)
3. A. Blais, R.-S. Huang, A. Wallraff, S.M. Girvin, R.J. Schoelkopf, Cavity quantum electrodynamics for superconducting electrical circuits: An architecture for quantum computation. Phys. Rev. A **69**, 062320 (2004)
4. A. Wallraff, D.I. Schuster, A. Blais, L. Frunzio, R.-S. Huang, J. Majer, S. Kumar, S.M. Girvin, R.J. Schoelkopf, Strong coupling of a single photon to a superconducting qubit using circuit quantum electrodynamics. Nature **431**, 162 (2004)
5. H. Paik, D.I. Schuster, L.S. Bishop, G. Kirchmair, G. Catelani, A.P. Sears, B.R. Johnson, M.J. Reagor, L. Frunzio, L.I. Glazman, S.M. Girvin, M.H. Devoret, R.J. Schoelkopf. Observation of high coherence in josephson junction qubits measured in a three-dimensional circuit QED architecture. Phys. Rev. Lett. **107**, 240501 (2011)
6. R. Barends, J. Kelly, A. Megrant, D. Sank, E. Jeffrey, Y. Chen, Y. Yin, B. Chiaro, J. Mutus, C. Neill, P. O'Malley, P. Roushan, J. Wenner, T.C. White, A.N. Cleland, J.M. Martinis, Coherent josephson qubit suitable for scalable quantum integrated circuits. Phys. Rev. Lett. **111**, 080502 (2013)
7. L. Tian, P. Rabl, R. Blatt, P. Zoller, Interfacing quantum-optical and solid-state qubits. Phys. Rev. Lett. **92**, 247902 (2004)
8. A.S. Sørensen, C.H. van der Wal, L.I. Childress, M.D. Lukin, Capacitive coupling of atomic systems to mesoscopic conductors. Phys. Rev. Lett. **92**, 063601 (2004)
9. D. Petrosyan, G. Bensky, G. Kurizki, I. Mazets, J. Majer, J. Schmiedmayer, Reversible state transfer between superconducting qubits and atomic ensembles. Phys. Rev. A **79**, 040304 (2009)
10. M. Hafezi, Z. Kim, S.L. Rolston, L.A. Orozco, B.L. Lev, J.M. Taylor, Atomic interface between microwave and optical photons. Phys. Rev. A **85**, 020302 (2012)
11. P. Rabl, D. DeMille, J.M. Doyle, M.D. Lukin, R.J. Schoelkopf, P. Zoller, Hybrid quantum processors: Molecular ensembles as quantum memory for solid state circuits. Phys. Rev. Lett. **97**, 033003 (2006)

12. D.I. Schuster, A. Fragner, M.I. Dykman, S.A. Lyon, R.J. Schoelkopf, Proposal for manipulating and detecting spin and orbital states of trapped electrons on helium using cavity quantum electrodynamics. Phys. Rev. Lett. **105**, 040503 (2010)
13. A. Imamoglu, Cavity QED based on collective magnetic dipole coupling: Spin ensembles as hybrid two-level systems. Phys. Rev. Lett. **102**, 083602 (2009)
14. J.H. Wesenberg, A. Ardavan, G.A.D. Briggs, J.J.L. Morton, R.J. Schoelkopf, D.I. Schuster, K. Mølmer, Quantum computing with an electron spin ensemble. Phys. Rev. Lett. **103**, 070502 (2009)
15. D. Marcos, M. Wubs, J.M. Taylor, R. Aguado, M.D. Lukin, A.S. Sørensen, Coupling nitrogen-vacancy centers in diamond to superconducting flux qubits. Phys. Rev. Lett. **105**, 210501 (2010)
16. F. Jelezko, T. Gaebel, I. Popa, A. Gruber, J. Wrachtrup, Observation of coherent oscillations in a single electron spin. Phys. Rev. Lett. **92**, 076401 (2004)
17. N. Bar-Gill, L. Pham, A. Jarmola, D. Budker, R. Walsworth, Solid-state electronic spin coherence time approaching one second. Nat. Commun. **4**, 1743 (2013)
18. N.B. Manson, J.P. Harrison, M.J. Sellars, Nitrogen-vacancy center in diamond: Model of the electronic structure and associated dynamics. Phys. Rev. B **74**, 104303 (2006)
19. Y. Kubo, F.R. Ong, P. Bertet, D. Vion, V. Jacques, D. Zheng, A. Dreau, J.F. Roch, A. Auffeves, F. Jelezko, J. Wrachtrup, M.F. Barthe, P. Bergonzo, D. Esteve, Strong coupling of a spin ensemble to a superconducting resonator. Phys. Rev. Lett. **105**, 140502 (2010)
20. A. Dewes, R. Lauro, F.R. Ong, V. Schmitt, P. Milman, P. Bertet, D. Vion, D. Esteve, Quantum speeding-up of computation demonstrated in a superconducting two-qubit processor. Phys. Rev. B **85**, 140503 (2012)
21. B. Julsgaard, C. Grezes, P. Bertet, K. Mølmer, Quantum memory for microwave photons in an inhomogeneously broadened spin ensemble. Phys. Rev. Lett. **110**, 250503 (2013)
22. Y. Kubo, C. Grezes, A. Dewes, T. Umeda, J. Isoya, H. Sumiya, N. Morishita, H. Abe, S. Onoda, T. Ohshima, V. Jacques, A. Dréau, J.-F. Roch, I. Diniz, A. Auffeves, D. Vion, D. Esteve, P. Bertet, Hybrid quantum circuit with a superconducting qubit coupled to a spin ensemble. Phys. Rev. Lett. **107**, 220501 (2011)
23. C. Grezes, B. Julsgaard, Y. Kubo, M. Stern, T. Umeda, J. Isoya, H. Sumiya, S. Abe, S. Onoda, T. Ohshima, V. Jacques, J. Esteve, D. Vion, D. Esteve, K. Moelmer, P. Bertet, Multimode storage and retrieval of microwave fields in a spin ensemble. Phys. Rev. X **4**, 021049 (2014)
24. A.I. Lvovsky, B.C. Sanders, W. Tittel, Optical quantum memory. Nat. Photonics **3**, 706–714 (2009)
25. V. Damon, M. Bonarota, A. Louchet-Chauvet, T. Chanelière, J.-L. Le Gouët, Revival of silenced echo and quantum memory for light. New J. Phys. **13**, 093031 (2011)
26. D.L. McAuslan, P.M. Ledingham, W.R. Naylor, S.E. Beavan, M.P. Hedges, M.J. Sellars, J.J. Longdell, Photon-echo quantum memories in inhomogeneously broadened two-level atoms. Phys. Rev. A **84**, 022309 (2011)
27. K. Tordrup, A. Negretti, K. Mølmer. Holographic quantum computing. Phys. Rev. Lett. **101**, 040501 (2008)
28. B. Julsgaard, K. Mølmer. Fundamental limitations in spin-ensemble quantum memories for cavity fields. Phys. Rev. A **88**, 062324 (2013)
29. D.I. Schuster, A.P. Sears, E. Ginossar, L. DiCarlo, L. Frunzio, J.J.L. Morton, H. Wu, G.A.D. Briggs, B.B. Buckley, D.D. Awschalom, R.J. Schoelkopf, High-cooperativity coupling of electron-spin ensembles to superconducting cavities. Phys. Rev. Lett. **105**, 140501 (2010)
30. R. Amsüss, Ch. Koller, T. Nöbauer, S. Putz, S. Rotter, K. Sandner, S. Schneider, M. Schramböck, G. Steinhauser, H. Ritsch, J. Schmiedmayer, J. Majer, Cavity QED with magnetically coupled collective spin states. Phys. Rev. Lett. **107**, 060502 (2011)
31. V. Ranjan, G. de Lange, R. Schutjens, T. Debelhoir, J.P. Groen, D. Szombati, D.J. Thoen, T.M. Klapwijk, R. Hanson, L. DiCarlo, Probing dynamics of an electron-spin ensemble via a superconducting resonator. Phys. Rev. Lett. **110**, 067004 (2013)
32. S. Probst, H. Rotzinger, S. Wünsch, P. Jung, M. Jerger, M. Siegel, A.V. Ustinov, P.A. Bushev, Anisotropic rare-earth spin ensemble strongly coupled to a superconducting resonator. Phys. Rev. Lett. **110**, 157001 (2013)

33. Y. Kubo, I. Diniz, A. Dewes, V. Jacques, A. Dréau, J.-F. Roch, A. Auffeves, D. Vion, D. Esteve, P. Bertet, Storage and retrieval of a microwave field in a spin ensemble. Phys. Rev. A **85**, 012333 (2012)
34. M. Sandberg, C.M. Wilson, F. Persson, T. Bauch, G. Johansson, V. Shumeiko, T. Duty, P. Delsing, Tuning the field in a microwave resonator faster than the photon lifetime. Appl. Phys. Lett. **92**(20), 203501–203503 (2008)
35. A. Palacios-Laloy, F. Nguyen, F. Mallet, P. Bertet, D. Vion, D. Esteve, Tunable resonators for quantum circuits. J. Low Temp. Phys. **151**, 1034 (2008)
36. E.L. Hahn, Spin echoes. Phys. Rev. **80**, 580–594 (1950)
37. A.G. Anderson, R.L. Garwin, E.L. Hahn, J.W. Horton, G.L. Tucker, R.M. Walker, Spin echo serial storage memory. J. Appl. Phys. **26**, 1324 (1955)
38. A. Jarmola, V.M. Acosta, K. Jensen, S. Chemerisov, D. Budker, Temperature and magnetic field dependent longitudinal spin relaxation in nitrogen-vacancy ensembles in diamond. Phys. Rev. Lett. **108**, 197601 (2012)
39. G. Balasubramian, P. Neumann, D. Twitchen, M. Markham, R. Koselov, N. Mizuochi, J. Isoya, J. Achard, J. Beck, J. Tissler, V. Jacques, P.R. Hemmer, F. Jelezko, J. Wrachtrup, Ultralong spin coherence time in isotopically engineered diamond. Nat. Mater. **8**, 383 (2009)
40. G. Wolfowicz, A.M. Tyryshkin, R.E. George, H. Riemann, N.V. Abrosimov, P. Becker, H. Pohl, M. Thewalt, S.A. Lyon, J. Morton, Atomic clock transitions in silicon-based spin qubits. Nat. Nanotechnol. **8**(6), 561–564 (2013)
41. A.J. Sigillito, H. Malissa, A.M. Tyryshkin, H. Riemann, N.V. Abrosimov, P. Becker, H.-J. Pohl, M.L.W. Thewalt, K.M. Itoh, J.J.L. Morton, A.A. Houck, D.I. Schuster, S.A. Lyon, Fast, low-power manipulation of spin ensembles in superconducting microresonators. Appl. Phys. Lett. **104**(22), 222407 (2014)
42. O.W.B. Benningshof, H.R. Mohebbi, I.A.J. Taminiau, G.X. Miao, D.G. Cory, Superconducting microstrip resonator for pulsed ESR of thin films. J. Magn. Reson. **230**, 84–87 (2013)
43. D.M. Toyli, C.D. Weis, G.D. Fuchs, T. Schenkel, D. Awschalom, Chip-scale nanofabrication of single spins and spin arrays in diamond. Nano Lett. **10**(8), 3168–3172 (2010)

Chapter 2
Background

The experiments reported in this thesis rely on two elements: Josephson superconducting circuits (the processor) and NV center spins in diamond (the memory). In this chapter, we introduce the minimum theoretical background needed to understand the work which follows.

2.1 Superconducting Circuits and Microwave Engineering

In this section, we provide the reader elements of theory on superconducting circuits and microwave engineering which are relevant for this work. We start with the simplest circuit, the superconducting resonator, which is of particular interest for our experiments as it is used as a bus between spins and circuits. We then see how resonators can be turned into active devices, using Josephson junctions. Along these lines, we describe how to implement the qubit concept by pushing Josephson circuits to the level of very large anharmonicity. We finally introduce the field of circuit quantum electrodynamics, which describes the interaction of a qubit with single photons in a resonator.

2.1.1 Superconducting Resonators

2.1.1.1 The LCR Resonator

We start with the quantum treatment of the simplest superconducting circuit that can be built: the LC resonator. Its schematic is given in Fig. 2.1, consisting of an inductance L in parallel with a capacitance C. We note V the voltage across the capacitance and I the current. As explained e.g. in [1, 2], the circuit can be quantized in terms

© Springer International Publishing Switzerland 2016
C. Grèzes, *Towards a Spin-Ensemble Quantum Memory for Superconducting Qubits*, Springer Theses,
DOI 10.1007/978-3-319-21572-3_2

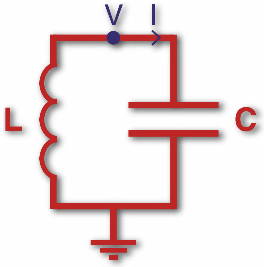

Fig. 2.1 **A *LC* resonator**

of two generalized conjugate quantum operators, $\hat{\Phi}$ the flux in the inductance and $\hat{Q}$ the charge accumulated on the capacitor, obeying $[\hat{\Phi}, \hat{Q}] = i\hbar$, with Hamiltonian:

$$\hat{H} = \frac{\hat{Q}^2}{2C} + \frac{\hat{\Phi}^2}{2L} \tag{2.1}$$

This harmonic oscillator Hamiltonian can be written:

$$\hat{H} = \hbar\omega_r \left(\hat{a}^\dagger\hat{a} + \frac{1}{2}\right) \tag{2.2}$$

where $\hat{a}^\dagger$, $\hat{a}$ are respectively the creation and annihilation operators

$$\hat{a}^\dagger = \frac{1}{\sqrt{2\hbar Z_r}}\left(\hat{\Phi} - iZ_r\hat{Q}\right) \tag{2.3}$$

$$\hat{a} = \frac{1}{\sqrt{2\hbar Z_r}}\left(\hat{\Phi} + iZ_r\hat{Q}\right) \tag{2.4}$$

with $\omega_r = 1/\sqrt{LC}$ the resonance frequency and $Z_r = \sqrt{L/C}$ the resonator impedance. The eigenstates $|n\rangle$ of $\hat{H}$ are called Fock states, satisfying $\hat{H}|n\rangle = \hbar\omega_r\left(n + \frac{1}{2}\right)|n\rangle$ with n the number of photons stored in the resonator. The relations Eqs. 2.3 and 2.4 can be inverted to obtain the expression of the flux and charge operators $\hat{\Phi}$ and $\hat{Q}$ and calculate their time derivatives to express the voltage and current operators $\hat{V} = i[\hat{H}, \hat{\Phi}]/\hbar$ and $\hat{I} = i[\hat{H}, \hat{Q}]/\hbar$ in term of the field operators:

$$\hat{V} = iV_{rms}(\hat{a}^\dagger - \hat{a}) \tag{2.5}$$

$$\hat{I} = \frac{V_{rms}}{Z_r}(\hat{a}^\dagger + \hat{a}) \tag{2.6}$$

with $V_{rms} = \omega_r\sqrt{\hbar Z_r/2}$ the root-mean-square vacuum fluctuations of the voltage. The current and voltage in the resonator give rise to associated electric (in the capacitance) and magnetic (around the inductance) fields:

$$\hat{E}(\mathbf{r}) = i\delta E_0(\mathbf{r})\left(\hat{a} - \hat{a}^\dagger\right), \ \hat{B}(\mathbf{r}) = \delta B_0(\mathbf{r})\left(\hat{a} + \hat{a}^\dagger\right) \tag{2.7}$$

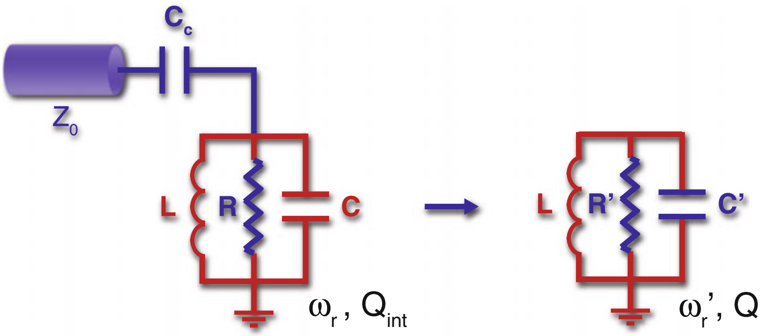

Fig. 2.2 A LCR resonator coupled to an input transmission line with characteristic impedance Z_0 through a gate capacitance C_c. It is equivalent to a resonator with effective resistance R' and capacitance C'. The resonator frequency and characteristic impedance are shifted to ω_r' and Z_r' with respect to that of the decoupled one

at position $\mathbf{r}$, with $\delta E_0(\mathbf{r})$ and $\delta B_0(\mathbf{r})$ their vacuum fluctuations. This electromagnetic field is used to couple the resonator to the qubit and the spins and thus play a major role throughout this manuscript.

In an experiment, a resonator can have internal losses and is coupled to measuring lines. We thus consider the more general case shown in Fig. 2.2 of a resonator with internal losses modelled by a resistance R, and coupled to an input transmission line with characteristic impedance Z_0 through a gate capacitance C_c. The capacitor acts as a semi-reflective mirror in optics and induces a strong impedance mismatch so that the electromagnetic field is confined in it. We want to determine the modified resonator frequency ω_r' and impedance Z_r'. The circuit is equivalently modeled as a modified LCR resonator with an effective resistance R' such that:

$$\frac{1}{R'} = \frac{1}{R} + \frac{1}{R_{ext}} \tag{2.8}$$

with $R_{ext}/Z_0 = 1/(C_c Z_0 \omega_r)^2 + 1$, and a new capacitance

$$C' = C + \frac{C_c}{1 + (C_c \omega_r Z_0)^2} \approx C + C_c \tag{2.9}$$

This slightly changes the resonance frequency and the impedance to $1/\sqrt{LC'}$ and $\sqrt{L/C'}$ respectively. An important quantity is the resonator quality factor, defined as $Q = R'/Z_r$. This quantity can be separated in two contributions:

$$Q^{-1} = Q_{int}^{-1} + Q_{ext}^{-1} \tag{2.10}$$

where $Q_{int} = R/Z_r$ is the internal quality factor, and $Q_{ext} = R_{ext}/Z_r$ the coupling quality factor. Associated damping rates are defined as $\kappa_L = \omega_r'/Q_{int}$ the rate at which the energy is dissipated in R and $\kappa = \omega_r'/Q_{ext}$ the rate at which the energy leaks out of the resonator into the measurement lines through C_c. In the usual case where the coupling capacitance is very small compared to the capacitance of the resonator $C_c \ll C'$:

$$\omega_r' \approx \omega_r, \quad Z_r' \approx Z_r, \quad R_{ext} \approx 1/Z_0 C_c^2 \omega_r^2 \tag{2.11}$$

so that the external damping rate writes:

$$\kappa = \omega_r^3 C_c^2 Z_0 Z_r \tag{2.12}$$

and equivalently

$$C_c = 1/\sqrt{Q_{ext} Z_0 Z_r \omega_r^2} \tag{2.13}$$

In the following, we continue noting the resonance frequency ω_r and the impedance Z_r by convenience.

2.1.1.2 Probing the Resonator from the Outside

To probe the resonators, they are connected to voltage sources through measurement lines. In the following, we consider the case often encountered in our experiments of a resonator coupled to two transmission lines (ports 1 and 2) with coupling capacitances $C_{c,1}$ and $C_{c,2}$ yielding the damping rates κ_1 and κ_2 through Eq. 2.12, and a voltage $V_1(t) = V_1 \cos(\omega t)$ applied to port 1 (see Fig. 2.3a). We note I_i the current flowing into the ith port and model the transmission lines by impedances Z_0, V the voltage across the resonator capacitance, and I the current through the inductance. An equivalent description, but more adapted to our experiments, is to replace the voltage source $V_1(t)$ by a wave $V_{1+}(t)$ incoming onto the resonator input via the transmission line and driving it, generating an intra-cavity field $V(t)$ and $I(t)$, and giving rise to outgoing waves $V_{1-}(t)$ and $V_{2-}(t)$ that describe the leakage of the intra-cavity field towards the measurement apparatus. In this scattering approach (see Fig. 2.3b), the behavior of the resonator is described by the so-called scattering matrix $S_{ij} = a_{out,i}/a_{in}$, with the classical input and output waves $a_{in/out,i}$ defined as

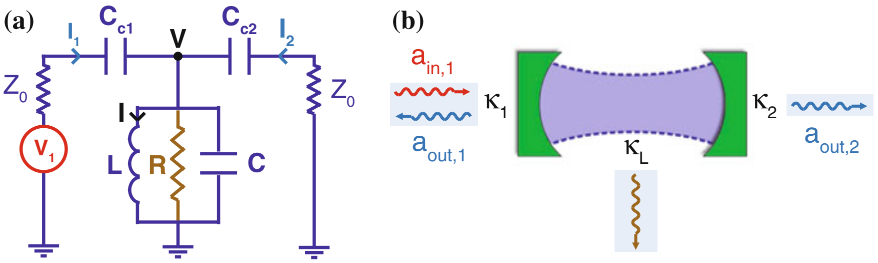

Fig. 2.3 Circuit and its equivalent in the input-output theory framework. a Electrical circuit. **b** Input-output theory framework

$$a_{in,i} = \frac{V_i + Z_0 I_i}{2\sqrt{Z_0}} = \frac{V_i^+}{\sqrt{Z_0}} \qquad \text{and} \qquad a_{out,i} = \frac{V_i - Z_0 I_i}{2\sqrt{Z_0}} = \frac{V_i^-}{\sqrt{Z_0}} \tag{2.14}$$

The quantum-mechanical extension of this classical scattering approach is provided by the input-output theory developed by Gardiner and Collett [3]. There, the intra-resonator field is described by the quantum-mechanical operator $\hat{a}(t)$, whose knowledge directly yields the resonator currents and voltages through Eqs. 2.5 and 2.6. Its evolution (in the Heisenberg representation) obeys to the master equation

$$\partial_t \hat{a}(t) = \frac{[\hat{a}(t), \hat{H}]}{i\hbar} - \left(\sum_i \frac{\kappa_i}{2}\right)\hat{a} + \sum_i \sqrt{\kappa_i}\hat{a}_{in,i}(t) \tag{2.15}$$

This intra-cavity field equation is complemented with a relation stating the continuity of the fields at each port i

$$\hat{a}_{in,i}(t) + \hat{a}_{out,i}(t) = \sqrt{\kappa_i}\hat{a}(t) \tag{2.16}$$

In these equations, the input and output fields $\hat{a}_{in,out}(t)$ are the quantum analog of the classical waves described earlier. In our experiments the drive fields will always be coherent states, so that we will take $\hat{a}_{in,1}(t) = \alpha_{in} e^{-i\omega t}$, with α_{in} normalized such that $|\alpha_{in}|^2$ is the number of photons per second at the resonator input, or equivalently $P = \hbar\omega|\alpha_{in}|^2$. Applying these equations to the linear resonator depicted in Fig. 2.3b yields:

$$\partial_t \alpha(t) = -i\omega_r \alpha(t) - \frac{\kappa + \kappa_L}{2}\alpha(t) + \sqrt{\kappa_1}\alpha_{in}(t), \tag{2.17}$$

with $\alpha(t) = \langle\hat{a}\rangle(t)$ the mean value of the intra-resonator field, $\kappa = \kappa_1 + \kappa_2$ the total resonator external damping rate. In steady-state $\alpha(t) = \alpha e^{-i\omega t}$, yielding

$$\alpha(\omega) = \frac{i\sqrt{\kappa_1}}{(\omega - \omega_r) + i\frac{\kappa+\kappa_L}{2}}\alpha_{in} \tag{2.18}$$

At resonance, the intra-cavity average photon number $\bar{n} = |\alpha|^2$ is

$$\bar{n} = \frac{4\kappa_1}{\hbar\omega_r(\kappa + \kappa_L)^2}P. \tag{2.19}$$

These equations allow us to obtain useful relations linking the resonator maximum voltages and currents V_0 and I_0 defined as $V(t) = V_0 \sin(\omega t)$ and $I(t) = I_0 \cos(\omega t)$ to the input power. Combining Eqs. 2.5, 2.6 and 2.19 yields

$$V_0 = \frac{\sqrt{8 Z_r \omega_r \kappa_1}}{\kappa + \kappa_L}\sqrt{P} \qquad \text{and} \qquad I_0 = \frac{\sqrt{8\omega_r \kappa_1 / Z_r}}{\kappa + \kappa_L}\sqrt{P} \tag{2.20}$$

Reflection measurement The reflection coefficient $r = \frac{\alpha_{out,1}}{\alpha_{in}}$ follows from Eqs. 2.16–2.18:

$$r(\omega) = \frac{\sqrt{\kappa_1}\alpha - \alpha_{in}}{\alpha_{in}} = \frac{i\kappa_1}{(\omega - \omega_r) + i\frac{\kappa+\kappa_L}{2}} - 1 \tag{2.21}$$

In the experiments reported in Chap. 5, in particular, we use a resonator with only one port so that $\kappa_2 = 0$ and $\kappa = \kappa_1$ in the above expressions. Depending on the rate between the coupling constant κ and the losses κ_L we can define three regimes characterized by different behaviors of the reflection coefficient (Fig. 2.4a):

- **The over-coupled regime** (red curves) defined by $\kappa \gg \kappa_L$. In this regime $|r| \approx 1$ for all frequencies and the phase ϕ undergoes a 2π shift at resonance

$$\phi = 2\arctan\left(2\frac{\omega - \omega_r}{\kappa}\right)$$

- **The critical coupling regime** (green curves) defined by $\kappa = \kappa_L$. For this regime the amplitude of r reaches 0 at resonance, while a discontinuity in its phase brings a phase shift of π.
- **The under-coupled regime** (blue curves) defined by $\kappa \ll \kappa_L$. In this regime the resonance corresponds to a dip in the amplitude of r and a shift $< \pi$ in its phase.

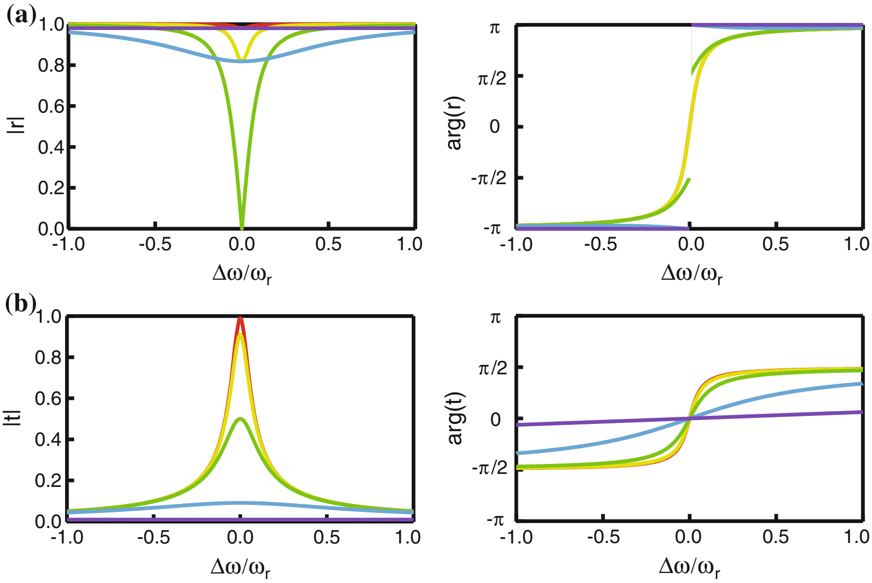

Fig. 2.4 **Probing the resonator.** **a** Reflection measurement. Frequency dependence of the reflection coefficient r for $\kappa_L = 0.01\kappa$ (*red*), $\kappa_L = 0.1\kappa$ (*yellow*), $\kappa_L = \kappa$ (*green*), $\kappa_L = 10\kappa$ (*blue*) and $\kappa_L = 100\kappa$ (*purple*). **b** Transmission measurement. Frequency dependence of the transmission coefficient t for the same values of damping

The width of both the dip and the phase shift decrease when κ_L/κ increases. Both the amplitude and the phase differ very slightly from their out-of-resonance value.

Transmission measurement The transmission coefficient $t = \frac{\alpha_{out,2}}{\alpha_{in}}$ follows from Eqs. 2.16–2.18:

$$t(\omega) = \frac{\sqrt{\kappa_2}\alpha}{\alpha_{in}} = \frac{i\sqrt{\kappa_1\kappa_2}}{(\omega - \omega_r) + i\frac{\kappa+\kappa_L}{2}}. \tag{2.22}$$

In the experiments reported in Chap. 4 we have $\kappa_1 = \kappa_2 = \kappa/2$. As in reflection measurements, depending on the rate between the coupling constant κ and the losses κ_L we can define three regimes characterized by different behaviors of the transmission coefficient (Fig. 2.4b):

- **The over-coupled regime** (red curves) defined by $\kappa \gg \kappa_L$, in which $|t|$ almost reaches 1 at resonances. The phase of t undergoes a π shift at resonance, whose width, as well as the width of $|t|$, is controlled by κ_L.
- **The critical coupling regime** (green curves) defined by $\kappa = \kappa_L$. In this regime, the amplitude of t reaches $1/2$ at resonance and the widths are controlled by both κ and κ_L.
- **The under-coupled regime** (blue curves) defined by $\kappa \ll \kappa_L$. In this regime the amplitude of t decreases when κ_L/κ increases and its width is essentially controlled by κ_L.

In an experiment, the resonator spectrum is often obtained with a vector network analyzer (VNA). This apparatus measures the S-matrix elements in reflection ($S_{11}(\omega)$) and in transmission ($S_{21}(\omega)$). Note that with respect to the coefficients defined and calculated above, the definitions are different so that $S_{11} = r^*$ and $S_{21} = t^*$.

2.1.1.3 Implementation: Lumped and Distributed-Element

LUMPED- ELEMENT RESONATORS

Resonators can be implemented with lumped capacitors and inductances on chip, provided their dimensions are much smaller than half the wavelength of a 3 GHz signal propagating in silicon (2 cm). An example is shown in Fig. 2.5. The resonator

Fig. 2.5 Picture of a lumped-element resonator

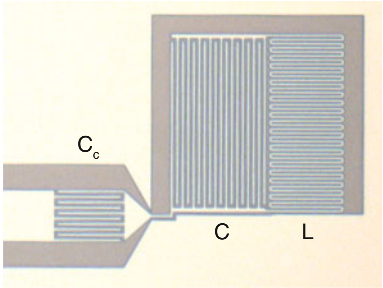

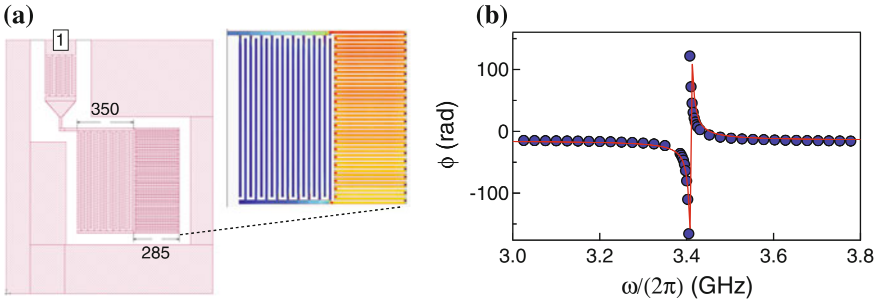

Fig. 2.6 Implementation of a superconducting resonator with lumped electrical elements. **a** Schematic of the simulated chip geometry, showing the resonator and the coupling capacitance to an input port with impedance 50 Ω. The computed alternative current flowing in the inductance is shown in the *inset*. **b** Computed (*dots*) and fitted (*lines*) reflected phase ϕ, yielding $\omega_r/(2\pi) = 3.41$ GHz and $Q = 300$

capacitance (C), inductance (L) and coupling capacitance to the external driving line (C_c) are made with interdigitated fingers and meander wires. The geometrical parameters (number of fingers, fingers length, length of the meanders wires,...) are chosen using a 2D electromagnetic simulator (Sonnet), to obtain the desired resonator physical parameters (ω_r, Z_r, Q). The software uses the physical description of the circuit (geometry, material properties,...), places a voltage source behind the input port of the circuit and solves by finite-element methods the Maxwell's equations to extract the reflection and transmission coefficients.

We show in Fig. 2.6a the Sonnet simulated chip geometry of the resonator pictured in Fig. 2.5, together with the computed alternative current flowing in the resonator inductance I when the drive frequency matches the LC resonance. Note that as expected for a lumped element circuit, the current is approximately constant throughout the wire used as an inductance. The reflected phase ϕ_r on the resonator function of the drive is given in Fig. 2.6c, showing the 2π phase shift at resonance. The fit of the resonance is used to estimate the resonator frequency ω_r and quality factor Q and to correct if needed the design in a next simulation step. To link the oscillating current in the resonator inductance to the magnetic field generated in its surrounding, we use COMSOL Multiphysics. Together with Eq. 2.20, this makes it possible to calculate the magnetic field amplitude $B_1(r)$ to which the spins are coupled, for a given microwave power incident at the resonator input.

DISTRIBUTED- ELEMENT RESONATORS

A resonator can also be built using a piece of transmission line of length Λ with an open circuit at each end (Fig. 2.7). A transmission line is characterized by its capacitance c and inductance l per unit length, and characteristic impedance $Z_0 = \sqrt{l/c}$. Adding boundary conditions creates stationary modes which propagate with phase velocity $\bar{c} = 1/\sqrt{lc}$. The details of the quantum treatment of the field in such resonator can be found e.g. in [4]. We give here the relevant results for the design of

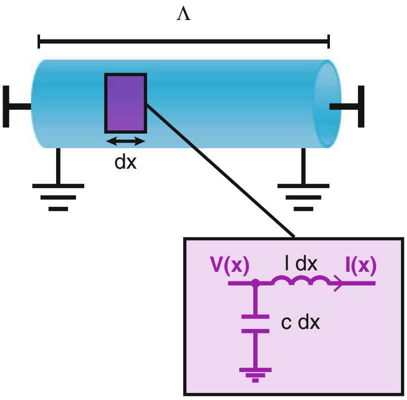

Fig. 2.7 Distributed-element resonators. A transmission line, with open circuits at each end, constitutes a microwave resonator

our experiments. The different stationary modes are equivalent LC resonators k with frequency $\omega_k = \frac{k\pi\bar{c}}{\Lambda}$ and impedance $Z_r = \frac{2}{\pi}Z_0$.
In our experiments, the fundamental mode $k = 1$ is the only one of interest, with frequency

$$\omega_r = \frac{\pi\bar{c}}{\Lambda} \tag{2.23}$$

This equivalent resonator [5] can be put in the form of the LCR resonator model with capacitance $C = \frac{\pi}{2}\cdot\frac{1}{Z_0\omega_r}$, inductance $L = \frac{2}{\pi}\cdot\frac{Z_0}{\omega_r}$, resistance $R = \frac{2}{\pi}\cdot Q_{int}Z_0$ and voltages and currents inside the resonator expressed in the form of Eqs. 2.5 and 2.6 with $V_{rms} = \omega_r\sqrt{\frac{\hbar Z_0}{\pi}}$. We use a particular type of transmission line geometry: the coplanar waveguide (CPW). It consists of a center strip conductor (of width S) that is separated by a gap (of width W) from ground planes (of width b) on either sides, as shown in Fig. 2.8a. To realize the resonator, the transmission line is terminated at one end by an open gap and connected at the other end to external line through coupling capacitance C_c. The effective dielectric constant felt by the electromagnetic mode propagating in the resonator derives from the relative dielectric constant of the substrate ϵ_r (Silicon in our experiment) as $\epsilon_{eff} = \epsilon_0(1+\epsilon_r)/2$ yielding a phase velocity $\bar{c} = c/\sqrt{\epsilon_{eff}}$. The value of $\bar{c}$ is used with formula Eq. 2.23 to determine the resonator length Λ required to obtain the desired resonance frequency. The coupling capacitance C_c sets the resonator quality factor according to Eq. 2.10.

The configuration of the electromagnetic field generated by the CPW resonator is shown in the inset of Fig. 2.8. There exist analytical expressions linking the voltage $V(z)$ and current $I(z)$ in the CPW to the electromagnetic field of Eq. 2.7. These expressions are used to calculate the magnetic field to which the spins are coupled in our experiments.

According to [6], the rms vacuum fluctuations of the magnetic field created by a wave traveling in the z direction along the resonator are:

$$\delta B_x(x,y,z) = -\frac{2\mu_0}{\eta b}\sqrt{\epsilon}\sum_{n=1}^{\infty}\frac{1}{F_n}\left[\frac{\sin(n\pi\delta/2)}{n\pi\delta/2}\sin\frac{n\pi\bar{\delta}}{2}\right]\cos\left(\frac{n\pi x}{b}\right)e^{-\gamma_n y}\cdot V(z)$$

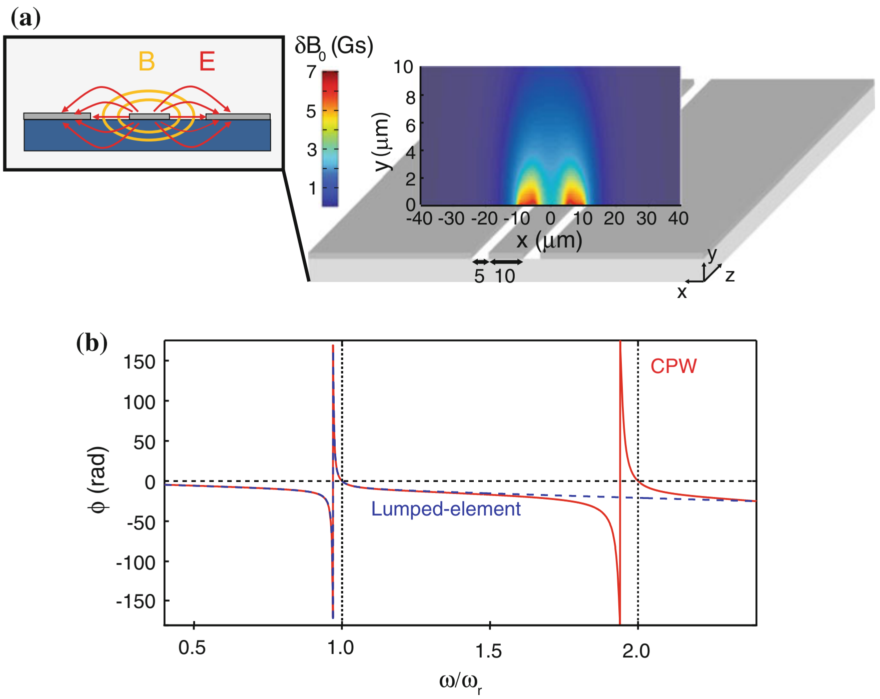

Fig. 2.8 Implementation of a superconducting resonator with a section of CPW line. a 3D schematic of the resonator showing the electromagnetic field. The rms vacuum fluctuations of the magnetic field δB_0 is computed for a typical resonator geometry (S, W = 10, 5 μm). **b** Reflected phase as a function of the reduced frequency ω/ω_r for a $\lambda/2$ resonator (*red solid line*). The first resonance frequency of the loaded resonator is shifted down with respect to that of the decoupled one. The fundamental mode of the distributed resonator is very close to those of a lumped element *LCR* resonator with the same C and Z_r (*blue dashed lines*)

$$\begin{aligned}\delta B_y(x,y,z) &= -\frac{2\mu_0}{\eta b}\sqrt{\epsilon}\sum_{n=1}^{\infty}\left[\frac{\sin\,(n\pi\delta/2)}{n\pi\delta/2}\,\sin\frac{n\pi\bar{\delta}}{2}\right]\sin\left(\frac{n\pi x}{b}\right)e^{-\gamma_n y}\cdot V(z)\\ \delta B_z(x,y,z) &= -i\frac{2\mu_0}{\eta b}\epsilon\left(\frac{4\pi cb}{\omega_r}\right)\sum_{n=1}^{\infty}\frac{1-\epsilon_{eff}}{nF_n}\left[\frac{\sin\,(n\pi\delta/2)}{n\pi\delta/2}\,\sin\left(\frac{n\pi\bar{\delta}}{2}\right)\right]\\ &\qquad \sin\frac{n\pi x}{b}e^{-\gamma_n y}\cdot V(z)\end{aligned} \tag{2.24}$$

with

$$V(z) = V_{rms}\cos\,(\pi z/\Lambda) \tag{2.25}$$

and a geometrical parameter

$$\gamma_n = \sqrt{\left(\frac{n\pi}{b}\right)^2 + \left(\frac{4\pi cb\sqrt{\epsilon_{eff}-1}}{n\omega_r}\right)^2} \tag{2.26}$$

In this expression, μ_0 is the vacuum permeability, $\eta = 376.7$ the vacuum impedance and $\delta = W/b, \bar{\delta} = (S+W)/b$, $F_n = \frac{b\gamma_n}{n\pi}$ are determined by the resonator geometry.

2.1.2 *Josephson Junction Based Circuits*

A non-linear and lossless element can be introduced in superconducting circuits to turn them into active devices. This element is the Josephson tunnel junction, which consists of two superconducting electrodes coupled through a thin layer of insulating material. In this section, we introduce the reader to Josephson junction based circuits. We discuss two particular implementations, the bistable and the frequency-tunable resonator and see that when pushed to the level of very large anharmonicity, Josephson circuits can be used to build qubits.

2.1.2.1 The Josephson Junction and Its Derivatives

The Josephson junction used together with inductances and capacitances to build superconducting circuits is depicted in Fig. 2.9. Its physics is based on the Josephson effect [7], which states that between two closely spaced superconducting electrodes separated by an insulating barrier, a supercurrent I_J flows according to the classical equations:

$$I_J = I_c \sin\varphi \tag{2.27}$$

$$V = \varphi_0 \frac{\partial\varphi}{\partial t} \tag{2.28}$$

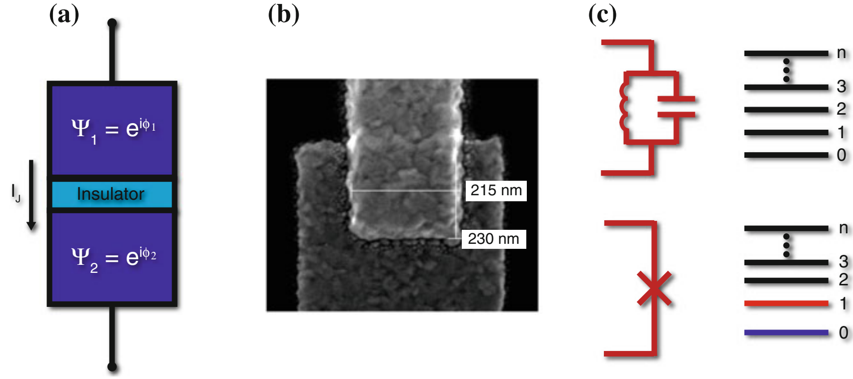

Fig. 2.9 The Josephson junction, a non-linear electrical element. a A Josephson junction is composed of two superconducting electrodes connected through an insulating barrier. **b** Scanning electron micrograph of a Josephson junction used in this thesis work: the electrodes are made of aluminum and the insulator of aluminum oxide. **c** A LC resonator has equally spaced energy levels which prevents any individual transition from being selectively addressed. A Josephson junction (represented by the *X symbol*) has unequally spaced energy levels, a property that can be used to bring non-linearity to a circuit

where $\varphi_0 = \hbar/2e$ is the reduced superconducting flux quantum, I_c the critical-current of the junction—that is the maximum supercurrent that the junction can support—and $\varphi = \varphi_1 - \varphi_2$ and V respectively the superconducting phase difference and voltage across the junction. This system of nonlinear equations represents the main results of the general theory of the Josephson junction which have many applications such as SQUID magnetic field detectors [8] and quantum limited oscillators, mixers and amplifiers [9, 10]. The dynamical behavior of the junction can be outlined in the expression of the derivative of the supercurrent I_J:

$$\frac{dI_J}{dt} = \frac{I_c \cos\varphi}{\varphi_0} V = \frac{I_c\sqrt{1-(I_J/I_c)^2}}{\varphi_0} V \tag{2.29}$$

The Josephson junction appears equivalent to a nonlinear inductance:

$$L_J(\varphi) = \frac{\varphi_0}{I_c\sqrt{1-(I_J/I_c)^2}} \approx \frac{\varphi_0}{I_c}\left(1 + \frac{(I_J/I_c)^2}{2} + O((I_J/I_c)^4)\right) \tag{2.30}$$

Note that for $I_J \ll I_c$, the junction behaves as a point-like inductance $L_J = \varphi_0/I_c$ whose value is entirely governed by the Josephson critical current. The energy associated with the phase difference φ across the Josephson junction writes:

$$E = E_J(1 - \cos\varphi) \tag{2.31}$$

where $E_J = I_c\varphi_0$ is called the Josephson energy. In addition, charge can accumulate on the capacitor C formed by the junction, giving rise to an electrostatic energy $E_C = Q^2/2C$. A quantum treatment of the Josephson junction is obtained by treating the flux $\Phi = \varphi_0\varphi$ and charge Q as conjugate operators with commutation relation $\left[\hat{\Phi}, \hat{Q}\right] = i\hbar$. The Hamiltonian writes:

$$\hat{H} = \frac{1}{2C}\hat{Q}^2 + E_J\left(1 - \cos\hat{\varphi}\right) \tag{2.32}$$

Here the nonlinearity present in the system is a key ingredient for realizing Josephson junction based circuits since it breaks the degeneracy of the energy level spacing in comparison to LCR resonator (Fig. 2.9c).

The SQUID: a tunable inductor Another element that we extensively use in our experiment is the SQUID that we describe here. It consists in a superconducting loop interrupted by two Josephson junctions (Fig. 2.10). We consider a balanced SQUID of same critical currents $I_{c,1} = I_{c,2} = I_c$ and note ϕ_1 and ϕ_2 the superconducting phase difference across each of the junctions. Due to flux quantization, a magnetic flux applied through the loop produces a difference Φ between these phases:

$$\Phi = \frac{\Phi_0}{2\pi}(\phi_1 - \phi_2) \tag{2.33}$$

Fig. 2.10 Electrical scheme of a SQUID

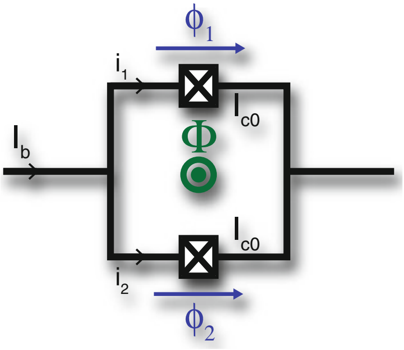

where $\Phi_0 = 2\pi\varphi_0$. When the self-inductance of the loop remains negligible compared to the inductance of the SQUID, the bias current through the SQUID writes:

$$I_b = 2I_c \cos\left(\pi\frac{\Phi}{\Phi_0}\right)\sin\left(\frac{\phi_1+\phi_2}{2}\right) \tag{2.34}$$

which shows that a SQUID behaves as a Josephson junction with a critical current $I_c(\Phi) = 2I_c\cos\left(\pi\frac{\Phi}{\Phi_0}\right)$, and therefore as a flux-tunable inductor with an inductance composed of a linear term

$$L_J(\Phi) = \frac{\varphi_0}{I_c(\Phi)} \tag{2.35}$$

with $I_c(\Phi) = 2I_c|\cos(\pi\frac{\Phi}{\Phi_0})|$ the flux-dependent critical current of the SQUID. Note that in addition, as already mentioned there exists a non-linear term dependent on the bias current I_b across the SQUID $\frac{\varphi_0}{2I_c^3(\Phi)}I_b^2$. This unwanted non-linear term arises when the bias current I_b is comparable to the critical current $I_c(\Phi)$.

2.1.2.2 Josephson Superconducting Resonators

Josephson junctions can be embedded in superconducting resonators to endow them with new functionalities. In our experiments, we are interested in two types of Josephson junctions based resonators. The first one, with a single junction, acts as a bistable hysteretic detector with the applied microwave field, called cavity Josephson bifurcation amplifier (CJBA) and will be used in our hybrid circuits to optimize the superconducting qubit measurement process. The second, with a SQUID, acts as a frequency flux-tunable resonator when supplied to an external magnetic flux Φ threading the SQUID loop, and as a quantum bus, will be engineered to transfer quantum states from the superconducting circuits processor to the spins memory.

THE CAVITY JOSEPHSON BIFURCATION AMPLIFIER

We present briefly here the physics of cavity Josephson bifurcation amplifier, that we use to realize a single-shot readout scheme for superconducting qubits in our hybrid circuits. A detailed discussion of the device can be found e.g. in [5, 9–11]. The CJBA is shown in Fig. 2.11, consisting of a transmission line resonator with a Josephson junction embedded in its central conductor. As discussed in Sect. 2.1.1.3, it can be modeled equivalently as a lumped elements resonator with capacitance C and inductance L plus a Josephson junction with inductance L_J. Its Hamiltonian, sum of harmonic oscillator Eq. 2.2 and Josephson junction terms Eq. 2.32, can be rewritten in the form of a Kerr birefringence Hamiltonian:

$$\hat{H} = \hbar\omega_r \left(\hat{a}^\dagger \hat{a} + \frac{K}{2} \hat{a}^{\dagger 2} \hat{a}^2 \right) \tag{2.36}$$

with resonance frequency

$$\omega_r = \frac{1}{\sqrt{(L_J + L)C}} \tag{2.37}$$

and Kerr constant

$$K = -\pi Z_r \frac{e^2}{h} \left(\frac{L_J}{L_J + L} \right)^3 \tag{2.38}$$

When driven under classical field $\beta_d(t) = \beta_d e^{-i\omega_d t}$ at frequency ω_d, the intra-cavity field α of Eq. 2.18 in the CJBA satisfies:

$$i \left(\Omega \frac{\kappa}{2} \alpha + K |\alpha|^2 \alpha \right) + \frac{\kappa}{2} \alpha = -i\beta_d \tag{2.39}$$

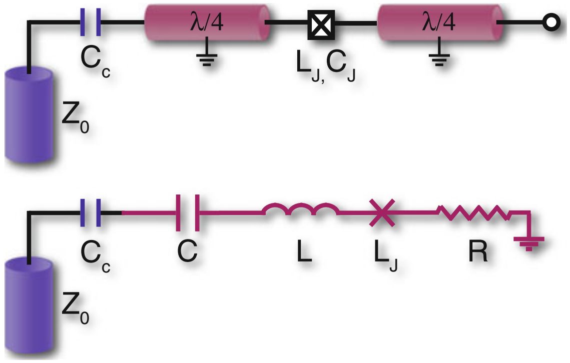

Fig. 2.11 The cavity Josephson bifurcation amplifier. The CJBA fabricated in this thesis work are nonlinear, open-end $\lambda/2$ resonator, consisting of two sections of transmission line joined by a Josephson junction. Its equivalent lumped elements circuit is a LC resonator with capacitance C and inductance L, plus a Josephson junction with inductance L_J

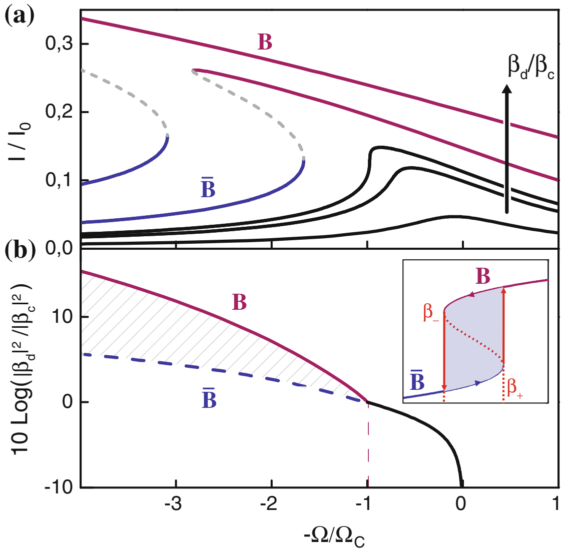

Fig. 2.12 **The CJBA: a hysteretic detector for the drive amplitude.** **a** Current in a CJBA as a function of the reduced drive detuning, plotted for various drive amplitude β_d. For drive detuning Ω_d larger than a threshold value Ω_r, the resonator becomes bistable above a certain power threshold $\beta_d > \beta_c$. **b** Phase diagram in the $\Omega - \beta_d$ plane, showing the region of low intracavity field ($\bar{\mathbf{B}}$), the region of high intracavity field (**B**), and the bistable region (*dashed*) where both $\bar{\mathbf{B}}$ and **B** dynamical states can exist. The intracavity field bifurcates (see *inset*) from one states to the other when increasing (decreasing) the drive until reaching β_+ (β_-)

where $\Omega = 2Q(1 - \frac{\omega_d}{\omega_r})$ is the reduced detuning, which accounts for off-resonance drive. For certain couple of drive parameters (β_d, ω_d), this equation has two solutions $\alpha_{i=1,2}$. Figure 2.12a shows the intracavity field α as a function of Ω, plotted for several values of the drive amplitude β_d. These double solutions appear when increasing the drive amplitude, and is conditioned by the drive frequency such that $\Omega > \Omega_r = \sqrt{3}$, the bistable region, in which we typically operate the CJBA to readout superconducting qubits. In Fig. 2.12b, we call $\bar{\mathbf{B}}$ and **B** respectively the low (α_1) and high (α_2) intracavity field state, and $\beta_\pm$, the bifurcation points, i.e. the points at which the system can change state. Starting with the resonator in $\bar{\mathbf{B}}$, the intra-cavity field remains in the lower branch while increasing the drive until reaching β_+, where it suddenly grows to reach the upper branch **B** (the bifurcation). Operated in this bistable region, the CJBA acts as a hysteretic detector for the drive amplitude.

THE FREQUENCY TUNABLE RESONATOR

Being a flux-tunable inductor as seen above, a SQUID loop can be inserted in a resonator to make it tunable in frequency with an applied local magnetic field. Such resonators are useful to transfer quantum states between two systems at different frequencies and are extensively used in our hybrid circuits between the circuits and

Fig. 2.13 The frequency tunable resonator

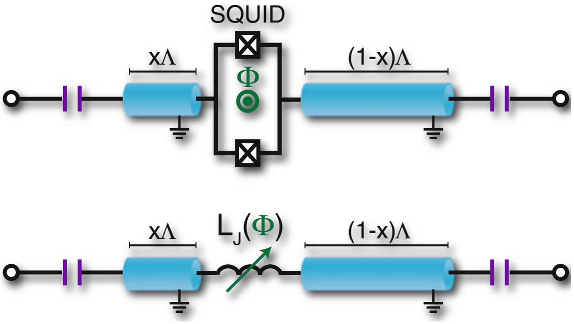

the spins. Its implementation with distributed element resonator is schematized in Fig. 2.13. A SQUID is inserted in the central conductor of a $\lambda/2$ coplanar waveguide resonator at the position x ($x \in [0, 1]$, with respect to Λ the length of the resonator). As shown in [12], the insertion of the SQUID is equivalent to the insertion of the flux tunable inductance $L(\Phi)$ given by Eq. 2.35. This modifies the resonator frequency, with a dependence on the position x of the insertion. When introduced in the middle of the resonator ($x = 1/2$), the resonance frequency is changed from ω_0 (without SQUID) to:

$$\omega_r(\frac{\Lambda}{2}, \Phi) = \frac{\omega_0}{1 + L_J(\Phi)\frac{\omega_0}{Z_r}} \tag{2.40}$$

and the quality factor Q_0 to

$$Q_c(\Phi) \approx Q_0\left(1 + 4L_J(\Phi)\frac{\omega_0}{Z_r}\right) \tag{2.41}$$

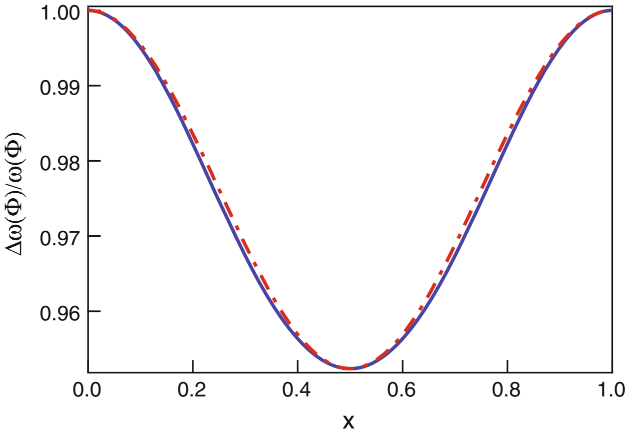

Fig. 2.14 Dependence of resonance frequency on the position of the SQUID in the resonator. $\Delta\omega_r(x\Lambda, \Phi_f)$ is shown at fixed applied magnetic flux Φ_f as a function of x. The line is fitted with Eq. 2.42 (*dashed* and *dotted line*)

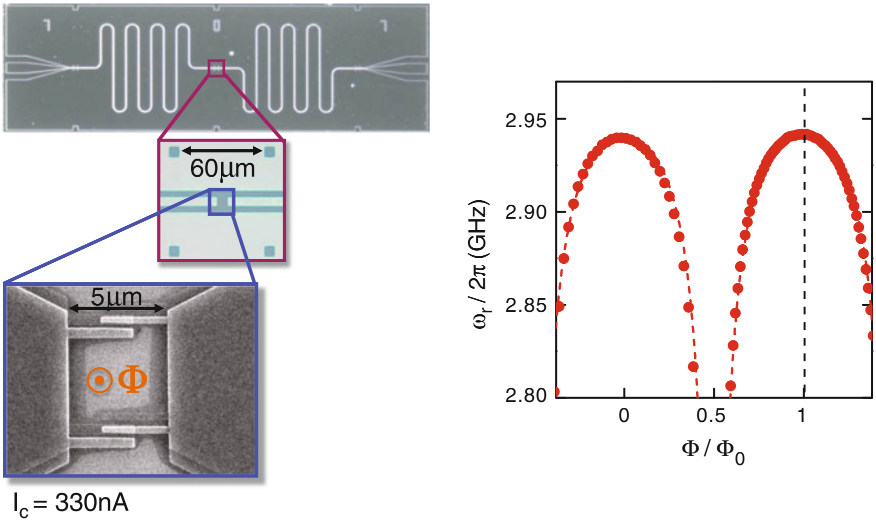

Fig. 2.15 **The tunable resonator.** The resonance frequency of a resonator containing a SQUID is tuned by varying the flux applied to the SQUID loop

In our experiments, for design reasons we have found preferable that the SQUID is not located at $x = 1/2$ but closer to the resonator end. We have thus extended the analysis to the case of an arbitrary value of x. To do so, we computed numerically the value of the resonance frequency as a function of x in the case where the ratio between the SQUID inductance $L_J(\Phi)$ and the resonator inductance Z_r/ω_0 is small compared to 1. The result is shown in Fig. 2.14. We find that it is well approximated by the intuitive formula:

$$\omega_r(x\Lambda, \Phi) = \omega_0 \left[1 - \sin^2(\pi x) \frac{L_J(\Phi)}{\frac{Z_r}{\omega_0} + L_J(\Phi)} \right] \tag{2.42}$$

The characterization of the resonator requires a probe power low enough to remain in the linear regime, i.e. $I_b \ll I_c(\Phi)$. Figure 2.15 shows the resonance frequency period with the variation of the flux through the SQUID loop operated in the linear regime, demonstrating that the resonator can be effectively tuned over hundreds of MHz.

2.1.2.3 Superconducting Artificial Atoms

To build an artificial atom, the non-linearity of Josephson junction based circuit has to be pushed to the level of very large anharmonicity so that individual levels can be addressed separately. In this case, the $|0\rangle$ to $|1\rangle$ transition can be used to implement the qubit concept. The specific Josephson circuit we used to implement artificial atoms in our experiments is the transmon qubit [13] pioneered by Schoelkopf's group at Yale, a variant of the Cooper Pair Box (CPB) developed in 1996 in the Quantronics group [14].

THE TRANSMON QUBIT

The Cooper-pair box artificial atom (CPB) consists in a superconducting island connected via a Josephson junction to a grounded reservoir (Fig. 2.16). The island is coupled to an input voltage source through a gate capacitance C_g. Cooper-pairs tunnel on and off the island via the Josephson junction. The gate circuit can be used to induce an excess charge $N_g = C_g V_g/(2e)$ on the island. The total number of Cooper-pairs having tunneled through the junction is described by the operator $\hat{N}$ and equivalently with its canonical conjugate, the superconducting phase difference $\hat{\theta}$ across the junction. We recall here the properties of the CPB that is needed to design and understand our experiment. An in-depth treatment of the Cooper-pair box can be found in A. Cottet's thesis [15]. The Hamiltonian of the CPB writes:

$$\hat{H} = E_C(\hat{N} - N_g)^2 - E_J \cos\hat{\theta} \tag{2.43}$$

with $E_C = (2e)^2/2C_\sigma$ and $C_\sigma = C_J + C_B + C_g$. Diagonalization of this Hamiltonian yields the circuit eigenenergies $\hbar\omega_i$ and eigenstates $|i\rangle$ so that the Hamiltonian can be recast in the form

$$\hat{H} = \hbar \sum_i \omega_i |i\rangle\langle i| \tag{2.44}$$

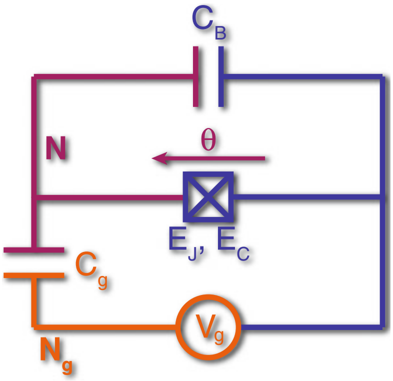

Fig. 2.16 **Circuit schematic of a Cooper Pair Box.** A superconducting island (*purple*) is connected to a reservoir (*blue*) through a Josephson junction with Josephson energy E_J, and a capacitance C_J. This island is also electrostatically coupled to ground through a geometric capacitor C_B, and to a voltage source V_g through a capacitor C_g. The gate circuit (*yellow*) can be used to induce an offset charge on the island

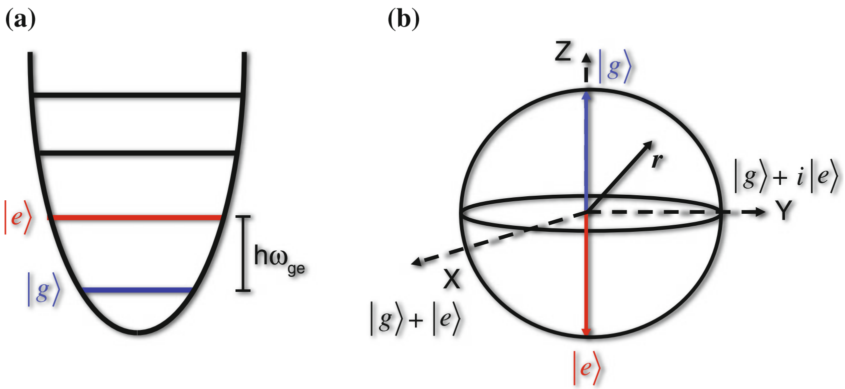

Fig. 2.17 **Superconducting qubits.** **a** The two lowest levels $|g\rangle$ and $|e\rangle$ are separated by a transition at ω_{ge}, that can be used to implement the qubit concept. **b** The Bloch vector of the qubit state (**r**) represents a pure quantum state if it falls on the surface of the Bloch sphere or a mixed quantum state if it falls inside the sphere. The north pole corresponds to the state $|g\rangle$, the south pole to $|e\rangle$. The intersections of the unit sphere with the x, y axes corresponds respectively to the state $|g\rangle + |e\rangle$ and $|g\rangle + i|e\rangle$

We use the two lowest levels, that we will call in the following $|g\rangle$ and $|e\rangle$ to implement the qubit concept. Any pure state of the qubit can be written in a linear combination $|\psi\rangle = \alpha|g\rangle + \beta|e\rangle$ with α and β complex numbers satisfying $|\alpha|^2 + |\beta|^2 = 1$. The state of the qubit can be mapped to the points on a sphere of radius 1, the Bloch sphere, with north pole corresponding to the state $|g\rangle$ and south pole to $|e\rangle$ and re-written in the spherical coordinates

$$|\psi\rangle = \cos(\theta/2)e^{-i\varphi/2}|g\rangle + \sin(\theta/2)e^{i\varphi/2}|e\rangle \tag{2.45}$$

with $\theta \in [0, \pi]$ and $\varphi \in [0, 2\pi]$, the polar and azimuth angles. The corresponding position **r**, also called the Bloch vector, is defined in Fig. 2.17b and can represent a pure or mixed state.

In our experiments, we use a split Cooper pair box with a balanced SQUID loop instead of a single Josephson junction to allow for tunability of the qubit frequency ω_{ge}. The Hamiltonian of this circuit shown in Fig. 2.18a recasts in the form of Eq. 2.43 of the Cooper pair box with Josepshon energy $E_J^*(\Phi)$ depending of the applied flux Φ to the SQUID loop:

$$E_J^*(\Phi) = E_J\sqrt{\frac{1 + \cos(\Phi/\varphi_0)}{2}} \tag{2.46}$$

In addition, the charging energy has been strongly reduced by designing a large geometrical capacitance C_B such that the qubit operates in the Josephson regime $E_J \gg E_c$ (Transmon). As shown in Fig. 2.18c, in this regime the charge dispersion of the energy levels of the Cooper pair box becomes extremely weak, thus rendering the qubit frequency practically insensitive to the value of the gate charge N_g.

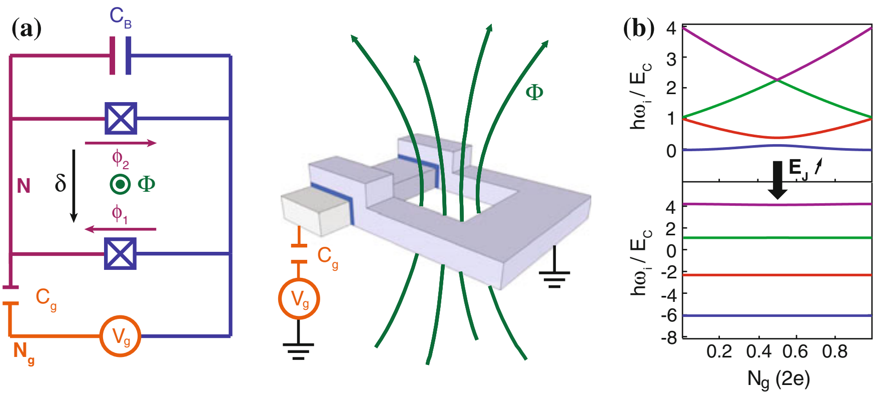

Fig. 2.18 Implementation of a superconducting qubit with a Transmon. a The Transmon qubit used in this thesis work is a split CPB with the Josephson junction replaced by a balanced SQUID loop and **b** operated in the regime $E_J \gg E_C$. The first energy levels of a Transmon qubit show a charge-dispersion curve almost completely flat

DECOHERENCE

Independently of the physical implementation (superconduting qubits, spins, atoms,. . .), the coupling to the environment deteriorates the quantum state supported by a qubit. This is the decoherence, which materializes in two processes:

- **Energy relaxation** The qubit in the excited state $|e\rangle$ decays to the ground state $|g\rangle$ by dissipating energy into its environment. This process involves the emission a photon with $\hbar\omega_{ge}$ and is characterized by an exponential decay time T_1.
- **Dephasing** The qubit transition frequency ω_{ge} randomly fluctuates due to interactions with the environment. This process involves loss of the phase coherence φ of the quantum state and is characterized by a decay time T_φ.

The Bloch sphere is a useful tool to visualize the states and the decoherence processes (Fig. 2.19). Relaxation precipitates the Bloch vector towards the ground state; Dephasing shrinks the Bloch vector towards the center of the sphere. Since energy relaxation also causes loss of phase coherence, the two times are often expressed as one characteristic decoherence timescale, the free induction decay time T_2^*, with

$$\frac{1}{T_2^*} = \frac{1}{2T_1} + \frac{1}{T_\varphi} \tag{2.47}$$

There is usually a tradeoff between protecting the qubit from decoherence on the one hand and being able to easily control, readout and couple it. Superconducting qubits can be easily manipulated but have typically coherence properties far lower than the one of isolated microscopic systems such as nuclear and electronic spins in crystals. One of the major challenges in superconducting circuits has actually been to improve the coherence properties from the first qubit operation in 1999 with

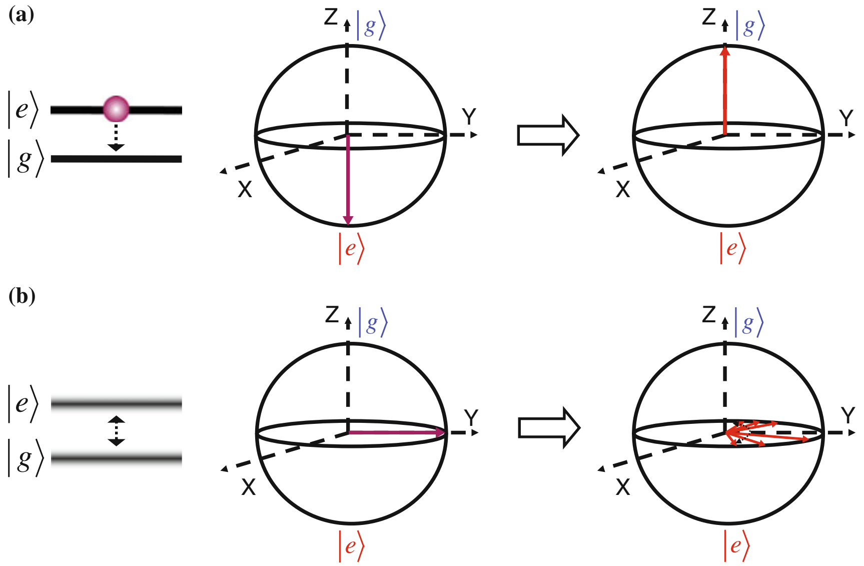

Fig. 2.19 Decoherence mechanisms. a A qubit in the excited state decays to the ground state via energy relaxation. **b** Interaction with the environment causes the energy level spacing between the qubit states to jitter leading to a loss of phase coherence called dephasing

5–10 ns range [16] to allow the implementation of quantum gate operation in multi-qubit small-scale processors. Progress in circuit design [17–20] and fabrication techniques has led to longer coherence times, up to tens of microseconds nowadays for transmon qubits [21, 22].

2.1.3 Circuit Quantum Electrodynamics

In this thesis, we use a resonator for coupling spins and superconducting qubits. Both are two-level systems (TLS) that can be described within the same framework when interacting with a planar resonator, referred as circuit quantum electrodynamics. In this section, we focus on the coupling between a resonator and a superconducting qubit on chip. Two regimes are of interest for our experiments: the resonant regime for quantum state transfer between the qubit and the bus resonator, and the dispersive regime for non-destructive measurement of the qubit state.

2.1.3.1 Qubit-Resonator Coupling

We consider the system shown in Fig. 2.20, in which a qubit of the transmon type, is capacitively coupled (C_g) to a CPW resonator, itself coupled (C_c) to the $50\,\Omega$ input transmission line. The Hamiltonian of the system is the sum of the Hamiltonians of the resonator (Eq. 2.2) and the qubit (Eq. 2.43), plus an interaction term $\hat{H}_{int}$ between

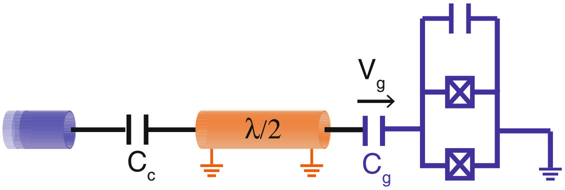

Fig. 2.20 Schematic of a typical CQED circuit, consisting of a Transmon qubit capacitively coupled to a transmission line resonator

them. For small couplings $C_g \ll C_c$, this interaction Hamiltonian approximates as the energy stored in the capacitance between the qubit and the resonator:

$$\hat{H}_{int} = \frac{1}{2} C_g \hat{V}_g^2 = \frac{1}{2} C_g \left(V_{rms} (\hat{a}^\dagger + \hat{a}) - \hat{V} \right)^2 \tag{2.48}$$

where $\hat{V}_g$ is the bias voltage at the coupling capacitance, V_{rms} the root-mean-square fluctuations of the voltage of the resonator introduced in Eqs. 2.5 and 2.6 and $\hat{V} = 2e/C_\Sigma \cdot (\hat{N}_g - \hat{N})$ the voltage across the Transmon electrodes (see Fig. 2.16). In the limit where $\beta = C_g/C_\Sigma \ll C_\Sigma$, we can restrict ourselves to the first order coupling term in V_{rms} such that[1]:

$$\hat{H}_{int} = 2e\beta V_{rms} \hat{N} (\hat{a}^\dagger + \hat{a}) \tag{2.49}$$

The coupling strength g between the qubit and the resonator can be identified by rewriting the interaction Hamiltonian in term of $\hat{\sigma}_+ = |e\rangle\langle g|$ and $\hat{\sigma}_- = |g\rangle\langle e|$ the raising and lowering operators of the qubit:

$$\hat{H}_{int} = \hbar g (\hat{\sigma}_+ + \hat{\sigma}_-)(\hat{a} + \hat{a}^\dagger) \tag{2.50}$$

with g given by

$$\hbar g = 2\beta V_{rms} \langle g|\hat{N}|e\rangle \tag{2.51}$$

In the case where the coupling between the resonator and the qubit is such that $g \ll \omega_r, \omega_{ge}$, we can ignore the terms in the interaction Hamiltonian that describe simultaneous excitation or desexcitation of the qubit and the resonator, and rewrite the total Hamiltonian in the rotating wave approximation:

$$\hat{H} = \hbar\omega_r \left(\hat{a}^\dagger \hat{a} + 1/2 \right) - \hbar \frac{\omega_{ge}}{2} \hat{\sigma}_z + \hbar g \left(\hat{a}\hat{\sigma}_+ + \hat{a}^\dagger \hat{\sigma}_- \right) \tag{2.52}$$

This is the Jaynes Cumming Hamiltonian. In an experiment, both the cavity and the qubit have losses, characterized by damping rates κ (cavity) and γ (qubit). The regime of interest, in which the coupling strength is much larger than all losses in the system, is called the strong coupling regime ($g \gg \kappa, \gamma$). In this case, losses are invisible on the time scale of the qubit-resonator interaction and the Jaynes-Cumming Hamiltonian can be analytically diagonalized. The two eigenstates of the individual systems (the intracavity field state $|n\rangle$ for the cavity and the ground state $|g\rangle$ and excited state $|e\rangle$ for the atom) are no longer eigenstates of the Hamiltonian Eq. 2.52 but instead a coherent superposition of both system states [14]:

---

[1] The terms in N_g which do not corresponds to coupling term but to a renormalization of the resonator capacitance are omitted.

$$|+, n\rangle = \cos\theta_n |e, n\rangle + \sin\theta_n |g, n+1\rangle \tag{2.53}$$

$$|-, n\rangle = -\sin\theta_n |e, n\rangle + \cos\theta_n |g, n+1\rangle \tag{2.54}$$

with θ_n a mixing angle defined as

$$\tan(2\theta_n) = -2g\frac{\sqrt{n+1}}{\Delta} \tag{2.55}$$

where $\Delta = \omega_{ge} - \omega_r$ is the frequency difference between the cavity and the qubit. The energies corresponding to these states are

$$\hbar\omega_{\pm,n} = \hbar\omega_r(n+1) \pm \hbar\frac{\Omega_{n,\Delta}}{2} \tag{2.56}$$

with $\Omega_{n\Delta}$ the vacuum Rabi frequency given by

$$\Omega_{n,\Delta} = \sqrt{4g^2(n+1) + \Delta^2} \tag{2.57}$$

In the experiment reported in Chap. 4, we exchange a single photon between the qubit and the resonator. This corresponds to the case $n = 0$. We show in Fig. 2.21 the frequencies $\omega_{\pm,0}$ as a function of the detuning Δ between the resonator and the qubit.

An avoided crossing of width $2g$ appears between the two eigenstates of the coupled system (see Fig. 2.21). This phenomenon is known as the vacuum Rabi splitting. If the qubit is prepared in state $|e\rangle$ at $t = 0$ with the cavity empty ($|e, 0\rangle$),

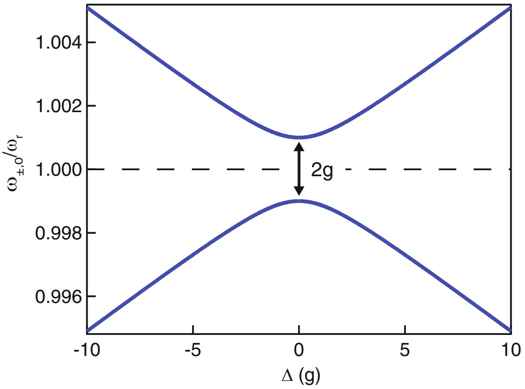

Fig. 2.21 Vacuum Rabi splitting. The frequency of the resonator shows an anti-crossing when approaching the qubit frequency ($\Delta = 0$)

the probability to find the system in state $|g, 1\rangle$ is:

$$P(t) = \frac{4g^2}{\Omega_{0,\Delta}^2} \sin^2\left(\frac{\Omega_{0,\Delta}}{2}t\right). \tag{2.58}$$

Resonant regime: vacuum Rabi oscillations When the cavity and the qubit are resonant such that $\Delta \ll g$, the frequency $\Omega_{0,\Delta} \approx 2g$. If the qubit is prepared in $|e\rangle$ at $t = 0$ with the cavity in $|0\rangle$, the probability to find the resonator in $|1\rangle$ at time t becomes:

$$P(t) = \sin^2(gt) = \frac{1 - \cos(2gt)}{2} \tag{2.59}$$

These oscillations are known as vacuum Rabi oscillations. After a time $\pi/2g$, the resonator is prepared in state $|1\rangle$ with probability 1; we will use this phenomenon in the experiments reported in Chap. 4 to transfer a quantum state from the qubit into the spin ensemble via a resonator.

Dispersive regime: cavity-pull When the cavity is far detuned from the TLS transition frequency such that $\Delta \gg g$, the probability (Eq. 2.58) to exchange a photon becomes negligible. This regime has been discussed e.g. in [5] and is called the dispersive regime. In this case, the Hamiltonian is approximated by an effective Hamiltonian:

$$\hat{H}_{disp} = \frac{1}{2}\hbar\omega'_{ge}\hat{\sigma}_z + \underbrace{\hbar(\omega'_r + \chi\hat{\sigma}_z)\left(\hat{a}^\dagger\hat{a} + \frac{1}{2}\right)}_{\text{cavity pull}} \tag{2.60}$$

with the dispersive shift $\chi = g^2/\Delta$. The term labeled as cavity pull remains the Hamiltonian of a harmonic oscillator, but with frequency $\omega'_r + \chi$ when the TLS is in its ground state and $\omega'_r - \chi$ when in its excited state. This qubit-state dependent frequency shift is the basis for qubit readout in cQED. We place ourselves in this dispersive regime to measure the superconducting qubit.

2.1.3.2 Resonant Qubit Manipulation

To drive the qubit, a microwave pulse at a frequency ω_d close to ω_{ge} is sent onto the resonator input. It generates a field of amplitude $|\alpha|e^{-i(\omega_d t + \phi_d)}$, whose action on the qubit is given by the Hamiltonian term $g|\alpha|\left[e^{-i(\omega_d t+\phi_d)}\hat{\sigma}_+ + e^{i(\omega_d t+\phi_d)}\hat{\sigma}_-\right]$. In the rotating frame at ω_d, the complete qubit Hamiltonian can then be rewritten as:

$$\hat{H}_d = \frac{\hbar\delta\omega}{2}\hat{\sigma}_z + \hbar\frac{\Omega_R}{2}\hat{\sigma}_n \tag{2.61}$$

with $\delta\omega = \omega_{ge} - \omega_d$ the qubit-drive detuning, $\Omega_R = 2g|\alpha|$ the Rabi frequency, and $\hat{\sigma}_n = \cos\phi_d\hat{\sigma}_x + \sin\phi_d\hat{\sigma}_y$. In the Bloch sphere representation (Fig. 2.22), the

Fig. 2.22 Qubit operations represented in the Bloch sphere rotating at the microwave frequency ω_d

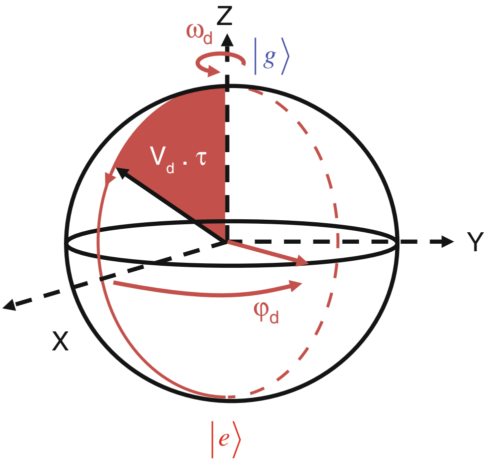

qubit Bloch vector precesses around an axis making an azimuthal angle ϕ_d with the x-axis, and an angle θ such that $\tan\theta = \delta\omega/\Omega_R$ with the x-y plane. By appropriate selection of the pulse duration and detuning, arbitrary rotations can be achieved on the Bloch sphere.

2.1.3.3 Non-destructive Qubit Readout with Josephson Bifurcation Amplifier

To measure the qubit state, we use the cavity pull effect seen in Sect. 2.1.3.1. The Transmon-resonator system is in the dispersive regime, where the resonator frequency is shifted up or down depending on the qubit state as expressed by Eq. 2.60. The common measurement technique consists in sending a microwave pulse at ω_r and measuring the relative phase reflected onto the resonator. At resonance, the reflected

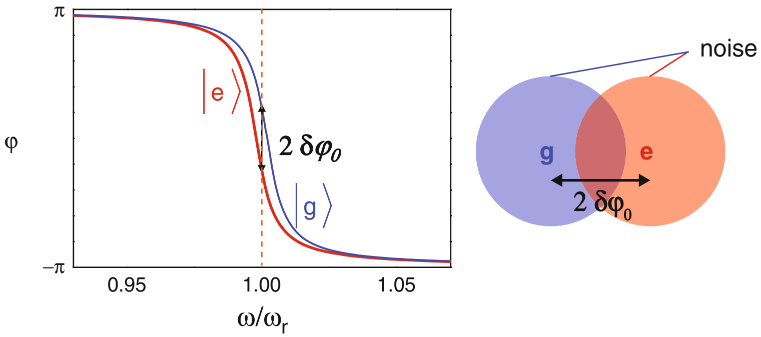

Fig. 2.23 Standard dispersive measurement technique. The phase of a reflected probe pulse is measured. The noise coming mainly from the cryogenic amplifier, introduces an uncertainty on the discrimination between $|g\rangle$ and $|e\rangle$ qubit states (*red* and *blue disks*), which depends on the averaging time, and which can be of the same order or even larger than the separation between the two vectors to be discriminated

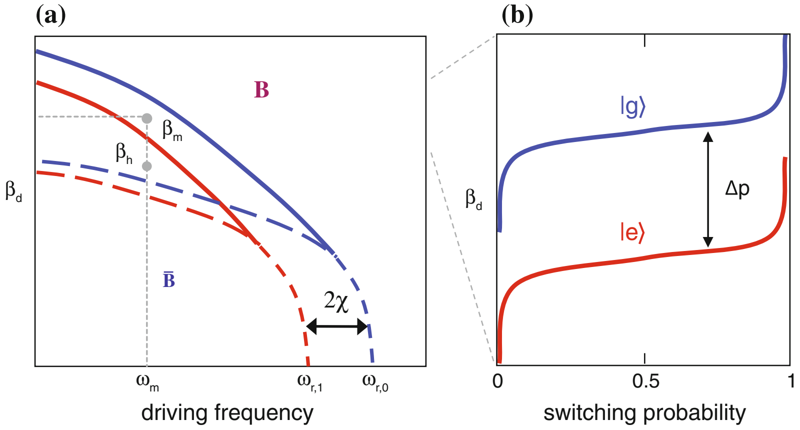

Fig. 2.24 **Single-shot qubit readout. a** Same CJBA phase diagram as on Fig. 2.12 for a CJBA embedding a qubit that shifts the diagram by $\pm\chi$ when being in its $|g\rangle$ and $|e\rangle$ states, respectively. **b** Probability of switching from $\bar{\mathbf{B}}$ to **B** as a function of the CJBA input drive amplitude β_d, shown for an embedded qubit in state $|g\rangle$ (*blue*) or $|e\rangle$ (*red*)

phase of the microwave signal onto the cavity undergoes a π shift (see Sect. 2.1.1.2). When coupled to the qubit, the frequency at which occurs this π-shift is dependent on the qubit state which defines a phase difference $\delta\varphi_0$ shown in Fig. 2.23. The discrimination between the two qubit states is obtained by averaging out to reduce the noise on the measured reflected phase.

However, as noise can be of the same order or even larger than $\delta\varphi_0$, requirement on the averaging is tight to obtain good signal to noise ratio. In our experiments, we optimize the measurement process by replacing the resonator by a cavity Josephson bifurcation amplifier (R), the hysteretic detector that we have seen Sect. 2.1.1.2. Figure 2.24 shows the phase diagram of the CJBA, indicating the stability regions of the different solutions $\bar{\mathbf{B}}$ (low-amplitude) and **B** (high-amplitude) of R for the two different qubit states $|g\rangle$ and $|e\rangle$. We take advantage of its hysteretic behavior in a measurement process separated in two steps:

- **Map the qubit state to the resonator:** at fixed drive frequency ω_m, the amplitude of the measurement pulse is quickly ramped from 0 to the value β_m as indicated in Fig. 2.24a. If the qubit is in state $|g\rangle$, R remains in the low-amplitude state $\bar{\mathbf{B}}$, while switches to the high-amplitude state **B** if in $|e\rangle$. In this way, the state of the qubit is mapped to one of the two intra-cavity field states of R, resonator which can be easily measured by standard microwave techniques;
- **Maintain and measure the resonator until its discrimination:** the measurement of the resonator has to be well averaged out, thus during a long time interval (typically 1–2 μs) to discriminate between the two oscillator states with certainty. To avoid further switching processes during the time needed to measure, the drive amplitude is lowered to a value β_h at which the switching probability of R is very small. At this point, we can measure R for an arbitrary long time without being limited by spurious switching events.

This measurement technique is qualified of single-shot readout and well-known for its robustness with readout contrast demonstrated up to 93 % in past experiments [23]. In our hybrid circuit experiments, we will use the CJBA as a tool for efficient qubit readout.

2.2 NV Center Spins in Diamond

We now turn to the second component of our hybrid circuits: the NV center spins in diamond. The Nitrogen-Vacancy center (NV) is an impurity in diamond which has drawn an increasing amount of interest in the quantum optics community for its spin and optical properties. The reason is that it is paramagnetic [24, 25], has good coherence properties [26, 27], and using Optically Detected Magnetic Resonance (ODMR) it is possible to optically read out and polarize the electron spin state [28]. We give in the following more details on its spin and optical properties which will be exploited to implement memory operations and explicit the specific sample properties required for our hybrid circuit implementations.

2.2.1 Structure

The NV center consists of a substitutional nitrogen atom (N) next to a vacancy (V) in an adjacent lattice site of the diamond crystalline matrix (Fig. 2.25). It has a trigonal symmetry around the crystallographic direction connecting the nitrogen and the vacancy that we refer to as the NV axis and note Z in the following. The NV axis coincides with $\langle 111\rangle$ directions of the diamond lattice which implies four different possible NV axis orientations. The electronic structure of the NV center determines its optical and spin properties. Three electrons are provided by the dangling bonds of the vacancy to neighboring carbon atoms, two by the dangling bonds of the nitrogen atom itself. This configuration forms the first kind of NV center, the NV^0, which is

Fig. 2.25 Schematic representation of the NV center in diamond

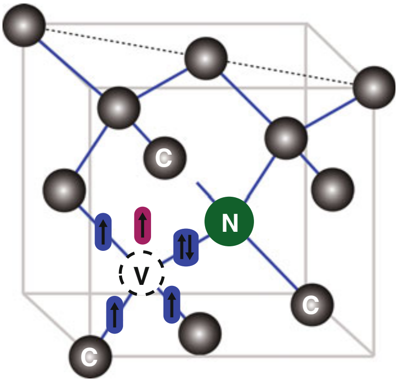

neutral and has electron spin $S = 1/2$. There are also cases where the NV center has captured an additional electron from other Nitrogen donors in the diamond: the negatively charged NV centers (NV^-). In this thesis work we concentrate exclusively on the latter one which has electron spin $S = 1$ and will omit '−' sign from now.

2.2.2 The NV Center Spin Qubit

Symmetry and structure determine the electronic properties of the NV center. In the case of NV, the electronic configuration leaves two unpaired electrons which couple together to form either triplet or singlet states. The determination of the exact energy level structure resulting of this coupling has combined many efforts both from the theoretical and experimental side including optical [29], electron [30] paramagnetic resonance. For the work we discuss in this thesis, we limit ourselves to relevant states, the electronic ground (^3A) and the first excited state (^3E) which both are spin triplet states, plus a singlet level ^1A present between the ground and excited states [28]. The schematic of the energy level diagram is shown in Fig. 2.26.

2.2.2.1 NV Qubit Transition: Spin Properties

The electronic ground state ^3A is a spin triplet ($S = 1$). The system can be described in the basis $m_S = 0, \pm 1$ (the spin quantization along Z, the NV axis) using the dimensionless spin-1 vectorial operator $\mathbf{S} = (\hat{S}_X, \hat{S}_Y, \hat{S}_Z)$, with

$$\hat{S}_X = \frac{1}{\sqrt{2}} \begin{pmatrix} 0 & 1 & 0 \\ 1 & 0 & 1 \\ 0 & 1 & 0 \end{pmatrix}, \hat{S}_Y = \frac{1}{\sqrt{2}} \begin{pmatrix} 0 & -i & 0 \\ i & 0 & -i \\ 0 & i & 0 \end{pmatrix}, \hat{S}_Z = \begin{pmatrix} 1 & 0 & 0 \\ 0 & 0 & 0 \\ 0 & 0 & -1 \end{pmatrix} \quad (2.62)$$

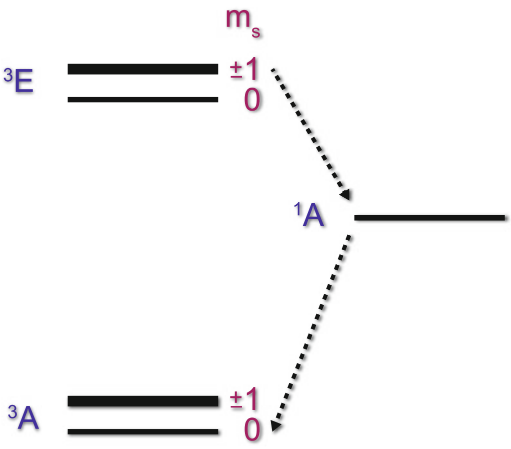

Fig. 2.26 Level diagram of the NV center, showing ground (^3A) and first excited (^3E) electronic states, as well as the ^1A state. A transition in the optical domain separates the two electronic states, which are both spin triplet ($S = 1$)

Note that restricting ourselves to a 2-level subspace, one obtains the relations $\hat{S}_{X,Y} = \frac{1}{\sqrt{2}}\hat{\sigma}_{x,y}$ between the spin-1 operators and the usual spin-1/2 Pauli matrices which will be used later in this manuscript. The spin Hamiltonian is a sum of the zero-field splitting ($\hat{H}_{ZF}$), the electron Zeeman shift ($\hat{H}_B$) and the hyperfine interaction with the nitrogen nucleus ($\hat{H}_{HF}$). These three contributions are described below.

Zero-field splitting The zero-field splitting $\hat{H}_{ZF}$ results from the dipole-dipole magnetic coupling between the two unpaired electron spins forming $S = 1$. As the name suggests it leads to a level splitting even in the absence of external magnetic field. The zero-field Hamiltonian can be written using the zero-field splitting tensor $\bar{\mathbf{D}}$:

$$\hat{H}_{ZF}/\hbar = \mathbf{S} \cdot \bar{\mathbf{D}} \cdot \mathbf{S} \tag{2.63}$$

$$= D_X \hat{S}_X^2 + D_Y \hat{S}_Y^2 + D_Z \hat{S}_Z^2 \tag{2.64}$$

which can be equivalently rewritten as[2]:

$$\hat{H}_{ZF}/\hbar = D\hat{S}_Z^2 + E\left(\hat{S}_X^2 - \hat{S}_Y^2\right) \tag{2.65}$$

where we defined $D = 3D_Z/2$ the zero-field splitting and $E = (D_X - D_Y)/2$ the strain induced splitting. Due to the axial symmetry of the NV center, D_X and D_Y should be identical. In our experiment however, a distortion of the trigonal symmetry appears due to the effect of strain and local electric fields on the orbital energy yielding $D_X \neq D_Y$ (and thus $E \neq 0$). As a result, the energy eigenstates $|\pm\rangle$ are not identical to the two pure spin eigenstates $|m_S = \pm 1\rangle$. The state $|\pm\rangle$ are linear combinations of $|m_S = \pm 1\rangle$, with at zero magnetic field $|\pm\rangle = (|m_S = +1\rangle \pm |m_S = -1\rangle)/\sqrt{2}$ separated in frequency by $2E$. Microwave transitions are induced between the $|m_S = 0\rangle$ ground state and either the $|+\rangle$ or the $|-\rangle$ excited states with transition frequency $\omega_\pm$ (Fig. 2.27). For our hybrid circuits, we use an ensemble of NV centers

Fig. 2.27 Electron spin levels of the electronic ground state

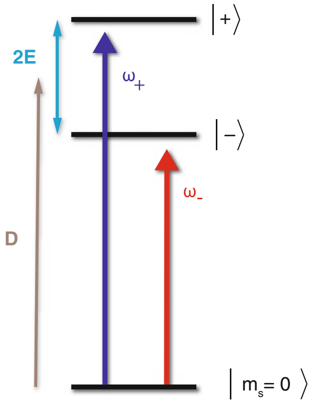

---

[2] The constants terms are omitted.

which involves a distribution of both the zero-field splitting $\rho(D)$ and strain induced splitting $\rho(E)$ Hamiltonian parameters. Average values are $D/2\pi = 2.878$ GHz and $E/2\pi$ between 1–5 MHz from sample to sample.

Zeeman interaction The Zeeman term appears upon the application of an external magnetic field $\mathbf{B_{NV}}$. It writes $\hat{H}_B/\hbar = -\gamma_e \mathbf{B_{NV}} \cdot \mathbf{S}$, with $\gamma_e = -g_e \mu_B/\hbar = -2\pi \times 2.8$ MHz/Gs the gyromagnetic moment of the NV electron spin ($g_e = 2$ [24] the NV Landé factor and μ_B the Bohr magneton). The Hamiltonian $\hat{H}_{ZF} + \hat{H}_B$ can be diagonalized. In Fig. 2.28, we show the spin energy states evolution with the external magnetic field $\mathbf{B_{NV}}$ applied parallel and perpendicular to the NV center axis for 2 MHz strain coefficient. When $B_{NV} \gg E/|\gamma_e|$, the strain-induced fine structure splitting becomes negligible compared to the Zeeman splitting, the states $|\pm\rangle$ are well approximated by the pure spin states $|m_S = \pm 1\rangle$ and the resonant frequencies $\omega_\pm$ tend towards their asymptotes $D \mp \gamma_e B_{NV}$. In our experiments, the magnetic field $\mathbf{B_{NV}}$ is applied parallel to superconducting bus resonator on a collection of NV center spins yielding different Zeeman shifts for the four spin groups of crystallographic NV orientations.

Hyperfine interaction The NV center is also coupled by hyperfine interaction to nearby nuclear spins. One can distinguish the contribution of the hyperfine coupling to the ^{14}N nuclear spin, which is present in each NV center and modifies appreciably its spectrum, from the hyperfine coupling to the ^{13}C spins in the diamond lattice, which has a different effect on each NV center and contributes to decoherence. We thus include in the NV Hamiltonian only the coupling to the nuclear spin-1 ($I = 1$)

Fig. 2.28 Energy states dependence of the microwave transitions $\omega_\pm$ under a magnetic field, applied parallel (perpendicular) to the NV center axis showing a linear (quadratic) Zeeman effect

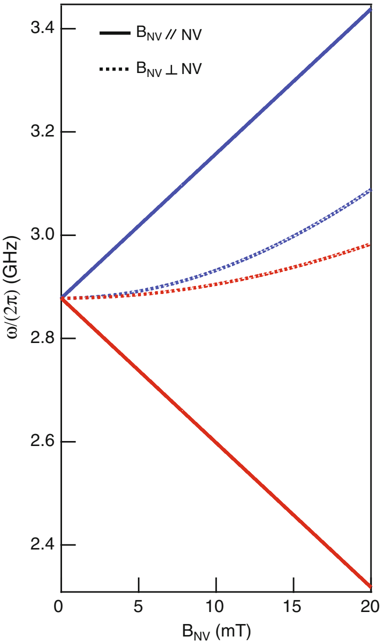

of the nitrogen atom ^{14}N. The hyperfine term can be written as $\hat{H}_{HF}/\hbar = \mathbf{S}\cdot\bar{\mathbf{A}}\cdot\mathbf{I}$ with $\mathbf{I}$ the dimensionless operator of the nitrogen nuclear spin and $\bar{\mathbf{A}}$ the hyperfine interaction tensor. The hyperfine tensor is given by [30]:

$$\bar{\mathbf{A}} = \begin{pmatrix} A_\perp & & \\ & A_\perp & \\ & & A_\parallel \end{pmatrix} \tag{2.66}$$

with $A_\perp/2\pi = 2.7\,\text{MHz}$ and $A_\parallel/2\pi = 2.14\,\text{MHz}$. In addition, the nitrogen atom has a quadrupole moment yielding a term $\hat{H}_P = P\hat{I}_Z^2$ with $P = -2\pi \times 5\,\text{MHz}$. In total, the NV Hamiltonian is:

$$\hat{H}/\hbar = \underbrace{\mathbf{S}\cdot\bar{\mathbf{D}}\cdot\mathbf{S}}_{ZF} - \underbrace{\gamma_e\mathbf{B_{NV}}\cdot\mathbf{S}}_{B} + \underbrace{\mathbf{S}\cdot\bar{\mathbf{A}}\cdot\mathbf{I}}_{HF} + P\hat{I}_Z^2 \tag{2.67}$$

The NV eigenstates are displayed in Fig. 2.29b, showing the effect of the strain as a lifting of degeneracy at zero field and the hyperfine interaction with ^{14}N as a splitting by approximately 2.17 MHz of the resonance into a triplet structure. In practice, one of the two transitions at frequencies $\omega_\pm$ between the spin ground state $|m_S = 0\rangle$ and the excited states $|\pm\rangle$ is used, equivalent to a two-level system with ground state $|g\rangle$ and excited state $|e\rangle$ and transition frequency ω_s. In this two level system description, the Hamiltonian of the NV center spin (Eq. 2.67) reduces to

$$\hat{H}_a = -\hbar\frac{\omega_\pm}{2}\hat{\sigma}_z \tag{2.68}$$

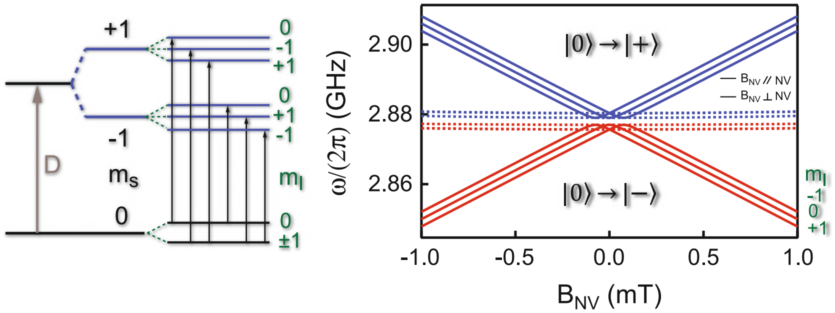

Fig. 2.29 NV energy diagram showing the Zeeman and hyperfine structure of the electronic ground state under a magnetic field applied parallel (perpendicular) to the NV center axis. Six microwave transitions are allowed. Under magnetic field applied perpendicular to the NV axis, the transitions $|m_S = 0, m_I = \pm1\rangle \rightarrow |m_S = +1, m_I = +1\rangle$ and $|m_S = 0, m_I = \pm1\rangle \rightarrow |m_S = +1, m_I = -1\rangle$ (respectively $|m_S = 0, m_I = \pm1\rangle \rightarrow |m_S = -1, m_I = +1\rangle$ and $|m_S = 0, m_I = \pm1\rangle \rightarrow |m_S = -1, m_I = -1\rangle$) are degenerated

An oscillating magnetic field $\mathbf{B_d(t)} = B_d \cos(\omega_d t) \cdot \mathbf{e_X}$ can be applied to drive the spin transitions. The corresponding Hamiltonian is $\hat{H}_d = -\gamma_e \mathbf{S} \cdot \mathbf{B_d}(t)$ and can be rewritten in the frame rotating at ω_d

$$\hat{H}_d/\hbar = -\gamma_e \frac{\hat{B}_d \cdot \hat{S}_X}{2} = -\gamma_e \frac{B_d}{2\sqrt{2}} \hat{\sigma}_x \tag{2.69}$$

which corresponds to a Rabi frequency $\Omega_R = \gamma_e B_d/\sqrt{2}$. In our experiments, the spins are driven via a resonator, with the oscillating magnetic field generated by the oscillating current in the resonator inductance. As explained earlier, it is possible to link the incoming microwave power P to this current, and the current to a spatially-dependent magnetic field $B_d(\mathbf{r})$. The last equation shows how to determine the Rabi frequency $\Omega_R(\mathbf{r}, P)$ of a spin located at position $\mathbf{r}$, which will be used in Chap. 5.

2.2.2.2 NV Qubit Initialization: Optical Properties

Spin state initialization can be obtained through the use of an optical transition to the electronic excited state which has the property to relax selectively in $|m_S = 0\rangle$ of the electronic ground state. For this, drive of the NV centers to the electronic excited state has to be implemented. The electronic ground and excited states of the NV centers are coupled through an electrical dipolar transition with zero phonon line (ZPL) at 1.945 eV (Fig. 2.30), corresponding to emission at $\lambda_{ZPL} = 638$ nm. This radiative transition is coupled to the phonons of the diamond matrix which allows for vibronic sideband excitations. Due to the availability, usually 532 nm laser light is used to excite from the triplet ground state to the excited one [31]. The optical transitions between ^3A and ^3E are spin conversing ($\Delta m_S = 0$). As a result, NV centers initially in the $|m_S = 0\rangle_{ground}$ (respectively in $|m_S = \pm 1\rangle_{ground}$) end up in the $|m_S = 0\rangle_{excited}$ (respectively in the $|m_S = \pm 1\rangle_{excited}$) excited state and can decay back through the same radiative transition.

There is however a second possibility given by intersystem crossing (ISC): once in the excited electronic state the NV center can return into the triplet ground state via the singlet metastable level ^1A. The decay back from the metastable state into the triplet ground state occurs preferentially into the $|m_S = 0\rangle_{ground}$ [32, 33]. The point is that ISC is strongly spin state dependent so that there is high probability from $|m_S = \pm 1\rangle_{excited}$ state to decay back via the metastable state while a very low

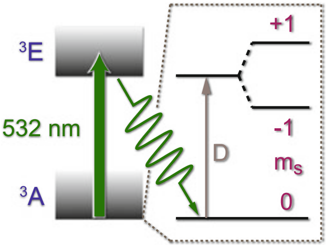

Fig. 2.30 Optical repumping of NV centers in their $m_S = 0$ ground state by application of green (532 nm) laser pulses exciting the ^3E-^3A transition

one from $|m_S = 0\rangle_{excited}$ state. Hence, after several optical cycles, the NV-centers are mainly polarized in the ground state $|m_S = 0\rangle_{ground}$ regardless of theirs former state: this is the optical repumping. This process occurs in few tens of nanoseconds at low temperature [34], sufficiently fast to be included in our memory protocol. The maximum spin polarization reachable using optical repumping is ~90 %, according to [35].

For experiments which do not require such fast pumping, or alternatively in which the amount of excited spins is intrinsically very low (for example the experiment 1 of this thesis work), cooling down in a dilution fridge at milliKelvin (mK) temperatures via the surrounding bath temperature is sufficient to ensure large polarization in $|m_S = 0\rangle$. Indeed for NV center at 30 mK, $\hbar\omega_{ge} \gg k_B T$ and the probability for a spin to be excited is $p_\pm = e^{-(\hbar\omega_{ge}/k_B T)} \approx 0.01$. Note however that the NV energy relaxation time is of order 5 ms [36] at room temperature, and even longer at low temperature. This implies that once excited, the relaxation of the spin polarization towards the equilibrium is long. Hence, it is possible that the temperature of the spins is different than the one of the cryostat, due to thermal excitation, i.e. via measurement transmission lines.

2.2.3 Coherence Times

The coherence properties of NV centers are characterized by the free-induction decay time T_2^* (measured by Ramsey fringes), the Hahn-echo decay time T_2 (measured by a spin-echo sequence), and the coherence time under dynamical decoupling sequences such as Carr-Purcell-Meiboom-Gil T_{2CPMG} (see Fig. 2.31). The value found for these

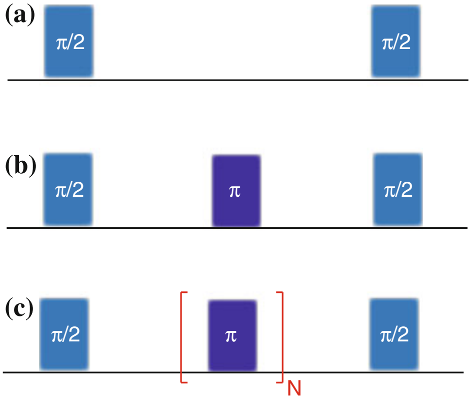

Fig. 2.31 Measuring the coherence times. a Ramsey sequence. Two $\pi/2$ rotations are performed, separated by a delay during which the spins precess freely. The envelope of the oscillations for increasing τ is characterized by the dephasing time T_2^*, associated to fluctuations of the environment. **b** Spin echo sequence. An intermediate π rotations around x is performed to refocus the dephasing due to static fluctuations. **c** Dynamical decoupling sequence. Successive π rotations are performed to refocus the dephasing due to dynamic fluctuations

times depends crucially on the local magnetic environment of each spin in a sphere of radius few tens of nanometers. In diamond, the main magnetic impurities are neutral nitrogen atom (the P1 centers) which have an electronic spin $1/2$ and carbon 13 nuclei with their nuclear spin $1/2$ present to $1.1\,\%$ abundance in natural carbon. The longest echo coherence times $T_2 = 2\,\mathrm{ms}$ were therefore measured in ultrapure samples growth by Chemical-Vapor Deposition (CVD) with very low nitrogen concentration as well as isotopically enriched carbon source. In such samples, the coherence time has been extended out up to $T_{2CPMG} = 0.5\,\mathrm{s}$ under Carr-Purcell-Meiboom-Gil dynamical decoupling sequences at low $(100\,\mathrm{K})$ temperatures [27]. This is five orders of magnitude longer than superconducting qubits, which motivates the idea of using NV centers for storing quantum information.

The crystals used in our experiments are however not as pure. Indeed, we need relatively large concentrations of NV centers of orders $\sim 1.76 - 17.6 \cdot 10^5\,\mu\mathrm{m}^3$ (1–10 ppm) to efficiently absorb microwave photon in superconducting resonator. These concentrations are not easily reached with sample grown by CVD. Our crystals instead are grown by a method called High-Pressure-High-Temperature (HPHT). HPHT diamond usually have a large nitrogen concentration of 1–100 ppm. NV centers are created from this nitrogen doped diamond in two steps: (i) irradiation with protons or with electrons of a diamond crystal to produce vacancies (ii) annealing at 800–1000° C to allow the vacancies to migrate and form the NV defect. This method unavoidably leaves a significant residual concentration of P_1 centers (1–100 ppm), which limits the spin coherence time (both T_2^* and T_2) to lower values than reported with CVD diamonds. In the experiments discussed here, these residuals P1 centers are the main cause of decoherence. The contribution of P1 centers to the decoherence has been thoroughly studied [37–40]. In particular, it was shown [41] that T_2^* and T_2 are inversely proportional to the P1 center concentration ($[P1]$), with the relations $1/T_2^* = -\gamma_e\sqrt{1.2 \cdot 10^{-4}[P1]^2 + 6.4 \cdot 10^{-4}}\ \mathrm{s}^{-1}$ and $1/T_2 = 1.4 \cdot 10^4 \times [P1]\,\mathrm{s}^{-1}$ (see Fig. 2.32). At low concentration, the contribution of the ^{13}C becomes dominant as evidenced by the saturation.

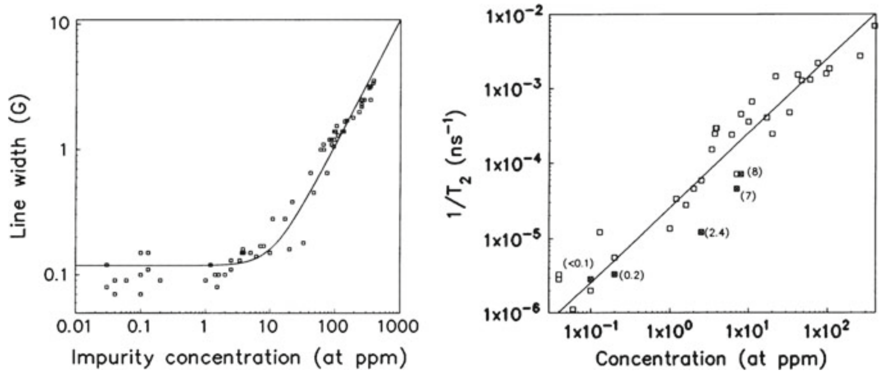

Fig. 2.32 Dependence of the coherence times on the P1 concentration [41]**.** Dependence of the linewidth $\gamma = 1/T_2^*$ (*left*) and spin-spin relaxation rate $1/T_2$ (*right*)

2.3 Coupling Ensembles of NV Center Spins to Superconducting Circuits

In our experiments, a superconducting resonator is used to mediate the interaction between the NV center spins and the rest of the circuit. In the following, we describe the spins-resonator system. We first evaluate the interaction strength of a single NV center spin to a superconducting resonator for typical cQED parameter. We will see that this coupling strength is too weak to allow for coherent exchange of quantum information, but instead an ensemble of such spin benefit from a collective enhancement. We will consider our experimental conditions in which the spin ensemble has both static distributions of spin-resonance frequency and coupling strength to the resonator and treat the dynamics of the spins-resonator system.

2.3.1 Single Spin-Resonator Coupling

Strictly speaking, NV centers are spin-1 systems so that it is not possible to write the interaction of the electronic spin with a resonator field on the Jaynes Cummings form of Sect. 2.1.3.1. However by applying a static bias on the spins, one can operate on one of these transitions only: the NV center is reduced to a two-level system with ground state $|g\rangle = |m_S = 0\rangle$, excited state $|e\rangle = |\pm\rangle$ and transition frequency $\omega_s = \omega_\pm$. The Hamiltonian of the single spin-resonator system can be written:

$$\hat{H} = \hat{H}_r + \hat{H}_a + \hat{H}_{int} \tag{2.70}$$

with $\hat{H}_r$ the free-field Hamiltonian given by Eq. 2.2, $\hat{H}_a$ the Hamiltonian of the NV center spin given by Eq. 2.68 and a coupling term function of $\mathbf{S}$ the magnetic dipole of the NV and $\mathbf{B}$ the magnetic field sustained by the resonator:

$$\begin{aligned}
\hat{H}_{int}/\hbar &= -\gamma_e \mathbf{S}\cdot\mathbf{B} && (2.71)\\
&= -\frac{\gamma_e}{\sqrt{2}}\left[\hat{\sigma}_x \delta B_x(\mathbf{r}) + \hat{\sigma}_y \delta B_y(\mathbf{r})\right](\hat{a}+\hat{a}^\dagger) && (2.72)\\
&= -\frac{\gamma_e}{\sqrt{2}}\left[\hat{a}\hat{\sigma}_+\{\delta B_x(\mathbf{r}) - i\delta B_y(\mathbf{r})\} + \hat{a}^\dagger\hat{\sigma}_-\{\delta B_x(\mathbf{r}) + i\delta B_y(\mathbf{r})\}\right] && (2.73)\\
&= g^*\hat{a}\hat{\sigma}_+ + g\hat{a}^\dagger\hat{\sigma}_- && (2.74)
\end{aligned}$$

with the (complex) spin-resonator coupling constant defined as

$$g = -\frac{\gamma_e\left[\delta B_x(\mathbf{r}) + i\delta B_y(\mathbf{r})\right]}{\sqrt{2}} \tag{2.75}$$

The modulus of this coupling constant can be estimated numerically for typical parameters of resonators in circuits, using the analytical expression for the magnetic field generated by a CPW waveguide Eq. 2.24. For a 50 Ω resonator on Silicon with geometrical parameters $S, W = 10, 5\,\mu\text{m}$ and resonance frequency $\omega_r/(2\pi) = 2.88\,\text{GHz}$, the magnetic field generated at the surface is $\sim$450 pT yielding a single-spin-resonator coupling constant

$$g \sim 2\pi \cdot 10\text{ Hz}. \tag{2.76}$$

This value is four orders of magnitude smaller than resonator linewidth κ reachable in circuit QED. The coupling strength of an individual NV center spins to one electromagnetic mode is thus too weak to allow for strong coupling ($g \gg \kappa, \gamma$) and subsequent coherent exchange of quantum information. This issue is overcome by using large ensembles of spins, as explained in the following.

2.3.2 Spin Ensemble-Resonator Coupling: Collective Effects

New effects appear when an ensemble of N spins is collectively coupled to a resonator. The goal of this section is to give the elements of theory relevant for understanding our quantum memory protocol and experiments, and to derive a number of formulas for the analysis.

2.3.2.1 The Tavis-Cummings Model

The Tavis-Cummings model [42] considers N identical spins-1/2 with frequency ω_s coupled with the same coupling constant g to a single cavity mode at frequency ω_r (see Fig. 2.33). The Hamiltonian writes:

$$\hat{H}_{TC}/\hbar = \omega_r \left(\hat{a}^\dagger \hat{a} + \frac{1}{2}\right) + \frac{\omega_s}{2} \sum_{j=1}^{N} \hat{\sigma}_z^{(j)} + g \sum_{j=1}^{N} \left(\hat{a}\hat{\sigma}_+^{(j)} + \hat{a}^\dagger \hat{\sigma}_-^{(j)}\right), \tag{2.77}$$

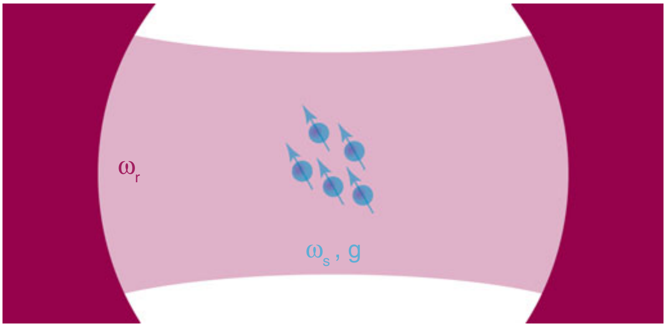

Fig. 2.33 The Tavis-Cummings model. N identical two-level systems of frequency ω_s are identically coupled to a single cavity mode with coupling strength g

with $\hat{\sigma}_{z,\pm}^{(j)}$ the Pauli spin operators of spin j. The internal states of the ensemble can be written in the 2^N-dimensional basis spanned by the states $\Pi_{j=1,..,N}|i\rangle_j$, with $i = g, e$. As a useful notation, we refer in the following to the collective ground state $|G\rangle \equiv |g_1 \ldots g_N\rangle$, and the state with only spin j excited $|E_j\rangle \equiv |g_1 \ldots e_j..g_N\rangle$. Introducing the collective spin operators $\hat{\mathcal{S}}_{X,Y,Z} = \sum_{j=1}^{N} \hat{\sigma}_{x,y,z}^{(j)}/2$ and $\hat{\mathcal{S}}_{\pm} = \sum_{j=1}^{N} \hat{\sigma}_{\pm}^{(j)}$, $\hat{H}_{TC}$ can be rewritten as:

$$\hat{H}_{TC}/\hbar = \omega_r \left(\hat{a}^\dagger \hat{a} + \frac{1}{2}\right) + \omega_s \hat{\mathcal{S}}_z + g\left(\hat{a}\hat{\mathcal{S}}_+ + \hat{a}^\dagger \hat{\mathcal{S}}_-\right), \tag{2.78}$$

called the Tavis-Cummings Hamiltonian.

THE COLLECTIVE BASIS

One key property of this Hamiltonian is that it commutes with the total spin $\hat{\mathcal{S}}^2 = \hat{\mathcal{S}}_x^2 + \hat{\mathcal{S}}_y^2 + \hat{\mathcal{S}}_z^2$, implying that its eigenvalue[3] $\mathcal{S}(\mathcal{S}+1)$ is a good quantum number whose value is constant in time. The system dynamics is thus restrained to subspaces with fixed $\mathcal{S}$, and it is therefore interesting to describe it in the basis of the simultaneous eigenstates of $\hat{\mathcal{S}}^2$ and $\hat{\mathcal{S}}_z$:

$$\hat{\mathcal{S}}^2|\mathcal{S}, m\rangle = \mathcal{S}(\mathcal{S}+1)|\mathcal{S}, m\rangle \tag{2.79}$$

$$\hat{\mathcal{S}}_z|\mathcal{S}, m\rangle = m|\mathcal{S}, m\rangle \tag{2.80}$$

where m can take any of the $(2\mathcal{S}+1)$ values $-\mathcal{S}, -\mathcal{S}+1, \ldots, \mathcal{S}-1, \mathcal{S}$. Note that these states are highly degenerated since there are only $N(N+3)/2$ possible values for the couple $(\mathcal{S}, m)$ whereas there are 2^N possible spin states. The degeneracy of the states $|\mathcal{S}, m\rangle$ is given by $\frac{N!(2\mathcal{S}+1)}{(N/2+\mathcal{S}+1)!(N/2-\mathcal{S})!}$ [43], implying that states with low values of $\mathcal{S}$ are much more numerous than states with large $\mathcal{S}$. At the extreme, states with $\mathcal{S} = N/2$ are non-degenerate.

Another relevant quantity is the degeneracy of states having a well-defined value of m, which is simply given by $\frac{N!}{(N/2+m)!(N/2-m)!}$, the number of different ways to flip $N/2+m$ spins among N. One sees that there is only one ground state corresponding to $|N/2, -N/2\rangle$, N states with a single excitation $m = -N/2+1$, among which 1 state $|N/2, -N/2+1\rangle$ and $(N-1)$ of the form $|N/2-1, -N/2+1\rangle$, $N(N-1)/2$ states with 2 excitations ($m = -N/2+2$), among which 1 with $\mathcal{S} = N/2$, $(N-1)$ with $\mathcal{S} = N/2-1$, and $N(N-3)/2$ with $\mathcal{S} = N/2-2$, ... A schematic description of the collective states summarizing their degeneracy is in Fig. 2.34.

---

[3] $\mathcal{S}$ takes any integer or half-integer value between 0 and $N/2$.

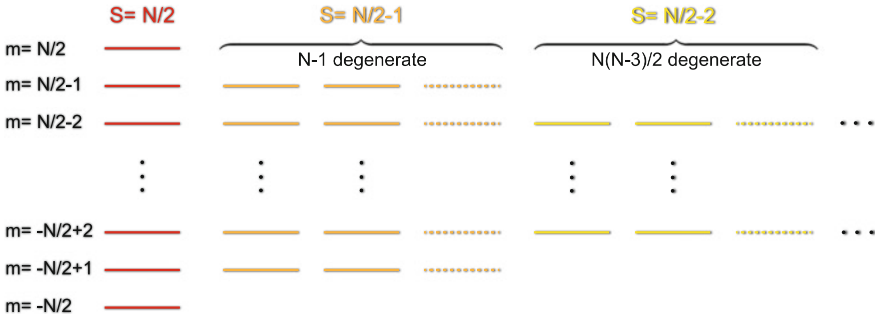

Fig. 2.34 Energy level diagram of an ensemble of N spins-1/2. States $\mathcal{S} \neq N/2$ are highly degenerate. There is one ground state corresponding to $|N/2, -N/2\rangle$, N states with a single excitation $m = -N/2+1$, among which 1 state $|N/2, -N/2+1\rangle$ and $(N-1)$ of the form $|N/2-1, -N/2+1\rangle$

COLLECTIVE ENHANCEMENT OF THE COUPLING

Of particular interest is the situation where the initial state is the collective ground $|G\rangle$, corresponding to $m = -N/2$ and hence $\mathcal{S} = N/2$. Since the Tavis-Cummings Hamiltonian preserves $\mathcal{S}$ and since the states $|N/2, m\rangle$ are non-degenerate, the system dynamics is restricted to the (N+1)-dimensional manifold of perfectly symmetric states for which $\mathcal{S} = N/2$, instead of the full 2^N-dimensional Hilbert space. Putting one excitation in the spin system can be done by absorbing a photon from the cavity, which excites the state $|B\rangle = |N/2, -N/2+1\rangle \equiv \mathcal{S}_+|G\rangle/|\mathcal{S}_+|G\rangle| = \sum_k |E_k\rangle/\sqrt{N}$. The $N-1$ other states with one excitation in the spin ensemble (i.e. with $m = -N/2+1$) can be written as $|D_j\rangle = \sum_{k=0}^{N-1} \exp^{ijk2\pi/N} |E_k\rangle/\sqrt{N}$ (with $j = 1, \ldots, N-1$). It is straightforward to see that $\langle D_j|B\rangle = 0$, which implies that all $|D_j\rangle$ states are of the form $|N/2-1, -N/2+1\rangle$. Since the $|D_j\rangle$ states are states with $\mathcal{S} = N/2-1$, they cannot be coupled to $|G\rangle$ by the Tavis-Cummings Hamiltonian, and one gets

$$\langle E, 0|\hat{H}|G, 1\rangle = (1/\sqrt{N}) \sum_i g = g\sqrt{N} \tag{2.81}$$

$$\langle D_j, 0|\hat{H}|G, 1\rangle = 0. \tag{2.82}$$

By describing the spin-cavity coupling in the collective basis, we thus come to the important conclusion that (for single-excitation states) only one collective state (*bright*) $|B\rangle$ is coupled to the cavity mode with a strength enhanced by a factor $\sqrt{N}$ compared to the single spin case, whereas $(N-1)$ collective spin states (*dark*) $|D_j\rangle$ are decoupled from the radiation field.

LOW- EXCITATION APPROXIMATION

In the limit of small excitation numbers, i.e. where $m + N/2 \ll N$, a useful approximation (called the Holstein-Primakoff approximation) is possible [44–46]. It consists in replacing each spin operator $\hat{\sigma}_{\pm}^{(j)}$ by bosonic operators $\hat{s}_j$,$\hat{s}_j^{\dagger}$ that verify $[\hat{s}_j, \hat{s}_j^{\dagger}] = 1$ using the following rules

$$\hat{\sigma}_{-}^{(j)} \to \hat{s}_j \tag{2.83}$$

$$\hat{\sigma}_{+}^{(j)} \to \hat{s}_j^{\dagger} \tag{2.84}$$

$$\hat{\sigma}_{z}^{(j)} \to -1 + 2\hat{s}_j^{\dagger}\hat{s}_j. \tag{2.85}$$

In doing so, one neglects all effects linked to the saturation of a spin since a harmonic oscillator can have an arbitrary number of excitations contrary to a spin. This approximation is thus only valid when the system dynamics is restricted to states for which $\langle \hat{s}_j^{\dagger}\hat{s}_j \rangle \ll 1$ or equivalently $\langle \hat{\sigma}_z^{(j)} \rangle + 1 \ll 1$. In our situation where the spin ensemble can only be collectively excited and thus where a large number of spins have the same average excitation, this is indeed equivalent to the condition stated at the beginning of this section that the total number of excitation of the ensemble verifies $m + N/2 \ll N$.

In the same way as previously, it is useful to describe the spins in the collective basis in the Holstein-Primakoff approximation, by defining the collective bosonic operators

$$\hat{b} = \frac{1}{\sqrt{N}} \sum_{k=0}^{N-1} \hat{s}_k \tag{2.86}$$

$$\hat{d}_j = \frac{1}{\sqrt{N}} \sum_{k=0}^{N-1} \exp^{ijk2\pi/N} \hat{s}_k \tag{2.87}$$

and their conjugate. It is then straightforward to show that the Tavis-Cummings Hamiltonian can be rewritten as

$$\hat{H}_{HP}/\hbar = \omega_r \left(\hat{a}^{\dagger}\hat{a} + \frac{1}{2} \right) + \omega_s(\hat{b}^{\dagger}\hat{b} + \sum_{j=1}^{N-1} \hat{d}_j^{\dagger}\hat{d}_j) + g_{ens}(\hat{a}^{\dagger}\hat{b} + \hat{a}\hat{b}^{\dagger}). \tag{2.88}$$

In the Holstein-Primakoff approximation, the coupling of N spins to a cavity with constant g can thus be described as a collection of N harmonic oscillators: one *bright mode b* coupled to the cavity mode with an enhanced coupling constant

$$g_{ens} = g\sqrt{N}, \tag{2.89}$$

and $N - 1$ *dark modes* d_j (with $j = 1, \ldots, N - 1$) completely decoupled from the cavity field. From the ground state $|G\rangle \equiv |0, \ldots, 0\rangle$, one can generate N different single-excitation states by applying one of the collective creation operators $\hat{b}^{\dagger}$ or $\hat{d}_j^{\dagger}$, and then $N(N + 1)/2$ two-excitation states by applying a second time one of these operators, and so forth. The single-excitation manifold is strictly identical to the

$m = -N/2 + 1$ collective spin states described earlier. The two-excitation manifold contains an excess of N states in the Holstein-Primakoff description (the states with 2 excitations in the same mode and 0 in the others), but for N large this is a small error compared to the much larger number of states with one excitation in two different modes, which are identical to the $m = -N/2 + 2$ collective spin states.

At this point it is interesting to make a side remark regarding thermal equilibrium of the spin ensemble at finite temperature T. In the limit where $k_B T \ll \hbar\omega_s$ the mean number of excited spins at equilibrium is approximately given by $N \exp(-\hbar\omega_s/k_B T) \ll N$, so that the Holstein-Primakoff approximation is valid. According to the previous discussion, the thermal state of the spin ensemble is thus well described by the thermal state of a collection of N independent harmonic oscillators. Even though the total number of excited spins $N \exp(-\hbar\omega_s/k_B T)$ can be very large, we thus come to the conclusion that each of the collective modes actually has a large probability $(1 - \exp(-\hbar\omega_s/k_B T))$ to be found in its ground state $|0\rangle$. This means that in order for our quantum memory to be initialized, the requirement is simply that the mean excitation of the collective bright mode should be small ($\exp(-\hbar\omega_s/k_B T) \ll 1$), and not that the total number of excited spins should be small ($N \exp(-\hbar\omega_s/k_B T) \ll 1$), which would be an impossible condition to fulfill in any realistic experiment.

Note however that if the memory uses n modes for storage, the requirement that each of these modes be initialized in its ground state becomes more stringent ($n \exp(-\hbar\omega_s/k_B T) \ll 1$), but for realistic values of $n = 10^2$–10^3, this still seems achievable experimentally.

EXCITATION SPECTRUM

The Hamiltonian $\hat{H}_{HP}$ can be very simply diagonalized by introducing two new operators which are linear combinations of the bright mode and the cavity field, called polaritons, and defined as

$$\hat{p}_+ = \cos\theta\hat{a} + \sin\theta\hat{b} \tag{2.90}$$

$$\hat{p}_- = -\sin\theta\hat{a} + \cos\theta\hat{b}, \tag{2.91}$$

with $\tan(2\theta) = -2g_{ens}/\Delta$, $\Delta = \omega_s - \omega_r$ being the frequency difference between the cavity and the spins. These bosonic operators (since $[\hat{p}_+, \hat{p}_+^\dagger] = [\hat{p}_-, \hat{p}_-^\dagger] = 1$) describe coupled spin-photon excitations. Introducing $\omega_{p,\pm} = \omega_r \pm \frac{1}{2}\sqrt{4g_{ens}^2 + \Delta^2}$, the Hamiltonian can then be written as

$$\hat{H}_{HP}/\hbar = \omega_s \sum_{j=1}^{N-1} \hat{d}_j^\dagger \hat{d}_j + \omega_{p,+}\hat{p}_+^\dagger \hat{p}_+ + \omega_{p,-}\hat{p}_-^\dagger \hat{p}_-. \tag{2.92}$$

which shows that the Hamiltonian eigenstates are tensor products of Fock states of the dark modes (at frequency ω_s) and the polaritonic modes (at frequencies $\omega_{p,\pm}$).

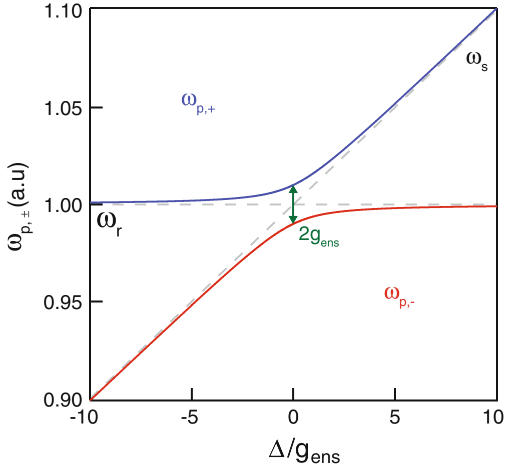

Fig. 2.35 Polaritonic modes. The system excitation spectrum consists of only the two polaritonic modes

Probing the system with a microwave tone coupled to the cavity input, the system excitation spectrum consists of only the two polaritonic modes since the dark modes are decoupled to the cavity and thus invisible. Sweeping the spin frequency across the cavity, one should thus observe an avoided level crossing (see Fig. 2.35), with minimal peak separation of $2g_{ens}$ obtained at resonance ($\Delta = 0$), where $\hat{p}_+ = (\hat{a} + \hat{b})/\sqrt{2}$ and $\hat{p}_- = (\hat{a} - \hat{b})/\sqrt{2}$. The experimental observation of such an anticrossing in the transmission spectrum of a resonator coupled to an ensemble of NV centers is reported in Chap. 4 and is the starting point of this thesis work.

DYNAMICS

Coming back to the Hamiltonian Eq. 2.88, we see that the interaction between the bright mode and the cavity is of the beam-splitter type $\hat{a}^\dagger \hat{b} + \hat{a}\hat{b}^\dagger$. It is well-known [47] that suddenly switching on resonantly this type of interaction for a well-chosen duration produces a dynamics corresponding to a SWAP operation, exchanging the two quantum states of the cavity and the bright mode. For instance, if the cavity is prepared at $t = 0$ in a single-photon Fock state $|1\rangle$ and the bright mode in its ground state $|0_b\rangle$, the coupled system quantum state $|\psi(t)\rangle$ will evolve at $t > 0$ as

$$|\psi(t)\rangle = \cos(g_{ens}t)|1, 0_b\rangle + \sin(g_{ens}t)|0, 1_b\rangle \tag{2.93}$$

which shows that the single-photon state will indeed be transferred from the resonator into the spin ensemble after an interaction time $\pi/(2g_{ens})$. This vacuum Rabi oscillation between the resonator and the bright mode of the spin ensemble is the basis for the *write* experiment that will be related in Chap. 4.

SUPERRADIANCE

Besides the collective enhancement of the coupling of the bright mode to the cavity field, another interesting phenomenon arises from the Tavis-Cummings Hamiltonian when the initial state is the fully excited state $|e_1 \ldots e_N\rangle$. This state is also symmetrical and can be identified as $|N/2, N/2\rangle$ in the collective spin basis. Being the state of maximal energy it eventually has to relax by spontaneous emission of photons into the electromagnetic mode defined by the cavity. The Tavis-Cummings Hamiltonian shows however that its relaxation should still take place in the basis of fully symmetrical states $\mathcal{S} = N/2$, going down the energy ladder from $|N/2, N/2\rangle$ until it reaches the ground state $|N/2, -N/2\rangle$, via states $|N/2, m \approx 0\rangle$, by steps of $\Delta m = -1$ corresponding to successive photon emissions.

Defining the photon spontaneous emission rate of an isolated spin as γ_1, the spin ensemble collective radiation rate (assuming that the cavity is rapidly damped so that the intra-cavity photon number stays $\approx$0) is given by $\gamma_1 |\langle m-1, N/2|\mathcal{S}_-|m, N/2\rangle|^2$, which was shown by Dicke to be equal to $I_0(N/2+m)(N/2-m+1)$. For $m = N/2$, this rate is $N\gamma_1$ as would be the case for independent emitters, but this quantity rapidly increases with decreasing m, reaching a maximum of $(N/2)^2\gamma_1$ when $m = 0$, after which it goes down again to $N\gamma_1$ when the system approaches its ground state. This implies that the photon emission of a collection of symmetrically excited spins does not take place as a simple exponential, as would be the case if each spin would radiate individually, but instead consists of a coherent pulse of light, which takes place in an overall much shorter time given by γ_1^{-1}/N and with a much stronger peak intensity of $N^2\gamma_1$.

This enhanced collective spontaneous emission is called superradiance and has been widely studied both theoretically and experimentally. In our context superradiance is relevant because it complicates the *read step* of our memory protocol, since as explained in Chap. 3 this step involves the application of a π pulse to the spins which precisely excites them into $|e_1 \ldots e_N\rangle$. The desexcitation of this state by emission of a superradiant pulse would be disastrous for the fidelity of the memory, and is prevented in the protocol described in Chap. 3.

2.3.2.2 The Realistic Model

In our experiments, several hypotheses of the Tavis-Cummings model are not satisfied (Fig. 2.36):

1. The spin-resonator coupling is far from being the same for each spin. Indeed, in our experiments (see Chaps. 4 and 5), the resonator is implemented by a superconducting planar circuit, on top of which the diamond crystal is fixed, and the magnetic field it generates (as well of course as its quantum fluctuations) is spatially inhomogeneous. This results in a position-dependent spin-resonator coupling constant $g_i = g(\mathbf{r_i})$, which now becomes a complex number since the field direction may vary between different spins. The distribution $\rho(g) = \sum_i \delta(g - |g_i|)$ characterizes the amplitude variations of the coupling constant in the continuous limit.

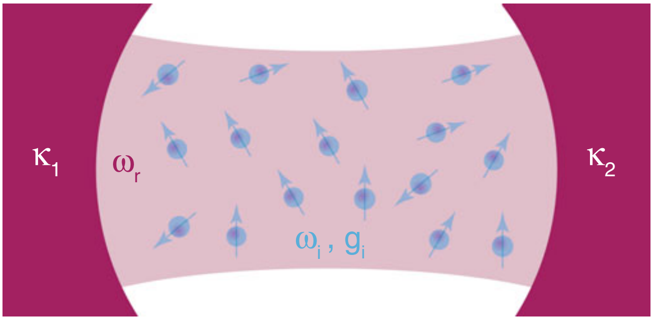

Fig. 2.36 **The realistic model.** The cavity is coupled to external transmission lines through coupling capacitances and has a finite damping rate $\kappa = \kappa_1 + \kappa_2$. The spin ensemble has both static distributions of spin-resonance frequency $\rho(\omega)$ and coupling strength $\rho(g)$

2. The NV centers throughout the ensemble have slightly different frequencies due to their different local magnetic environments (see Sect. 2.2.3). This inhomogeneous broadening is described by a (static) distribution of frequency

$$\rho(\omega) = \sum_i |g_i|^2 \delta(\omega - \omega_i) \tag{2.94}$$

   around the central frequency ω_s.
3. The cavity has a finite damping rate κ due to coupling to the line and internal losses, implying that the quantum states inside the resonator have a finite lifetime.

COUPLING CONSTANT INHOMOGENEITY

The coupling constant inhomogeneity would not alter any of the conclusions reached in the previous section, provided all spins have the same frequency ω_s. Indeed one can redefine the bright mode in the Holstein-Primakoff approximation as $\hat{b} = 1/g_{ens} \sum_{k=1}^{N} g_k \hat{s}_k$, with

$$g_{ens} = (\sum_{j=1}^{N} |g_j|^2)^{1/2} = (\int g^2 \rho(g) \cdot dg)^{1/2} \tag{2.95}$$

the collective coupling constant, as well as $N - 1$ orthogonal dark modes d_j $(j = 1, \ldots, N-1)$ (without giving their explicit expression, which would be more tedious than in the previous section). It is then straightforward to see that the Tavis-Cummings Hamiltonian can be rewritten exactly in the form of Eq. 2.88, implying that all the previous conclusions about collective effects would be completely unchanged, apart from a re-definition of the ensemble coupling constant provided by Eq. 2.95. In the remaining of this work we will use these new definitions of the bright mode b, and of g_{ens}. Note that with these definitions of $\rho(\omega)$ and g_{ens}, one finds that $\int \rho(\omega) d\omega = g_{ens}^2$.

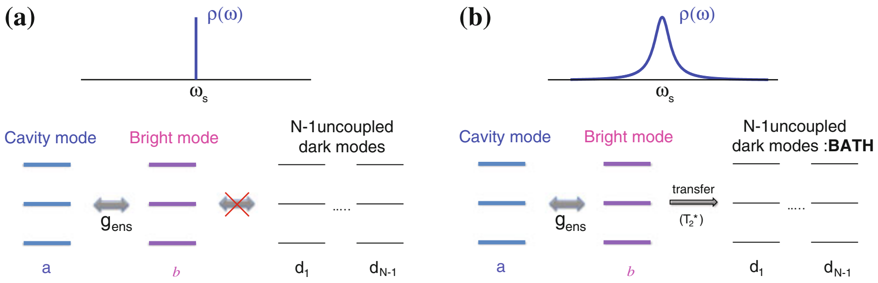

Fig. 2.37 **Transfer from the bright mode to the dark mode subspace enabled by inhomogeneous broadening.** In the homogeneous case (**a**), the cavity and bright mode constitutes a closed system. The bright mode is coupled to the bath of dark modes in case of inhomogeneous broadening (**b**), which make it possible the transfer to the multimode dark mode subspace

INHOMOGENEOUS BROADENING

The inhomogeneity in resonance frequency of the NV centers has more profound consequences. This can be seen qualitatively by noting that if the ensemble is prepared in the state $|1_b\rangle \equiv \hat{b}^\dagger|0_b\rangle = (\sum_{k=1}^N g_k|E_k\rangle)/g_{ens}$ at $t = 0$, it will evolve at later time into $(\sum_{k=1}^N g_k e^{-i(\omega_k-\omega_s)t}|E_k\rangle)/g_{ens}$. The overlap of this state with $|1_b\rangle$ varies in time as the Fourier transform of $\rho(\omega-\omega_s)$. It therefore decays in a time $T_2^* = 2/\Gamma$, Γ being the characteristic width of the $\rho(\omega)$ distribution (see below for a more quantitative definition).

At times $t \gg T_2^*$, the system is thus in a state with $m = -N/2+1$ but orthogonal to $|1_b\rangle$, which therefore belongs to the sub-space spanned by the $N-1$ dark states $|1_{d_j}\rangle$. This brings us to the important conclusion that in the presence of inhomogeneous broadening, the cavity and bright mode do not constitute a closed system any more because the bright mode is now coupled to the large ensemble of dark modes (Fig. 2.37), which act as a bath because of their extremely large number (of order 10^{11} in our experiments). As we will see in Chap. 3, this quantum state transfer from the bright mode into the dark mode subspace is a key resource of our quantum memory protocol because it can be reversed with the appropriate pulse sequence.

2.3.2.3 Coupling Regimes

We now address the issue of whether the coherent collective effects discussed in the idealized model (vacuum Rabi oscillations,...) pertain in the realistic model. Somewhat qualitatively, one can expect two different situations, depending on the relative values of g_{ens}, κ, Γ:

- **If** $g_{ens} \gg \kappa, \Gamma$ (*strong coupling regime*), one can expect that the dynamics will be dominated by the collective radiative effects seen previously. The low-energy excitation spectrum should display a visible avoided level crossing [45, 46]; it should be possible to coherently transfer a quantum state between the resonator and the bright mode of the spin ensemble (even though this state will eventually leak out into the dark modes); and if all the spins are inverted, they should emit a superradiant pulse [48]. This regime is called the *strong coupling regime*. Being able to reach it is a key requirement in some steps of our quantum memory protocol. It requires samples with a large number of spins, but with narrow linewidth.

- **If** $g_{ens} \ll \kappa, \Gamma$ (*weak coupling regime*), no anticrossing is visible; no coherent state transfer is possible; and as discussed in [48], superradiance is suppressed.

The cross-over between weak and strong coupling can also be quantified using a dimensionless number, the so-called cooperativity defined as

$$C = \frac{2g_{ens}^2}{\kappa\Gamma}. \tag{2.96}$$

If $C \gg 1$, the system is in the strong coupling regime, and in the weak coupling regime if $C \ll 1$.

THE KEY PARAMETERS

The ensemble coupling constant g_{ens} The ensemble coupling constant g_{ens} is a central quantity to describe the spin-resonator coupling. We demonstrate here a formula that provides a simple way to estimate g_{ens} as a function of basic experimental parameters, and which will be used extensively throughout this thesis. We have seen in Sect. 2.3.1 that a single NV center spin located at position $\mathbf{r}$ is coupled to the rms vacuum magnetic field fluctuations of the resonator $\delta\mathbf{B}_0(\mathbf{r})$ with a coupling constant of modulus $|g(\mathbf{r})| = (|\gamma_e|/\sqrt{2})|\delta\mathbf{B}_0(\mathbf{r})|\sin\theta(\mathbf{r})$, $\theta(\mathbf{r})$ being the angle between $\delta\mathbf{B}_0(\mathbf{r})$ and the NV axis. To proceed, we note that the energy E_n of a n-photon Fock state in the cavity is equal to $(n+1/2)\hbar\omega_r$, but can also be written as $E_n = \frac{2}{2\mu_0}\int d\mathbf{r}\langle n|\hat{B}(\mathbf{r})^2|n\rangle = \frac{2n+1}{\mu_0}\int d\mathbf{r}|\delta B_0(\mathbf{r})|^2$, so that

$$\int d\mathbf{r}|\delta B_0(\mathbf{r})|^2 = \frac{\mu_0\hbar\omega_r}{2}. \tag{2.97}$$

For a sample of volume V with a homogeneous concentration of NV centers ρ_{NV}, this allows us to rewrite

$$g_{ens} = \frac{|\gamma_e|}{\sqrt{2}}[\rho_{NV}\int_V d\mathbf{r}|\delta B_0(\mathbf{r})\sin\theta(\mathbf{r})|^2]^{1/2} = -\frac{|\gamma_e|}{\sqrt{2}}\sqrt{\frac{\rho_{NV}\mu_0\hbar\omega_r}{2}}\sqrt{\alpha\eta}, \tag{2.98}$$

where η and α are dimensionless numerical factors defined as

$$\eta = \frac{\int_V d\mathbf{r}|\delta B_0(\mathbf{r})|^2}{\int d\mathbf{r}|\delta B_0(\mathbf{r})|^2} \tag{2.99}$$

and

$$\alpha = \frac{\int_V d\mathbf{r}|\delta B_0(\mathbf{r})\sin\theta(\mathbf{r})|^2}{\int_V d\mathbf{r}|\delta B_0(\mathbf{r})|^2}. \tag{2.100}$$

The first parameter η is called the filling factor, and describes what fraction of the magnetic mode volume is occupied by the spins. In our experiments, the diamond is often glued on top of the resonator. If the resonator is of the coplanar waveguide type of total length L, with the diamond symmetrically covering a section of length l as in Chap. 4, it is straightforward to see that $\eta = \int_{(L-l)/2}^{(L+l)/2} dx \sin^2\left(\frac{\pi x}{L}\right)/L$. If the diamond covers a section of length l of a lumped-element inductance of length L, then $\eta = l/(2L)$. The second parameter, α, should be evaluated numerically. It is of order 1 and accounts for the fact that the resonator magnetic field is not necessarily transverse to the NV axis. Overall, we get

$$g_{ens} = |\gamma_e|\sqrt{\frac{\mu_0 \hbar\omega_r \rho_{NV}\alpha\eta}{4}}. \tag{2.101}$$

It is interesting to note that all the geometric factors are included in the dimensionless parameters η and α. This can be intuitively understood by the fact that reducing the transverse dimensions of a CPW resonator by a factor β would enhance the vacuum fluctuations of the magnetic field by the same factor β, thus increasing the single-NV-resonator coupling constant also by β, but it would also reduce by a factor β^2 the total number of spins N, which exactly compensates the previous gain since g_{ens} scales like $\sqrt{N}$. Provided the filling factor is maximized, the only way to increase further g_{ens} is thus to increase the sample concentration ρ_{NV}.

The characteristic width Γ The definition of Γ, which was introduced as the characteristic width of $\rho(\omega)$, can be precised. If the spin distribution is well-behaved (a single Lorentzian or Gaussian peak), its definition is straightforward as the peak width. But if the ensemble contains spins with different frequencies, due to either hyperfine coupling with a nucleus, or to a different Zeeman shift, $\rho(\omega)$ then may consist of a sum of peaks with possibly widely different center frequencies. Note that in the definition above, g_{ens} includes a sum over all the spins regardless of their resonance frequency, with a contribution from spins that are completely off-resonance with the cavity. This issue is solved by using the following definition [48] in the above criteria for strong / weak coupling:

$$\Gamma^{-1} \equiv \frac{1}{g_{ens}^2}\int_{-\infty}^{+\infty} \frac{\rho(\omega)d\omega}{\gamma/2 + i(\omega - \omega_s)}, \tag{2.102}$$

with $\omega_s = \int_{-\infty}^{+\infty} \rho(\omega)\omega d\omega/g_{ens}^2$ being the average spin frequency. That definition makes the criteria above well-defined regardless of the detailed shape of $\rho(\omega)$.

In the following, we illustrate these qualitative statements by explicitly computing several physical quantities useful in our experiments for given spin and coupling constant densities $\rho(\omega)$ and $\rho(g)$, and show how they evolve between the weak and strong coupling regimes.

2.3.3 *The Resonator-Spins System in the Low-Excitation Regime*

In this section we restrict ourselves to calculating quantities in the weak excitation regime, where the Holstein-Primakoff approximation holds. We first derive analytical expressions for the system spectrum, as probed by measuring its transmission or reflection coefficient (see Fig. 2.38). We then compute the system dynamics with the cavity initialized in a single-photon Fock state, a situation implemented in the experiments described in Chap. 4. Here we rely on the work performed by our collaborators at Institut Néel I. Diniz and A. Auffèves described in detail in [46], and the closely related work performed at Aarhus University [45].

2.3.3.1 Master Equation

Our starting point is the cavity—spin ensemble Hamiltonian in the Holstein-Primakoff approximation, taking into account the inhomogeneity of spin frequency, and written in the individual spin basis using the bosonic operators $\hat{s}_j$:

$$\hat{H}_{HP2}/\hbar=\omega_r\left(\hat{a}^\dagger\hat{a}+\frac{1}{2}\right)+\sum_{j=1}^{N}\omega_j\hat{s}_j^\dagger\hat{s}_j+\sum_{j=1}^{N}\left(g_j^*\hat{s}_j^\dagger a+g_j\hat{s}_j a^\dagger\right)+i\sqrt{\kappa_1}(\beta a^\dagger-\beta^* a), \tag{2.103}$$

where the last term describes the cavity drive through port 1, with $\beta(t)=\beta_0 e^{-i\omega t}$, $|\beta_0|^2$ being the number of photons per second at the cavity input. In order to apply input-output theory and to obtain tractable expressions, damping phenomena are described in the Markov approximation. For the cavity field this is well justified,

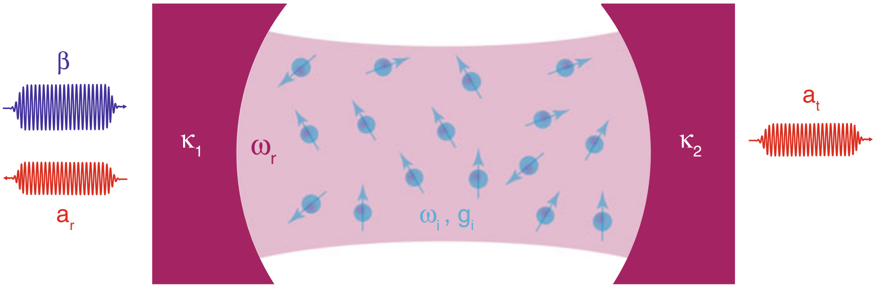

Fig. 2.38 Probing the resonator-spins system

as known from quantum optics. For the spins, the situation is more complex. Spins have negligibly low energy relaxation rates at cryogenic temperatures, as will be showed in the following chapters. Spin dephasing is in general non-Markovian, since as explained in the previous section it is caused by a spin bath which has a slow and complex dynamics. Nevertheless, since in this work we are mainly interested in treating quantitatively the static effects of inhomogeneous broadening, we will make a crude approximation and take as a transverse damping rate the Hahn-echo decoherence rate T_2^{-1} (which implies treating the corresponding bosonic operator as having its energy damped at a rate $\gamma = 2T_2^{-1}$). Note that in all the results of this section, this decoherence rate simply adds up to the width Γ of the spin frequency distribution $\rho(\omega)$; since $\gamma \ll \Gamma$ the exact modelling of decoherence is not very critical. These approximations yield the following Lindblad master equation for the system density matrix ρ

$$\frac{\partial \hat{\rho}}{\partial t} = \frac{1}{i\hbar}\left[\hat{H}_{HP2}, \hat{\rho}\right] + \sum_k \Omega[\hat{c}_k]\hat{\rho} \tag{2.104}$$

where $\Omega[\hat{c}_k]\hat{\rho} \equiv -\frac{1}{2}\hat{c}_k^\dagger \hat{c}_k \hat{\rho} - \frac{1}{2}\hat{\rho}\hat{c}_k^\dagger \hat{c}_k + \hat{c}_k \hat{\rho} \hat{c}_k^\dagger$ describes each damping phenomenon by a jump operator $\hat{c}_k$. For cavity damping, $\hat{c}_1 = \sqrt{\kappa + \kappa_L}\hat{a}$, and for spin damping $\hat{c}_{2,j} = \sqrt{\gamma}\hat{s}_j$. In this way the following equations are obtained:

$$\partial_t \langle \hat{a} \rangle = -[(\kappa + \kappa_L)/2 + i\omega_r]\langle \hat{a} \rangle - i\sum_{j=1}^{N} g_j \langle \hat{s}_j \rangle + \sqrt{\kappa_1}\beta(t) \tag{2.105}$$

$$\partial_t \langle \hat{s}_j \rangle = -(\gamma/2 + i\omega_j)\langle \hat{s}_j \rangle - i g_j^* \langle \hat{a} \rangle \tag{2.106}$$

Looking for steady-state solutions of the form $\langle \hat{a} \rangle(t) = a_0 e^{-i\omega t}$ and $\langle \hat{s_j} \rangle(t) = s_{j0} e^{-i\omega t}$, we get

$$s_{j0} = -\frac{i g_j^*}{\gamma/2 + i(\omega_j - \omega)} a_0 \tag{2.107}$$

which yields

$$a_0 = \frac{i\sqrt{\kappa_1}\beta_0}{\omega - \omega_r + i\frac{\kappa + \kappa_L}{2} - K(\omega)}, \tag{2.108}$$

where we have introduced the function

$$K(\omega) \equiv \sum_j \frac{|g_j|^2}{\omega - \omega_j + i\frac{\gamma}{2}} = \int_{-\infty}^{+\infty} \frac{\rho(\omega')d\omega'}{\omega - \omega' + i\frac{\gamma}{2}}. \tag{2.109}$$

From the previous equations it appears that all the information about the spins is included in the function $K(\omega)$ which is therefore an important quantity on which we will give more details later. In an experiment, one measures the field either transmitted by the cavity or reflected on it. Using input-output theory as explained in the beginning of this chapter, one obtains the transmitted field as $a_t(\omega) = \sqrt{\kappa_2} a_0(\omega)$, so that the transmission coefficient $t(\omega) = a_t(\omega)/\beta_0$ writes

$$t(\omega) = \frac{i\sqrt{\kappa_1 \kappa_2}}{\omega - \omega_r + i\frac{\kappa + \kappa_L}{2} - K(\omega)}. \tag{2.110}$$

In the same manner, the reflection coefficient $r(\omega) = \sqrt{\kappa_1} a_0(\omega)/\beta_0 - 1$ is found to be given by

$$r(\omega) = \frac{i\kappa_1}{\omega - \omega_r + i\frac{\kappa + \kappa_L}{2} - K(\omega)} - 1. \tag{2.111}$$

2.3.3.2 Measuring the Parameters of the System

The spin susceptibility The function $K(\omega)$ contains all the information that can be accessed by measuring the microwave transmission or reflection coefficients of the spin-resonator system. It should thus not be a surprise that this function is directly linked to the quantity measured in dc magnetic resonance, namely the spin susceptibility $\chi(\omega)$, defined as the ratio of the induced magnetization $M_x(t)$ and the applied microwave field $H_x(t)$. More precisely, for an applied field $H_x(t) = 2H_1 \cos(\omega t)$, the induced magnetization is

$$M_x(t) = 2H_1(\chi'(\omega)\cos(\omega t) + \chi''(\omega)\sin(\omega t))$$

with $\chi = \chi' - i\chi''$ [49]. This changes the resonator inductance L into $L(1 + 4\pi\eta\chi(\omega))$, η being the filling factor and χ the complex spin susceptibility in cgs units. The resonator frequency is therefore shifted by $-2\pi\eta\omega_r Re(\chi)$, and the extra field damping rate is $-2\pi\eta\omega_r Im(\chi)$. This yields the following direct link between $K(\omega)$ and $\chi(\omega)$:

$$\chi(\omega) = -K^*(\omega)/(2\pi\eta\omega_r). \tag{2.112}$$

Another important point is that in the limit where $\gamma \ll \Gamma$ (which is always satisfied in our systems), $K(\omega)$ is directly linked to the spin density function by the relation [45]

$$\rho(\omega) = -\frac{1}{\pi} Im[K(\omega)]. \tag{2.113}$$

The cooperativity Given the definition of Γ by Eq. 2.102, $\Gamma^{-1} = iK(\omega_s)/g_{ens}^2$. This implies that the cooperativity verifies

$$C = \frac{2g_{ens}^2}{\kappa\Gamma} = \frac{2iK(\omega_s)}{\kappa}. \tag{2.114}$$

Since on the other hand $K(\omega)$ is directly linked to the reflection and absorption coefficients at frequency ω, this implies that the cooperativity can be directly accessed by measuring $r, t(\omega_s)$. This relation is most useful in the case of reflection on a lossless ($\kappa_L = 0$) one-sided ($\kappa_2 = 0$) cavity at resonance with the spins ($\omega_s = \omega_r$), in which case:

$$r(\omega_s) = \frac{i\kappa_1}{i\frac{\kappa_1}{2} - K(\omega_s)} - 1 = \frac{1-C}{1+C}. \tag{2.115}$$

This relation shows in particular that at resonance, perfect absorption of an incoming microwave by the spins is achieved for the impedance matching condition $C = 1$, which determines the threshold between the weak and the strong coupling regimes. It also offers a convenient way of determining the system parameters in the weak coupling regime, since measuring the reflection coefficient at resonance yields the cooperativity which straightforwardly leads to the value of g_{ens}. In the strong coupling regime, this relation is still valid but inconvenient since $r(\omega) \approx -1$ as long as $C \gg 1$; in that limit g_{ens} is much more conveniently determined by the polaritonic peak separation.

2.3.3.3 Spectroscopy and Dynamics

SPECTROSCOPY

It is possible to obtain analytical expressions of $K(\omega)$ for typical distributions. For a Lorentzian $\rho(\omega) = g_{ens}^2 \frac{w/2\pi}{(\omega-\omega_s)^2+(w/2)^2}$, one can show [45, 46] that

$$K(\omega) = \frac{g_{ens}^2}{(\omega - \omega_s) + i\frac{w+\gamma}{2}}. \tag{2.116}$$

Using the definition of the characteristic width Γ introduced earlier, one gets as expected $\Gamma = (w + \gamma)/2$. In the case of three hyperfine components (as for NV centers), the spin distribution consists of a sum of 3 Lorentzian peaks centered on frequencies $\omega_{s,j} = \omega_s + j\Delta_{hf}$ with $\Delta_{hf}/2\pi = 2.17\,\text{MHz}$ and $j = -1, 0, +1$ yielding

$$\rho(\omega) = \sum_{j=-1,0,+1} \frac{g_{ens}^2}{3} \frac{w}{2\pi} \frac{1}{[\omega - (\omega_s + j\Delta_{hf})]^2 + (w/2)^2}. \tag{2.117}$$

The corresponding K function is

$$K(\omega) = \sum_{j=-1,0,+1} \frac{g_{ens}^2/3}{\omega - (\omega_s + j\Delta_{hf}) + i\frac{w+\gamma}{2}}, \tag{2.118}$$

with a characteristic width

$$\Gamma = \left(\frac{w+\gamma}{2}\right) \cdot \frac{(\frac{w+\gamma}{2})^2 + \Delta_{hf}^2}{(\frac{w+\gamma}{2})^2 + \frac{1}{3}\Delta_{hf}^2}. \tag{2.119}$$

Note that in the limit $w \ll \Delta_{hf}$, one finds $\Gamma \approx 3(w+\gamma)/2$. If the cavity is resonant with only one of the three peaks, the cooperativity would therefore be the same, should one consider the three peaks as making part of the ensemble, or only this resonant peak and disregard the two others (since the collective coupling would then be reduced by $\sqrt{3}$, but the width Γ by 3).

Figure 2.39 shows the single- and triple-Lorentzian Re$[K(\omega)]$ and Im$[K(\omega)]$, for $g_{ens}/2\pi = 1$ MHz. When increasing Γ, the three peaks corresponding to the hyperfine components disappear and merge in a single peak, a case sometimes encountered in our experiment.

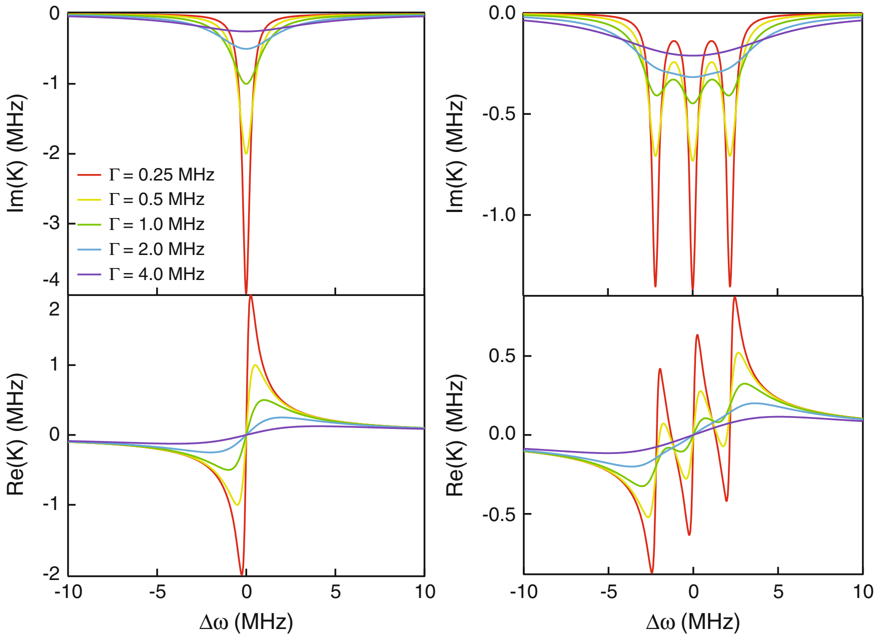

Fig. 2.39 The K-function. The imaginary and real part of the function $K(\omega)$ are displayed respectively on the *top* and on the *bottom* for a Lorentzian (*left*) and sum of three Lorentzian (*right*) distributions

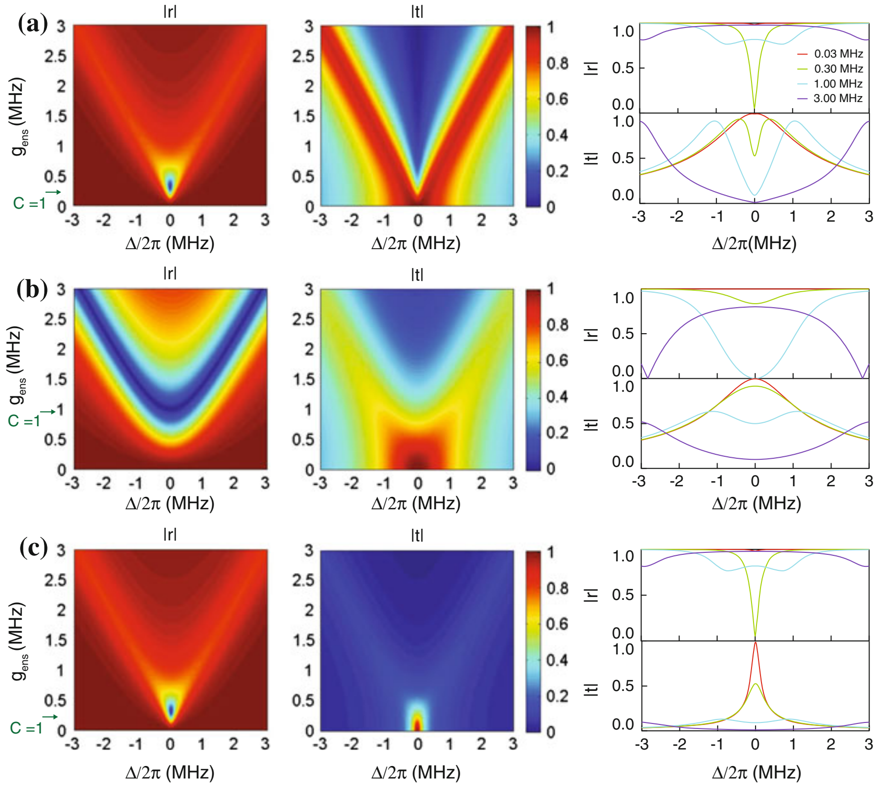

Fig. 2.40 Reflection and transmission of a resonator resonantly coupled to a single Lorentzian distribution of spins. The strong coupling is manifested by the appearance of two polaritonic signal separated by $2g_{ens}$ when $g_{ens} > \max(\kappa/2, \Gamma) = 2\pi \times 1$ MHz. In the *left panel*, the graphs for $g_{ens}/2\pi = 0.03$ MHz (*red*), 0.3 MHz (*green*), 1 MHz (*light blue*) and 3 MHz (*blue*)

We can now explicitly evaluate the expressions Eqs. 2.22 and 2.111 giving the resonator transmission and reflection coefficient. We show in Fig. 2.40 a two-dimensional plot of the modulus of the reflection and transmission coefficients of a resonator resonantly coupled ($\omega_r = \omega_s$) to a spin ensemble with a single Lorentzian distribution, as a function of the collective coupling strength g_{ens}.

The reflection coefficient (on the left) is computed for the condition of the experiment reported in Chap. 5 in which the resonator has only one port ($\kappa = \kappa_1$). The transmission coefficient (on the right) for the condition of the experiment reported in Chap. 4 in which the resonator has two identical ports ($\kappa_1 = \kappa_2 = \kappa/2$). In both cases we assume a lossless cavity $\kappa_L = 0$.

Starting from the decoupled cavity reflection / transmission coefficients ($g_{ens} = 0$), the first effect of the spins (for low values of g_{ens}, i.e. in the weak coupling regime) is to produce absorption dips. This is the situation commonly encountered in magnetic resonance, where in general $C \ll 1$ so that the spins only bring minor

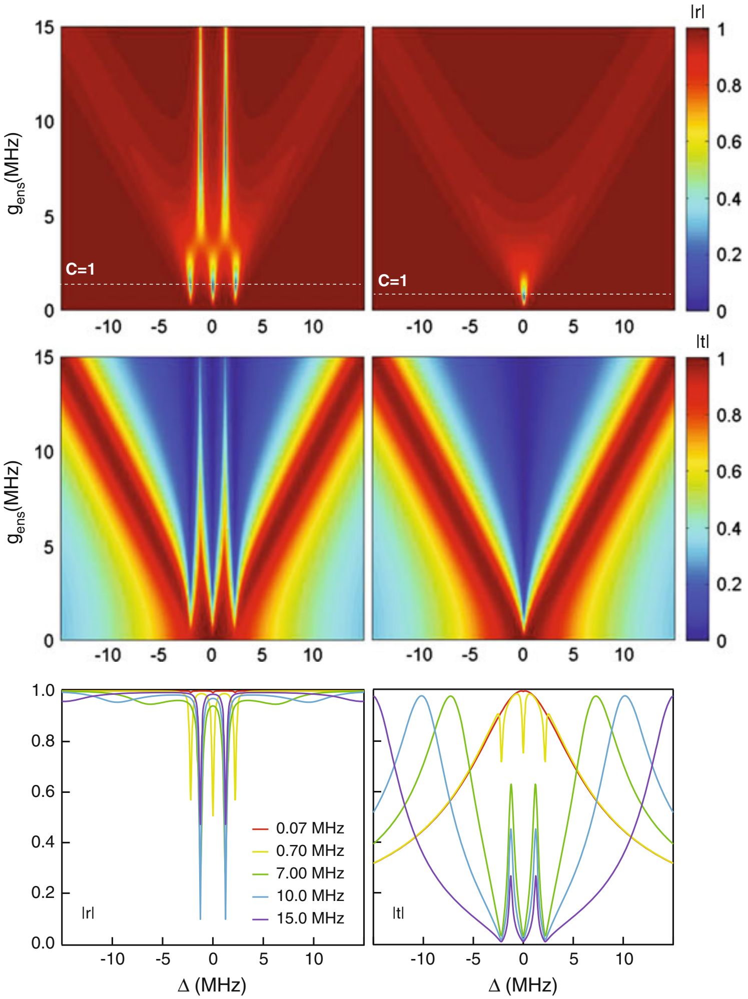

Fig. 2.41 Reflection and transmission of a resonator resonantly coupled to a distribution of NV center spins. Case $\Gamma/(2\pi) = 0.1$ MHz and $\kappa/(2\pi) = 10$ MHz. The same condition for the single Lorentzian distribution is shown on the *right* for comparison. In the *bottom panel*, the graphs for $g_{ens}/2\pi = 0.07$ MHz (*red*), 0.7 MHz (*yellow*), 7 MHz (*green*), 10 MHz (*light blue*) and 15 MHz

changes to the cavity frequency and quality factor. The depth of these absorption dips increases with g_{ens}, until it reaches perfect absorption on the reflection coefficient ($r(\omega_s) = 0$, or $t(\omega_s) = 1/2$ in transmission), which corresponds to the situation $C = 1$ as already explained. For larger values of g_{ens}, the two polaritonic peaks, separated by $2g_{ens}$, become visible, marking the strong coupling regime.

Figure 2.41 shows the reflection and transmission spectra for NV centers with $\kappa/(2\pi) = 10$ MHz and $\Gamma/(2\pi) = 0.1$ MHz. The same condition for a single-

Lorentzian distribution is plotted on the right for comparison. In the weak coupling regime, the hyperfine structure is directly visible as 3 distinct absorption peaks. Note that the condition $C = 1$, corresponding to $r(\omega_s) = 0$, is reached at a $\sqrt{3}$ larger g_{ens} for the NV center case than in the case of a single Lorentzian, since the number of spins in each peak is divided by 3. At the other extreme, for $g_{ens} \gg \Delta_{hf}$, only two polaritonic peaks are visible, exactly as in the single-Lorentzian case, which implies that the details of the spin distribution function are "washed out" in the strong coupling regime. In the intermediate regime where $g_{ens} \approx \Delta_{hf}$, an interesting phenomenon occurs, with the appearance of two narrow peaks in the spectrum, which are reminiscent of dark modes [46].

DYNAMICS

As will be clear in Chaps. 4 and 5, we also need to compute the dynamics of an excitation initially stored in the system, in the absence of external drive. We follow the main lines of the derivation done in [46]. We consider the spin-resonator system, described by Hamiltonian Eq. 2.103 without drive, and initialized at $t = 0$ in state $|1, G\rangle$, i.e. with all spins in their ground state and 1 photon in the resonator. The goal is to determine the probability at $t > 0$ that the excitation is still in the resonator $p(t) = |\alpha(t)|^2$ with $\alpha(t) = \langle 0|\, a(t)a^\dagger(0)\, |0\rangle$. This quantity can be calculated by considering an effective non-Hermitian Hamiltonian

$$H_{eff}/\hbar = \begin{pmatrix} \tilde{\omega}_0 & ig_1 & ig_2 & \dots \\ -ig_1 & \tilde{\omega}_1 & & \\ -ig_2 & & \tilde{\omega}_2 & \\ \vdots & & & \ddots \end{pmatrix}. \tag{2.120}$$

with complex angular frequencies $\tilde{\omega}_r = \omega_r - i\kappa/2$ and $\tilde{\omega}_k = \omega_k - i\gamma/2$. Introducing the vector $X(t)$ of coordinates $\left[\left\langle a(t)a^\dagger(0)\right\rangle, \dots, \left\langle \hat{b}_j(t)a^\dagger(0)\right\rangle, \dots\right]$ it can be shown that $dX/dt = -(i/\hbar)H_{eff}X$. The formal solution to this equation is

$$X(t) = \mathcal{L}^{-1}[(s + iH_{eff}/\hbar)^{-1}X(0)] \tag{2.121}$$

with $X(0) = x_G$ and $x_G \equiv (1, 0, \dots, 0)$. This implies that $\alpha(t) = x_G{}^\dagger \cdot X(t) = \mathcal{L}^{-1}\,[t_1(s)]$ with $t_1(s) = x_G{}^\dagger \cdot (s + iH_{eff})^{-1} \cdot x_G$ and $\mathcal{L}[f(s)] = \int e^{-st} f(t)dt$, s being a complex number. Since $t_1(s)$ is not singular on its imaginary axis, we only need the transmission coefficient t_1 given by Eq. 2.22 in Sect. 2.3 for pure imaginary argument $s = -i\omega$ to perform the Laplace transform inversion. The computation of the intracavity field $\alpha(t)$ follows.

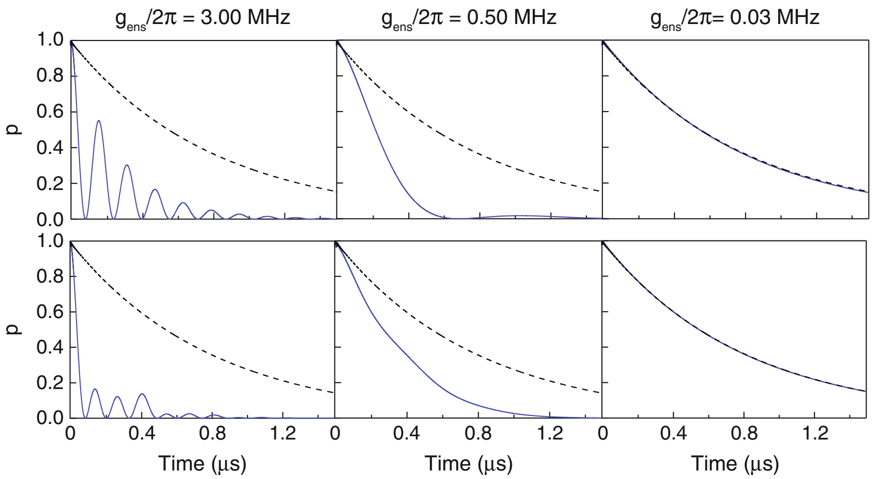

Fig. 2.42 Dynamics of a photon in a resonator resonantly coupled to a distribution of spins. Probability $p(t)$ for a single Lorentzian (*top*) and sum of three Lorentzian (*bottom*) spin distributions. The exchange of the photon is only possible in the strong coupling regime $g_{ens} \gg \kappa, \Gamma$. The case $g/2\pi = 0\,\mathrm{MHz}$ that reveals the damping in the cavity alone is plotted in *dashed line*

We show in Fig. 2.42 the computed probability $p(t)$ for different coupling strengths g_{ens} in the case of the single Lorentzian and sum of three Lorentzian spin distributions, assuming a width $w/2\pi = 1\,\mathrm{MHz}$ for each Lorentzian peak, and taking $\gamma = 0$. The resonator is resonant with the spins ($\omega_r = \omega_s$) and has a damping rate $\kappa = 1.2 \times 10^6\,\mathrm{s}^{-1}$. When the coupling constant is low so that the two systems are in the weak coupling regime (right panel), p is exponentially damped with a time constant slightly shorter than in the absence of spins, which shows that the absorption of the spin takes place on a longer time scale and is therefore not able to efficiently absorb the photon before it leaks out of the cavity. Increasing the coupling constant makes the absorption faster, up to the point that coherent effects are visible (middle then left panel, strong coupling case). There, oscillations are seen in $p(t)$ with period π/g_{ens}, revealing the coherent exchange of a single excitation between the two systems. The damping of the oscillations is due mainly this time to the transfer of the energy from the bright spin mode into the spin dark modes (with a time constant $T_2^* = 2/w = 300\,\mathrm{ns}$), as evidenced from the fact that it takes place faster than cavity damping. In the case of the Lorentzian triplet distribution, the conclusions are unchanged, except that the oscillations in the strong coupling regime are non-periodic and non-exponentially damped. Corresponding experimental results are reported in Chap. 4.

2.3.4 The Resonator-Spins System Under Strong Drive Powers

The Holstein-Primakoff approximation, in which the spin operators are linearized, makes it possible to compute the quantum dynamics of the resonator-spin ensemble system, as explained in the previous section and required for the experiments described in Chap. 4 where single-photon fields are stored into the ensemble. But in order to retrieve this quantum field after writing into the spin-ensemble memory, a π pulse should be applied to all the spins (see Introduction), which requires strong classical microwave pulses and clearly implies a breakdown of the Holstein-Primakoff approximation. A quantitative estimate of the fidelity of the quantum memory requires not only a calculation of the mean values of the spin and field operators, but also of their quantum statistics, which then becomes a difficult theoretical problem in particular because of inhomogeneous broadening, as explained above. In this section we qualitatively outline the steps taken by our collaborator B. Julsgaard, from Aarhus University, to address this problem numerically as explained in more details in [50, 51]. The simulations developed at this occasion will be used extensively in Chap. 5 to compute the response of the spins to microwave pulses beyond the HP approximation, including Hahn-echo pulse sequences.

2.3.4.1 The Model

The cavity—spin ensemble system is modelled by the following Hamiltonian, which takes into account the inhomogeneity of spin frequency and of coupling constant, and which includes the effect of a drive through port 1:

$$\hat{H}_2/\hbar = \omega_r\left(\hat{a}^\dagger\hat{a}+\frac{1}{2}\right)+\sum_{j=1}^{N}\omega_j\hat{\sigma}_z^{(j)}+\sum_{j=1}^{N}\left(g_j\hat{\sigma}_+^{(j)}\hat{a}+g_j^*\hat{\sigma}_-^{(j)}\hat{a}^\dagger\right)+i\sqrt{\kappa_1}(\beta\hat{a}^\dagger-\beta^*\hat{a}). \tag{2.122}$$

Damping is treated as in the previous section by a master equation approach using the Lindblad formalism. This implies as before that the baths are Markovian, which constitutes a crude approximation when applied to the spins. The cavity damping operator is kept unchanged. Spin decoherence is described by the operator $\hat{c'}_{2,j} = \sqrt{\gamma_2/2}\hat{\sigma}_-$ which damps the phase of a state superposition at the Hahn-echo damping rate γ_2.

2.3.4.2 Integration

To treat the problem, the approach developed in [50] consists in dividing the spin ensemble into M sub-ensembles, each of them containing a smaller number of spins N_m with homogeneous coupling strength g_m and frequency ω_m. This subdivision is done according to the distributions of coupling constant and frequency $\rho(g)$ and $\rho(\omega)$ which are input to the problem. As explained in Sect. 2.3.2.1 about the Tavis-Cummings model, this allows to re-write the Hamiltonian using only the collective spin operators $\hat{S}^{(m)}_{x,y,z}$, which considerably reduces the number of variables. In the end, there are $3M + 2$ operators (3 for each spin subdivision, and 2 for the two field quadratures $\hat{X} = (\hat{a} + \hat{a}^{\dagger})/\sqrt{2}$ and $\hat{P} = -i(\hat{a} - \hat{a}^{\dagger})/\sqrt{2}$) whose evolution needs to be computed. The time-dependence of their mean values is thus obtained by solving a set of $3M + 2$ coupled differential equations, which can achieved numerically provided M is not too large. This is the approach used for the simulations presented in Chap. 5, where we compute the response of the spins to strong resonant microwave pulses and to Hahn-echo sequences.

Knowing the mean value evolution is not sufficient to assess the fidelity of a quantum memory. Indeed, a quantum state of the field is characterized also by its fluctuations. Imagine that an input field in a coherent state $|\alpha\rangle$ is stored in the memory, with mean values $\langle\hat{X}\rangle = \alpha$ and $\langle\hat{P}\rangle = 0$. The variance of these quadratures $\hat{X}$ and $\hat{P}$ then verifies $\langle\delta X^2\rangle = \langle\delta P^2\rangle = 1/2$. These values should be preserved at the end of the protocol: the final state of the field should still be in a state of minimal uncertainty, otherwise the fidelity will be low even though the mean values of the quadrature are faithfully restored. Fortunately, the approach outlined above not only makes it possible to integrate the time evolution of the operators mean value, but also of their co-variance matrix. Indeed this matrix has a dimension of $(3M + 2)^2$; its coefficients are governed by intricate equations which were derived in [50]. Again, for M not too large, this set of coupled $(3M + 2)^2$ differential equations can be integrated numerically.

References

1. B. Yurke, J.S. Denker, Quantum network theory. Phys. Rev. A **29**, 1419–1437 (1984)
2. M.H. Devoret, *Quantum Fluctuations in Electrical Circuits* (Elsevier, 1997), p. 351
3. M.J. Collett, C.W. Gardiner, Squeezing of intracavity and traveling-wave light fields produced in parametric amplification. Phys. Rev. A **30**, 1386 (1984)
4. A. Blais, R.-S. Huang, A. Wallraff, S.M. Girvin, R.J. Schoelkopf, Cavity quantum electrodynamics for superconducting electrical circuits: an architecture for quantum computation. Phys. Rev. A **69**, 062320 (2004)
5. A. Palacios-Laloy, Superconducting qubit in a resonator: test of the Leggett-Garg inequality and single-shot readout (2010)
6. R.N. Simons, *Coplanar Waveguide Circuits, Components, and Systems* (Wiley, 2001)
7. B. Josephson, Possible new effects in superconductive tunneling. Phys. Lett. **1**, 251–253 (1962)
8. J. Clarke. *The SQUID Handbook: Fundamentals and Technology of SQUIDs and SQUID Systems* (Wiley, 2005)
9. I. Siddiqi, R. Vijay, F. Pierre, C.M. Wilson, M. Metcalfe, C. Rigetti, L. Frunzio, M.H. Devoret, RF-driven Josephson bifurcation amplifier for quantum measurement. Phys. Rev. Lett. **93**, 207002 (2004)
10. R. Vijay, M.H. Devoret, I. Siddiqi, Invited review article: the Josephson bifurcation amplifier. Rev. Sci. Instrum. **80**(11), 111101–1111017 (2009)

11. F. Mallet, F.R. Ong, A. Palacios-Laloy, F. Nguyen, P. Bertet, D. Vion, D. Esteve, Single-shot qubit readout in circuit quantum electrodynamics. Nat. Phys. **5**, 791 (2009)
12. A. Palacios-Laloy, F. Nguyen, F. Mallet, P. Bertet, D. Vion, D. Esteve, Tunable resonators for quantum circuits. J. Low Temp. Phys. **151**, 1034 (2008)
13. J. Koch, T.M. Yu, J. Gambetta, A.A. Houck, D.I. Schuster, J. Majer, A. Blais, M.H. Devoret, S.M. Girvin, R.J. Schoelkopf, Charge-insensitive qubit design derived from the cooper pair box. Phys. Rev. A **76**, 042319 (2007)
14. V. Bouchiat, D. Vion, P. Joyez, D. Esteve, M.H. Devoret, Quantum coherence with a single cooper pair. Physica Scripta **T76**, 165 (1998)
15. A. Cottet, Implementation of a quantum bit in a superconducting circuit. Ph.D. thesis, Université Paris VI, Paris, 2002
16. Y. Nakamura, Y.A. Pashkin, J.-S. Tsai, Coherent control of macroscopic quantum states in a single-cooper-pair box. Nature **398**, 786 (1999)
17. J.E. Mooij, T.P. Orlando, L. Levitov, L. Tian, C.H. van der Wal, S. Lloyd, Josephson persistent-current qubit. Science **285**(5430), 1036–1039 (1999)
18. J.M. Martinis, S. Nam, J. Aumentado, C. Urbina, Rabi oscillations in a large Josephson-junction qubit. Phys. Rev. Lett. **89**, 117901 (2002)
19. D. Vion, A. Aassime, A. Cottet, P. Joyez, H. Pothier, C. Urbina, D. Esteve, M.H. Devoret, Manipulating the quantum state of an electrical circuit. Science **296**(5569), 886–889 (2002)
20. I. Chiorescu, P. Bertet, K. Semba, Y. Nakamura, C.J.P.M. Harmans, J.E. Mooij, Coherent dynamics of a flux qubit coupled to a harmonic oscillator. Nature **431**(7005), 159–162 (2004)
21. H. Paik, D.I. Schuster, L.S. Bishop, G. Kirchmair, G. Catelani, A.P. Sears, B.R. Johnson, M.J. Reagor, L. Frunzio, L.I. Glazman, S.M. Girvin, M.H. Devoret, R.J. Schoelkopf, Observation of high coherence in Josephson junction qubits measured in a three-dimensional circuit QED architecture. Phys. Rev. Lett. **107**, 240501 (2011)
22. R. Barends, J. Kelly, A. Megrant, D. Sank, E. Jeffrey, Y. Chen, Y. Yin, B. Chiaro, J. Mutus, C. Neill, P. O'Malley, P. Roushan, J. Wenner, T.C. White, A.N. Cleland, J.M. Martinis, Coherent Josephson qubit suitable for scalable quantum integrated circuits. Phys. Rev. Lett. **111**, 080502 (2013)
23. F. Mallet, F.R. Ong, A. Palacios-Laloy, F. Nguyen, P. Bertet, D. Vion, D. Esteve, Single-shot qubit readout in circuit quantum electrodynamics. Nat. Phys. **5**(11), 791–795 (2009)
24. J. Loubser, J.A. van Wyk, Electron spin resonance in the study of diamond. Rep. Prog. Phys. **41**, 1201 (1978)
25. N.R.S. Reddy, N.B. Manson, E.R. Krausz, Two-laser spectral hole burning in a colour centre in diamond. J. Lumin. **38**, 46–47 (1987)
26. G. Balasubramian, P. Neumann, D. Twitchen, M. Markham, R. Koselov, N. Mizuochi, J. Isoya, J. Achard, J. Beck, J. Tissler, V. Jacques, P.R. Hemmer, F. Jelezko, J. Wrachtrup, Ultralong spin coherence time in isotopically engineered diamond. Nat. Mater. **8**, 383 (2009)
27. N. Bar-Gill, L. Pham, A. Jarmola, D. Budker, R. Walsworth, Solid-state electronic spin coherence time approaching one second. Nat. Commun. **4**, 1743 (2013)
28. N.B. Manson, J.P. Harrison, M.J. Sellars, Nitrogen-vacancy center in diamond: model of the electronic structure and associated dynamics. Phys. Rev. B **74**, 104303 (2006)
29. A. Gruber, A. Dräbenstedt, C. Tietz, L. Fleury, J. Wrachtrup, C. Von Borczyskowski, Scanning confocal optical microscopy and magnetic resonance on single defect centers. Science **276**(5321), 2012–2014 (1997)
30. S. Felton, A.M. Edmonds, M.E. Newton, P.M. Martineau, D. Fisher, D.J. Twitchen, Electron paramagnetic resonance studies of the neutral nitrogen vacancy in diamond. Phys. Rev. B **77**, 081201 (2008)
31. N. Aslam, G. Waldherr, P. Neumann, F. Jelezko, J. Wrachtrup, Photo-induced ionization dynamics of the nitrogen vacancy defect in diamond investigated by single-shot charge state detection. New J. Phys. **15**(1), 013064 (2013)
32. J. Harrison, M.J. Sellars, N.B. Manson, Optical spin polarisation of the nv centre in diamond. J. Lumin. **107**(1), 245–248 (2004)

33. J. Harrison, M.J. Sellars, N.B. Manson, Measurement of the optically induced spin polarisation of NV centres in diamond. Diam. Relat. Mater. **15**(4), 586–588 (2006)
34. A. Batalov, C. Zierl, T. Gaebel, P. Neumann, I.-Y. Chan, G. Balasubramanian, P.R. Hemmer, F. Jelezko, J. Wrachtrup, Temporal coherence of photons emitted by single nitrogen-vacancy defect centers in diamond using optical Rabi-oscillations. Phys. Rev. Lett. **100**(7), 077401 (2008)
35. L. Robledo, L. Childress, H. Bernien, B. Hensen, P.F.A. Alkemade, R. Hanson, High-fidelity projective read-out of a solid-state spin quantum register. Nature **477**, 574 (2011)
36. M.V. Gurudev Dutt, L. Childress, L.Jiang, E. Togan, J. Maze, F. Jelezko, A.S. Zibrov, P.R. Hemmer, M.D. Lukin, Quantum register based on individual electronic and nuclear spin qubits in diamond. Science **316**(5829), 1312–1316 (2007)
37. R. Hanson, O. Gywat, D.D. Awschalom, Room-temperature manipulation and decoherence of a single spin in diamond. Phys. Rev. B **74**, 161203 (2006)
38. V.V. Dobrovitski, A.E. Feiguin, D.D. Awschalom, R. Hanson, Decoherence dynamics of a single spin versus spin ensemble. Phys. Rev. B **77**, 245212 (2008)
39. J.R. Maze, J.M. Taylor, M.D. Lukin, Electron spin decoherence of single nitrogen-vacancy defects in diamond. Phys. Rev. B **78**, 094303 (2008)
40. N. Zhao, S.-W. Ho, R.-B. Liu, Decoherence and dynamical decoupling control of nitrogen vacancy center electron spins in nuclear spin baths. Phys. Rev. B **85**, 115303 (2012)
41. J.A. van Wyk, E.C. Reynhardt, G.L. High, I. Kiflawi, The dependences of esr line widths and spin-spin relaxation times of single nitrogen defects on the concentration of nitrogen defects in diamond. J. Phys. D Appl. Phys. **30**, 1790–1793 (1997)
42. M. Tavis, F.W. Cummings, Exact solution for an n-molecule-radiation-field hamiltonian. Phys. Rev. **170**, 379 (1968)
43. R.H. Dicke, Coherence in spontaneous radiation processes. Phys. Rev. Lett. **93**, 99 (1954)
44. T. Holstein, H. Primakoff, Field dependence of the intrinsic domain magnetization of a ferromagnet. Phys. Rev. **58**, 1098 (1940)
45. Z. Kurucz, J.H. Wesenberg, K. Mølmer, Spectroscopic properties of inhomogeneously broadened spin ensembles in a cavity. Phys. Rev. A **83**, 053852 (2011)
46. I. Diniz, S. Portolan, R. Ferreira, J.M. Gérard, P. Bertet, A. Auffèves, Strongly coupling a cavity to inhomogeneous ensembles of emitters: potential for long-lived solid-state quantum memories. Phys. Rev. A **84**, 063810 (2011)
47. S. Haroche, J.-M. Raimond, *Exploring the Quantum* (Oxford University Press, 2006)
48. B. Julsgaard, K. Mølmer, Reflectivity and transmissivity of a cavity coupled to two-level systems: coherence properties and the influence of phase decay. Phys. Rev. A, **85**, 013844 (2012)
49. A. Abragam, *Principles of Nuclear Magnetism* (Oxford Science Publications, Clarendon Press, 1986)
50. B. Julsgaard, C. Grezes, P. Bertet, K. Mølmer, Quantum memory for microwave photons in an inhomogeneously broadened spin ensemble. Phys. Rev. Lett. **110**, 250503 (2013)
51. C. Grezes, B. Julsgaard, Y. Kubo, M. Stern, T. Umeda, J. Isoya, H. Sumiya, S. Abe, S. Onoda, T. Ohshima, V. Jacques, J. Esteve, D. Vion, D. Esteve, K. Moelmer, P. Bertet, Multimode storage and retrieval of microwave fields in a spin ensemble. Phys. Rev. X **4**, 021049 (2014)

Chapter 3
Proposal: A Spin Ensemble Quantum Memory for Superconducting Qubits

This chapter is dedicated to the presentation of the quantum memory protocol, on which our experiments are based. It describes the storage in parallel of multiple quantum states into a spin ensemble, and their on-demand retrieval. Simulations of this protocol performed by B. Julsgaard are presented at the end of this chapter with realistic experimental parameters.

3.1 Spin-Based Quantum Memory

3.1.1 Motivations

Superconducting qubits have emerged in recent years as promising candidates for the realization of a large-scale quantum processor. At the time of writing this thesis, up to five-qubit processors were realized [1–4] in which bi- and tripartite entanglement can be produced to run compiled versions of quantum algorithms [5–7]. The scaling up to larger processor however is slowed down by technical issues, mainly the increasing complexity of the circuit [8] and the relatively short coherence time of superconducting qubits [8, 9] ($\sim 10\,\mu$s). This has motivated alternative quantum computing approaches such as holographic quantum computing [10] that make use of collective excitations in an ensemble of microscopic systems with long coherence times to implement a multi-qubit register. The memory is combined with a few(2)-qubit processor that performs the single and multi-qubit gates (see Fig. 3.1).

From the quantum computation point of view, such a system works like a genuine quantum Turing machine with the memory providing the storage system to protect quantum states from decoherence and the few-qubits processor providing the "hardware" to perform quantum gates. In this architecture, the quantum operations are restricted to few-qubit gates but with a reservoir of *n* quantum states to create multi-qubits entanglement. The advantages are that it is protected against decoherence

© Springer International Publishing Switzerland 2016
C. Grèzes, *Towards a Spin-Ensemble Quantum Memory for Superconducting Qubits*, Springer Theses,
DOI 10.1007/978-3-319-21572-3_3

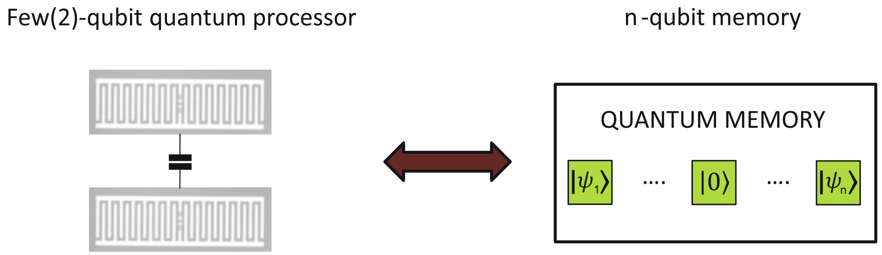

Fig. 3.1 Concept of the hybrid quantum processor combining a few(2)-qubits processor and a n-qubit register. The quantum operations are restricted to few-qubit gates but with a reservoir of n quantum states to create up to n-qubits entanglement

at the level of the coherence time of the memory to perform long calculation and relies on a superconducting qubit processor with limited complexity, that is close to the actual state of the art. Such architecture comes however with new challenges. The multi-qubit register must be able to receive n quantum states possibly entangled (*write*), retrieve them on-demand without affecting the others (*read*), and be re-initialized in the ground state between successive memory operations (*reset*). We designed a protocol made of the *write*, *read* and *reset* steps for a memory made of an ensemble of spins, that we describe below.

3.1.2 Spin Ensemble Quantum Memory: Principles

Optical quantum memories The protocol is inspired from related experiments on optical quantum memories based on atom and ion ensembles [11]. Optical quantum memory protocols can be divided in two families. A number of proposals and experiments rely on a nonlinear phenomenon occurring in atomic systems that have the appropriate energy level structure (Λ-transition), the so-called Electromagnetic-Induced Transparency [12–15]. These protocols are not easily transposed to our situation, since NV centers have a V-level structure instead of a Λ. We instead take inspiration of another class of optical quantum-memory protocols, based on photon echoes. In these experiments, an optical pulse carrying the quantum state is first collectively absorbed by the ensemble. Due to inhomogeneous broadening that causes each ion in the ensemble to have a slightly different Larmor frequency, the resulting collective quantum state is rapidly dephased. Two types of strategies can then be envisioned to retrieve the initial state. The first strategy requires to be able to tailor the shape of the spin frequency distribution prealably to the storage of the quantum state. This is possible for rare-earth-ions-doped crystals, in which one can achieve arbitrarily sharp frequency profiles by spectral hole burning, which transfers atoms of a certain frequency class into states that are not coupled to the radiation field. For these systems, Controlled Reversible Inhomogeneous Broadening [16, 17] or Atomic-Comb-Frequency [18, 19] protocols have been shown to be efficient for storing quantum states of the light. Spectral hole burning is however impossible for

NV centers which only have three ground state levels. Fortunately, another class of protocols does not require any tailoring of the spin frequency distribution. They rely on the application of sequences of π pulses to the ions in order to make them return in phase at a later time and to re-emit collectively the quantum state initially absorbed. This is the basis of our protocol that we describe below.

Microwave quantum memory protocol Our protocol is built on the same principle, adapted to the requirements of a cQED setup working at millikelvin temperatures, and taking advantage of the new possibilities offered by Josephson quantum circuits. The ensemble of spins is embedded in a superconducting resonator to ensure efficient absorption of microwave photons. A SWAP operation first transfers state $|\psi\rangle$ from the external superconducting qubit processor (QuP) to the resonator field. This field is then collectively absorbed by the bright mode of the spin ensemble, after which it is transferred into the spin dark modes due to inhomogeneous broadening of the ensemble (see Sect. 2.3.2.2). To retrieve the state, refocusing techniques based on the application of π pulses to the spins are applied. The implementation of these ideas faces a number of contradictory requirements: (i) the resonator and the spins must be in the strong coupling regime ($C \gg 1$) for the SWAP operation (see Sect. 2.3.3.3), (ii) after the π-pulse inversion, the spin ensemble must remain stable, which implies to the contrary a weak spin-resonator coupling ($C \ll 1$) to avoid superradiant pulse emission (see Sect. 2.3.2.1), and (iii) the whole statistics of the collective spin must be restored at the single quantum level. Our protocol combines the application of π-pulses with dynamical tuning of the resonator frequency and quality factor to address these issues. It is associated to the physical setup depicted in Fig. 3.2. The bus resonator, with frequency ω_r and damping rate κ both tunable, is coupled to the spin ensemble

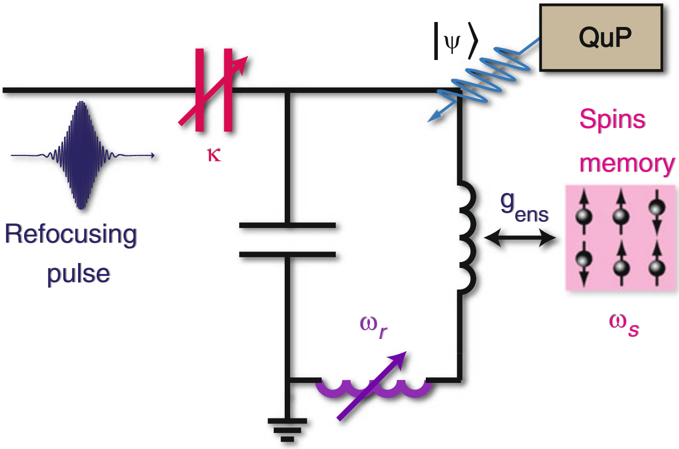

Fig. 3.2 Quantum memory circuit. The resonator, with frequency ω_r and damping rate κ tunable at the nanosecond scale, is coupled to the spin ensemble (frequency ω_s) with coupling strength g_{ens}. An external processor (QuP) delivers a quantum state $|\psi\rangle$ to the bus resonator, to be stored into the spin ensemble. Refocusing pulses are applied to the spins via the resonator

with frequency ω_s and spin linewidth Γ, with an ensemble coupling constant g_{ens}. Refocusing pulses are applied to the spins via the resonator. Such resonators with tunable parameters can be realized using SQUIDs, as described in Chaps. 2 and 6. In the next section, we describe in more details the steps of the protocol.

3.2 Spin Ensemble Quantum Memory Protocol

3.2.1 The Write Step: Storage of N Quantum States $|\psi_1\rangle \dots |\psi_n\rangle$

The *write* step of the protocol consists in storing a quantum state $|\psi\rangle$ into the spin ensemble. The resonator receives $|\psi\rangle$ from the external superconducting qubit processor, which initializes the cavity-field state. As seen in Sect. 2.3.3.3, the subsequent transfer from the resonator to the spin ensemble is only possible if the two systems are in the strong coupling regime $g_{ens} \gg \kappa, \Gamma$. The damping rate of the resonator is set purposely to $\kappa_{min} = \omega_r / Q_{max}$ to satisfy this condition. The microwave photon carrying out the state $|\psi\rangle$ is transferred to the spins by tuning the resonator at the average spin frequency ω_s for a time $T_{swap} = \pi/(2g_{ens})$ after which the cavity frequency is detuned at the "parking" frequency ω_p such that $(\omega_s - \omega_p) \gg g_{ens}$. This corresponds to the SWAP operation described in Sect. 2.3.2.1, during which the coupled system quantum state evolves (using Eq. 2.93 in Sect. 2.3.2.1) from $|\psi_{rs}(0)\rangle = |\psi\rangle \times |0_b\rangle$ to $|\psi_{rs}(T_{swap})\rangle = |0\rangle \times |\psi_b\rangle$. As seen in Sect. 2.3.2.2, in the presence of inhomogeneous broadening, the bright mode b is coupled to the $N-1$ dark modes d_j, which are decoupled from the electromagnetic mode of the cavity (see Fig. 3.3a). Hence, the quantum state $|\psi\rangle$ is transferred from the bright mode into the dark modes subspace. The dark states are naturally protected against spontaneous emission in the cavity, a key property for the storage of quantum information.

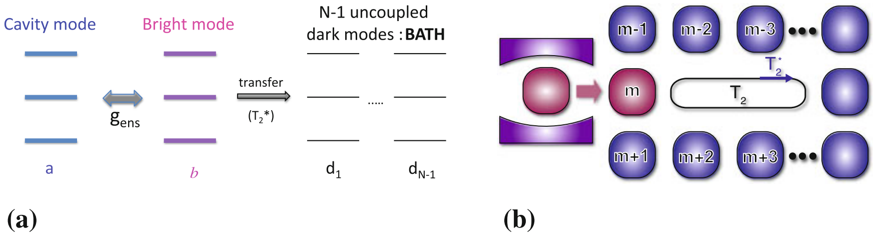

Fig. 3.3 Storage of *n* quantum states into the spin ensemble. a Storage process. The resonator receives $|\psi\rangle$ from the external superconducting qubit processor (QuP), which initializes the cavity-field state. The microwave photon is collectively absorbed by the spin ensemble and is transferred into the dark modes subspace in a time of order T_2^*. **b** Multimode ability. Collective excitations of the spins can be used to simultaneously encode a large number of qubits. As seen from the collective spin mode coupled to the cavity, the other modes behave as a conveyor belt, with loading time the free induction decay time (T_2^*) and life time the Hahn-echo decay time (T_2)

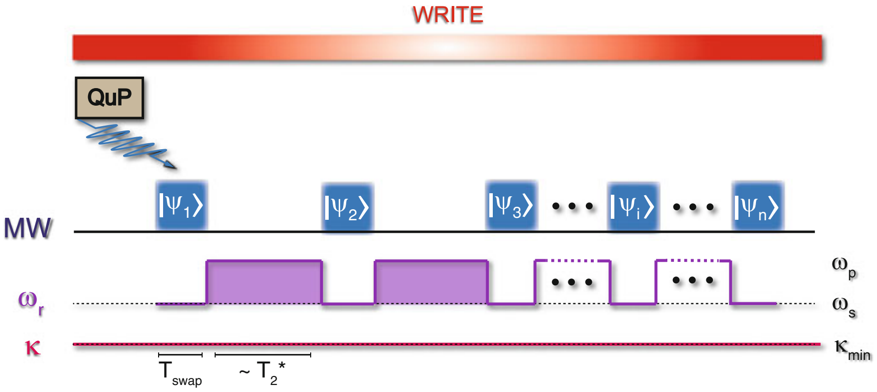

Fig. 3.4 **The write step of the protocol.** Successive swap operations separated by time of order T_2^* are performed to store various quantum states $|\psi_1\rangle \ldots |\psi_n\rangle$ into the spin ensemble

This storage into the dark modes of the spins takes place in a time of order $T_2^* = 2/\Gamma$, the free induction decay time of the spins. This transfer to the dark modes subspace due to inhomogeneous broadening confers its multimode ability to the memory. As seen from the bright mode coupled to the cavity, the dark modes behave as a conveyor belt with loading time the free induction decay time (T_2^*) and life time the Hahn-echo decay time (T_2), as illustrated in Fig. 3.3b.

After the transfer to the dark mode subspace, the bright mode is accessible again for storage. Hence, successive *write steps* separated by time of order T_2^* can be performed to store various quantum states $|\psi_1\rangle \ldots |\psi_n\rangle$ in orthogonal modes of the spins (see Fig. 3.4). The lifetime of the memory is approximately the Hahn-echo decay time T_2, so that the maximal number of stored quantum states is of order $n \sim T_2/T_2^*$.

3.2.2 The Read Step: On-Demand Retrieval of $|\psi_i\rangle$

The *read* step of the protocol consists in retrieving one of the states $|\psi_i\rangle$ stored in the spin ensemble. This state initially stored into the dark modes is actively restored into the bright mode by using refocusing techniques derived from the Hahn echo [20].

3.2.2.1 The Building Block: The Two-Pulse Hahn Echo

The Hahn echo relies on the use of short radio frequency pulses to manipulate the macroscopic magnetic moment of an ensemble of spins. The sequence is sketched in Fig. 3.5a in the Bloch sphere representation. A $\pi/2$ pulse is first applied around x which flips the macroscopic magnetic moment of the spins along $-y$. This pulse initiates a free precession of the spins in the equatorial plane. As spins in an inhomogeneous ensemble have different Larmor frequencies, some spins precess faster and some slower than the average magnetization that causes the later to decay in a time T_2^*, the free induction decay time. At time τ, a π-pulse is applied so that the spin Bloch vector undergoes a π rotation around the x-axis. The slower spins become ahead of the average magnetic moment and the fast ones trail behind. As spins continue to precess in the same direction at their Larmor frequency, they rephase together along $+y$ direction at 2τ, time at which the magnetic moment vector adds constructively to produce a spontaneous induction signal called echo.

This refocusing effect is the basis of the two-pulse echo protocol (2PE) used in classical memory experiment [21]. It is sketched in Fig. 3.5b. The initial $\pi/2$-pulse is replaced by multiple photon pulses (called θ_i) absorbed by the spins at time $t = t_i$ and a refocusing pulse (R) applied at $t = \tau$ triggers the emission of echo pulses e_i at $t = 2\tau - t_i$ (therefore in the reverse order). The phase $\phi_{e,i}$ of the echo is related to $\phi_{\theta,i}$ and ϕ_R the phases of the incoming and refocusing pulses by the relation $\phi_{e,i} = -(\phi_{\theta,i} - \phi_R)$.

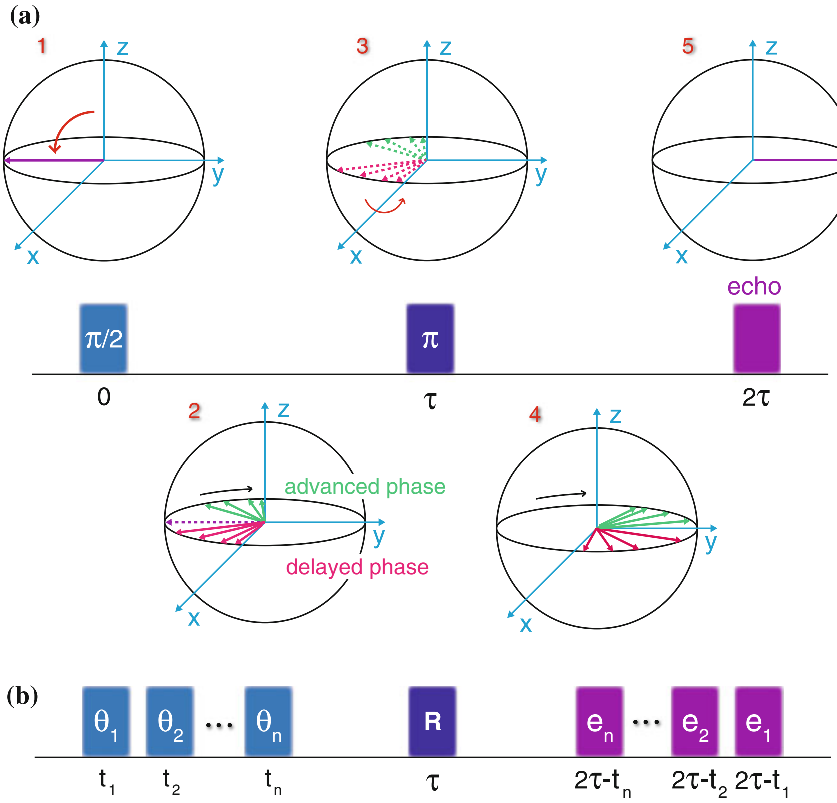

Fig. 3.5 The building block of the read operation. a Standard Hahn echo. A π pulse applied at time τ acts as a time reversal for the spins, which leads to a rephasing at time 2τ with the emission of an echo. **b** Two-pulse Hahn echo (2PE). Weak pulses θ_i are stored into the spin ensemble at times t_i, followed by the application of a refocusing pulse at time τ that triggers the emission of echo pulses e_i at times $2\tau - t_i$ (therefore in reverse order)

One could imagine extending very simply the 2PE to the quantum regime by replacing the classical pulse θ_i by incoming fields in well-defined states $|\psi_i\rangle$. As explained in [22], this strategy however cannot provide a high fidelity quantum memory. The main reason is that when the echo signal appears the whole medium is still inverted and acts as a noise amplifier: the spontaneous emission produces a noise comparable to the retrieved signal. The efficiency of the retrieval is thus fundamentally limited by fluorescence. Even if the 2PE cannot reach the quantum regime, it has the unique ability to rephase atoms independently of the effect inducing the inhomogeneous distribution. As such, it is a tool for the design of more elaborate protocols able to reach the quantum regime. In the following, we use the 2PE as a building block for designing our quantum memory protocol for microwave photons.

3.2.2.2 Reaching the Quantum Regime with Silenced Primary Echo

In order to reach the quantum regime, one possible strategy consists in applying a second refocusing pulse, which ensures that the final echo is formed in a non-inverted spin ensemble. This however requires to "silence" the first echo, which otherwise would carry away the quantum information. Optical quantum memory protocols have proposed silencing either by using phase mismatch effects arising from the laser pulse propagation (ROSE protocol [23, 24]), or by artificially broadening the atomic resonance at the time of the first echo (HYPER protocol [25]).

In our protocol, we make use instead of dynamical detuning of the cavity to silence the primary echo, as was independently proposed in [26]. In this case, spins rephase at 2τ but cannot re-emit. The information remains stored in the memory and spins pursue their evolution at their own Larmor frequency. As shown in Fig. 3.6, at time $t = 2\tau_1 + \tau_2$, a second refocusing pulse is applied to make them rephase again at $t = 2(\tau_1 + \tau_2)$ in a non-inverted medium. The echo described by the density matrix ρ, restores the initial state $|\psi\rangle\langle\psi|$.

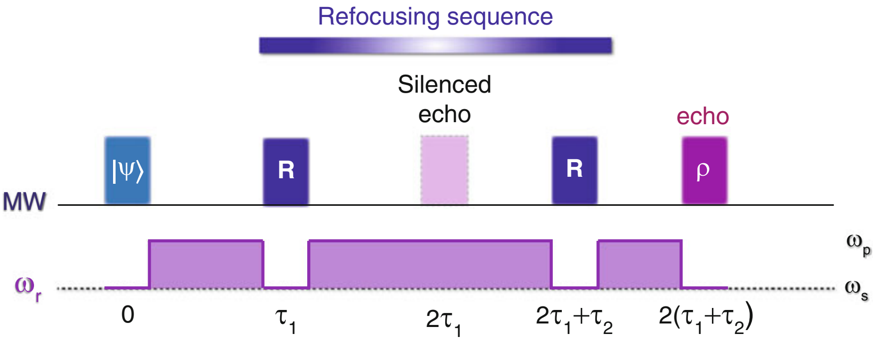

Fig. 3.6 Extension to the quantum regime. A second refocusing pulse is applied that brings the spins back into the ground state. The first echo is "silenced" to preserve all information for the second echo

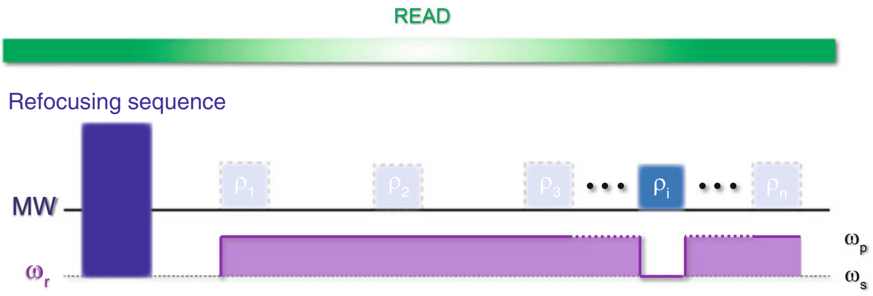
READ
Refocusing sequence
MW
ω_r
ρ_1
ρ_2
ρ_3
ρ_i
ρ_n
ω_p
ω_s

Fig. 3.7 The read step of the protocol. On-demand retrieval is obtained by dynamically detuning the cavity to retrieve selectively a state $|\psi_i\rangle$, while prohibiting the echo of others states $|\psi_j\rangle$ to keep them in the memory

On-demand retrieval is obtained by extending this protocol to multiple states with dynamical detuning of the cavity to select retrieval of $|\psi_i\rangle$, while prohibiting the echo of others states $|\psi_j\rangle$ to keep them stored in the memory for a later retrieval (Fig. 3.7). Note that due to the presence of two refocusing pulses, the states are retrieved in the same order as they were stored, contrary to the 2PE case.

3.2.3 The Full Quantum Memory Protocol

The whole quantum memory protocol combines the strategies presented above (see Fig. 3.8). The cavity state $|\psi\rangle$ delivered by the QuP is first transferred to the spins by setting $\omega_r = \omega_s$ for a time T_{swap}, after which the cavity is "parked" at $\omega_r = \omega_p$. For a high-fidelity storage, the damping rate is set to $\kappa = \kappa_{min}$ so that the spin ensemble and the resonator are in the strong coupling regime ($C \gg 1$).

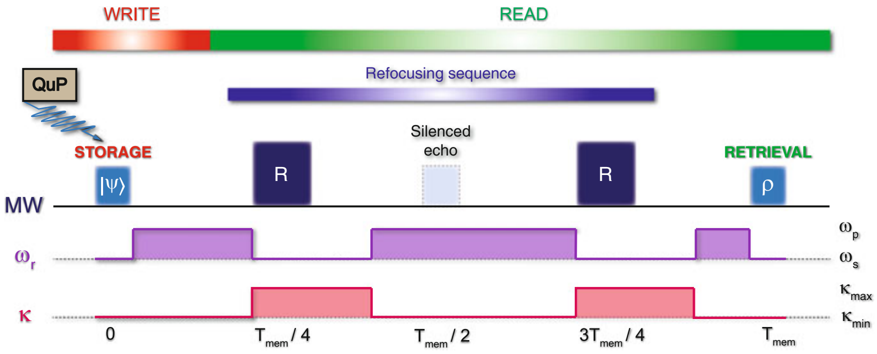
WRITE
READ
QuP
Refocusing sequence
STORAGE
$|\psi\rangle$
R
Silenced echo
R
RETRIEVAL
ρ
MW
ω_r
κ
ω_p
ω_s
κ_{max}
κ_{min}
0
$T_{mem}/4$
$T_{mem}/2$
$3T_{mem}/4$
T_{mem}

Fig. 3.8 Quantum memory protocol. The cavity-field state $|\psi\rangle$ delivered by the QuP is stored at $t = 0$ and retrieved at $t = T_{mem}$

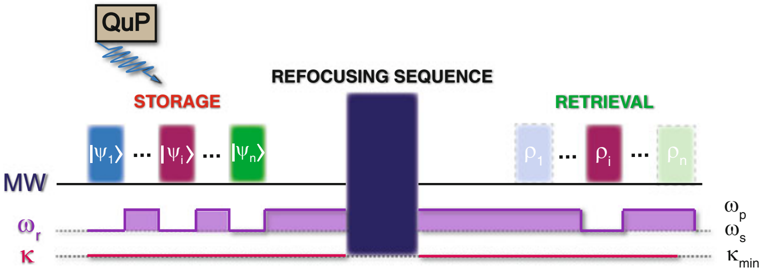

Fig. 3.9 Extension of the quantum memory protocol to multimode storage and on-demand retrieval

Next, in order to refocus the spin dephasing, two refocusing pulses at $t = T_{mem}/4$ and $t = 3T_{mem}/4$ are applied with $\omega_r = \omega_s$. The stabilization of the inverted spin ensemble is ensured by setting $\kappa = \kappa_{max}$ so that the cooperativity parameters fulfills $C < 1$ during and immediately after the refocusing pulses. In between, the cavity is set to $\omega_r = \omega_p$ to silence the first echo at $t = T_{mem}/2$. After the second refocusing pulse, the quantum state is retrieved from the spin ensemble by setting $\omega_r = \omega_s$ during T_{swap}, after which it is finally transferred to the QuP. The extension to multimode storage and on-demand retrieval is depicted in Fig. 3.9.

3.3 Simulations

Numerical simulations of the quantum memory protocol described above were performed by our collaborator B. Julsgaard at Aarhus University. We present here the key results of his simulations and refer to [27] for further details on the analysis. The simulations use the realistic model for NV centers described in Sect. 2.3.2.2 and account for typical spin frequency $\rho(\omega)$ and coupling strength $\rho(g)$ distributions. The parameters entering in the simulations correspond to realistic experimental parameters ($g_{ens} = 2\pi \cdot 3.5\,\text{MHz}$, $T_2^* = 0.16\,\mu\text{s}$, $T_2 = 100\,\mu\text{s}$, $T_1 = +\infty$, and quality factors $Q_{min} = 100$ and $Q_{max} = 10^4$ for the cavity). The refocusing pulses are hyperbolic secant π-pulses [28], which are pulses known to tolerate frequency and coupling strength inhomogeneity (see Chap. 6). The peak power of the external driving field is chosen to be $100\,\mu\text{W}$, an experimentally acceptable power in a dilution refrigerator. The dynamical evolution is calculated numerically as explained in Sect. 2.3.4, by dividing the spins into M sub-ensembles, keeping account of the mean values and covariances between cavity-field quadratures, $\hat{X}$ and $\hat{P}$, and spin components, $\hat{S}_x^{(m)}$, $\hat{S}_y^{(m)}$, and $\hat{S}_z^{(m)}$ of the m'th sub-ensemble. The results are displayed in Fig. 3.10.

The mean values of $\hat{X}$ and $\hat{P}$ are shown when a weak coherent cavity-field state is delivered at $t = 0$. We see in the inset that even though the cavity field is very strong during the inversion pulses at $t \approx 2.5\,\mu\text{s}$ and $t \approx 7.5\,\mu\text{s}$, the field relaxes to negligible levels prior to memory retrieval. Due to an imperfect storage process [marked by the arrow in Fig. 3.10] a minor part of the field is left in the cavity (14 % in

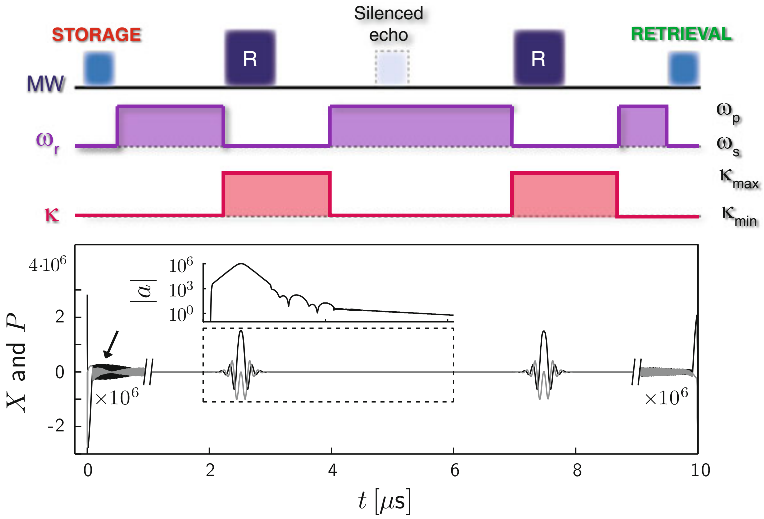

Fig. 3.10 Simulations of the storage and retrieval of a weak coherent cavity-field state. (*Top*) Schematic timing of pulses and cavity parameters (ω_s and κ) used for the simulations. (*Bottom*) Cavity-field mean values, $\langle \hat{X} \rangle$ (*black*) and $\langle \hat{P} \rangle$ (*gray*) versus time. The *inset* re-plots the *dashed-line* region with $|\hat{a}|$ on the logarithmic vertical scale

field strength or 2 % in energy units), but most importantly at $t = T_{mem}$ we retrieve into the cavity a mean value corresponding to 79 % of the initial state. To assess the performance of the quantum memory, the above simulation was repeated with various other coherent input states. A selection of these is shown in Fig. 3.11 in terms of retrieved mean values and variances of the quadratures of the field (gray circles) as compared to those of the input states (black circles). The stored and retrieved

Fig. 3.11 Storage and retrieval efficiency. Various input states (*black*) and output states (*gray*, sign reversed) examined in the protocol. The center of circles mark mean values whereas the radii mark the standard deviation σ of the state

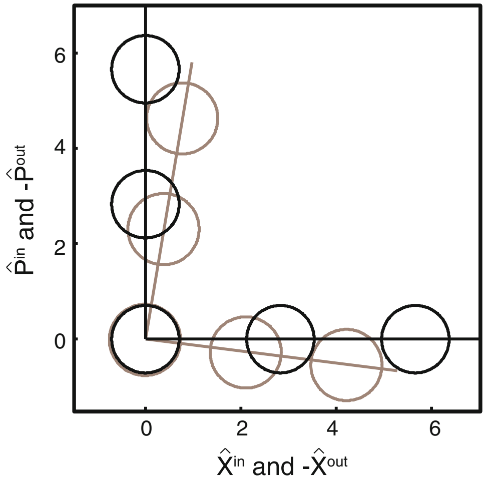

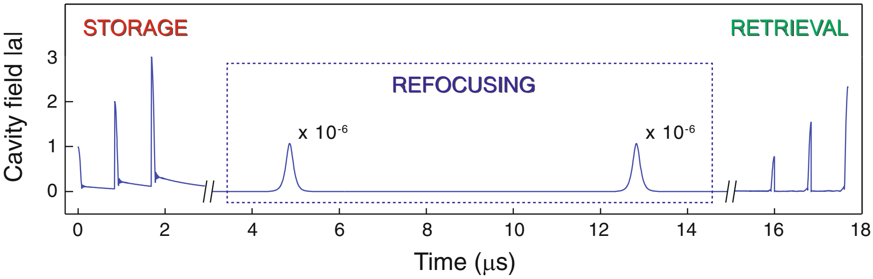

Fig. 3.12 **Multimode ability.** The cavity field $|\hat{a}|$ versus time in a multi-mode storage example with three input fields separated by $0.84\,\mu$s and memory time $16\,\mu$s

relations constitute a linear map, which (i) presents a reduction factor for the mean values ∼0.79 and (ii) shows a variance of the retrieved states ∼1.11. The fact that the reduction factor and the variance are close to 1 suggests respectively that the energy and the phase of the quantum state are almost conserved along the protocol. Since any quantum state can be expressed as a superposition of coherent states, the memory should work for arbitrary input states, in particular for Schrödinger cats [29]. The simulated efficiency of storage and retrieval with realistic experimental parameters is $E = 79\,\%$ after $T_{mem} = 10\,\mu$s storage. For optimized samples, that is in the limit T_2, $Q_{max} \to \infty$ and homogeneous distribution of coupling strengths, the efficiency $E = 97\,\%$ was calculated, limited by the finite spin-resonator coupling and imperfection of the refocusing pulse.

As demonstrated experimentally for classical pulses [21], the spin-ensemble quantum memory is multi-mode in nature, which we confirm in the simulations by storing and retrieving three pulses as exemplified in Fig. 3.12. The number of storage modes that can be faithfully addressed and refocused is estimated to be $n \sim 100$ for these sample parameters.

References

1. A. Dewes, R. Lauro, F.R. Ong, V. Schmitt, P. Milman, P. Bertet, D. Vion, D. Esteve, Quantum speeding-up of computation demonstrated in a superconducting two-qubit processor. Phys. Rev. B **85**, 140503 (2012)
2. M. Neeley, R.C. Bialczak, M. Lenander, E. Lucero, M. Mariantoni, A.D. O'Connell, D. Sank, H. Wang, M. Weides, J. Wenner, Y. Yin, T. Yamamoto, A.N. Cleland, J.M. Martinis, Generation of three-qubit entangled states using superconducting phase qubits. Nature **467**, 570–573 (2010)
3. L. DiCarlo, M.D. Reed, L. Sun, B.R. Johnson, J.M. Chow, J.M. Gambetta, L. Frunzio, S.M. Girvin, M.H. Devoret, R.J. Schoelkopf, Preparation and measurement of three-qubit entanglement in a superconducting circuit. Nature **467**, 574–578 (2010)
4. R. Barends, J. Kelly, A. Megrant, A. Veitia, D. Sank, E. Jeffrey, T.C. White, J. Mutus, A.G. Fowler, B. Campbell, Y. Chen, Z. Chen, B. Chiaro, A. Dunsworth, C. Neill, P. O'Malley, P. Roushan, A. Vainsencher, J. Wenner, A.N. Korotkov, A.N. Cleland, J.M. Martinis, Superconducting quantum circuits at the surface code threshold for fault tolerance. Nature **508**, 500–503 (2014)

5. L. DiCarlo, J.M. Chow, J.M. Gambetta, L.S. Bishop, B.R. Johnson, D.I. Schuster, J. Majer, A. Blais, L. Frunzio, S.M. Girvin, R.J. Schoelkopf, Demonstration of two-qubit algorithms with a superconducting quantum processor. Nature **460**, 240–244 (2009)
6. M. Mariantoni, H. Wang, T. Yamamoto, M. Neeley, R.C. Bialczak, Y. Chen, M. Lenander, E. Lucero, A.D. O'Connell, D. Sank, M. Weides, J. Wenner, Y. Yin, J. Zhao, A.N. Korotkov, A.N. Cleland, J.M. Martinis, Implementing the quantum von Neumann architecture with superconducting circuits. Science **334**, 61–65 (2011)
7. E. Lucero, R. Barends, Y. Chen, J. Kelly, M. Mariantoni, A. Megrant, P. O'Malley, D. Sank, A. Vainsencher, J. Wenner, T. White, Y. Yin, A.N. Cleland, J.M. Martinis, Computing prime factors with a Josephson phase qubit quantum processor. Nat. Phys. **8**, 719–723 (2012)
8. R. Barends, J. Kelly, A. Megrant, D. Sank, E. Jeffrey, Y. Chen, Y. Yin, B. Chiaro, J. Mutus, C. Neill, P. O'Malley, P. Roushan, J. Wenner, T.C. White, A.N. Cleland, J.M. Martinis, Coherent Josephson qubit suitable for scalable quantum integrated circuits. Phys. Rev. Lett. **111**, 080502 (2013)
9. H. Paik, D.I. Schuster, L.S. Bishop, G. Kirchmair, G. Catelani, A.P. Sears, B.R. Johnson, M.J. Reagor, L. Frunzio, L.I. Glazman, S.M. Girvin, M.H. Devoret, R.J. Schoelkopf, Observation of high coherence in Josephson junction qubits measured in a three-dimensional circuit QED architecture. Phys. Rev. Lett. **107**, 240501 (2011)
10. K. Tordrup, A. Negretti, K. Mølmer. Holographic quantum computing. Phys. Rev. Lett. **101**, 040501 (2013)
11. A.I. Lvovsky, B.C. Sanders, W. Tittel, Optical quantum memory. Nat. Photonics **3**, 706–714 (2009)
12. T. Chaneliere, D.N. Matsukevich, S.D. Jenkins, S.-Y. Lan, T. Kennedy, A. Kuzmich, Storage and retrieval of single photons transmitted between remote quantum memories. Nature **438**(7069), 833–836 (2005)
13. M.D. Eisaman, A. André, F. Massou, M. Fleischhauer, A.S. Zibrov, M.D. Lukin, Electromagnetically induced transparency with tunable single-photon pulses. Nature **438**(7069), 837–841 (2005)
14. K.S. Choi, H. Deng, J. Laurat, H.J. Kimble, Mapping photonic entanglement into and out of a quantum memory. Nature **452**(7183), 67–71 (2008)
15. J. Laurat, K.S. Choi, H. Deng, C.W. Chou, H.J. Kimble, Heralded entanglement between atomic ensembles: preparation, decoherence, and scaling. Phys. Rev. Lett. **99**, 180504 (2007)
16. A.L. Alexander, J.J. Longdell, M.J. Sellars, N.B. Manson, Photon echoes produced by switching electric fields. Phys. Rev. Lett. **96**, 043602 (2006)
17. M.P. Hedges, J. Longdell, Y. Li, M.J. Sellars, Efficient quantum memory for light. Nature **465**(7301), 1052–1056 (2010)
18. M. Afzelius, C. Simon, H. de Riedmatten, N. Gisin, Multimode quantum memory based on atomic frequency combs. Phys. Rev. A **79**, 052329 (2009)
19. M. Afzelius, I. Usmani, A. Amari, B. Lauritzen, A. Walther, C. Simon, N. Sangouard, J. Miná ř, H. de Riedmatten, N. Gisin, S. Kröll, Demonstration of atomic frequency comb memory for light with spin-wave storage. Phys. Rev. Lett. **104**, 040503 (2010)
20. E.L. Hahn, Spin echoes. Phys. Rev. **80**, 580–594 (1950)
21. H. Wu, R.E. George, J.H. Wesenberg, K. Mølmer, D.I. Schuster, R.J. Schoelkopf, K.M. Itoh, A. Ardavan, J.J.L. Morton, G.A.D. Briggs, Storage of multiple coherent microwave excitations in an electron spin ensemble. Phys. Rev. Lett. **105**, 140503 (2010)
22. J. Ruggiero, J.-L. Le Gouët, C. Simon, T. Chanelière, Why the two-pulse photon echo is not a good quantum memory protocol. Phys. Rev. A **79**, 053851 (2009)
23. V. Damon, M. Bonarota, A. Louchet-Chauvet, T. Chanelière, J.-L. Le Gouët, Revival of silenced echo and quantum memory for light. New J. Phys. **13**, 093031 (2011)
24. J. Dajczgewand, J.-L. Le Gouët, A. Louchet-Chauvet, T. Chanelière, Large efficiency at telecom wavelength for optical quantum memories. Opt. Lett. **39**(9), 2711–2714 (2014)
25. D.L. McAuslan, P.M. Ledingham, W.R. Naylor, S.E. Beavan, M.P. Hedges, M.J. Sellars, J.J. Longdell, Photon-echo quantum memories in inhomogeneously broadened two-level atoms. Phys. Rev. A **84**, 022309 (2011)

26. M. Afzelius, N. Sangouard, G. Johansson, M.U. Staudt, C.M. Wilson, Proposal for a coherent quantum memory for propagating microwave photons. New J. Phys. **15**(6), 065008 (2013)
27. B. Julsgaard, C. Grezes, P. Bertet, K. Mølmer. Quantum memory for microwave photons in an inhomogeneously broadened spin ensemble. Phys. Rev. Lett. **110**, 250503 (2013)
28. M.S. Silver, R.I. Joseph, D.I. Hoult, Selective spin inversion in nuclear magnetic resonance and coherent optics through an exact solution of the Bloch-Riccati equation. Phys. Rev. A **31**, R2753 (1985)
29. H. Wang, M. Hofheinz, M. Ansmann, R.C. Bialczak, E. Lucero, M. Neeley, A.D. O'Connell, D. Sank, M. Weides, J. Wenner, A.N. Cleland, J.M. Martinis, Decoherence dynamics of complex photon states in a superconducting circuit. Phys. Rev. Lett. **103**, 200404 (2009)

Chapter 4
Experiment 1 (Write): Coherent Storage of Qubit States into a Spin Ensemble

This chapter is dedicated to the presentation of the first experiment, where we have tested the write step of our memory protocol. Three different quantum systems are integrated on the same chip for this experiment: an ensemble of NV center spins, a superconducting qubit, and a superconducting resonator acting as a quantum bus between the qubit and the spins. Qubit states are coherently stored into the spin ensemble via the bus resonator.

4.1 State of the Art and Principle of the Experiment

The prerequisite for the transfer of quantum information from a superconducting circuit to a spin ensemble is to reach the strong coupling regime. At the time of writing this thesis, this regime has been evidenced spectrocopically for various types of spins embedded in superconducting resonators, including NV center spins in diamond. These experiments lay the foundations of this thesis work towards a spin ensemble memory.

4.1.1 State of the Art

In the experiments related to this thesis work, ensembles of typically 10^{12} electron spins in millimeter to centimeter sized crystals are coupled to the magnetic field sustained by a planar resonator. The first demonstration of strong coupling to a resonator was obtained in the group [1] shortly before the beginning of this thesis work, with an ensemble of NV center spins in diamond. In a parallel experiment, Schuster et al. [2] observed a similar coupling with both nitrogen impurities (P1 centers) in diamond, and chromium ion spins (Cr^{3+}) in sapphire. More recently, Amsuss et al. [3] and Ranjan et al. [4] made further work with NV centers and

© Springer International Publishing Switzerland 2016
C. Grèzes, *Towards a Spin-Ensemble Quantum Memory for Superconducting Qubits*, Springer Theses,
DOI 10.1007/978-3-319-21572-3_4

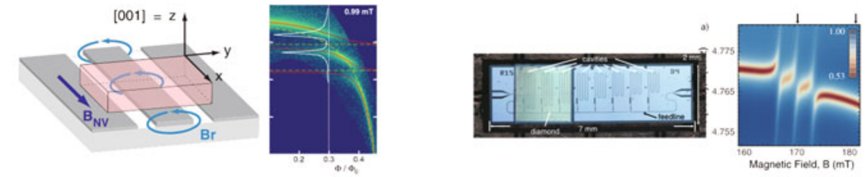

NV centers in diamond (Kubo et al., PRL 2010) Cr^{3+} in sapphire (Schuster et al., PRL 2010)

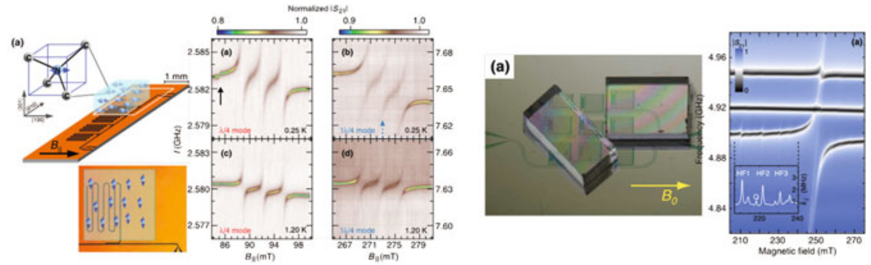

N impurities in diamond (Ranjan et al., PRL 2012) Er^{3+} in Y_2SiO_5 (Bushev et al., PRL 2013)

Fig. 4.1 State of the art

nitrogen impurities in diamond, and Bushev et al. [5, 6] with erbium rare-earth ion spins (Er^{3+}) in Y_2SiO_5 crystal. An overview of the state of art is depicted in Fig. 4.1. In these experiments, the strong coupling is manifested as described in Sect. 2.1.3.1, by the presence of a vacuum Rabi splitting in the resonator spectrum. We present now in details the experiment performed in the group with an ensemble of NV centers in diamond, the starting point of the experiment described in this chapter.

4.1.2 Strong Coupling of NVs to a Superconducting Resonator

The hybrid circuit that was developed for this experiment combines two components: a superconducting resonator and an ensemble of NV center spins in diamond. The resonator is a $\lambda/2$ CPW resonator with an array of four SQUIDS inserted in its central conductor to make its frequency $\omega_r(\Phi)$ tunable with a locally applied flux Φ threading the SQUID loops (see Sect. 2.1.2.2). It has been measured separately at 40 mK, showing a tunability over hundreds of MHz below its maximum resonance frequency $\omega_r/2\pi = 2.94\,\text{GHz}$, and a quality factor $\sim 2 \cdot 10^4$ at the zero field NV center frequency. The diamond crystal is of the HPHT type, with a NV concentration of $\sim 1.2 \cdot 10^6\,\mu\text{m}^{-3}$ (6.8 ppm). A spin linewidth $w/2\pi = 6\,\text{MHz}$ was measured at room temperature. The setup of this experiment is shown in Fig. 4.2.

The diamond single crystal ($3 \times 3 \times 0.5\,\text{mm}^3$) is placed on top of the superconducting circuit and positioned in the middle of the CPW resonator where the magnetic field is maximum to maximize the ensemble coupling constant. The spin Zeeman

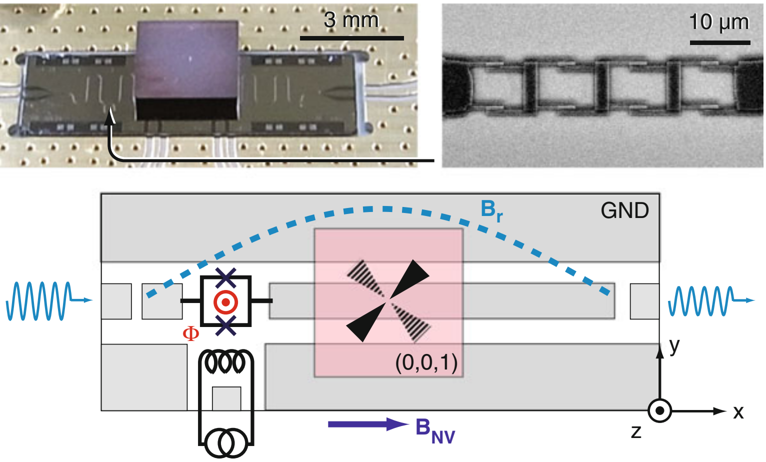

Fig. 4.2 Strong coupling of a spin ensemble to a superconducting resonator [1]**: scheme of the experiment.** (*top left*) A diamond crystal containing NV center spins is placed on top of the superconducting circuit and positioned in the middle of the superconducting coplanar resonator. (*top right*) A SQUID array is inserted in the central conductor to tune the resonator frequency with an on-chip wire producing a flux Φ in the SQUIDs. (*bottom*) A magnetic field B_{NV} is applied, making the same angle with the four possible NV axis orientations

splitting is tuned with a magnetic field B_{NV} making the same angle with the four possible NV axis orientations. The fraction η of the resonator mode volume occupied by the spins and the angular factor α introduced in Sect. 2.3.2.2 are respectively 0.29 and 0.81. Combined with the measured NV density, this yields (using Eq. 2.101 in Sect. 2.3.2.2) a predicted ensemble coupling constant $g_{ens}^{th}/2\pi = 11.6\,\text{MHz}$. This value satisfies $g_{ens}^{th} \gg \Gamma, \kappa$, bringing theoretically the experiment in the strong coupling regime.

Strong coupling signature The strong coupling is evidenced spectroscopically. The resonator transmission spectrum $S_{21}(\omega)$ was measured with a vector network analyzer, at microwave power weak enough to not modify the spin polarization (see Sect. 2.3.3). The transmission spectrum as a function of Φ is shown in Fig. 4.3 for an applied magnetic field $B_{NV} = 1.98\,\text{mT}$. Two avoided crossings are observed when the resonator is tuned through the NV center spin-resonance frequencies. This is the signature of the strong coupling between the NV ensemble and the resonator as described in Sect. 2.1.3.1. The fit yields $g_+/2\pi = g_-/2\pi = 11\,\text{MHz}$, in quantitative agreement with the predicted value g_{ens}^{th}. This experiment demonstrates the strong coupling of an ensemble of NV center spins to a superconducting resonator, a prerequisite to the implementation of the *write step* of the memory protocol.

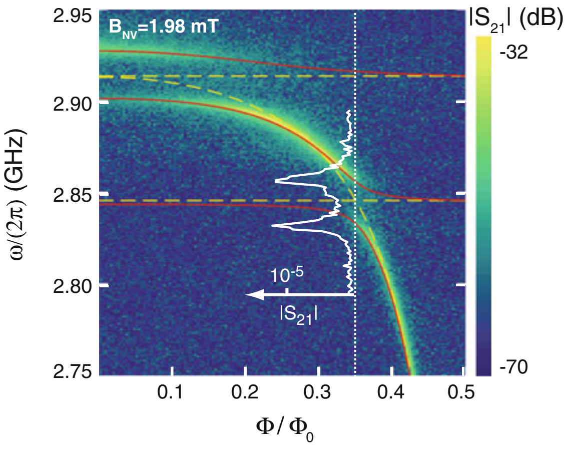

Fig. 4.3 Strong coupling of a spin ensemble to a superconducting resonator [1]**: spectroscopic evidence for strong coupling.** The resonator transmission spectrum S_{21} shows two anticrossings whenever the tunable resonator frequency crosses the NV transitions $|0\rangle \rightarrow |+\rangle$ and $|0\rangle \rightarrow |-\rangle$. *Red solid* (*yellow dashed*) *lines* are fits to the eigenfrequencies of the coupled (decoupled) resonator-spin system as described in Sect. 2.3.2.1. A transmission spectrum (*white overlay*) is also shown in linear units in the middle of the anticrossing with the NV transition $|0\rangle \rightarrow |-\rangle$

4.1.3 Principle of the Experiment

The *write step* of the memory protocol described in Chap. 3 consists in storing a quantum state $|\psi\rangle$ delivered by an external superconducting qubit processor (QuP) into a spin ensemble. The *write* experiment aims at demonstrating this operation with the QuP materialized by a single superconducting qubit. The physical setup and protocol proposed are depicted in Fig. 4.4. They are articulated around three

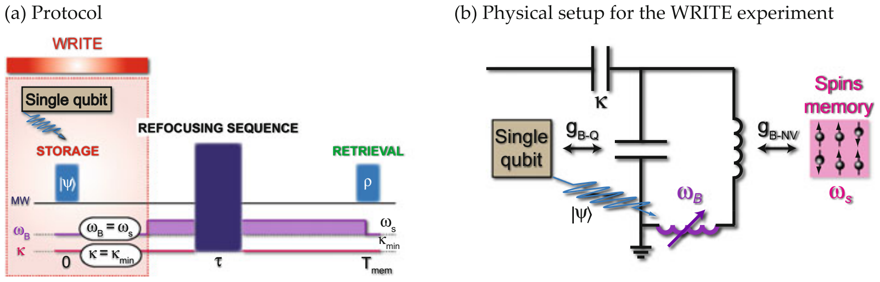
(a) Protocol

(b) Physical setup for the WRITE experiment
WRITE
Single qubit
REFOCUSING SEQUENCE
STORAGE
RETRIEVAL
$|\psi\rangle$
ρ
MW
ω_B
κ
$\omega_B = \omega_s$
$\kappa = \kappa_{min}$
0
τ
ω_s
κ_{min}
T_{mem}
κ
Single qubit
$g_{B\text{-}Q}$
$g_{B\text{-}NV}$
Spins memory
ω_B
ω_s
$|\psi\rangle$

Fig. 4.4 Principle of the experiment. a Quantum states delivered by a QuP, materialized by a single superconducting qubit, are stored into the spin ensemble. **b** The resonator, with frequency ω_B tunable and high quality factor, is strongly coupled to both the spin ensemble (frequency ω_s) with an ensemble coupling strength g_{B-NV} and a qubit (frequency ω_Q) with coupling strength g_{B-Q}. The qubit delivers quantum states to the bus resonator to be stored into the spins memory

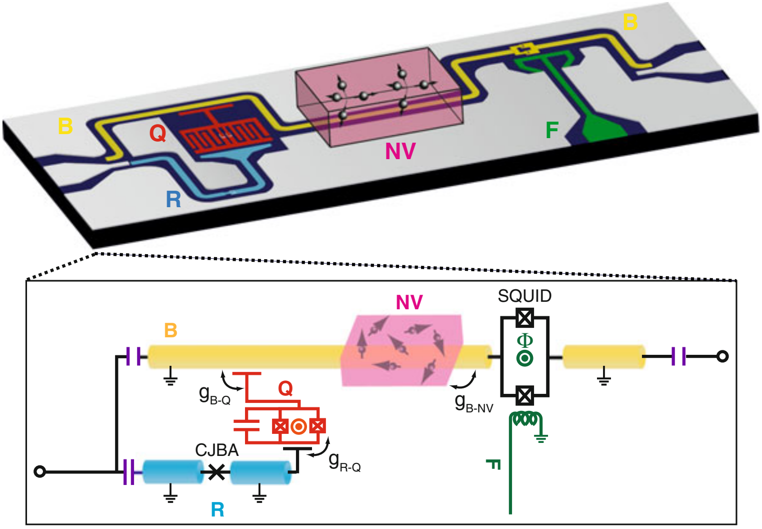

Fig. 4.5 Designing the write experiment: schematic of the hybrid quantum circuit. The quantum bus B (in *yellow*), a coplanar waveguide resonator, is coupled to Q (in *red*) and to NV (in *pink*). It contains a SQUID that makes its frequency tunable by applying in its loop a flux via an on-chip current line F (in *green*). The qubit Q is electrostatically coupled to a nonlinear resonator R (in *blue*) which is used to manipulate and readout its state

components: an ensemble of NV center spins, a superconducting qubit, and a superconducting resonator acting as a quantum bus between the qubit and the spins. The protocol requires that the bus resonator is strongly coupled to both the qubit and the spin ensemble to enable coherent exchange of quantum information, and made frequency tunable to transfer this information from one component to the other.

To demonstrate that the qubit state is preserved during the storage, the state is retrieved without refocusing, and compared to the initially encoded one. Hence the qubit must not be only an instrument for preparing the quantum state but also a precise readout apparatus for the comparison. This calls experimentally for the conception of a good qubit manipulation and readout circuitry. We show in Fig. 4.5 a 3D schematic of the hybrid circuit together with the corresponding electrical scheme. The bus resonator B (in yellow) is electrostatically coupled to the qubit Q (in red) with coupling strength g_{B-Q} and magnetically coupled to NV (in pink) with g_{B-NV}. It is implemented as a $\lambda/2$ CPW resonator made frequency tunable by inserting a SQUID loop in the resonator central line. The qubit is coupled with coupling constant g_{R-Q} to a manipulation and readout circuit R (in blue) that contains a hysteretic detector to ensure an efficient readout. We explain in the next section how the hybrid circuit is designed and describe the manipulation and readout techniques that we use to operate it.

4.2 Experimental Realization

4.2.1 The Hybrid Quantum Circuit

4.2.1.1 Diamond Sample Properties

The superconducting circuit is designed for matching the properties of the spin ensemble. The diamond is a polished (110) plate of dimensions $2.2 \times 1 \times 0.5\,\mathrm{mm}^3$ taken from a type-Ib HPHT crystal prepared by our collaborator Pr. Isoya in Tsukuba University. The diamond contained initially $7 \cdot 10^6\,\mu\mathrm{m}^{-3}$ (40 ppm) of neutral substitutional nitrogen (P1 centers) as measured by IR absorption. It was irradiated by 2 MeV electrons at 700° C with a total dose of $6.4 \cdot 10^{18}\,\mathrm{e/cm}^2$ and annealed at 1000° C for 2 h in vacuum. The high temperature irradiation was employed to minimize residual unwanted defects. The diamond sample was characterized at room temperature by our collaborators A. Dreau and V. Jacques at ENS de Cachan. The measurement of the resulting concentration of negatively-charged NV centers proceeds by comparing the sample photoluminescence (PL) to the one obtained from a single NV center. For that purpose, a continuous laser source operating at 532 nm wavelength was tightly focused on the sample through a high numerical aperture oil-immersion microscope objective. The NV center PL was collected by the same objective, spectrally filtered from the remaining pump light and directed to a silicon avalanche photodiode. After calibration of the PL response associated with a single NV center, a PL raster scan of the sample directly yields the NV center content since the excitation volume is known.

As shown in the left panel of Fig. 4.6, the NV center concentration is rather inhomogeneous over the sample, with an average density of $\rho_{NV} = 4.4 \cdot 10^5\,\mu\mathrm{m}^{-3}$ (2.5 ppm). Electron spin resonance (ESR) measurements have been performed at room temperature by applying a microwave field with a copper microwire placed on the diamond surface. In addition, a static magnetic field $B \approx 1.5\,\mathrm{mT}$ was applied

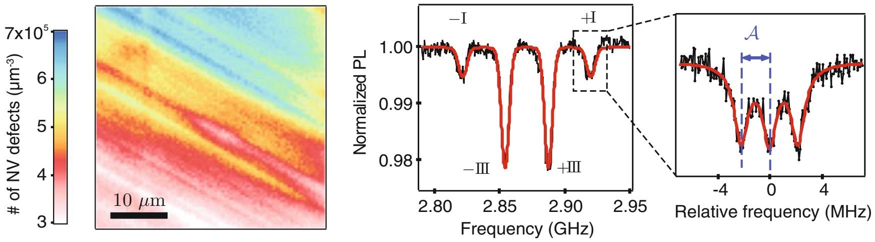

Fig. 4.6 **The diamond: characterization at room temperature.** (*left*) Two-dimensional map of the NV center density for a depth of 5 µm inside the diamond sample. (*right*) Optically detected ESR spectrum with a static magnetic field $B \approx 1.5\,\mathrm{mT}$ applied along the [111] axis of the diamond crystal. Four ESR lines are observed, corresponding to $|0\rangle \rightarrow |\pm\rangle$ spin transitions for the two subsets of NV centers crystalline orientations (±III and ±I). The fit with Lorentzian functions (*inset*) leads to $\mathbf{A}_{||} = 2.14 \pm 0.02\,\mathrm{MHz}$ as expected from hyperfine interaction with ^{14}N nuclear spins

along the [111] axis of the diamond crystal. As explained in Chap. 2, such a magnetic field orientation allows both to lift the degeneracy of $m_s = \pm 1$ spin sublevels and to divide the NV center ensemble into two sub-groups of crystallographic orientations (I and III) which experience different Zeeman splitting. Optically detected ESR spectra were recorded by sweeping the frequency of the microwave field while monitoring the PL intensity.

As shown in the right panel, when the microwave frequency is resonant with a transition linking $m_s = 0$ and $m_s = \pm 1$ spin sublevels, ESR is evidenced as a dip of the PL signal owing to the spin-dependent PL response of the NV centers [7], as explained in Chap. 2. The study has been focused on the ESR line at $\omega_{+I}/2\pi = 2.915\,\text{GHz}$, which corresponds to the $|0\rangle \rightarrow |+\rangle$ spin transition for the subset of [111]-oriented NV centers. The nitrogen atom of NV centers in our sample being a ^{14}N isotope, each electron spin state is further split into three sublevels by the hyperfine interaction with a splitting 2.17 MHz between ESR frequencies associated with different nuclear spin projections (see Sect. 2.2.2.1). This hyperfine structure is easily observed in our sample at low microwave power.

To probe the coherence properties of this subset of NV centers, the Ramsey sequence described in Sect. 2.2.3 is applied. As seen in the left panel of Fig. 4.7), the free induction decay signal exhibits beating frequencies which correspond to the

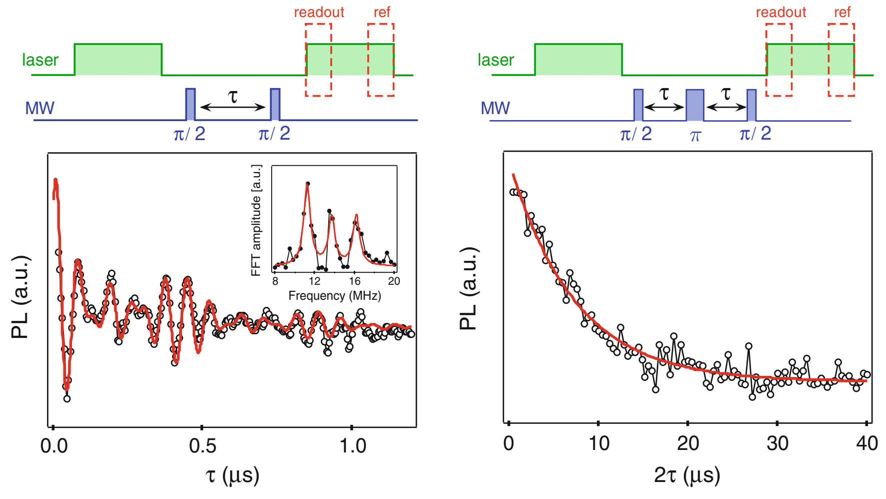

Fig. 4.7 **The diamond: coherence times at room temperature.** (*left*) Ramsey fringes recorded for the subset of [111]-oriented NV centers with a microwave detuning $\delta = 13\,\text{MHz}$ from the ESR line at $\omega_{+I}/2\pi = 2.915\,\text{GHz}$. The laser pulses used in the Ramsey sequence have a duration of 30 μs and the laser power is set at 40 mW. For data analysis, the NV center PL recorded during the first 10 μs of the laser pulses is used for spin-state read-out while the PL recorded during the last 10 μs is used as reference. The *red solid line* is data fitting with the function $\exp[-\tau/T_2^*] \times \sum_{i=-1}^{1} \cos\left[2\pi(\delta + i\mathbf{A}_\parallel)\tau\right]$. The *inset* shows the Fourier-transform of the free induction decay. *Solid lines* are data fitting with Lorentzian functions. (*right*) Measurement of the coherence time T_2 for the subset of [111]-oriented NV centers using a $\pi/2 - \tau - \pi - \tau - \pi/2$ spin echo sequence. Data fitting with an exponential decay leads to $T_2 = 7.3 \pm 0.4$ μs

hyperfine components of the NV center ESR lines. The fit yields $T_2^* = 390 \pm 30$ ns and its Fourier transform spectrum reveals the ^{14}N hyperfine structure with a linewidth $w/2\pi = 810 \pm 90$ kHz for each peak (see inset of Fig. 4.7). Spin echo coherence time of the NV center ensemble reaches $T_2 = 7.3 \pm 0.4$ μs (right panel).

4.2.1.2 Superconducting Circuit Design

We now discuss the parameters of each component of the superconducting circuit in details, explaining the relevant design goals and presenting the parameter choice we made.

QUBIT AND READOUT CIRCUIT DESIGN

The design of the qubit is motivated by three requirements: it must have (i) a frequency in the dynamical frequency range of the bus resonator, (ii) a coherence time sufficiently long to allow for coherent exchange with the resonator and (iii) be weakly coupled to the readout circuitry to enable its measurement via dispersive techniques. The qubit and its coupling to the readout circuitry are designed accordingly using the microwave solver SONNET (see Sect. 2.1.1.3). The geometry used for the simulation is shown in Fig. 4.8. The Josephson junction is modeled separately by an inductance that matches the Josephson inductance to complete the SONNET simulation. We design $C_Q = 100$ fF and the two Josephson junctions with area 150×200 nm to obtain the charging energy $E_C/h = 0.68$ GHz and Josephson energy $E_J/h = 6.5$ GHz. This ensures that the qubit is in the Transmon regime $E_J \gg E_C$ and has a transition frequency $\sqrt{2E_C E_J}/h = 2.97$ GHz ideally placed between the NV zero-field and bus frequencies (see below). The qubit is further equipped with a fast magnetic flux line to tune its resonance frequency, which was however not used in our experiments.

The readout circuit is a cavity Josephson bifurcation amplifier described in Sect. 2.1.2.2, made of two pieces of CPW transmission lines with a Josephson junction placed in the middle. It is capacitively coupled on one side to the input transmis-

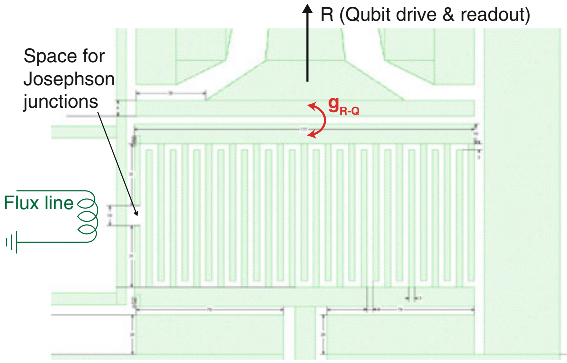

Fig. 4.8 The qubit and its coupling to the readout circuitry. Schematic of the simulated chip geometry, showing the Transmon capacitance, the space for the Josephson junction and the coupling to the readout circuitry

sion line and on the other side to the qubit. As explained in Sect. 2.1.3.3, the state-dependent dispersive shift of the resonator for readout can be maximized by increasing the coupling constant g_{R-Q} to the qubit, reducing its frequency detuning Δ_{R-Q} with respect to the qubit. We design accordingly the qubit-readout-resonator coupling constant $g_{R-Q}/2\pi = 40\,\mathrm{MHz}$, the frequency at $\omega_R/2\pi = 3.86\,\mathrm{GHz}$ corresponding to a detuning $\Delta_{R-Q}/2\pi = 860\,\mathrm{MHz}$. The Kerr constant $2\pi K_R/\omega_R = -4.5 \cdot 10^{-6}$ and quality factor $Q = 10^3$ are chosen to optimize the Josephson bifurcation amplifier response, with an estimated time $T_{meas} = 100\,\mathrm{ns}$ for mapping the qubit state to the oscillator This implies that the relaxation time T_1^Q of the qubit has to be longer than $1\,\mu\mathrm{s}$ to limit the relaxation probability during the measurement interval to about 5 %.

BUS RESONATOR DESIGN

The design of the bus resonator is motivated by two requirements: it must (i) have a dynamical frequency tunability between the qubit and the spin ensemble frequencies to transfer quantum states between the two components, (ii) be strongly coupled with both the qubit and the spin ensemble such that the two components can coherently exchange quantum states via the resonator. The first requirement implies to use a SQUID-based resonator as described in Sect. 2.1.2.2. As explained in this section, the frequency of such resonator can be tuned only below its bare frequency. We thus aim for a resonator frequency ω_B higher than both the qubit and the spin ensemble frequencies. The second requirement implies for the resonator to have a coherence time much longer than the time needed to exchange the information between the bus resonator and the qubit $(\pi/(2g_{B-Q}))$ and the spins $(\pi/(2g_{B-NV}))$.

We design accordingly the CPW bus resonator of length Λ with a SQUID embedded in its central conductor at position 0.8Λ. The length is adjusted to $\Lambda = 18.8\,\mathrm{mm}$ to obtain a resonance frequency without SQUID $\omega_B = \pi\bar{c}/\Lambda = 2\pi \times 3.15\,\mathrm{GHz}$. With the SQUID embedded, we estimate (using Eq. 2.42 in Sect. 2.1.2.2) the resonance frequency at zero flux $\omega_B(0)/2\pi = 3.10\,\mathrm{GHz}$, higher than the qubit and NV frequencies, as required for this experiment. The resonator is terminated at both ends by elbow couplers to the measuring lines with $C_1 = C_2 = 2\,\mathrm{fF}$ setting the bare quality factor $Q_0 = 10^5$, which corresponds to a bus damping rate $\kappa \sim 0.19 \cdot 10^6\,\mathrm{s}^{-1}$ (and coherence time $T_1^B = 3.3\,\mu\mathrm{s}$).

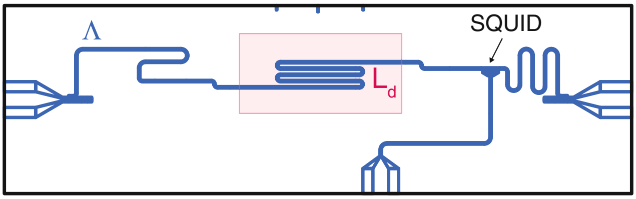

Fig. 4.9 The bus resonator: the design. It is made with a section of CPW transmission line terminated at both ends with elbow couplers. A SQUID is embedded in its central conductor to make its frequency tunable. The diamond covers a length L_d of the resonator length Λ

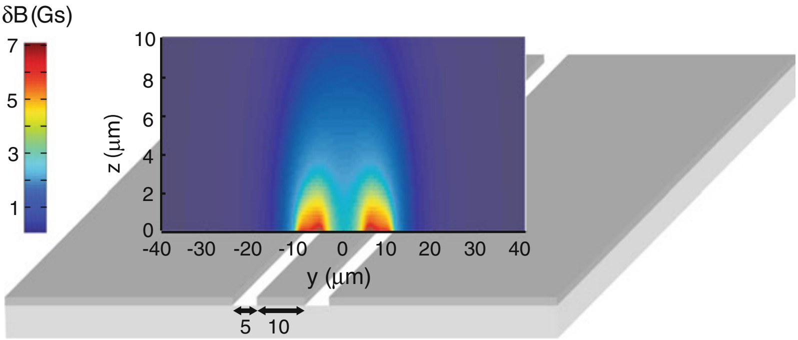

Fig. 4.10 The bus resonator: the AC magnetic field to which the spins are coupled. Amplitude of the microwave field generated by the bus resonator driven at resonance by a incident microwave of power 1 μW

Strong coupling requests that the coupling strengths of the bus resonator to the qubit g_{B-Q} and to the spins g_{B-NV} are much larger than the bus damping rate κ. These coupling strengths are set respectively for the qubit and the spins by the electrical and magnetic fields sustained by the resonator (see Sect. 2.1.1.3). In this work, the resonator is designed with 10 μm central conductor and 5 μm gap width. The dielectric constant is $\epsilon_{eff} = \frac{\epsilon_{Si}+1}{2} = 6.45$, set by the Silicon substrate. The coupling capacitance to the qubit C_{B-Q} is located at 0.2 Λ. At this position, the vacuum fluctuations of the electrical field are reduced by a factor $\cos(0.2\,\pi) = 0.81$. We design accordingly $C_{B-Q} = 3\,\text{fF}$ to obtain a coupling to the bus resonator $g_{B-Q} = 2e(C_{B-Q}/C_Q)\delta V_{rms}\langle 1|n|0\rangle = 2\pi \times 10\,\text{MHz}$ much larger than the bus resonator damping rate κ.
Similarly, the coupling strength to the spins g_{B-NV} is set by the vacuum fluctuations of the magnetic field sustained by the CPW transmission line (shown in Fig. 4.10). As we have seen in Sect. 2.3.2.2, the fraction η of the mode volume occupied by the spins increases with the resonator section of CPW transmission line covered by the diamond crystal. We design accordingly the resonator with a meander shape in the middle of the resonator on top of which the diamond crystal will be positioned (see Fig. 4.9). The coupling strength g_{B-NV} between the resonator and the spin ensemble is estimated in the next section.

4.2.1.3 The Device

The superconducting circuit is fabricated on a silicon chip oxidized over 50 nm, using the process described in Appendix A. A 150 nm thick niobium layer is first deposited by magnetron sputtering and then dry-etched in a SF_6 plasma to pattern the readout resonator R, the bus resonator B, the current lines for frequency tuning, and the input waveguides. Finally, the transmon qubit Q, the coupling capacitance between Q and B, the Josephson junction of R, the SQUID in B, are fabricated by double-angle evaporation of aluminum through a shadow mask patterned using

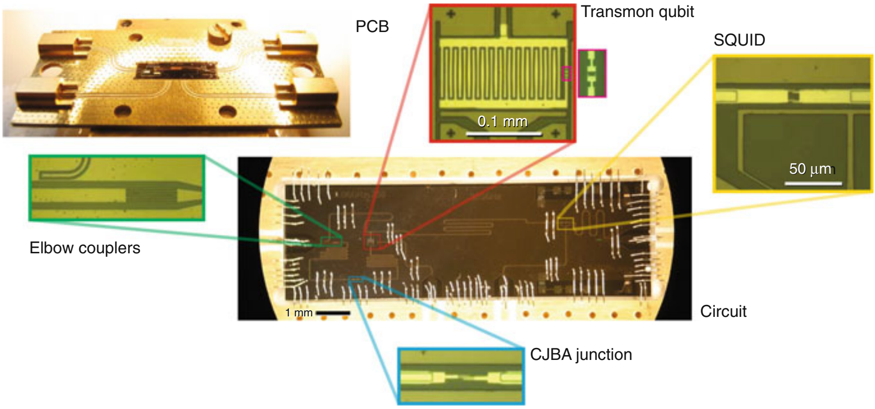

Fig. 4.11 **The fabricated circuit with panels zooming to its most important features**

e-beam lithography. The first layer of aluminum is oxidized in a Ar-O_2 mixture to form the oxide barrier of the junctions.

The flux line is a 50 Ω CPW transmission line passing nearby the resonator SQUID at a distance of $d \approx 12\,\mu\text{m}$. The ground plane between the resonator and the central conductor of the flux line has been removed to eliminate unwanted shielding currents. The chip is finally attached with wax on a microwave printed circuit board (PCB) made out of TMM_{10} ceramics and wire bonded to it. The whole is enclosed in a copper box. We show in Fig. 4.11 the scanning optical and electron micrographs of the circuit.

The diamond is positioned in the middle of the bus resonator mode, on top of the meanders (see Fig. 4.12). A superconducting coil which produces a magnetic field B_{NV} is attached to the copper box containing the sample to tune the NV frequency. B_{NV} is parallel to the [1, 1, 1] NV crystalline axis. The NV frequencies being sensitive only to the projection of B_{NV} along the NV axis, two groups of NVs thus experience different Zeeman effects: those along [1, 1, 1] (denoted I) and those along either of the three other $< 1, 1, 1 >$ axes (denoted III as they are 3 times more numerous). This results in four different ESR frequencies $\omega_{I\pm,III\pm}$. We call from now $g_{ens,I}$ and $g_{ens,III}$ the coupling strengths of the I and III spin groups respectively.

Given the position and the orientation of the diamond, we estimate the coupling strength of the spin ensemble to the bus resonator via the filling η and angular α factors introduced in Sect. 2.3.2.2. The length of the CPW transmission line covered by the diamond is $L_d = 8.5\,\text{mm}$, yielding (using Eq. 2.99 in Sect. 2.3.2.3) a filling factor[1] $\eta = 0.38$. We obtain the angular factor α from the spin average orientation with respect to the resonator microwave field shown in Fig. 4.10. For group I, the angular factor is $\alpha_I = 1$ as the NV axis is parallel to the resonator waveguide.

---

[1] Note that we did not consider an eventual gap between the diamond and the circuit for the calculation.

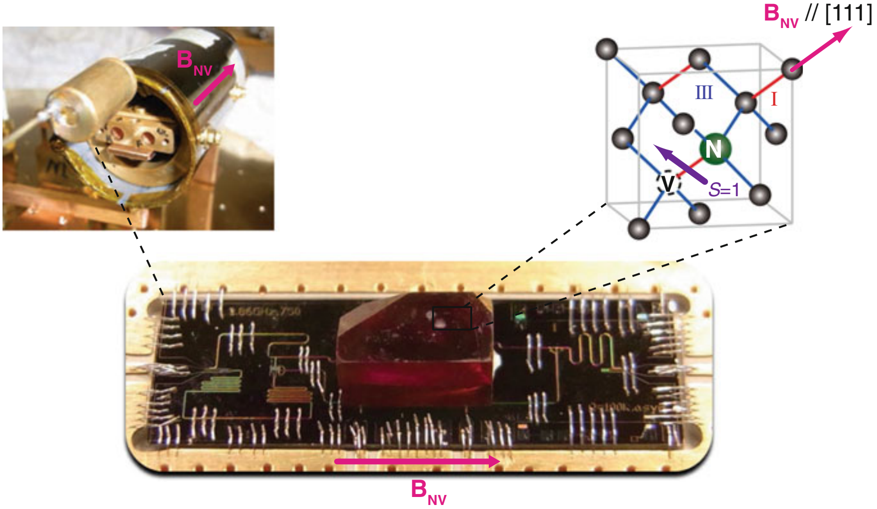

Fig. 4.12 **Hybrid quantum circuit for the write experiment.** The diamond crystal containing the NV center spins is glued on the chip surface, in the middle of the bus resonator. A magnetic field B_{NV} is applied parallel to the [1, 1, 1] crystallographic axis, resulting in different Zeeman splittings for centers having the NV axis parallel to B_{NV} (ensemble *I*, in *red*) and those having their axis along the three other $< 1, 1, 1 >$ axes (ensemble *III*, in *blue*)

For group *III*, we consider the projection of the NV axis on the resonator, which yields (using Eq. 2.100 in Sect. 2.3.2.3) $\alpha_{III} = 0.57$. Using the NV concentration ρ_{NV} measured in Sect. 4.2.1.1, we estimate the ensemble coupling constants using Eq. 2.101 in Sect. 2.3.2.3:

$$\mathrm{g}^{\mathrm{th}}_{\mathrm{ens,I}} = 2\pi \times 4.4 \ \ \mathrm{MHz} \tag{4.1}$$

$$\mathrm{g}^{\mathrm{th}}_{\mathrm{ens,III}} = 2\pi \times 5.8 \ \ \mathrm{MHz}. \tag{4.2}$$

where we introduce a factor $\sqrt{3}/2$ for $g^{th}_{ens,III}$ (respectively $1/2$ for $g^{th}_{ens,I}$) since *III* are 3 times more numerous than *I*. The total estimated coupling constant is $g^{th}_{ens} = \sqrt{g^2_{ens,I} + g^2_{ens,III}} = 2\pi \times 7.3\,\mathrm{MHz}$.

4.2.2 *Measurement Setup*

4.2.2.1 The Experimental Setup

The experiment is performed in a cryogen free dilution refrigerator. This refrigerator has four stages at different temperature (70 K, 4 K, 1 K, 30 mK) separated by shields to minimize radiative energy transfer. The sample is thermally anchored to the mixing chamber at 30 mK. At this temperature, the spins and the qubit are with good approximation in the ground state (see Sect. 2.3.2.1). The hybrid circuit is characterized either by microwave reflection or transmission measurement. For that purpose, microwave signals are sent and retrieved through transmission lines which connect the measurement apparatus at RT to the 30 mK stage. These transmission lines are made of CuNi (or Ag-CuNi) coax from room temperature to 4 K and superconducting NbTi down to 30 mK to ensure low microwave attenuation. Semi-flexible Copper microwave coaxial cables are used at 30 mK. A schematic of the measurement setup is shown in Fig. 4.13.

The setup is designed to reduce the thermal and technical noises reaching the sample and to ensure the lowest possible noise temperature at the output. To reduce thermal noise from the room temperature, the input line (*MW in*) contains several filters and successive attenuators thermally anchored at different temperatures. The input noise at 300 K is absorbed by attenuators which subsequently re-emit thermal noise at their own physical temperature. As the signal-to-noise ratio depends mostly on the last attenuator on the chain, we concentrated the attenuation on lower stages.

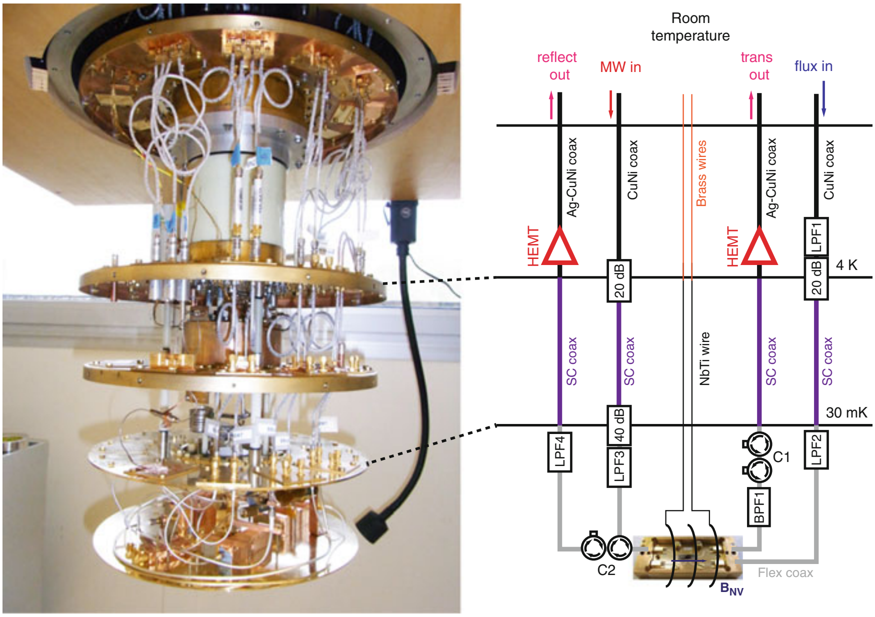

Fig. 4.13 Picture and wiring scheme of the dilution refrigerator. LPF1, LPF2, LPF3, and LPF4 are low-pass filters with cutoff frequencies 1.35 GHz, 450 MHz, 5.4 GHz, and 5.4 GHz, respectively. BPF1 is a band-pass filter with a bandwidth of 2.5–4 GHz. C1, C2 are double circulator. CuNi coax is a coaxial cable made of CuNi, and Ag-CuNi coax is a silver-plated CuNi coaxial cable. SC coax is a superconducting NbTi coaxial cable. Flex coax is a low-loss flexible coaxial cable. Rectangles represent ports terminated by 50 Ω. The cryogenic microwave amplifier is a CITCRYO 1-12 from Caltech, with gain ~38 dB and noise temperature ~5 K at 3 GHz. A DC magnetic field B_{NV} is applied parallel to the chip by passing a DC current through an outer superconducting coil. The sample box and the coil are surrounded by two magnetic shieldings consisting of a lead cylinder around which permalloy tape is wrapped. The sample box, coil, and the shieldings are thermally anchored at the mixing chamber

For the same reason, a cryogenic amplifier is placed at the 4 K stage on both output lines (*reflect out* and *trans out*) to ensure low noise measurement.

As amplifiers inject noise backwards to their input, an isolator must be introduced between the sample and the amplifier. In our setup, this isolation is made by a double circulator (C) which acts as a strong attenuator in the reverse direction. This one is connected to a 50 Ω charge, which allows the propagation of signals in a given direction, the reverse way being attenuated by twice the single circulator attenuation (2 × 20 dB). C2 is additionally used to separate the input signal from the reflected signal. To tune the bus resonator, an additional line (*flux in*) able to support hundreds of μA is required. As for the input line, attenuators and filters are introduced to reduce thermal noise. The attenuation is used only at 4 K to avoid Joule heating at the mixing chamber. Since the bandwidth of our current pulses is not greater than 100 MHz, high frequency are also attenuated to minimize thermal excitations in the bus resonator. This is ensured by a home-made Eccosorb filters with a 50 Ω input impedance and a cutoff frequency of 500 MHz placed at 30 mK. To avoid any DC resistance at 30 mK, the filter is covered with superconducting solder.

4.2.2.2 Signal Generation and Acquisition

The setup at room temperature is shown in Fig. 4.14. Two types of microwave signals are applied: (i) pulses near the qubit resonance to manipulate its state (drive pulses), (ii) pulses near the frequency of the readout resonator R for qubit measurement (readout pulses). Both are made using a DC-coupled IQ mixer before being combined and sent to the sample through *MW in*. The readout pulse is recovered through *reflect out* after reflection on the sample, amplified with a total gain of 45 dB and mixed down using an IQ mixer with a local oscillator synchronous to the microwave tone used for its generation. The output IQ quadratures are then filtered, amplified, balanced and finally sampled by an Acquiris DC282 fast digitizer before transfer to a computer for processing. In addition, DC pulses are shaped and sent through *flux in* to tune the resonator frequency via the fast current line on-chip.

The drive pulse (Fig. 4.15) consists of a truncated Gaussian microwave pulse at the qubit frequency ω_Q with voltage drive $V_d(t) = A_G(t)\cos(\omega_Q t + \varphi)$. The microwave tone is generated by an Anritsu MG3692 microwave generator and shaped to a Gaussian $A_G(t)$ with an IQ mixer with I and Q signals generated by an arbritrary waveform generator Tektronix AWG5014C (AWG). The parameters $(A_G(t) \cdot \tau, \varphi)$ are carefully tailored to apply qubit rotations in the Bloch sphere as explained in Sect. 2.1.3.2. X-Y pulse generation by microwave sideband mixing is implemented for precise rotation, as further explained in the next section.

The measurement pulse consists (Fig. 4.16) of a microwave tone at the frequency of the readout resonator ω_R. It is generated by an Anritsu MG3692 microwave generator mixed with the DC pulses generated by an arbitrary waveform generator Agilent AFG3252. Its shape is related to the CJBA characteristics described in Sect. 2.1.3.3. During the time t_R, the pulse rises linearly up to the vicinity of the bifurcation point β_+, where it stays for a short time t_m, during which a bifurcation of the CJBA $\overline{\mathbf{B}} \rightarrow \mathbf{B}$ may occur depending on the qubit state. The resonator state is then maintained while

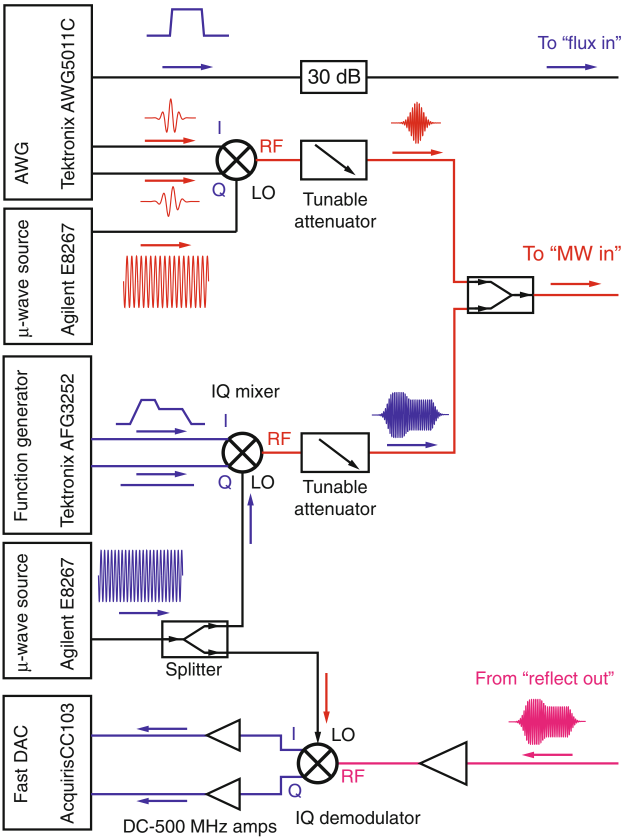
AWG
Tektronix AWG5011C
30 dB
To “flux in”
I
RF
Q
LO
Tunable attenuator
µ-wave source
Agilent E8267
To “MW in”
Function generator
Tektronix AFG3252
IQ mixer
I
RF
Q
LO
Tunable attenuator
µ-wave source
Agilent E8267
Splitter
From “reflect out”
Fast DAC
AcquirisCC103
I
LO
RF
Q
DC-500 MHz amps
IQ demodulator

Fig. 4.14 **Configuration of the setup at room temperature**

Fig. 4.15 **The drive pulse.** The microwave signal at frequency ω_Q is modulated by a Gaussian shape

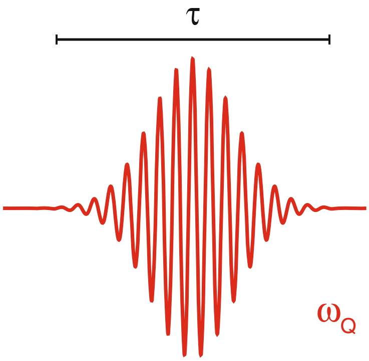

the phase measurement is performed during a long plateau t_h at lower power (to stabilize the resonator oscillations).

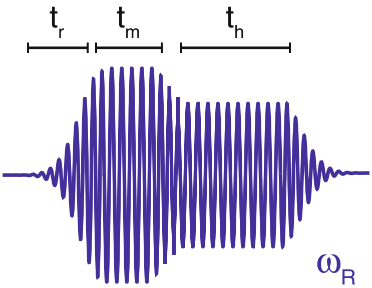

Fig. 4.16 **The readout pulse.** The microwave signal at frequency close to ω_R is modulated by a complex shape with 3 characteristic times. The pulse rises linearly in a time t_R similar to the resonator rise-time κ^{-1}, is maintained during t_m in the vicinity of the bifurcation point β_+ to let the transition of the resonator $\overline{\mathbf{B}} \rightarrow \mathbf{B}$ occurs and finally hold for at time t_h at slightly lower power for measurement

X-Y pulse generation for qubit manipulation Precise manipulation of the qubit requires a good understanding of the imperfections of the IQ mixer used to shape the drive pulse. This element has four ports, LO, RF, I and Q where LO is used as the main input port and RF as the output port (see Fig. 4.17). Given the two input signals I and Q, the IQ mixer splits the incoming microwave signal LO in two channels and multiplies the first one by $I(t)$ while the second one is first phase shifted by $\pi/2$ and multiplied by $Q(t)$. Finally the two channels are combined back together to produce the output signal RF:

$$\mathrm{V_{RF}(t) = I(t)V_{LO}\cos(\omega_{LO}t) + Q(t)V_{LO}\sin(\omega_{LO}t)} \tag{4.3}$$

One can use this device to mix a DC pulse (I) with a continuous microwave signal at the exact qubit frequency (LO) to create a rectangular pulse signal resonant with the qubit transition at frequency ω_Q (with no signal in Q). In reality however, the IQ mixer is not perfect and suffers from leakage that prevents precise qubit manipulations. In our experiments instead, we choose a carrier frequency LO slightly lower than the resonance frequency ($\omega_{LO} = \omega_Q - \Delta_{QS}$) and use I-Q inputs to up-convert the signal to the qubit frequency. Microwave leaks are thus off reso-

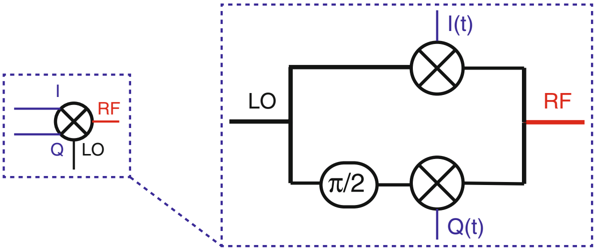

Fig. 4.17 **Diagram of an IQ mixer**

nance and do not affect the qubit. This is called the single sideband mixing technique [8]. In addition we use a truncated Gaussian shape $a_G(t)$ for I and Q as it has a narrower width in the frequency space than the rectangular one. The advantage of using a Gaussian pulse is that its Fourier transform is again a Gaussian, which, in contrast to a rectangular pulse, does not exhibit side lobes in the frequency domain and thus minimizes the leakage to higher qubit levels. When supplied with $I(t) = a_G(t)\cos(\Delta_{QS}t + \varphi)$ and $Q(t) = a_G(t)\sin(\Delta_{QS}t + \varphi)$ the output becomes $V_{RF}(t) = A_G(t)\cos\left[(\omega_{LO} + \Delta_{QS})t + \varphi\right]$, resonant with the qubit frequency ω_Q, with $A_G(t) = a_G(t) \cdot V_{LO}$. In our experiments, we use $\Delta_{QS} = 50\,\text{MHz}$.

This complex pulse generation calls for a calibration of the amplitude and phase imbalance of the IQ mixer (see Fig. 4.18), which would otherwise cause unwanted harmonics to appear. To do so, the signal out of the IQ mixer is split in two paths, the first sent connected to the measurement lines, and the second plugged to a spectrum analyzer. An automatic loop based on a function minimization procedure adjusts the generation of $I(t)$ and $Q(t)$ up to the full suppression of the undesired frequencies. This adjustment proceeds in two steps: (i) offset correction (via respective compensations I_0 and Q_0) to suppress the carrier at ω_{LO}, (ii) amplitude and phase corrections (via a common compensation $ce^{-i\varphi_c}e^{-i(\Delta_{QS}t+\varphi)}$) to suppress the lower sideband, such that:

$$I(t) = I_o + Re\left[a_G(t)e^{-i(\Delta_{QS}t+\varphi)} + ce^{-i\varphi_c}e^{-i(\Delta_{QS}t+\varphi)}\right] \tag{4.4}$$

$$Q(t) = Q_o + Im\left[a_G(t)e^{-i(\Delta_{QS}t+\varphi)} + ce^{-i\varphi_c}e^{-i(\Delta_{QS}t+\varphi)}\right] \tag{4.5}$$

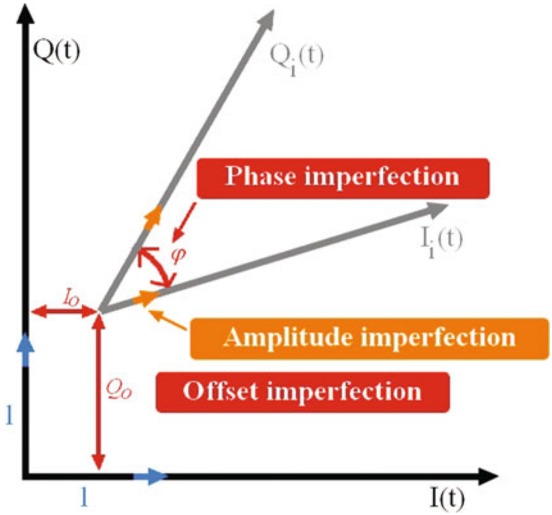

Fig. 4.18 IQ mixer calibration. The correction for the IQ mixer imperfections is represented in the complex domain, with the IQ basis without calibration (in *grey*), and the orthogonal IQ basis obtained with calibration (in *black*)

4.3 Operating the Hybrid Quantum Circuit

This section is dedicated to the characterization of the hybrid circuit and its operation. We first present measurement of each component. We then discuss the coupling of the bus resonator to both the qubit and the spins.

4.3.1 Superconducting Circuit Characterization

4.3.1.1 Qubit Characterization

QUBIT READOUT

We first calibrate the readout pulse. The general principle of qubit readout through the CJBA is described in Sect. 2.1.3.3. We have seen that two parameters are important: the drive frequency ω_{Rd} and drive power P. In this section we explain how to choose them prior to qubit characterization. The qubit readout will be further optimized later by adjusting the readout process described here to the specific qubit parameters determined in the section that follows. We first determine by reflectometry the resonance frequency ω_R of the CJBA with the qubit in the ground state $|g\rangle$ and largely detuned from the resonator. Microwave power and frequency are swept over a large range around the expected bifurcation point β_+ and the reflected phase measured (see Fig. 4.19).

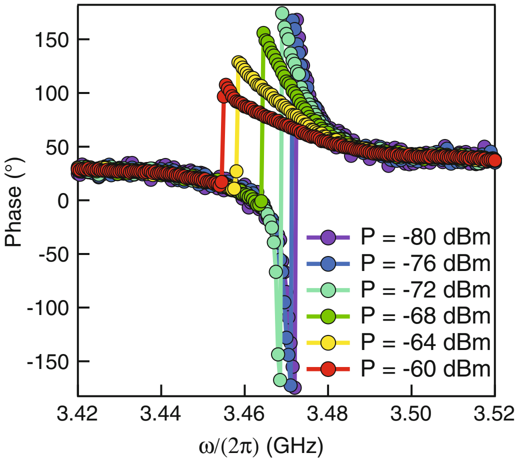

Fig. 4.19 Characterization of the CJBA. The phase of the reflection coefficient for probe microwave powers $P = -80, -76, -72, -68, -64, -60$ dBm (from *purple* to *red*) is shown as a function of the probe frequency. The *purple curve* shows a π-shift at $\omega_R/2\pi = 3.472$ GHz, the readout resonator frequency. At powers above -72 dBm, the resonance shifts and acquires a reduced phase shift ($<\pi$) indicating that the resonator becomes non-linear. The readout parameters for qubit readout are chosen $P_d = -64$ dBm and $\omega_{Rd}/2\pi = 3.458$ GHz to operate in the hysteretic region of the CJBA

At the lowest powers (purple and blue curves), the resonator is in the linear regime and the reflected phase undergoes a π-shift at $\omega_R/2\pi = 3.472\,\text{GHz}$, the base resonance frequency of the readout resonator R. To operate in the hysteretic region, we ensure a relative drive detuning $\Omega = 2Q(\omega_{Rd}/\omega_R - 1) > \sqrt{3}$ and choose the frequency of the readout pulse at $\omega_{Rd}/2\pi = 3.456\,\text{GHz}$. The power $P_d = -64\,\text{dBm}$ is chosen accordingly (the yellow curve in Fig. 4.19) to place ourselves at the point β_m seen in Sect. 2.1.3.3 at which the resonator can switch from $\overline{\mathbf{B}} \to \mathbf{B}$. For the shape of the readout pulse, we choose the rise time $t_r = 80\,\text{ns}$, the time $t_m = 350\,\text{ns}$ allowed for the bifurcation and $t_h = 2000\,\text{ns}$ for measurement.

During the time window t_h, the IQ quadratures are low-passed filtered at 200 MHz, and digitized at a sampling rate of 1 GSample/s. The IQ signals are then averaged over the readout pulse to obtain a single measurement point in the IQ plane. This sequence is repeated a large number of times (typically 10^4) to obtain the statistical distribution of IQ points shown in the left panel of Fig. 4.20. Since the switching is a stochastic process, we will observe two distinct sets of points (clusters) close to the transition power. At the point β_m we have chosen, the variance $\sigma_{IQ}^2 = \sum_i \left((I_i - \bar{I}_i)^2 + (Q_i - \bar{Q}_i)^2\right)/n$ of the obtained IQ data points is the largest.

We further subtract the averages ($I_0 = \sum_i I_i/n$, $Q_0 = \sum_i Q_i/n$) from the data and perform a transformation to project the measured (I, Q) points on the principal axis joining the two clusters of the distribution (the red line). In this way we obtain a bivalued one-dimensional probability distribution corresponding to the $\overline{\mathbf{B}}$ and $\mathbf{B}$ states (in the right panel of Fig. 4.20). If the measurement window t_h is large enough and no switching events occurs during the measurement (i.e. β_m well chosen), the two clusters do not overlap, and we have a perfect discrimination between them. The measurement yields the resonator switching probability P_{sw}, a quantity directly linked to the qubit excited state probability P_e, the quantity of interest in our experiment.

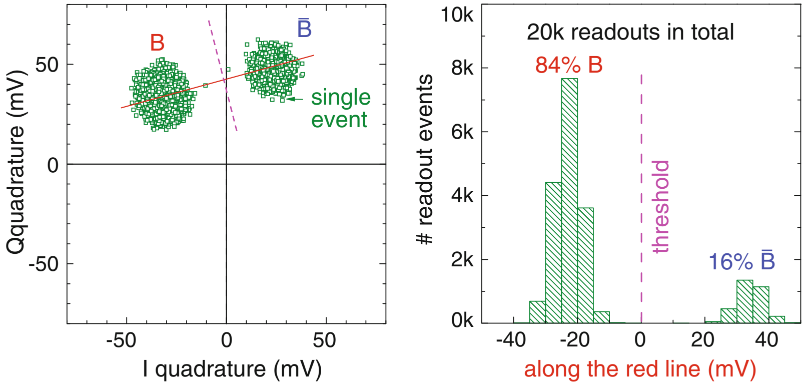

Fig. 4.20 **Qubit readout.** (*left*) Example of bimodal distribution of the time-averaged (I, Q) measured. The red dotted line perpendicular to the principal axis joining the two modes of the distribution and going through the mean quadratures (I_0, Q_0) provides an optimal separation between the two clusters corresponding to the $\bar{B}$ and B states. The signal projected on the principal axis (*red line*) yield an histograms (*right*) revealing a switching probability of 84 % for the example shown

QUBIT SPECTROSCOPY

To measure the qubit $|g\rangle \rightarrow |e\rangle$ transition frequency, we drive the qubit with a long microwave pulse (3 µs) whose frequency is scanned around the expected qubit frequency. The drive power is ensured to be high enough to excite the qubit in $|e\rangle$ so that the readout resonator R undergoes a transition $\overline{\mathbf{B}} \rightarrow \mathbf{B}$. The resonator R is measured over $5 \cdot 10^3$ identical sequences to obtain the switching probability P_{sw}. Figure 4.21 shows P_{sw} as a function of the drive frequency at low (top) and large (bottom) driving power. The peak that appears in the top panel corresponds to the qubit $|g\rangle \rightarrow |e\rangle$ transition frequency. A second smaller peak is visible at 2.6207 GHz, suggesting a fluctuation of the qubit transition from one frequency to the other during the measurement. This effect, possibly due to tunneling of an out-of-equilibrium quasiparticle between the two transmon islands, will reappear later in this section. At large drive power (see bottom panel), a peak appears at lower frequency. It corresponds to the excitation to the third level $|g\rangle \rightarrow |f\rangle$ by 2 photons. By fitting the $|g\rangle \rightarrow |e\rangle$ and $|g\rangle \rightarrow |f\rangle$ resonances with a Lorentzian model we obtain the qubit frequencies $\omega_{ge}/2\pi = 2.6215\,\text{GHz}$ and $\omega_{gf}/2\pi = 2 \times 2.538\,\text{GHz}$. Note that the measured resonance frequency is 350 MHz lower than the design value, which

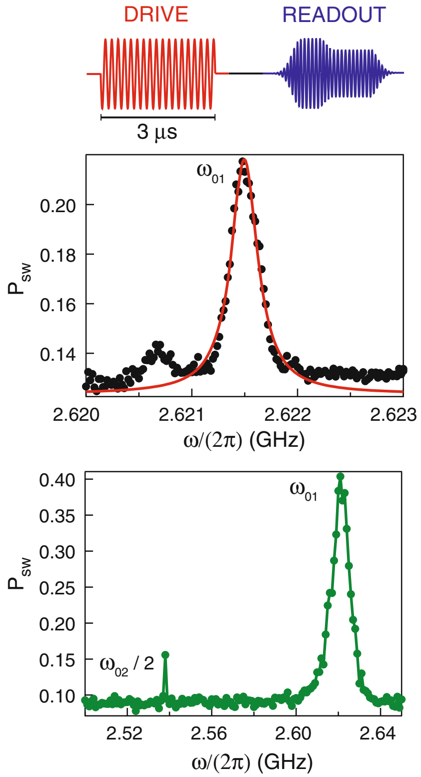

Fig. 4.21 Measurement of the qubit frequency. The switching probability P_{sw} measured after a 3 µs drive is shown as a function of the drive frequency. Low power spectroscopy (*top*) shows only the $|g\rangle \rightarrow |e\rangle$ transition of the qubit at frequency ω_{ge}, whereas the 2-photons $|g\rangle \rightarrow |f\rangle$ transition at frequency $\omega_{gf}/2$ is also observed at higher power (*bottom*). A Lorentzian function (*red line*) is fitted to the spectroscopic line at low power yielding qubit frequency $\gamma_Q/2\pi = 2.6215\,\text{GHz}$ and linewidth $\gamma_Q/2\pi = 0.13\,\text{MHz}$

places the qubit below the NV zero field frequency. Using the set of formulas given in Sect. 2.1.2.3, we obtain $E_J/h = 5.2\,\text{GHz}$ the Josephson energy and $E_C/h = 0.66\,\text{GHz}$ the charging energy. The measured charging energy is in good agreement with the design but E_J corresponds to 80 % of the design value. The energy E_J is still much larger than E_c placing the qubit in the Transmon regime, as required for our experiment. In the following, we refer most of the time to $\omega_Q = \omega_{ge}$ the qubit $|g\rangle \rightarrow |e\rangle$ transition frequency.

RABI OSCILLATIONS

To prepare the qubit in the desired state, we have to calibrate the single qubit gates. We perform Rabi oscillations by driving resonantly the qubit $|g\rangle \rightarrow |e\rangle$ transition with pulses of increasing areas. The state is measured immediately afterwards. From the fit of the Rabi oscillations, shown in Fig. 4.22, we obtain the Rabi frequency $\Omega_Q/2\pi = 20\,\text{MHz}$, which we use to program precise qubit rotations. Here the $\pi/2$-pulse and π-pulse length are respectively 11.5 and 23 ns. For this measurement, we operate at low power in order to minimize the population of $|f\rangle$ via 2-photon process. The Rabi oscillations visibility is limited here at 55 % due the imprecision of the current qubit readout and initialization. Optimization will be performed later in this section.

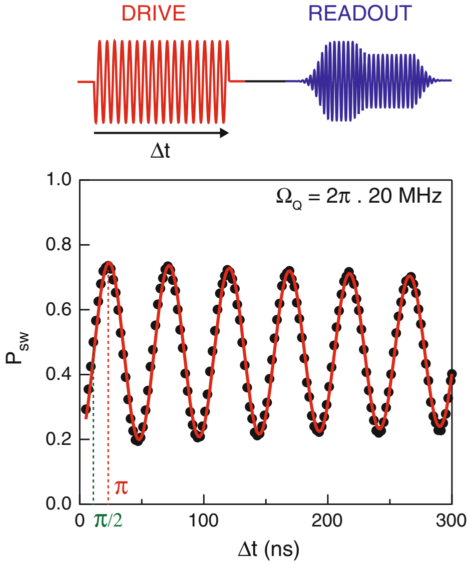

Fig. 4.22 Measurement of the qubit gates: the Rabi oscillations. The switching probability P_{sw} is measured after a drive pulse at ω_Q of increasing effective duration Δt (*black points*). The *line* is a fit by an exponentially decaying sine function from which we obtain the Rabi frequency $\Omega_Q/2\pi = 20\,\text{MHz}$ and decay time $T_R = 1.5\,\mu\text{s}$. The π and $\pi/2$ qubit gates correspond respectively to $T_\pi = 2\pi/\Omega_Q$ and $T_{\pi/2} = \pi/\Omega_Q$

RELAXATION AND DEPHASING TIMES MEASUREMENT

The $|g\rangle \rightarrow |e\rangle$ relaxation time T_1^Q of the qubit is measured by preparing the qubit in $|e\rangle$ by applying a π-pulse and let it evolve freely afterwards for a given delay time Δt before reading out its state. As seen in the left panel of Fig. 4.23, the switching probability P_{sw} decreases exponentially. The fit with $P_{sw} = P_{sw,0} + P_{sw,A} \exp -t/T_1^Q$ yields $T_1^Q = 1.75\,\mu\text{s}$. Note that $P_{sw,0}$ contains an offset linked to the readout techniques and has to be further converted in P_e the probability to find the qubit in $|e\rangle$ to estimate the effective electromagnetic temperature of the qubit. This conversion is made later in this section.

We also characterize the free induction decay time of the qubit by a Ramsey fringe experiment that consists in two $\pi/2$-pulses separated by a delay Δt and a readout immediately afterwards. The two microwave pulses are slightly detuned by ω_D from the qubit frequency ω_{ge}. As the pulse is non-resonant, the qubit Bloch vector undergoes a rotation at frequency ω_D during the free time Δt. The second $\pi/2$-pulse reveals the phase of the superposition. The resulting signal, so-called Ramsey fringes, oscillates at ω_D ($2\pi \times 5\,\text{MHz}$ in our experiment) due to the oscillations between the qubit dipole and the microwave source. The Ramsey oscillations decay with characteristic time $T_{2,Q}^*$ the free induction decay time of the qubit (see Sect. 2.1.2.3). The right panel of Fig. 4.23 shows the results of this measurement averaged out over 5×10^3 identical sequences. Note that a beating is visible. It is due to the fluctuation of the qubit frequency that we have already seen in the spectroscopy. The fit (red curve) yields $T_{2,Q}^* = 2.23\,\mu\text{s}$, or equivalently a qubit linewidth $\gamma_Q = 2/T_{2,Q}^* \sim 2\pi \times 0.14\,\text{MHz}$, which is in good agreement with our observation in the qubit spectroscopy of

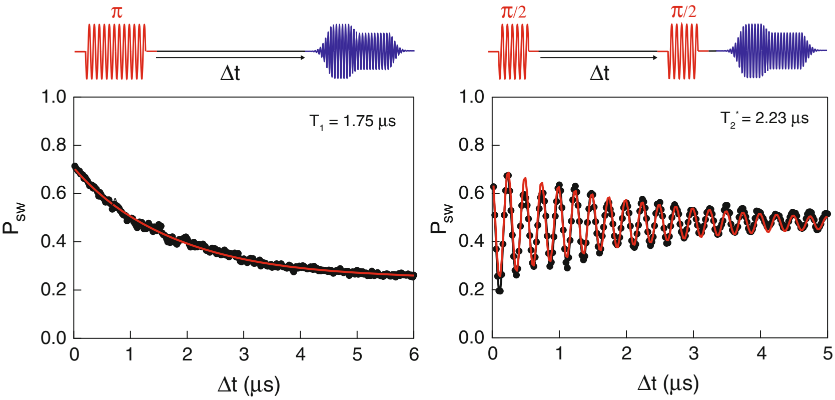

Fig. 4.23 **Measurement of the qubit coherence times.** (*left*) T_1 measurement. The switching probability P_{sw} is measured as a function of the delay time Δt between the preparation of the qubit in the excited state $|e\rangle$ and the actual measurement of the qubit state (*black points*). The line is a fit by a decaying exponential yielding $T_1^Q = 1.75\mu\text{s}$. (*right*) T_2^* measurement. The switching probability P_{sw} is measured at the end of the Ramsey sequence as a function of the delay time Δt between the two $\pi/2$ pulses. The line is a fit by an exponentially decaying sine function yielding $T_{2,Q}^* = 2.23\,\mu\text{s}$

Fig. 4.21. Knowing the relaxation time and the free induction decay time, we deduce (using Eq. 2.47 in Sect. 2.1.2.3) the pure dephasing time of our qubit $T_\phi = 6.15\,\mu\text{s}$.

OPTIMIZED QUBIT OPERATIONS

Using the measured qubit parameters, we can optimize the discrimination of the two qubit states and convert the probability P_{sw} of switching of the resonator R into the probability P_e of finding the qubit in $|e\rangle$. The reason for which P_e is not directly given by P_{sw} is due to readout errors caused either by

- **Limited dispersive shift** χ induced by the qubit on the readout resonator R,
- **Unavoidable qubit relaxation** between the end of the drive and the time at which readout effectively takes place.

These errors can be modeled with two parameters: the probability e_0 that the resonator switches despite the qubit being in $|g\rangle$ at the end of the drive, and the probability e_1 that the resonator doesn't switch when the qubit is in $|e\rangle$. In order to determine e_0 and e_1, we measure the switching probability as a function of the input power while either leaving the qubit in state $|g\rangle$ or exciting it into the state $|e\rangle$ via π-pulse. In the following we assume that the swap from state $|g\rangle$ to $|e\rangle$ is 100 % efficiency, that is $P_e = 1$ just after the π-pulse qubit operation. Figure 4.24 shows the corresponding switching probability $P_{sw,0}$ and $P_{sw,\pi}$, thereafter called the S-curves. The optimal input power for readout corresponds to the maximum of the readout contrast function $c = P_{sw,\pi} - P_{sw,0}$, indicated by the dotted blue vertical line.

Conversion to $\mathbf{P_e}$ For the conversion, an additional complication arises from the fact that the qubit has a small but finite probability $P_{e,eq}$ to be found in $|e\rangle$ even at thermal equilibrium, due to the rather low qubit frequency chosen in the experiment to match the NV centers. We therefore first estimate $P_{e,eq}$ by fitting the shape of $P_{sw,0}$ and $P_{sw,\pi}$ to a simple model, yielding $P_{e,eq} = 0.08$ in our experiment (see Fig. 4.24). This corresponds to an effective electromagnetic temperature of 50 mK, slightly higher than the cryostat base temperature 30 mK, possibly due to imperfect filtering of the flux lines. We then find e_0 and e_1 by solving the system of two equations:

$$P_{sw,0} = e_0(1 - P_{e,eq}) + (1 - e_1)P_{e,eq}, \tag{4.6}$$

$$P_{sw,\pi} = e_0 P_{e,eq} + (1 - e_1)(1 - P_{e,eq}). \tag{4.7}$$

This allows to determine P_e from the directly measured P_{sw} since

$$P_{sw} = e_0(1 - P_e) + (1 - e_1)P_e. \tag{4.8}$$

Fighting the qubit relaxation with $|e\rangle$ to $|f\rangle$ shelving In the limited $c_{max} = 65\,\%$ readout contrast measured in Fig. 4.24, there is a large part which can be attributed to the unavoidable qubit relaxation in $|g\rangle$ during the measurement pulse. To reduce this effect, one can use the $|e\rangle$ to $|f\rangle$ shelving technique introduced in [9]. As the qubit nearly behaves like an harmonic oscillator, the probability of transition between

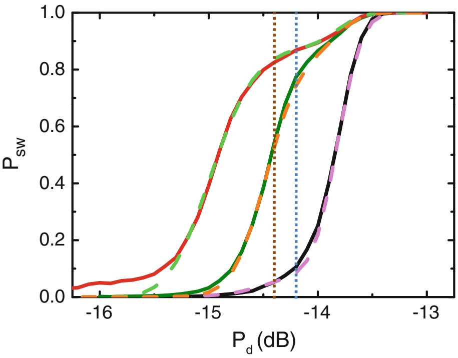

Fig. 4.24 Converting P_{sw} to P_e. The switching probability P_{sw} is shown as a function of readout pulse power P_R (*S-curves*). *Black solid line S-curve* with the qubit in thermal equilibrium. *Olive solid line S-curve* with the qubit prepared in $|e\rangle$ by a π pulse just before the readout. *Red solid line S-curve* with the qubit prepared in $|e\rangle$ by a π pulse, measured with a composite readout pulse including a π pulse on the $|e\rangle - |f\rangle$ transition followed by the usual readout pulse. *Dashed lines* represent fits of these *S-curves* using a sum of three Erf functions (corresponding to the three transmon states $|g\rangle$, $|e\rangle$, $|f\rangle$) with different weights. In this way the thermal population of the qubit $P_{e,eq} = 0.08$ is evaluated as explained in the text. *Dotted blue vertical line* indicates the readout power used for simple readout pulses, *dotted brown vertical line* indicates the readout power used for the composite readout pulse method

states of the same parity $\langle n|\hat{H}|n+2\rangle \approx 0$. A transfer of all the population of state $|e\rangle$ into the next excited state $|f\rangle$ thus take advantage of a very low decay from $|f\rangle$ to $|g\rangle$ and decreases the overall relaxation during the readout. For that, we apply a π pulse on the $|e\rangle - |f\rangle$ transition just prior to readout, resulting in a so-called composite readout pulse. Readout errors e_0 and e_1 are lowered accordingly and the contrast enhanced to $c_{max} = 78\,\%$ (see Fig. 4.24).

Due to technical complications, we use the composite readout pulse method only in experiments reported in Sect. 4.4.1 of this thesis. The other experiments are performed with simple readout pulses. As a result two different sets of errors e_0 and e_1 were determined for each of the two types of readout pulses. For composite readout pulses, we find $e_0 = 0$ and $e_1 = 0.1$, indicating a very high fidelity readout consistent with [9]. Without the composite readout pulse we find $e_0 = 0$ and $e_1 = 0.33$. From these values we convert the measured P_{sw} into P_e in all the following experiment. After all optimizations, we can perform again a Rabi measurement (Fig. 4.25). As expected from the S-curve, the contrast of the Rabi oscillations is around 78 %. Note that since we have changed the qubit drive from rectangular to Gaussian shape, we have to recalibrate the quantum gates. The $\pi/2$-pulse and π-pulse durations are respectively 24 and 38 ns.

Fig. 4.25 Rabi oscillations obtained for optimized qubit manipulation and readout. The optimization includes a drive with Gaussian pulse and readout with composite readout pulse

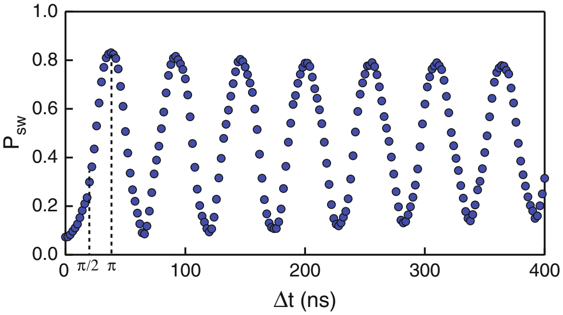

4.3.1.2 Bus Resonator Characterization

The bus resonator B is characterized by microwave transmission measurement. The spectrum is obtained with a vector network analyzer as introduced in Sect. 2.1.1.2, with a probe power low enough to stay in the linear regime of the SQUID inductance (see Sect. 2.1.2.2). The transmission spectrum S_{21} as a function of the probe frequency ω is shown on the left of Fig. 4.26. In absence of flux applied to the SQUID ($\Phi = 0$), the resonator frequency is $\omega_B/2\pi = 3.004\,\text{GHz}$ and quality factor $Q = 3 \cdot 10^4$, corresponding to a resonator damping rate $\kappa = 0.6 \cdot 10^6\,\text{s}^{-1}$. The dependence of the resonator frequency with Φ is shown in the right panel, confirming that the resonator can be tuned over several MHz below its bare resonance frequency. The periodic modulation is in good agreement with the model described in Sect. 2.1.2.2 for parameters close to design values. As already observed in similar samples, Q decreases when the resonator is tuned to lower frequencies due to flux noise [10, 11]. Around the NV center frequency of 2.88 GHz, we find $Q = 1 \cdot 10^4$, corresponding to a resonator energy damping rate $\kappa = 1.9 \cdot 10^6\,\text{s}^{-1}$.

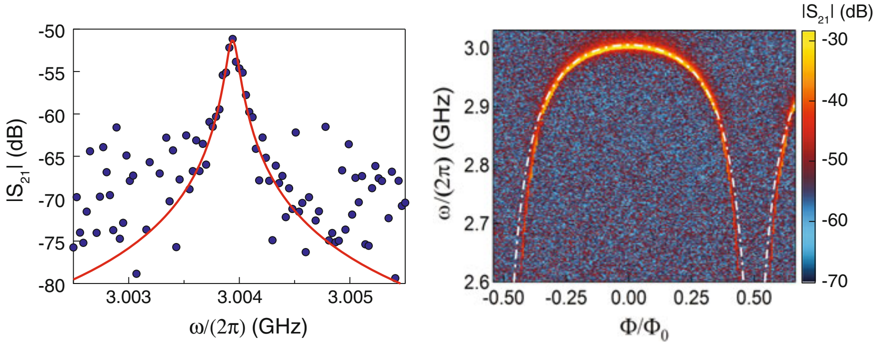

Fig. 4.26 Characterization of the bus resonator. (*left*) Resonance line of the bus resonator at $\Phi = 0$ (*dots*). The line is a fit with a Lorentzian. (*right*) Two-dimensional plot of the resonator spectrum as a function of the applied flux Φ. The fit (*white dash-dotted line*) yields a SQUID critical current $2I_{c0} = 1.3\,\mu\text{A}$

4.3.2 Transferring Qubit States to the Bus Resonator

4.3.2.1 Coupling the Qubit to the Bus Resonator

The prerequisite for transferring qubit states to the bus resonator is to be in the strong coupling regime $g_{B-Q} > \kappa, \gamma_Q$. This is evidenced spectroscopically by tuning the bus through the qubit $|g\rangle \rightarrow |e\rangle$ transition (Fig. 4.27). The spectrum shows a vacuum Rabi splitting with coupling constant $g_{B-Q}/2\pi = 7.5\,\mathrm{MHz}$. Since this value is much larger than the resonator damping rate $\kappa = 0.6 \cdot 10^6\,\mathrm{s}^{-1}$ and qubit linewidth $\gamma_Q/2\pi = 0.13\,\mathrm{MHz}$, the two systems are in the strong coupling regime.

4.3.2.2 Transferring Qubit States: SWAP Versus aSWAP Transfer

We now explain how to exchange quantum state between the qubit and the bus resonator. The first option is the resonant transfer (SWAP operation) which uses the vacuum Rabi oscillations described in Sect. 2.1.3.1. Experimentally, the resonator ω_B is suddenly tuned in resonance with ω_Q for a duration $\pi/(2g_{B-Q})$. We show in the left panel of Fig. 4.28 the resulting vacuum Rabi oscillations for the qubit prepared in $|e\rangle$.

In our experiment however, we found out that such a resonant SWAP operation was not stable enough to allow subsequent data acquisition during more than ~15 min. The problem is caused by flux noise in the SQUID loop, which causes $\omega_B(\Phi)$ to drift over time so that the flux pulse amplitude needed to perform the vacuum Rabi oscillations in resonance also changes in time.[2]

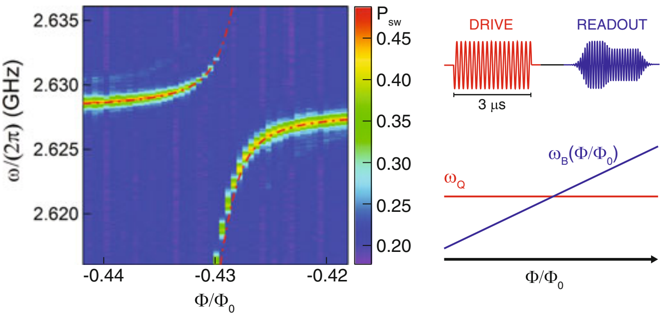

Fig. 4.27 Spectroscopic evidence of strong coupling between the bus resonator and the qubit. The procedure is depicted on the *right*: a qubit spectroscopy is performed for increasing applied flux Φ through the SQUID loop of the bus resonator. When $\omega_B(\Phi)$ matches the qubit frequency ω_Q, the qubit spectrum shows an anticrossing. The *red line* is a fit with the model described in Sect. 2.1.3.1, yielding $g_{B-Q}/2\pi = 7.2\,\mathrm{MHz}$

---

[2] We found a much larger flux noise at the working point $B_{NV} = 1.4\,\mathrm{mT}$ of the experiments which follow, probably due to vortices being trapped in the superconducting thin films around the SQUID.

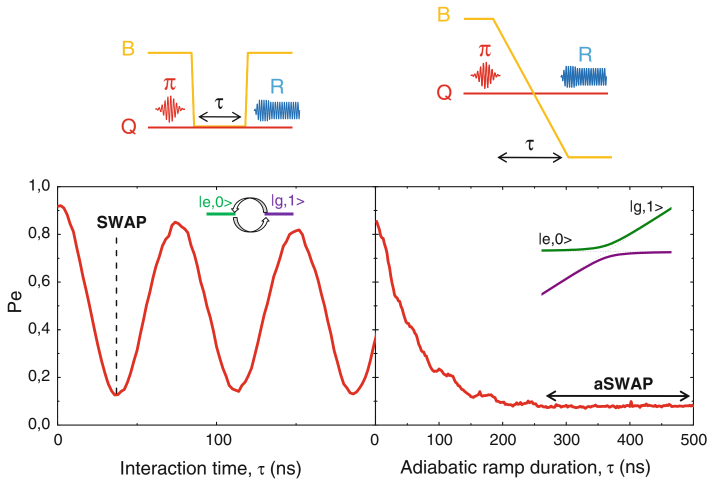

Fig. 4.28 Comparison between resonant and adiabatic SWAP pulses. (*left*) principle of a resonant SWAP. After excitation of the qubit in $|e\rangle$, B is put suddenly into resonance with Q for an interaction time τ during which $|e, 0_B\rangle$ and $|g, 1_B\rangle$ swap periodically. After a time $\tau = 37$ ns, the qubit excitation is transferred to B. (*right*) principle of an adiabatic SWAP (aSWAP). The qubit is excited in $|e\rangle$, after what ω_B is ramped through ω_Q in a time τ, and the state of Q is finally read-out. For long enough ramp durations (for this sequence $\tau > 300$ ns), the qubit excited state population is fully transferred into the bus

Fig. 4.29 The aSWAP

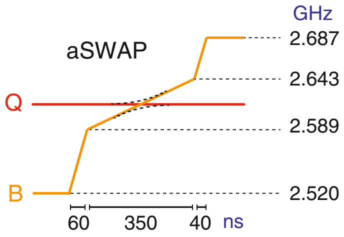

To circumvent this problem, we resort instead to adiabatic SWAP operations (aSWAP) in which ω_B is adiabatically ramped through ω_Q resonance so that state $|e, 0_B\rangle$ is adiabatically converted into $|g, 1_B\rangle$, yielding the same operation as the resonant SWAP (on the right). Finding good parameters for the pulse requires some optimization since a too fast pulse would not be adiabatic, while a too slow pulse would strongly reduce the signal because of energy relaxation either in the qubit or in the bus. The final parameters that we used are ω_B starts at 2.52 GHz, is first ramped up to 2.589 GHz in 60 ns, then to 2.643 GHz in 350 ns, then to 2.687 GHz in 40 ns, as shown in Fig. 4.29.

4.3.3 Coupling the NV Spin Ensemble to the Bus Resonator

The strong coupling between the bus resonator and the spin ensemble is evidenced spectroscopically. A magnetic field $B_{NV} = 1.4\,\text{mT}$ is applied to lift the degeneracy of the spin group *I* and *III*, resulting in four different ESR frequencies $\omega_{I\pm,III\pm}$ as explained in Sect. 4.2.1.3. Throughout the experiments reported in the rest of this chapter, we keep this magnetic field B_{NV} unchanged. We measure the microwave transmission $S_{21}(\omega)$ of the bus B, while scanning its frequency ω_B over the four ESR frequencies. The microwave power used corresponds to a maximum intracavity energy of ~100 photons at resonance, a value low enough to maintain the spin polarization at thermal equilibrium. The two-dimensional plot of the transmission spectrum as a function of the magnetic flux Φ through the SQUID embedded in B is shown in Fig. 4.30. We observe four anticrossings in the spectrum when ω_B matches the spin resonance frequency at $\omega_{+I}/2\pi = 2.91$ GHz, $\omega_{-I}/2\pi = 2.84$ GHz, $\omega_{+III}/2\pi = 2.89$ GHz, and $\omega_{-III}/2\pi = 2.865$ GHz. The anticrossings correspond to the vacuum Rabi

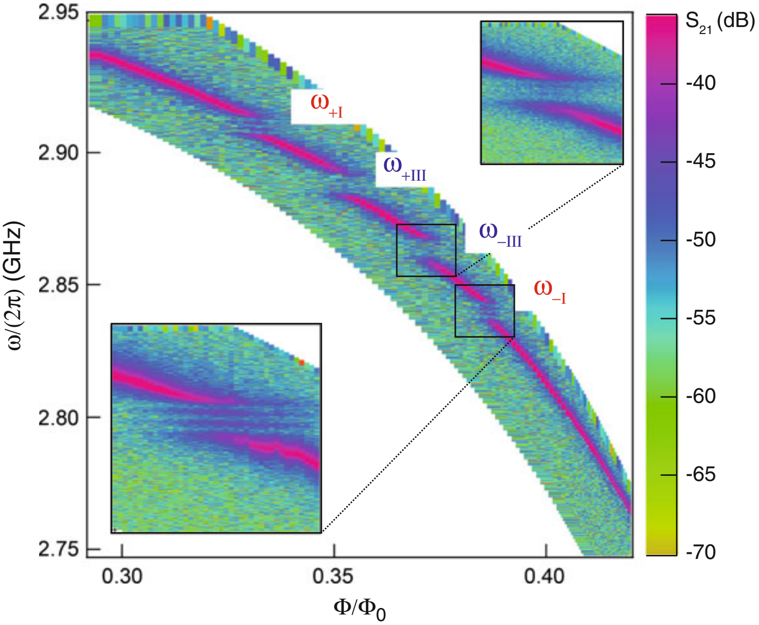

Fig. 4.30 Spectroscopic evidence of strong coupling between the bus resonator and the spins. Two-dimensional plot of the transmission $|S_{21}|(\omega, \Phi)$ through B in dB units, with Φ expressed in units of the superconducting flux quantum $\Phi_0 = h/2e$, at $B_{NV} = 1.4\,\text{mT}$. The resonator transmission spectrum S_{21} shows four anticrossing when the bus resonator frequency crosses the NV transitions $|0\rangle \rightarrow |+\rangle$ and $|0\rangle \rightarrow |-\rangle$ of the two spin groups. The *insets* are zooms on the anticrossing at $\omega_{-,I}$ and $\omega_{-,III}$ showing the hyperfine structure due to the interaction with the spin-one nitrogen nuclei

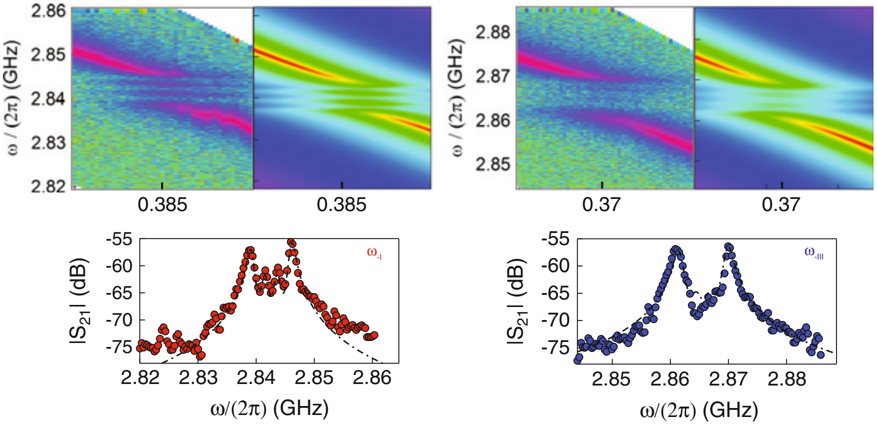

Fig. 4.31 Comparison to the model. (*top*) Measured and computed spectrum around the $|0\rangle \rightarrow |-\rangle$ transition of the spin group *I* (*left*) and *III* (*right*). Color scale goes from −70 to −40 dB. (*bottom*) Measured (*dots*) and computed (*line*) transmission spectrum close to the middle of the anticrossing with the $|0\rangle \rightarrow |-\rangle$ transition of the spin group *I* (*left*) and *III* (*right*). The asymmetries that results from a slight detuning between the spin central frequency and the resonator is well explained by the model

splittings, a signature of strong coupling between the spins and the bus resonator. The triplet shape characteristic of the NV hyperfine structure (see Sect. 2.2.2) is visible in the insets.

The transmission spectrum can be understood using the model described in Sect. 2.3.3. We use a three Lorentzian distribution (Eq. 2.118) and compute the transmission coefficient (Eq. 2.110) with the parameters $\omega_B(\Phi)$ and κ of our experiments. For the coupling strength g_{ens} and spin linewidth w entering in the model, we use parameters determined later in this chapter using the time-domain results shown in Fig. 4.33 which yield $g_{ens,\pm I}/2\pi = 2.9$ MHz, $g_{ens,\pm III}/2\pi = 3.8$ MHz, $w_I/2\pi = 1.6$ MHz and $w_{III}/2\pi = 2.4$ MHz. As seen in Fig. 4.31, the agreement is excellent. The hyperfine structure is nearly washed out for group *III*, not due to a larger linewidth but due to a larger g_{ens} as explained in Sect. 2.3.3.3.

Note that we use a different spin linewidth for the two spin groups. We attribute the larger linewidth of the spins from group *III* to a residual misalignment of B_{NV} with respect to the [1, 1, 1] axis of the crystal which causes each of the three $< 1, 1, 1 >$ axes non-collinear with the field to undergo slightly different Zeeman shifts.[3] Note also that the 1.6 MHz linewidth of the spins from group *I* is twice larger than measured optically, possibly due to the spatial inhomogeneity of the initial nitrogen concentration in the sample. Concerning the coupling strengths, the ratio $g^2_{ens,III}/(3g^2_{ens,I}) = 0.58$ is in good agreement with the expected group ratio $\alpha_{III}/\alpha_I = 0.57$ (see Sect. 4.2.1.2). Note however that these coupling strengths are reduced by a factor 1.5 with respect to the values we have predicted in Sect. 4.2.1.3.

---

[3] A misalignment of 1° would be enough to cause a broadening such as we observe.

We attribute this reduction to a gap between the diamond and the circuit induced by the glue we used to attached the diamond on top of the resonator,[4] or to a reduction of the NV density close to the diamond surface due to polishing damage. Despite this, the coupling strengths still satisfy $g_{ens,I} > \kappa, \Gamma_I$ and $g_{ens,III} > \kappa, \Gamma_{III}$, barely bringing the experiment in the strong coupling regime.

4.4 Storage of Qubit States into a NV Spin Ensemble

We now test the *write step* of the memory protocol. The goal of this experiment is to demonstrate that qubit states can be stored into the spin ensemble. This implies that (i) a single photon can be exchanged between the qubit and the spin ensemble and (ii) the quantum state carried by the photon is not altered during the storage process. We describe in the following the corresponding experiments.

4.4.1 Storing a Single Photon from the Qubit into the Spin Ensemble

In this section, a single microwave photon is exchanged coherently between the qubit, the bus resonator and the spin ensemble.

4.4.1.1 Protocol for Storage of $|e\rangle$ into the Spins Memory

The qubit is prepared in $|\psi\rangle = |e\rangle$ to be stored into the spin ensemble memory. The protocol is sketched in Fig. 4.32:

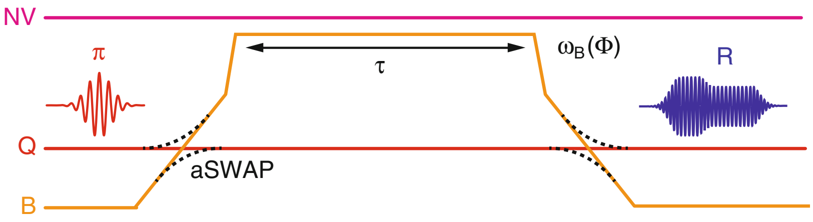

Fig. 4.32 Protocol for storage of a single quantum of excitation from the qubit to the spin ensemble. The sequence shows the microwave pulses used for exciting the qubit in $|e\rangle$ (*red*) and for reading it out (*blue*), as well as transition frequencies of the quantum bus (*orange*), qubit (*red*), and spins (*magenta*)

---

[4] Numerical simulations show that a 1 µm gap reduces the coupling strength by 1.2.

1. Preparation of the qubit in $|e\rangle$
2. Application of a aSWAP to convert $|e\rangle$ into the bus Fock state $|1_B\rangle$
3. The bus resonator B is brought in or near resonance with the spin ensemble for an interaction time τ
4. Retrieval of the state from the resonator to the qubit by another aSWAP
5. Readout of the final qubit state

Each of these steps is achieved using the methods and parameters described in the previous section, at $B_{NV} = 1.4\,\mathrm{mT}$ yielding four different ESR frequencies $\omega_{\pm,I}/\omega_{\pm,III}$ (see Fig. 4.31) with corresponding independent collective spin modes. The sequence is repeated 10^4 times for each value of τ to obtain the qubit excited probability $P_e(\tau)$ which indicates the remaining photon population in the bus after its interaction with the spins and hence the efficiency of the quantum state transfer between the bus and the spins.

4.4.1.2 Experimental Results and Analysis

The results of the measurements are summarized in Fig. 4.33. The left panel shows $P_e(\tau)$ when the bus resonator is tuned into resonance with either ω_{-I} or ω_{-III} ESR frequency.

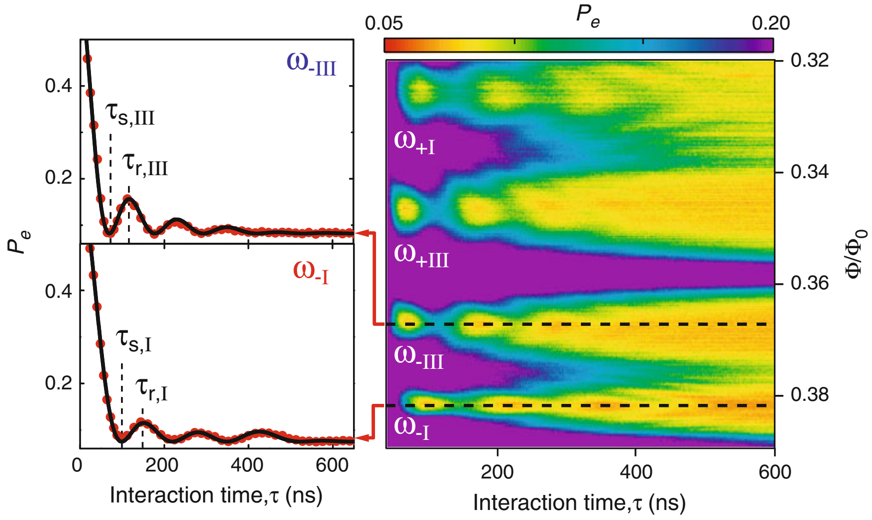

Fig. 4.33 **Storage of a single quantum of excitation from the qubit to the spin ensemble.** (*left*) Experimental (*dots*) and theoretical (*dash-dotted line*) probability $P_e(\tau)$ for ω_B tuned to ω_{-III} (*top graph*) or ω_{-I} (*bottom graph*), showing the vacuum Rabi oscillation between the bus resonator and the spin ensemble. (*right*) Two-dimensional plot of P_e versus interaction time τ and flux pulse height Φ, showing resonance with the four spin groups. Chevron-like patterns are observed, showing a faster oscillation with reduced amplitude when ω_B is detuned from the spin resonance, as expected. Note that the difference between the ω_- and ω_+ patterns in the same NV group is simply caused by the non-linear dependence of ω_B on Φ [10]

We first note that $P_e(0) = 0.6$ instead of its maximum possible value 0.92 (see Sect. 4.3.1.1), due to energy relaxation (with time constant $T_1^B = 1/\kappa = 3.3\,\mu\text{s}$) in the bus resonator during the aSWAP steps. This effect simply reduces the overall contrast of our data and does not affect the following conclusions on the spin-resonator interaction. At finite τ, P_e shows damped oscillations, that reveal the exchange of a single quantum of excitation between the quantum bus and the spin ensemble. At $\tau_{s,III} = 65\,\text{ns}$ (respectively $\tau_{s,I} = 97\,\text{ns}$), the single photon is fully transferred into the collective spin variable coupled to B and at $\tau_{r,III} = 116\,\text{ns}$ ($\tau_{r,I} = 146\,\text{ns}$), it is partially retrieved back into the bus resonator. As already explained in Sect. 2.3.3.3, the damping of the oscillations is due to the inhomogeneous broadening of the spins, which causes a leak of energy with rate $w_{I,III}$ from the bright mode (coupled to the resonator) into the spin dark modes. At long times, the curve converges towards $P_e = 0.08$, similar to the equilibrium qubit excited state population as explained above. We conclude that the spin bright mode is at the same effective temperature as the qubit, that is 50 mK, with a 92 % probability to be found in its collective ground state, as requested to be in the quantum regime.

The measurements in Fig. 4.33 are accurately reproduced (dash-dotted line) by a calculation of the spin-resonator dynamics performed by I. Diniz at Institut Néel which treats the spins in the Holstein-Primakoff approximation with a static inhomogeneous distribution, as described in Sect. 2.3.3. We take into account the NV center hyperfine structure by considering a spin distribution consisting of 3 Lorentzian peaks separated by 2.3 MHz,[5] with the linewidth of each hyperfine peak and the ensemble coupling constant as the only adjustable parameters, yielding $w_I/2\pi = 1.6\,\text{MHz}$ and $g_{ens,I}/2\pi = 2.9\,\text{MHz}$, and $w_{III}/2\pi = 2.4\,\text{MHz}$ and $g_{ens,III}/2\pi = 3.8\,\text{MHz}$. These linewidths indicate a free-induction decay time $T_2^* = 2/w \approx 200\,\text{ns}$ for group *I* and 140 ns for group *III*. Note that the hyperfine structure is responsible for the non-exponential damping of $P_e(\tau)$, and even leads to revivals in the curve taken at $\omega_B = \omega_{-I}$. By varying the bus resonator frequency during the interaction with the spins, it is possible to map the 4 spin resonances as shown in the right panel. Chevron patterns are observed as expected for a SWAP interaction.

Storage efficiency We discuss the significance of these measurements in light of the quantum memory protocol described in Chap. 3. At first sight, one could conclude that the transfer efficiency of the qubit excitation into the spin memory is rather low, since we find $P_e(\tau_r)$ to be much lower to $P_e(0)$. This would be the case if the goal of the experiment was to use the bright mode as storage medium for the quantum state. But as explained in Chap. 3, we in fact consider the leakage of the quantum state from the bright mode into the bath of dark modes as being a part of the whole memory protocol, instead of being a detrimental effect, since our goal is precisely to later retrieve this quantum information into the bright mode using refocusing pulses.

---

[5] The splitting of 2.3 MHz between the three peaks of the hyperfine structure is slightly larger than the value reported in most articles which is 2.17 MHz. Our data are however not precise enough to determine precisely whether this difference actually reflects a change in the hyperfine interaction parameters of the NV center at low temperature.

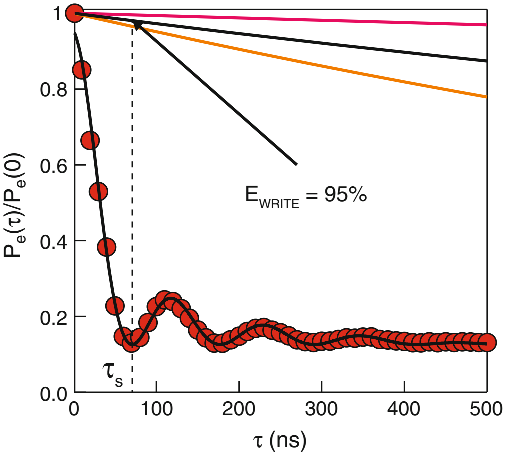

Fig. 4.34 The storage efficiency. The energy relaxation in the resonator (*orange*) and in the spins (*pink*) are superimposed on the curve $P_e(\tau)/P_e(0)$ when the bus resonator is tuned on resonance with ω_{-III}. The efficiency of the storage process is extracted from the average of the two decays (*black*) as the value at full storage τ_s over the value at $\tau = 0$, yielding 95 %

In that perspective, the only loss of quantum information in the process shown in Fig. 4.34 actually comes from energy damping in the resonator (with a time constant $T_1^B = 3.3\,\mu\text{s}$), and from non-static spin dephasing (with time constant $T_2 = 7.3\,\mu\text{s}$). An estimate of the fidelity of this process is thus given by[6] $\exp(-\tau_s/(2T_1^B))\exp(-\tau_s/(2T_2)) \approx 95\,\%$, which is sufficiently high for a quantum memory and could be optimized with improved parameters. Note that despite a single photon can be fully transferred from the bus resonator into the spins in a time τ_s of the order or shorter than T_2^*, the spin ensemble memory would not be immediately ready to accept a new quantum state. Indeed it still takes a time of order $2-3 \times T_2^*$ for the bright mode to be damped into the dark modes, after which a new incoming quantum state could indeed be stored, as shown by the fact that $P_e(\tau)$ is back to its equilibrium value for $\tau > 3T_2^*$ in Fig. 4.33.

4.4.1.3 SWAP Versus aSWAP B-Q Pulses

In the previous measurement, we use an aSWAP for both Q to B, and B to Q transfer to limit the effect of flux noise on the resonator frequency. The aSWAP is however longer than the SWAP, which induces larger losses during the transfer. We estimate that the long B-Q aSWAP (2×450 ns) accounts for 72 % of the energy loss that involves $P_e(0) = 0.6$. The fact that we use an adiabatic passage here thus reduces the overall energy we exchange with the spin ensemble. To determine if we can instead use a SWAP between Q and B, we compare in Fig. 4.35 the very same experiment with same degree of averaging for a SWAP B-Q transfer. In the non-adiabatic case, we observe very fast oscillations around 250 MHz, almost corresponding to the

---

[6] The factor 1/2 accounts for the fact that the excitation is shared between the bus and the spin ensemble during the time needed for the swap operation.

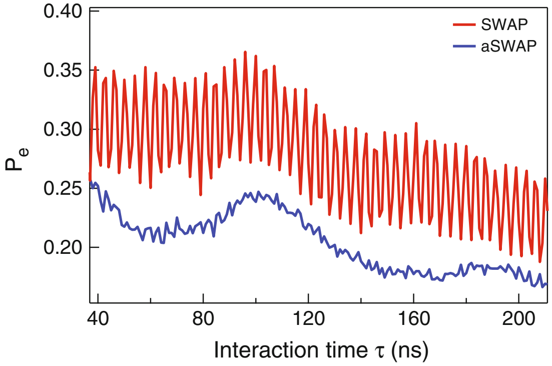

Fig. 4.35 Comparison between storage using SWAP and aSWAP B-Q transfer. The probability $P_e(\tau)$ is shown for ω_B tuned to ω_{-III}

frequency difference between the resonator at this step of the protocol and the qubit frequency. These oscillations are attributed to an imperfect SWAP between Q and the B. Since $\omega_B(\Phi_Q) = \omega_Q$ is obtained at a flux Φ_Q close to $\Phi_0/2$, the flux noise on the SQUID is large, yielding a bad resonance of the bus resonator with the qubit during the SWAP operation. As a result, an entanglement between the qubit and the bus resonator is created, and phase coherence appears between the two systems. This phase rotates at the frequency $\Delta_{BQ} = \omega_B - \omega_Q$, the frequency difference between the resonator and the qubit: the second SWAP (from B to Q) interferes with the first SWAP (from B to Q) inducing the oscillations which appear in $P_e(\tau)$. It is thus not possible to use a SWAP for transfer between B and Q in this experiment.

4.4.2 Storing a Coherent Superposition from the Qubit to the Spin Ensemble

We have stored a qubit prepared in the excited state $|e\rangle$ in the spin ensemble. But this does not prove that superpositions of the qubit states with a well-defined phase can be stored into the spin ensemble and recovered. To determine if the phase information is preserved, we follow a superposition state along its storage in the spin ensemble and reconstruct its matrix density (state tomography) at each iteration step.

4.4.2.1 Protocol for Storage of $|g\rangle + |e\rangle$ into the Memory

The qubit is prepared in a coherent superposition $|g\rangle + |e\rangle$ to be stored into the spin ensemble memory. The protocol is sketched in Fig. 4.36:

1. Preparation of the qubit in $|g\rangle + |e\rangle$
2. Application of a aSWAP to convert $|g\rangle + |e\rangle$ into the bus state $|0_B\rangle + |1_B\rangle$
3. The bus resonator B is brought in or near resonance with the spin ensemble for an interaction time τ

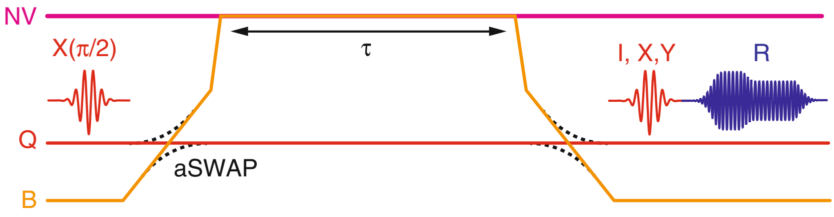

Fig. 4.36 Protocol for storage a coherent superposition of states from the qubit to the spin ensemble. The sequence shows the microwave pulses used for exciting the qubit in $\frac{1}{\sqrt{2}}(|g\rangle + |e\rangle)$ (*red*) and for reading it out (*blue*), as well as transition frequencies of the quantum bus (*orange*), qubit (*red*), and spins (*magenta*). Quantum state tomography is performed to determine the qubit state by applying either I, X, or $-Y$ operation to the qubit before reading out the Z component

4. Retrieval of the state from the spin ensemble to the qubit through the bus resonator
5. Measurement of the qubit density matrix ρ_{ge} by quantum state tomography

This experiment is performed in the same experimental conditions as in Sect. 4.4.1.1, except that at the end of the sequence we perform a full qubit quantum state tomography to analyze the phase coherence of the retrieved state.

4.4.2.2 Experimental Results and Analysis

For this experiment, we focus on $|m_S = -1\rangle$ of spin group I. The sequence in Fig. 4.36 is repeated three times to determine the three components of the Bloch vector of the qubit after an interaction time τ. First, after no operation on the qubit to obtain the z-component; second, after a rotation of the qubit around X that projects the Bloch vector of the qubit along the Bloch sphere z-axis to obtain its y-component; finally, after a rotation of the qubit around $-Y$ to obtain the x-component. After substracting a trivial rotation around $\mathbf{z}$ occurring at frequency $\left(\omega_{-I} - \omega_Q\right)$, we reconstruct the trajectory of the Bloch vector as a function of the interaction time τ.

Figure 4.37 shows the resulting measurement of $\langle\sigma_X(\tau)\rangle$, $\langle\sigma_Y(\tau)\rangle$ and $\langle\sigma_Z(\tau)\rangle$, the projection of the Bloch vector on **x**, **y** and **z** axis, when the bus is brought in resonance with ω_{-I}. The off-diagonal element ρ_{ge} of the final qubit density matrix is plotted in the bottom panel of Fig. 4.37. This is the element which quantifies its coherence. We find that no population is left in the qubit at the end of the sequence for $\tau = \tau_{s,I}$, as expected for a full storage of the initial state into the ensemble. Then, coherence is retrieved at $\tau = \tau_{r,I}$, although with an amplitude ~5 times smaller than its value at $\tau = 0$ (i.e. without interaction with the spins). Note the π phase shift occurring after each storage-retrieval cycle, characteristic of 2π rotations in the two-level space $\{|1_B, 0_{-I}\rangle, |0_B, 1_{-I}\rangle\}$.

We have demonstrated here that the storage preserves the phase coherence, which confirms that arbitrary quantum state $|\psi\rangle$ can be successfully stored into the spin ensemble memory.

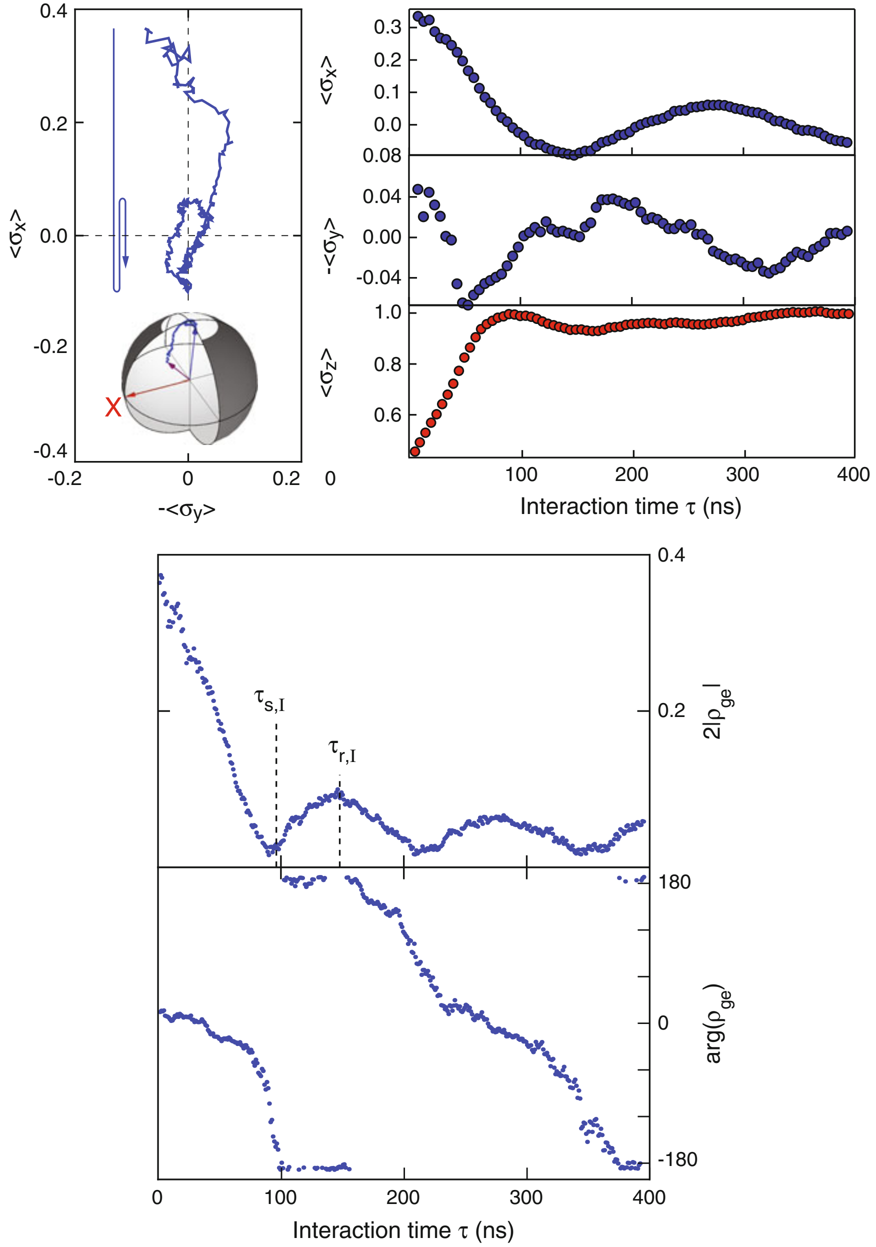

Fig. 4.37 **Storage of a coherent superposition of states from the qubit to the spin ensemble.** (*top left*) Trajectory of the qubit Bloch vector on the Bloch sphere, and its projection on the equatorial plane. (*top right*) Components of the Bloch vector $\langle\sigma_x\rangle$, $\langle\sigma_y\rangle$ and $\langle\sigma_z\rangle$. (*bottom*) Modulus and phase of the off-diagonal element ρ_{ge} of the qubit density matrix as a function of interaction time τ

4.4.3 Entanglement Between the Spin Ensemble and the Resonator

In the course of the interaction between the spin ensemble and the bus resonator, the two systems become entangled. In this section we show how to probe this entanglement.

4.4.3.1 Protocol for Probing the Entanglement

The resonator B is prepared in $|1_B\rangle$ via the qubit and entangled with the spin ensemble. The protocol is illustrated in Fig. 4.38:

1. Preparation of the qubit in $|e\rangle$
2. Application of aSWAP to convert $|e\rangle$ into the bus Fock state $|1_B\rangle$
3. Creation of B-NV entanglement by placing the bus resonator in resonance with the spin ensemble for a duration $\tau_{\pi/2} = \tau_s/2$ (thereafter called a B-NV halfswap)
4. The bus resonator B is detuned from the spin ensemble by ω_D for a duration τ during which the spins evolve freely

At this point, the joint bus-spin ensemble state is an entangled state $\left(|1_B, 0_s\rangle + e^{i\varphi}|0_B, 1_s\rangle\right)/\sqrt{2}$ with a phase $\varphi = \delta\omega\tau$.

5. Conversion of the phase φ into population $|1_B, 0_s\rangle$ by a second B-NV halfswap
6. Readout of the qubit to obtain P_e

This experiment is performed in the same experimental conditions as in Sect. 4.4.1.1. By repeating the sequence with increasing duration τ, we obtain information on the free evolution of the spin ensemble.

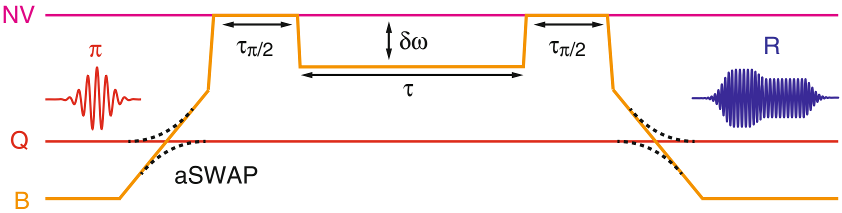

Fig. 4.38 Protocol for Ramsey-like experiment on the spin ensemble at the single-photon level. The sequence shows the microwave pulses used for exciting the qubit in $|e\rangle$ (*red*) and for reading it out (*blue*), as well as transition frequencies of the quantum bus (*orange*), qubit (*red*), and spins (*magenta*). B is then detuned from the spins by $\delta\omega/2\pi = 38$ MHz during a time τ

4.4.3.2 Experimental Results and Analysis

For this experiment, we focus on $|m_S = -1\rangle$ of spin group *I*. The resulting $P_e(\tau)$ for $\delta\omega = 38\,\text{MHz}$ is shown in Fig. 4.39. Oscillations at frequency $\delta\omega$ are visible which confirms that the resonator and the spins are entangled after the first halfswap pulse. We see however that these oscillations are modulated by a beating pattern. We applied a Fourier transform to the signal (see inset Fig. 4.39) and found that the signal is actually composed of three frequencies separated by $3 \pm 1\,\text{MHz}$. Note that the resolution in frequency is limited here by the 1 ns resolution of the flux pulse waveform generator. This beating observed in the qubit excited state probability is directly caused by the hyperfine structure of NV centers, the Fourier transform showing the three hyperfine lines. The envelope of the oscillations decays with characteristic time $T_2^* \sim 200\,\text{ns}$, the spin free induction decay time. This experimental sequence is simulated in a similar way as the single photon experiment (see [12] for more details), using the same parameters. As seen in Fig. 4.39, the simulation captures quantitatively both the beatings and the oscillations damping.

This experiment demonstrates that the fine structure of a microscopic system can be probed at the single photon level with a superconducting qubit.

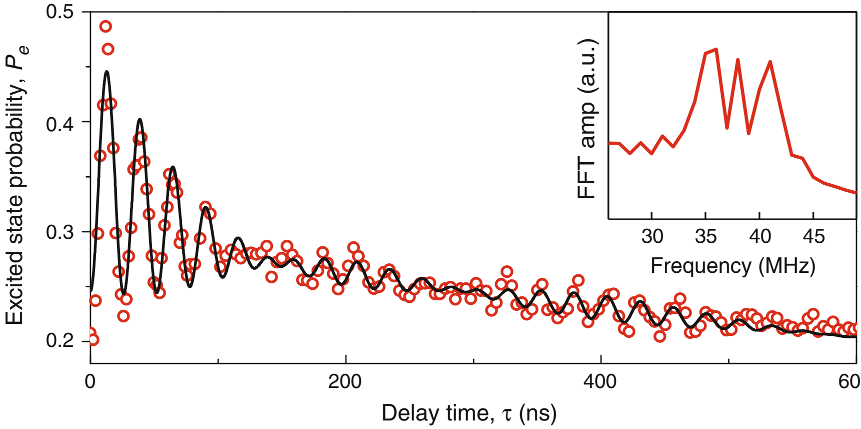

Fig. 4.39 Ramsey-like experiment on the spin ensemble at the single-photon level. Measured (*red circles*) and calculated (*black line*) probability $P_e(\tau)$, as well as its Fourier transform (*inset*) revealing the NV centers hyperfine structure

4.5 Conclusions on Experiment 1: The Write Step

The combination of results of Sects. 4.4.1 and 4.4.2 demonstrates that arbitrary quantum states $|\psi\rangle$ can be exchanged between the qubit and the spin ensemble, with preserved phase coherence. The storage, as described in Chap. 3, takes place within a characteristic time $T_2^* \sim 200\,\text{ns}$, the time needed for the quantum state transferred from the qubit to the collective variable coupled to B to be transferred into the bath of dark modes, in which coherence can be stored. The experimental results are explained quantitatively, with common parameters used for the modeling of the different experiments. Considering the inhomogeneous broadening as being part of the protocol, we estimate that the overall fidelity of the *write step* $E_{WRITE} \sim 95\,\%$, a value compatible with quantum memory operation. The fidelity here, is limited by the damping in the resonator during the transfer to the spin ensemble. It can be further improved by increasing the rate at which the transfer occurs, that is by increasing the coupling strength between the spins and the bus resonator. Before ending this chapter, we note that a similar experiment was performed at the same time as the one reported here, demonstrating the coherent exchange of a single quantum of excitation between a flux qubit and an ensemble of NV center spins in diamond [13]. In this work done at NTT, the flux qubit was directly coupled to an ensemble of $3.3 \cdot 10^7$ NV center spins, and vacuum Rabi oscillations observed between the qubit and the spin ensemble (see Fig. 4.40). In a later experiment performed in the same configuration [14], the same

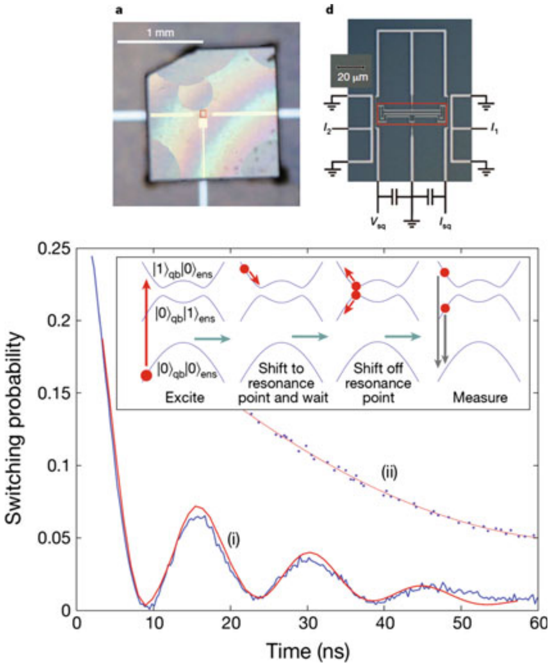

Fig. 4.40 Coherent coupling of a superconducting flux qubit to an electron spin ensemble in diamond [13]. (*top*) Experimental set-up of the NV diamond sample attached to a flux qubit system. (*bottom*) Vacuum Rabi oscillations of the flux qubit/NV$^-$ ensemble coupled system

group proceeded to the storage of arbitrary quantum states prepared by the flux qubit in the spin ensemble and probed the entanglement between the qubit and the spin ensemble, similar to our results reported in Sects. 4.4.2 and 4.4.3.

References

1. Y. Kubo, F.R. Ong, P. Bertet, D. Vion, V. Jacques, D. Zheng, A. Dreau, J.F. Roch, A. Auffeves, F. Jelezko, J. Wrachtrup, M.F. Barthe, P. Bergonzo, D. Esteve, Strong coupling of a spin ensemble to a superconducting resonator. Phys. Rev. Lett. **105**, 140502 (2010)
2. D.I. Schuster, A.P. Sears, E. Ginossar, L. DiCarlo, L. Frunzio, J.J.L. Morton, H. Wu, G.A.D. Briggs, B.B. Buckley, D.D. Awschalom, R.J. Schoelkopf, High-cooperativity coupling of electron-spin ensembles to superconducting cavities. Phys. Rev. Lett. **105**, 140501 (2010)
3. R. Amsüss, Ch. Koller, T. Nöbauer, S. Putz, S. Rotter, K. Sandner, S. Schneider, M. Schramböck, G. Steinhauser, H. Ritsch, J. Schmiedmayer, J. Majer, Cavity QED with magnetically coupled collective spin states. Phys. Rev. Lett. **107**, 060502 (2011)
4. V. Ranjan, G. de Lange, R. Schutjens, T. Debelhoir, J.P. Groen, D. Szombati, D.J. Thoen, T.M. Klapwijk, R. Hanson, L. DiCarlo, Probing dynamics of an electron-spin ensemble via a superconducting resonator. Phys. Rev. Lett. **110**, 067004 (2013)
5. P. Bushev, A.K. Feofanov, H. Rotzinger, I. Protopopov, J.H. Cole, C.M. Wilson, G. Fischer, A. Lukashenko, A.V. Ustinov, Ultralow-power spectroscopy of a rare-earth spin ensemble using a superconducting resonator. Phys. Rev. B **84**, 06050 (2011)
6. S. Probst, H. Rotzinger, S. Wünsch, P. Jung, M. Jerger, M. Siegel, A.V. Ustinov, P.A. Bushev, Anisotropic rare-earth spin ensemble strongly coupled to a superconducting resonator. Phys. Rev. Lett. **110**, 157001 (2013)
7. A. Gruber, A. Dräbenstedt, C. Tietz, L. Fleury, J. Wrachtrup, C. Von Borczyskowski, Scanning confocal optical microscopy and magnetic resonance on single defect centers. Science **276**(5321), 2012–2014 (1997)
8. E. Lucero, M. Hofheinz, M. Ansmann, R.C. Bialczak, N. Katz, M. Neeley, A.D. O'Connell, H. Wang, A.N. Cleland, J. M. Martinis, High-fidelity gates in a single josephson qubit. Phys. Rev. Lett. **100**, 247001 (2008)
9. F. Mallet, F.R. Ong, A. Palacios-Laloy, F. Nguyen, P. Bertet, D. Vion, D. Esteve, Single-shot qubit readout in circuit quantum electrodynamics. Nat. Phys. **5**, 791 (2009)
10. A. Palacios-Laloy, F. Nguyen, F. Mallet, P. Bertet, D. Vion, D. Esteve, Tunable resonators for quantum circuits. J. Low Temp. Phys. **151**, 1034 (2008)
11. M. Sandberg, C.M. Wilson, F. Persson, T. Bauch, G. Johansson, V. Shumeiko, T. Duty, P. Delsing, Tuning the field in a microwave resonator faster than the photon lifetime. Appl. Phys. Lett. **92**(20), 203501–203503 (2008)
12. Y. Kubo, C. Grezes, A. Dewes, T. Umeda, J. Isoya, H. Sumiya, N. Morishita, H. Abe, S. Onoda, T. Ohshima, V. Jacques, A. Dréau, J.-F. Roch, I. Diniz, A. Auffeves, D. Vion, D. Esteve, P. Bertet, Hybrid quantum circuit with a superconducting qubit coupled to a spin ensemble. Phys. Rev. Lett. **107**, 220501 (2011)
13. X. Zhu, S. Saito, A. Kemp, K. Kakuyanagi, S. Karimoto, H. Nakano, W.J. Munro, Y. Tokura, M.S. Everitt, K. Nemoto, M. Kasu, N. Mizuochi, K. Semba, Coherent coupling of a superconducting flux qubit to an electron spin ensemble in diamond. Nature **478**(7368), 221–224 (2011)
14. S. Saito, X. Zhu, R. Amsüss, Y. Matsuzaki, K. Kakuyanagi, T. Shimo-Oka, N. Mizuochi, K. Nemoto, W.J. Munro, K. Semba, Towards realizing a quantum memory for a superconducting qubit: Storage and retrieval of quantum states. Phys. Rev. Lett. **111**, 107008 (2013)

Chapter 5
Experiment 2 (Read): Multimode Retrieval of Few Photon Fields from a Spin Ensemble

This chapter is dedicated to the presentation of the second experiment, where we made progress on the implementation of the read step of our memory protocol. Multiple few-photons microwave pulses initially stored in the spin ensemble are retrieved by applying refocusing techniques. An active reset of the spins by optical repumping is also implemented.

5.1 Principle of the Experiment

The *read step* of the memory protocol described in Chap. 3 consists in retrieving quantum states initially stored into a spin ensemble. The retrieval is triggered by a refocusing sequence which combines the application of microwave pulses with dynamical tuning of the resonator frequency and quality factor. The *read* experiment aims to demonstrate an important building block of this operation: the two-pulse Hahn echo described in Sect. 3.2.2.1, which consists in retrieving multiple stored microwave fields with a single refocusing pulse. As a first step, we use classical microwave pulses and only focus on the mean value of the field, bearing in mind that as explained in Chap. 3 it is not possible to retrieve the full quantum statistics of an incoming coherent state with a single refocusing pulse. The protocol and physical setup are depicted in Fig. 5.1. They are articulated around two components: an ensemble of NV center spins and a superconducting resonator. The few photon microwave pulses are sent via the resonator to which the spins are coupled. The protocol requires that the resonator and the spin ensemble are in the low-cooperativity regime to ensure the stability of the inverted ensemble in the cavity after refocusing, as explained in Sect. 3.1.2.

Designing the corresponding experiment at the quantum level imposes a number of requirements which represent experimental challenges: (i) for quantum states to be well defined, thermal excitations should be absent from the system, implying that both the spin ensemble have a high degree of polarization and the microwave field

© Springer International Publishing Switzerland 2016

C. Grèzes, *Towards a Spin-Ensemble Quantum Memory for Superconducting Qubits*, Springer Theses,
DOI 10.1007/978-3-319-21572-3_5

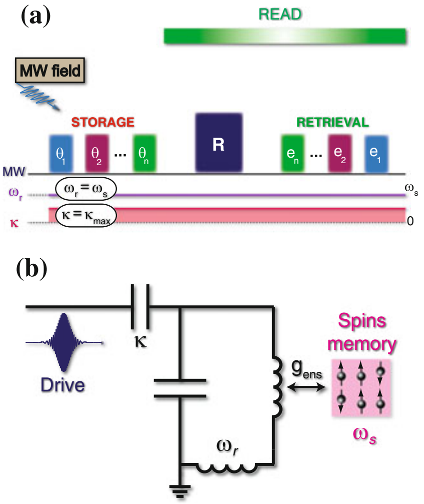

Fig. 5.1 Principle of the experiment. a Successive few-photons microwave pulses θ_i are stored in the spin ensemble. A single refocusing pulse R acts as time-reversal for the spins and triggers the retrieval of the stored pulses as echoes e_i in reverse order. **b** The resonator and the spin ensemble are weakly coupled with coupling strength g_{ens}. Microwave pulses θ_i and R are applied to the spins through the resonator

is in its ground state with high probability, (ii) applying refocusing pulses to the spins requires large microwave powers potentially incompatible with the detection of quantum fields and (iii) the echo emitted by the spins should faithfully restore the initial field in the resonator, which implies that the echo recovery efficiency E, that we define as the ratio of the energy radiated during the echo to the energy of the incoming pulses, should be close to 1. To summarize, reaching the quantum regime requires a mean excitation per mode (both microwave and spin) $n_{MW,sp} \ll 1$, input microwave fields with intra-cavity photon number $\bar{n} \approx 1$, and an echo efficiency E close to 1.

The state of the art in this direction is the experiment performed by Wu et al. [1] with an ensemble of phosphorus donors in silicon at 10 K in the three-dimensional microwave cavity of an electron paramagnetic resonance spectrometer. In this experiment, multiple microwave pulses applied through the cavity are stored in different collective modes of the spin ensemble and retrieved with a single refocusing pulse (see Fig. 5.2), demonstrating the multi-mode character of the two-pulse Hahn echo. This experiment is performed in the classical regime, with [2] $n_{MW,sp} \approx 20$, $\bar{n} \approx 10^{14}$, and an echo recovery efficiency $E \approx 10^{-10}$.

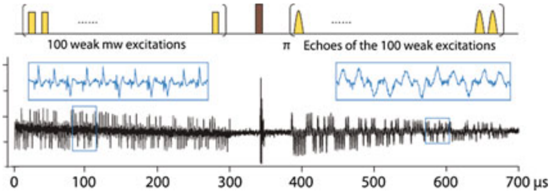

Fig. 5.2 Storage of multiple coherent microwave excitations in an electron spin ensemble [1]. Storage of 100 microwave excitations. After the refocusing pulse the stored excitations are recovered in reverse time order

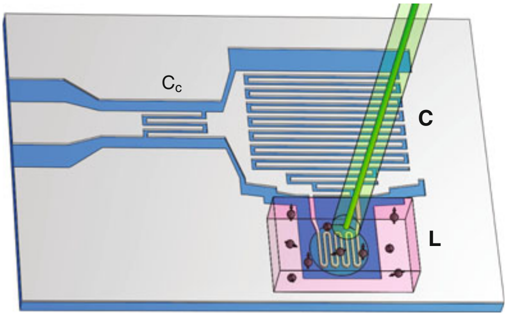

Fig. 5.3 **Designing the read experiment: schematic of the hybrid circuit.** The ensemble of NV center spins (*pink*) is coupled to a planar superconducting lumped element resonator. Laser pulses can be shone on the diamond through an optical fiber glued to its top face

We design the *read* experiment to come closer to the quantum regime. To do so, we operate in a dilution refrigerator at mK temperatures, store and retrieve at the few photon level and optimize the power of the refocusing pulse.

As shown below, spins relax very slowly towards their ground state at mK temperatures and an active spin reset is needed for achieving a reasonable repetition rate (>1 Hz), as requested by experiments at the single photon level. This active reset is implemented using the optical repumping described in Sect. 2.2.2.2. To ensure its compatibility with the operation of the circuit in the dilution refrigerator, the optical power is minimized by concentrating the spin ensemble in a small region. This is achieved by using a lumped element resonator that makes it possible to place the diamond on top of the inductance only, while still ensuring a large filling factor η for coupling. We show in Fig. 5.3 a 3D schematic of the device with relevant components. A fiber in which light can be injected for optical repumping of the spins is included in the setup. We explain in the next section how this hybrid circuit is designed.

5.2 Experimental Realization

5.2.1 The Hybrid Quantum Circuit

5.2.1.1 Diamond Sample Properties

As in the experiment reported in Chap. 4, the diamond sample we use was prepared by our collaborator Pr. Isoya in Tsukuba University. It is a polished [100] plate of dimensions $3 \times 1.5 \times 0.5\,\text{mm}^3$ taken from a synthetic type-Ib diamond crystal containing initially a P1 center concentration of $3.52 \cdot 10^6\,\mu\text{m}^{-3}$ (20 ppm). It was prepared to obtain NV centers as explained in Sect. 4.2.1.1 using two cycles of irradiation and annealing. Compared to the previous sample, the NV concentration

$\rho_{NV} \approx 3.52 \cdot 10^5\,\mu\text{m}^{-3}$ (2 ppm) is slightly lower. This was chosen on purpose in order to minimize optical absorption of the light at 532 nm, which has to go through the whole diamond for reaching the spins at the interface with the superconducting circuit. The concentration of remaining neutral substitutional nitrogen (P1 centers) is predicted accordingly around $2.81 \cdot 10^6\,\mu\text{m}^{-3}$ (16 ppm). We have seen in Sect. 2.2.3 that in such samples with large P1 center concentration, NV centers have a linewidth $w/2\pi \approx 1$ MHz for each peak and an echo coherence time $T_2 \approx 10\mu$s.

5.2.1.2 Superconducting Circuit Design

The experiment needs to be in the low-cooperativity regime to ensure the stability of the spin ensemble after refocusing pulses (see Chap. 2). We have seen in Chap. 3 that a convenient way to satisfy this criterion is to lower the quality factor of the cavity. We target accordingly a resonator with frequency around the zero-field electron spin resonance $\omega_r/2\pi \approx 2.88$ GHz and low quality factor such that the resonator damping rate satisfies:

$$\begin{aligned} C = \frac{g_{ens}^2}{\kappa\Gamma} < 1 \;\Leftrightarrow\; \kappa &> \Gamma^{-1}\left(\frac{g_{NV}\mu_B}{\sqrt{2}}\sqrt{\alpha\eta\mu_0\hbar\omega_s\rho_{NV}}\right)^2, \\ &> 2\pi \cdot 25.5\,\text{MHz}, \end{aligned} \tag{5.1}$$

where we used $\Gamma \approx w$, the diamond sample parameters ρ_{NV} and w of Sect. 5.2.1.1, and ideal filling and angular factors ($\eta = 1/2$ and $\alpha = 1$). Besides the target resonator parameters, the resonator geometry is constrained by the necessity of minimizing the laser power needed to repump the spins. Our resonator is designed purposely to have an inductance area $\approx 100 \times 100\,\mu\text{m}^2$, well separated from the two capacitor electrodes by 500 μm. This configuration makes it possible to place the diamond on top of the inductance only, thus restricting the diamond region to be illuminated for optical repumping while still optimizing the spin filling factor. Note that positioning the diamond far from the resonator capacitance also avoids shifting the resonator frequency due to the diamond dielectric constant. We explain below how the geometry of the resonator is refined to satisfy both the requirement on the resonator microwave parameters and the magnetic field generated for coupling to the spins.

Microwave simulation with Sonnet simulator The resonator geometry is chosen based on the constraint on its inductance area. We design the inductance with a meander shape (3 μm wide lines), determine its value using Sonnet, and design the capacitor accordingly to target resonance frequency $\omega_r/2\pi = 1/\sqrt{LC} = 2.88$ GHz. The resonator with its coupling capacitance is then simulated as a whole and its geometry adjusted iteratively to obtain the desired resonance frequency and quality factor. We show in Fig. 5.4 the final geometry of the chip together with the outcome of the Sonnet simulation. The fit (using Eq. 2.21 in Sect. 2.1.1.2) of the computed phase of the reflection coefficient yields $\omega_r/2\pi = 2.88$ GHz and $Q = 93$. To determine the resonator impedance $Z_r = \sqrt{L/C}$, we compute the current flowing in the inductance

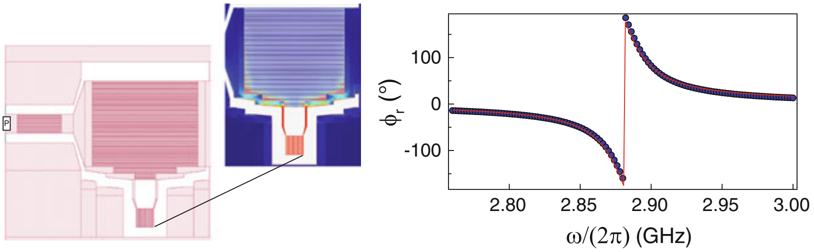

Fig. 5.4 **The resonator: the microwave parameters.** (*Right*) Schematic of the simulated chip geometry, showing the resonator and the coupling capacitance to an input port (P) with impedance 50 Ω. The computed AC current flowing in the inductance is shown in the *inset*. (*Left*) Computed (*dots*) and fitted (*lines*) reflected phase ϕ_r, yielding $\omega_r/2\pi = 2.88$ GHz and $Q = 93$

for a 1V drive microwave at ω_r, yielding $Z_r = \sqrt{L/C} = 26\,\Omega$. This corresponds to a total inductance $L = Z_r/\omega_r = 1.4$ nH which arises from the meander wire connecting the two capacitor electrodes on top of which the diamond is placed, and from the capacitor fingers. Simulations indicate that the meander wire inductance is $L_w = 0.82$ nH (not shown). Since the diamond crystal covers only this wire, the spin filling factor is[1] $\eta \approx (1/2)L_w/L = 0.29$.

Magnetic field computation with COMSOL Multiphysics In this experiment, refocusing pulses are applied via the resonator to perform spin rotation. It is thus important to determine the Rabi frequency $\Omega(\mathbf{r})$ of a spin at position $\mathbf{r}$ for a given applied microwave power P. The magnetic field generated by the resonator above the inductance is computed using the AC/DC module of COMSOL Multiphysics. For the simulation, we neglect the curved section of the meanders inductance and consider only wire sections parallel to the z-axis, an approximation well justified by the aspect ratio of the inductance. The wires are modeled as shown in Fig. 5.5 as $3 \times 0.3\,\mu$m perfect conductors with homogeneous current density. The magnetic field B created by 1 A flowing in the resonator inductance is computed. We observe that the

Fig. 5.5 **The resonator: the AC magnetic field to which the spins are coupled.** Amplitude of the microwave field generated by the resonator above the inductance for a 10 μW incident microwave power at resonance. The field lines are superimposed on the graph

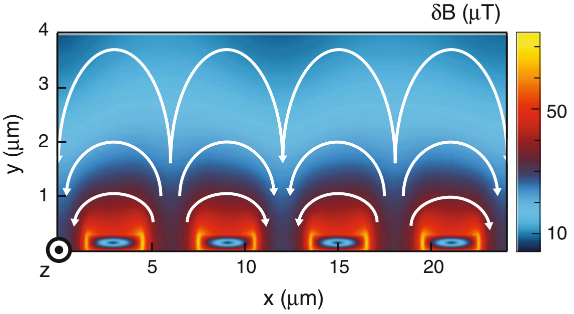

---

[1] Note that we did not consider an eventual gap between the diamond and the circuit for the calculation.

superposition of the field created by the wires yields a strong spatial inhomogeneity both in x and y directions. This makes precise spin rotation difficult to achieve.

5.2.1.3 The Device

The device is shown in Fig. 5.6 with the diamond on top of the superconducting circuit. The resonator is fabricated in Niobium following the process described in Appendix A. The diamond crystal is placed on top of the resonator inductance and oriented such that the applied magnetic field B_{NV} is parallel to the $[1, 1, 0]$ crystalline axis. Half of the electronic spins (sub-ensemble denoted *N-Orth* in blue) thus make an angle $\beta = 35.3°$ with B_{NV}, whereas the other half (sub-ensemble denoted *Orth* in red) are orthogonal to the field. This results in four different ESR frequencies $\omega_{Orth,\pm}(B_{NV})$ and $\omega_{N-Orth,\pm}(B_{NV})$. The NV axis directions $\mathbf{k}$ for the two NV center groups *Orth* and *N-Orth* are:

$$\hat{\hat{k}}_{Orth} = \begin{bmatrix} 0 \\ -\sin(\beta) \\ \pm\cos(\beta) \end{bmatrix}, \quad \hat{\hat{k}}_{N-Orth} = \begin{bmatrix} \pm\cos(\beta) \\ \sin(\beta) \\ 0 \end{bmatrix}. \tag{5.2}$$

The angular factors $\alpha_{Orth} = 0.83$ and $\alpha_{N-Orth} = 0.50$ are calculated (using Eq. 2.100 in Sect. 2.3.2.2) from the magnetic field computed with COMSOL. Using

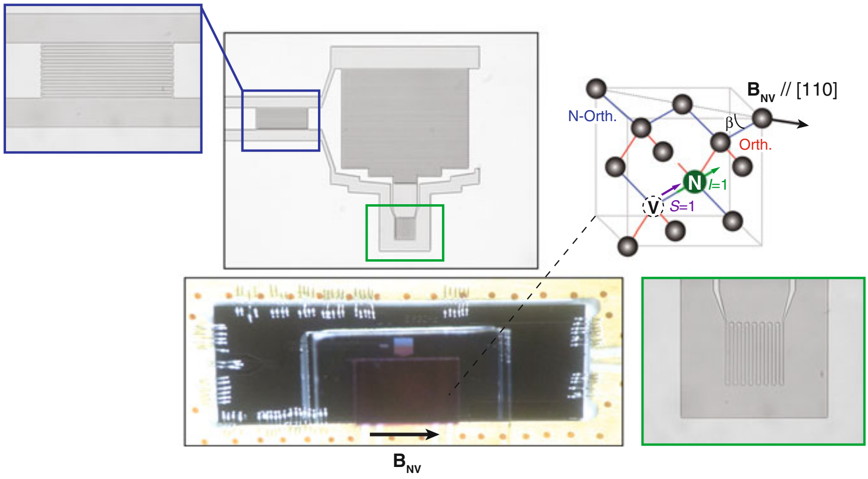

Fig. 5.6 The hybrid circuit for the read experiment. The diamond crystal (*dark pink*) containing the NV center spins is placed on top of the resonator inductance. A spacer (transparent) is glued on the diamond top face, on which the fiber will be attached. A magnetic field B_{NV} is applied parallel to the $[1, 1, 0]$ crystalline axis, resulting in different Zeeman splitting for centers having the NV axis orthogonal to B_{NV} (denoted *Orth*, in *red*) and those making an angle $\beta = 35.3°$ with B_{NV} (denoted *N-Orth*, in *blue*)

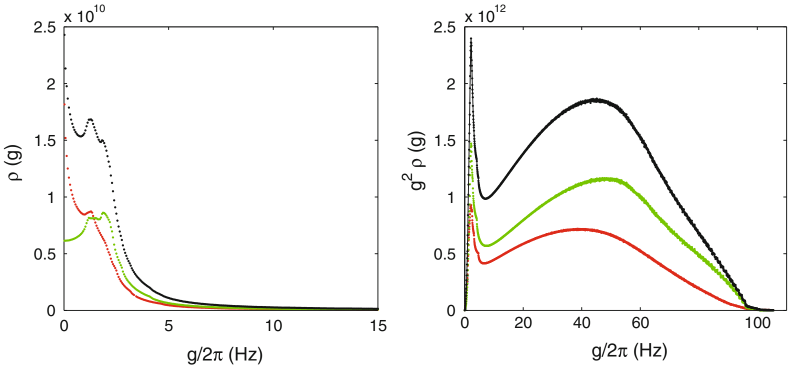

Fig. 5.7 Distribution of g-parameters. The distribution $\rho(g)$ is shown normalized as $\int_0^{+\infty} \rho(g)dg = N$ for the *N-Orth* spin group (*red*), the *Orth* group (*green*) and for all the spins (*black*). A 0.7 µm distance between the resonator and the diamond crystal was considered for this simulation. This sets the maximum frequency cut-off observed in both graphs. (*Left*) The distribution $\rho(g)$ zoomed in on the low frequency part. (*Right*) The function $g^2\rho(g)$ shown on the entire range of frequencies

the NV concentration $\rho_{NV} = 2\,\text{ppm}$ and the filling factor $\eta = 0.29$, we estimate the ensemble coupling constants:

$$g^{th}_{ens,Orth} = 2\pi \times 4.46\,\text{MHz}, \tag{5.3}$$

$$g^{th}_{ens,N-Orth} = 2\pi \times 3.46\,\text{MHz}. \tag{5.4}$$

The total estimated coupling constant is $g^{th}_{ens} = \sqrt{g^2_{ens,Orth} + g^2_{ens,N-Orth}} \approx 2\pi \times 5.64\,\text{MHz}$. We calculate the coupling strength distribution $\rho(g)$ numerically by integrating the magnetic field computed in Sect. 5.2.1.2 with the homogeneous NV concentration estimated in Sect. 5.2.1.1. The resulting distribution $\rho(g) = \int \tilde{g}\delta(\tilde{g} - g)d\tilde{g}$ is shown in Fig. 5.7, where we have assumed a 0.7 µm spacing between the resonator and the diamond crystal to account for the glue between the crystal and the chip. Note that according to its definition, $\int g^2\rho(g)dg = g^2_{ens}$.

5.2.2 Measurement Setup

5.2.2.1 The Experimental Setup

The sample is placed in the same sample holder as in Chap. 4, modified to incorporate the optical fiber, and thermally anchored at 30 mK in the dilution refrigerator. The schematic of the wiring inside the cryostat is shown in Fig. 5.8. Compared to the former experiment in which we operated at the single photon level, we work in this experiment with larger microwave fields and repump optically the spins in the ground

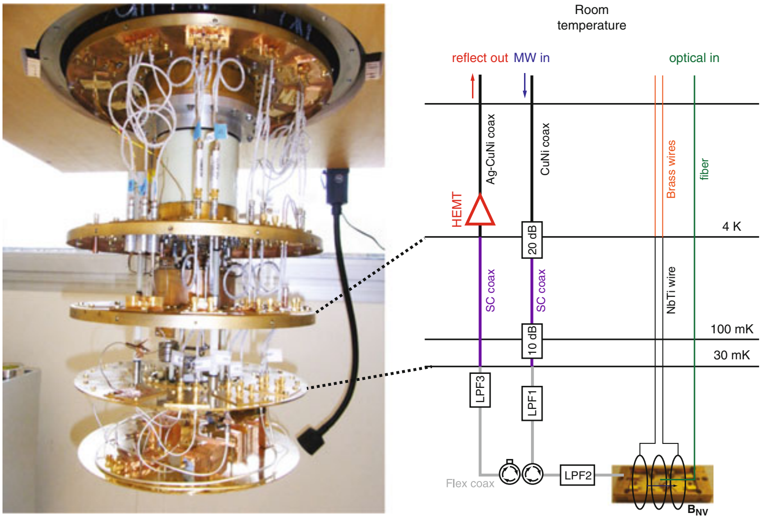

Fig. 5.8 **Scheme of the wiring inside the dilution refrigerator.** LPF1, LPF2 and LPF3 are low-pass filters with cutoff frequencies 5.4, 4.7 and 5.4 GHz, respectively. CuNi coax is a coaxial cable made of CuNi, and Ag-CuNi coax is a silver-plated CuNi coaxial cable. SC coax is a superconducting NbTi coaxial cable. Flex coax is a low-loss flexible coaxial cable. *Rectangles* represent ports terminated by 50 Ω. The cryogenic microwave amplifier is a CITCRYO1-12 from Caltech, with gain ∼38 dB and noise temperature ∼5 K at 3 GHz. A DC magnetic field B_{NV} is applied parallel to the chip by passing a DC current through an outer superconducting coil. The sample box and the coil are surrounded by two magnetic shieldings consisting of a lead cylinder around which permalloy tape is wrapped. The sample box, coil, and the shieldings are thermally anchored at the mixing chamber with base temperature 30 mK (note that in the experiments using active reset of the spins with 1.47 mW laser power, the temperature was 400 mK instead)

state, which makes the constraint on the noise reaching the sample less stringent. To apply refocusing pulses with sufficient microwave power at the sample input, we thus reduce purposely the attenuation on the input microwave line (20 dB at 4 K and 10 dB at 100 mK). This results in a thermal field of ∼5 photons in the resonator.

The sample is characterized by microwave reflectometry. The microwave signals are sent through an input transmission line (*MW in*) and retrieved from an output line (reflect out). The signal reflected on the sample is separated from the input signal by a double circulator, routed through a 5.4 GHz lowpass filter, amplified by a CITCRYO1-12 cryogenic amplifier, and is finally demodulated at room temperature. The microwave setup at room temperature depends on the physical quantity to be measured in the experiment, and is detailed in the corresponding sections.

An optical fiber is installed in the refrigerator to guide light from the optical setup at room temperature down to the sample at 30 mK (see Fig. 5.9). Throughout this chapter, P refers to the microwave power at the input of the resonator and P_L to the optical power out of the fiber at 30 mK. In the next section, we explain the optical setup in greater details.

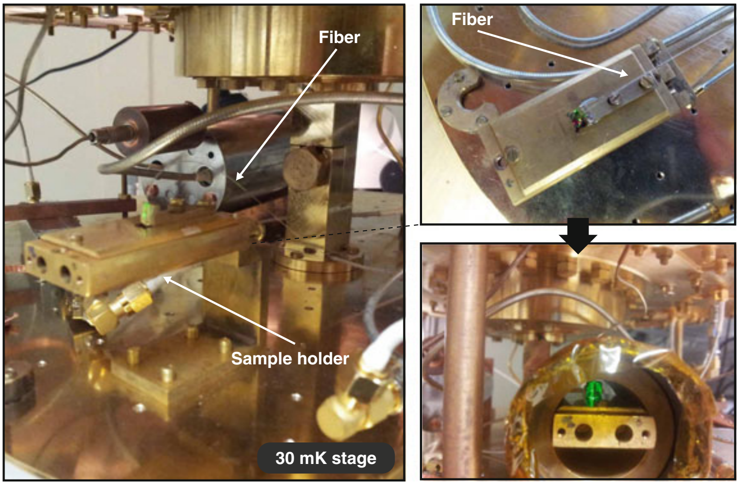

Fig. 5.9 **The 30 mK stage.** The optical fiber guides light down to the sample at 30 mK, and is glued on it after alignment

5.2.2.2 The Optical Setup

One challenge in bringing light down to the low temperature stage in a dilution refrigerator is the limited cooling power (typically 100 μW at 100 mK). This requests a special attention to the optical setup to minimize the optical power. Since our cryostat had no optical window, we used an optical fiber to guide light from the optical setup at room temperature down to the sample at 30 mK.

OPTICAL PULSE GENERATION AT ROOM TEMPERATURE

The schematic of the optical setup at room temperature is shown in Fig. 5.10. A frequency-doubled YAG laser (Laser Quantum gem) delivers 50 mW of 532 nm light. Optical pulses are generated with the help of an acousto-optic modulator (AOM), which is mounted on a 2D translation and a rotation stage for precise alignment with the laser beam. It is driven by radiofrequency pulses at 10 MHz generated by a rf source gated by dc pulses delivered by an arbitrary waveform generator (AWG). An iris is used to separate the first-order diffracted beam which is modulated from the unmodified zero-order beam. To improve the pulse shaping, the AOM is used in a double pass configuration: the first-order diffracted beam is retroreflected for a second pass through the AOM. The second pass is separated from the input beam thanks to a quarter-wave plate followed by a polarizing beam-splitter. The focalization system made of a beam expander and plano-convex lenses was used to increase the efficiency of the AOM which is inversely proportional to the incident beam diameter.

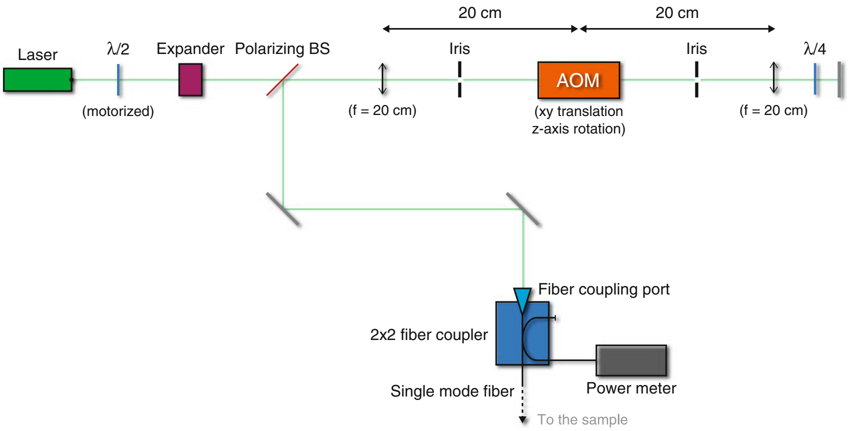

Fig. 5.10 Full schematic of the optical setup. The laser beam at 532 nm passes through a half-wave plate ($\lambda/2$) mounted on a motorized rotation stage controlled by the computer in order to choose the angle of the beam polarization. The beam is then expanded by a ×5 expander to 4 mm and sent to the AOM through a polarizing beam splitter that selects the vertical component of the beam polarization and throw the horizontal one out of the setup (purposely to control the optical power). The beam is then focussed inside the AOM at the diffraction spot size by a convergent lens with focal length 20 cm. The angle of incidence in the AOM is adjusted with a rotation stage, on which is mounted the AOM to satisfy the Bragg diffraction condition. The first order diffracted beam out of the AOM is selected by an iris and reflects on a mirror for a second passage in the AOM. The pulsed beam is finally redirected, coupled to a single mode fiber, and splitted in two paths (90 % sent to the sample at 30 mK and 10 % to a powermeter.)

To couple the pulsed beam into the single-mode fiber, we use a commercial aspheric fiber-port coupler with effective focal lens 18.3 mm. The focal lens value was chosen such that the diffraction-limited spot size matches the mode field diameter of the single-mode fiber. Two mirrors mounted on kinematic holders are used to adjust the angle and position of the beam incident on the fiber-port to optimize the coupling of the light into the fiber. Note that the fiber port is not protected from ambient light that could potentially be guided down in the dilution refrigerator via the fiber. This effect has proven to be non-critical for the case of our optical fiber, as most of the thermal radiation at room temperature sits at ∼10 µm while the transmission of our fiber is strongly suppressed above 1 µm wavelength.

With all losses taken in account, we couple 3.3 % of the light out of the laser to the fiber. This value includes 64 % conversion efficiency for the first pass in the AOM, 84 % for the second and 6.5 % coupling efficiency of light into the fiber. This fiber is connected to a 2 × 2 fiber optic coupler to separate the optical signal in two paths. In this way, 90 % of the input signal is sent to the dilution fridge while 10 % is sent to a powermeter (Fig. 5.11).

For power control, a half-wave plate mounted on a motorized rotation stage with 1 arcs resolution is placed at the output of the laser to control the angle of beam polarization. This makes it possible to control precisely the optical power sent to the

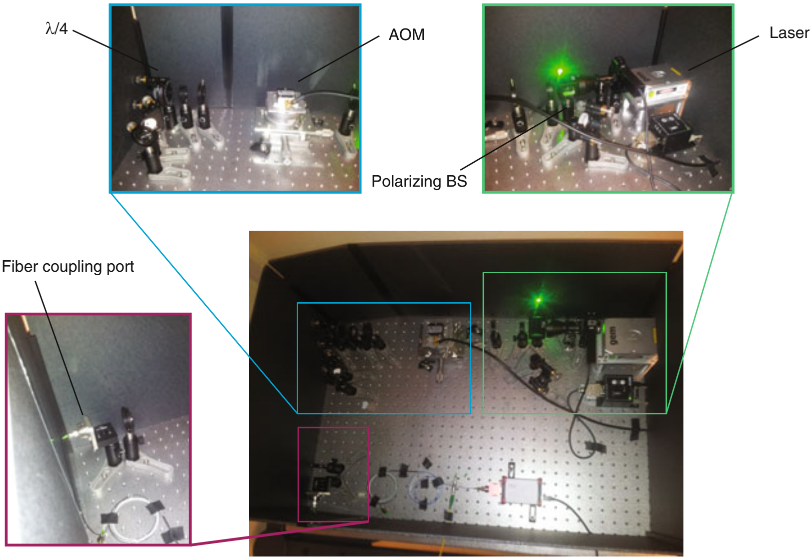

Fig. 5.11 The optical setup at room temperature with *panel* zooming to its most important features. The laser (*green panel*) output a 0.8 mm diameter beam at 532 nm. Optical pulses are shape by double pass in the AOM (*blue panel*) and finally coupled into the single mode fiber (*purple panel*) that connect the setup at room temperature to the 30 mK stage

sample with the polarizing beam splitter, as shown in the *left* panel of Fig. 5.12. To analyze the optical pulse shape, the beam is further separated in two paths with a beam splitter before the fiber coupler. The second path is routed to a fast photodetector whose output voltage is monitored with an oscilloscope as shown in the *right* panel of Fig. 5.12.

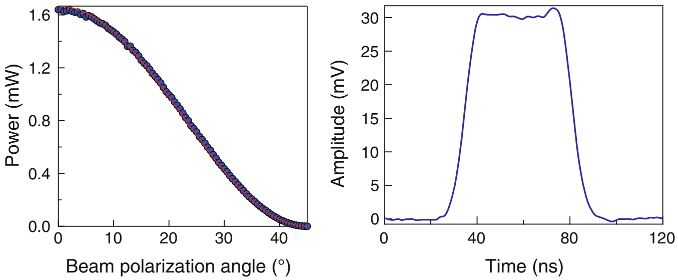

Fig. 5.12 Optical pulses. (*Left*) The optical power at the sample stage is controlled with 10 μW resolution up to 1.65 mW using a half wave plate mounted on a motorized rotation stage. (*Right*) The optical pulse shape is designed with 10 ns resolution by double pass in the AOM

MOUNTING THE FIBER ON THE HYBRID CIRCUIT AT 30 MK

As explained above, we have to minimize the optical power used for spin polarization to avoid heating up the cryostat. Room temperature experiments have shown that a single spin can be repumped using $100\,\mu$W power at 532 nm focused on $1\,\mu\mathrm{m}^2$ in 10 ns [3]. Since the diamond crystal is homogeneously doped, some light is absorbed by the NV centers before it reaches the bottom of the crystal where the spins coupled to the resonator are found. We measured this absorption to be of order 30 %, which is therefore not a significant issue.

Concentrating the light in the region of the diamond just above the inductance is needed to save optical power. Without optical windows, we have two choices. The first one is to build an optical setup on the low temperatures stage of the dilution refrigerator that focuses the beam outgoing the fiber to the $100 \times 100\,\mu\mathrm{m}^2$ area of interest. As thermal contraction occur during the cooling down, an alignment at room temperature before closing the refrigerator would not be sufficient and such a setup would require delicate in situ piezoelectric position control. The second strategy is to attach the fiber directly to the sample. Because we want to target a small diamond region and that thermal contractions also affect the sample holder, it is undesirable to attach the fiber to it.

Instead we decide to align the fiber directly on top of the inductance of the resonator and to glue it to the diamond, with the help of a stereomicroscope with large working distance at room-temperature. The fiber is mounted in the dilution refrigerator and aligned as shown in Fig. 5.14. It is a single mode fiber with numerical aperture 0.13 connected on one side with FC/PC connector to the optical setup at room temperature and left naked on the other side. The $100\,\mu$m core is surrounded by a coating that brings the total diameter of the fiber to $124\,\mu$m. To make it enter the outer vacuum chamber, we use a home-made vacuum feedthrough inspired from [4], made of a Swagelok that crushes the fiber within a little Teflon piece (see Fig. 5.13). The fiber was first cleaved in two parts, stripped, and inserted into the feedthrough, after what it was spliced with the other part of the fiber. The fiber then goes down to the sample via holes in the dilution refrigerator temperature stages, bringing negligible heat load. Radiation is also not an issue since the mean occupation of an optical mode at room-temperature is fully negligible. Once at the low temperature stage, the fiber is stripped over 1 cm, mounted on a triaxial translation stage and placed for alignment under an optical microscope as shown in Fig. 5.14. The short bare fiber part is then glued to a 1 mm thick glass spacer itself glued to the diamond, so that

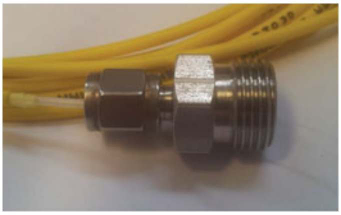

Fig. 5.13 The vacuum optical fiber feedthrough. The fiber is crushed into a little piece of Teflon mounted on a Swagelok to enter into the outer vacuum chamber of the dilution refrigerator

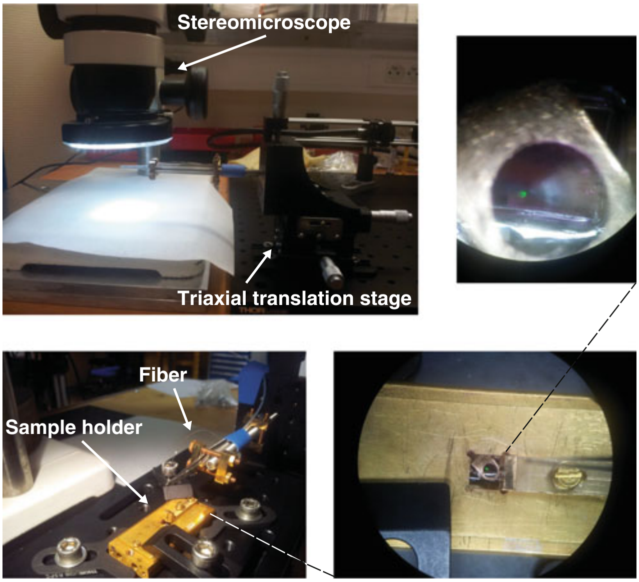

Fig. 5.14 Alignment setup. (*Top left*) The fiber is mounted on a triaxial translation stage, placed under a stereomicroscope with large working distance and dropped though a hole in the sample box (*bottom left*) to be attached to the sample (*bottom right*). The *top right* picture shows the light beam reflected on the niobium (green spot) and the inductance (black square) as seen through the optical microscope during the alignment process

the fiber-to-sample distance is 1.5 mm. This corresponds to a nominal beam diameter of 230 μm at the sample, therefore matching the area covered by the resonator meander wire. Given the technical difficulties of the whole process, the accuracy of the alignment is estimated of order 0.5 mm.

Note that for the goal that has been set to minimize the optical power by shining only the small diamond region of interest, this poor alignment accuracy is not satisfying. In Chap. 6, we will present an experiment in which the laser light is sent through optical windows, and that shows better alignment.

5.3 Spectroscopy of the Resonator-Spins System

In this section, we present the spectroscopic measurement of the hybrid circuit at zero-magnetic field and extract the relevant parameters that will be used in the following. The resonator is first characterized with the spins effectively decoupled from the resonator. The hybrid circuit is then measured to extract the coupled system parameters and spin distributions.

5.3.1 Characterization of the Resonator

The resonator is characterized by microwave reflection measurement. To measure its bare parameters, we need to detune or effectively decouple the spins from the resonator. For that, we saturate them through the resonator with a strong microwave tone. When saturated, spins do not absorb photons and are effectively decoupled from the electromagnetic field of the resonator until they relax. Accordingly, a 10 s microwave pulse of -20 dBm power is first applied through the resonator at the NV zero-field frequency. The reflection spectrum of the resonator is then obtained immediately afterwards with a VNA. The time window during which the measurement takes place is 5 s which is much shorter than the spin relaxation time $\sim$5 min (see next section). The reflection coefficient $S_{11,sat}$ is shown in Fig. 5.15. The resonator response appears on the reflected phase as a π shift, with no signal on the amplitude except on a large-scale frequency dependence. The absence of dip in the amplitude at resonance here indicates that the internal loss κ_L of the resonator is much smaller than its bandwidth κ. The fit of the reflected phase (using Eq. 2.21 in Sect. 2.1.1.2) yields $\omega_r/2\pi = 2.88$ GHz and $Q = 80 \pm 8$, equivalent to a damping rate $\kappa = 226.2 \pm 22.6 \cdot 10^6\ \mathrm{s}^{-1}$. The spectral measurement performed with the VNA yields a 10 % uncertainty for Q due to the large-scale frequency dependence. Indeed,

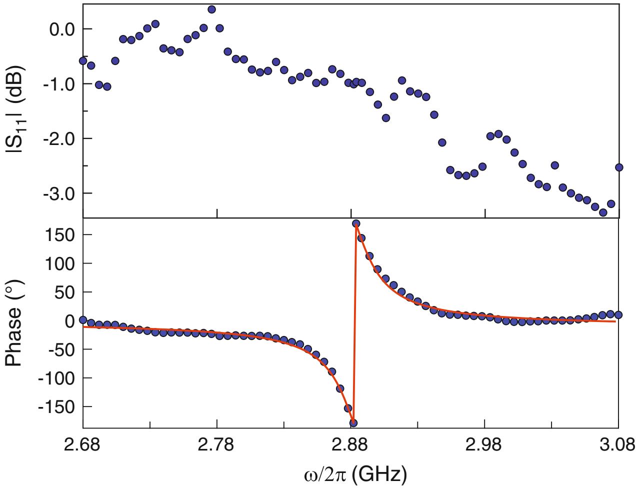

Fig. 5.15 **Reflection coefficient S_{11} of the resonator.** The amplitude and phase reflected onto the resonator is shown when the spins are saturated and do not contribute to the signal. The fit of the phase response (*red line*) yields resonator frequency $\omega_r/2\pi = 2.88$ GHz and quality factor $Q = 80 \pm 8$. The effect of spurious resonances in the measurement setup is visible in the amplitude signal

the reflected phase contains a ripple and it is difficult to fit the width of the shift of the resonator phase response and deduce Q from it.[2]

This large-scale frequency dependence is due to losses and spurious resonances in the microwave cables and components of the transmission lines. The reflection coefficient $r(\omega)$ is related to the measured reflection coefficient $S_{11}(\omega)$ through a complex frequency-dependent transmission coefficient[3] $G(\omega)$:

$$S_{11}^*(\omega) = r(\omega)G(\omega). \tag{5.5}$$

An important point for the following is that $S_{11,sat}$ is linked by $G(\omega)$ to the steady-state reflection coefficient of an empty cavity r_{th} given by Eq. 2.21 and thus gives a direct calibration of $G(\omega)$. In the following sections, we always renormalize with $S_{11,sat}$ to get rid of $G(\omega)$ and subsequently access the response of the spins.

5.3.2 *System Spectroscopy at Zero-Magnetic Field*

The response of the spins at zero-magnetic field is measured with the VNA by the same reflection measurement but without applying the saturation pulse. The probe power corresponds to $\bar{n} \approx 20$ photons in the resonator so that the Holstein-Primakoff approximation is valid and the method developed in Sect. 2.3.3.2 can be used to extract the coupled system parameters and the spin distribution. The reflected amplitude and phase as a function of the probe frequency is shown in the left panel of Fig. 5.16 with the spins at equilibrium. Compared to the case where spins are saturated (black curve), dips are visible in the reflected amplitude $|S_{11}|$. These dips correspond to absorption by the NVs. For reaching the information of the spins, we convert $S_{11}(\omega)$ into the reflection coefficient $r(\omega)$, and subsequently into the spin susceptibility $\chi''(\omega)$ (and equivalently the coupling density profile $\rho(\omega)$) using Eqs. 2.111 and 2.112 in Sect. 2.3.3. To calibrate for the frequency dependence of the transmissions lines ($G(\omega)$), we renormalize S_{11} by $S_{11,sat}$ and express the reflection coefficient $r(\omega)$:

$$r(\omega) = \frac{S_{11}^*(\omega)}{S_{11,sat}^*(\omega)} r_{th}(\omega) \tag{5.6}$$

The right and bottom panels of Fig. 5.16 show respectively the reflection coefficient r and the spin susceptibility $\chi''(\omega)$. In the following, we use this measurement to extract the coupled system and distribution of NV Hamiltonian parameters.

---

[2] We will determine Q with better accuracy later in this manuscript.

[3] The sign $*$ is not physical but accounts for a difference of sign convention between theory and the vector network analyzer (see Sect. 2.1.1.2).

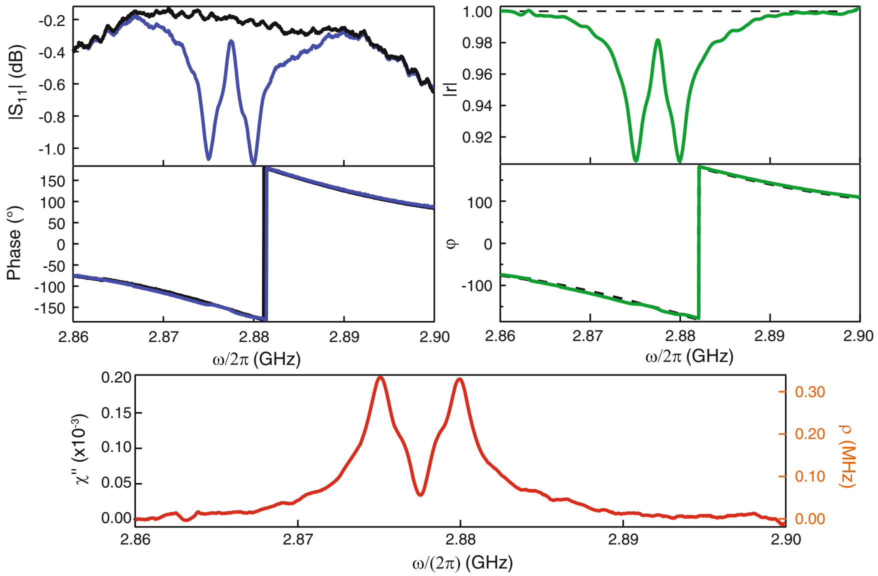

Fig. 5.16 **Response of the spins at zero magnetic field as seen through the resonator.** (*Top left*) Amplitude and phase of the reflection coefficient S_{11} showing the resonator resonance on the phase and the spin absorption on the amplitude. (*Top right panel*) Corresponding calibrated reflection coefficient. (*Bottom*) Measured spin signal expressed in spin susceptibility χ'' (on the left vertical axis) and in coupling density profile (on the right vertical axis)

5.3.2.1 The Coupled System Parameters

At zero magnetic field, both degenerate spin groups *Orth* and *N-Orth* contribute to the absorption. The reflected amplitude on the right panel of Fig. 5.16 shows two broad peaks corresponding to ω_- and ω_+ transitions. On the $|0\rangle \rightarrow |+\rangle$ transition, the spin absorption reaches a maximum at $\omega_e/2\pi = 2.8795\,\text{GHz}$ with $r = 0.905$. We can deduce directly the cooperativity for the spins at equilibrium (using Eq. 2.115 in Sect. 2.3.3.2):

$$C^{eq} = \frac{1-r}{1+r} \approx 0.05 \ll 1. \tag{5.7}$$

We then extract the ensemble coupling constant for the spins at equilibrium by integrating the spin coupling density profile on the bottom panel of Fig. 5.16 over the frequency range available (dividing by 2 to account for one transition only):

$$g_{ens}^{eq} = \sqrt{\int \rho(\omega) d\omega/2} \approx 2\pi \cdot 1.15\,\text{MHz} \tag{5.8}$$

Since g_{ens} depends on the spin polarization, the measured g_{ens}^{eq} cannot be compared to g_{ens}^{th} estimated for the spins completely polarized in Sect. 5.2.1.3 at this stage. The spin polarization at equilibrium is measured later in this chapter, to make possible the comparison.

5.3.2.2 The Distribution of NV Hamiltonian Parameters

It is possible to quantitatively understand the shape of the measured spin susceptibility in Fig. 5.16, assuming phenomenological distributions of the parameters entering the NV centers Hamiltonian. The main idea is that our ensemble of NV centers has a certain frequency distribution because the Hamiltonian parameters have a distribution: the z component of the field b has a distribution $\rho_b(b)$ due to the local environment of each NV, the strain parameter E has another distribution $\rho_E(E)$, and the zero-field splitting D has a distribution $\rho_D(D)$. The reasoning is further described in Appendix B.

Here we apply the method that we have developed to determine the distributions of NV Hamiltonian parameters $\rho(D)$, $\rho(E)$ and $\rho(dB)$ to be used for analysis in the following. To do so, we assume a Lorentzian distribution for both $\rho_b(b)$ and $\rho_D(D)$ with respective widths db_0 and dD_0 and guess the function $\rho_E(E)$. We find that a bi-exponential distribution $\rho_E(E) = [\exp(-E/E_1) + A_1 \exp(-E/E_2)]/(E_1 + A_1 E_2)$ yields a computed $\tilde{\chi}''(\omega, B_{NV} = 0)$ that reproduces semi-quantitatively the data. In total we use the following parameters: $db0 = 0.21\,\text{Gs}$, $dD_0/2\pi = 0.15\,\text{MHz}$, $E_1/2\pi = 0.5\,\text{MHz}$, $E_2/2\pi = 10\,\text{MHz}$, $A_1 = 0.2$. In this way we obtain the spin susceptibility at $B_{NV} = 0\,\text{mT}$ (see Fig. 5.17). The corresponding $\rho_E(E)$ distribution is shown in inset. These distributions of Hamiltonian parameters will be used in the following to compute theoretical spin susceptibility at arbitrary magnetic B_{NV}. We remind that the experimental susceptibility includes contributions both from the spins that are orthogonal to B_{NV} and from those that are non-orthogonal,

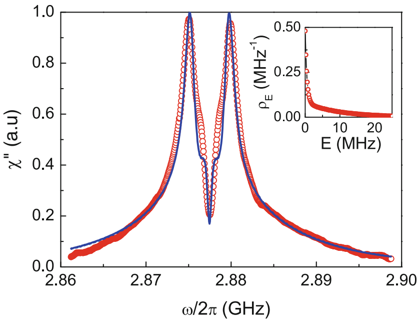

Fig. 5.17 Rescaled spin susceptibility $\chi''(\omega, B_N V = 0)$. *Open red circles* are experimental data, *solid blue line* is the theory computed with the bi-exponential strain distribution $\rho_E(E)$ shown in the *inset*, with a Lorentzian $\rho_b(b)$ and $\rho_D(D)$ with respective widths $dB_0 = 0.21\,\text{Gs}$ and $dD_0/2\pi = 150\,\text{kHz}$

each of those having a very different resonance frequency dependence on B_{NV} as seen in Sect. 2.2.2.1. Each group contains exactly half of the total number of spins contributing to the signal; however, we have seen in Sect. 5.2.1.3 that spins from each group have a different coupling constant to the resonator field due to the angle they make with this field. This difference in coupling constant can be incorporated using the angular factor α (entering in the expression of the coupling constant in Eq. 2.101) such that the total $\chi''(\omega, B_{NV}) = \frac{\alpha_{N-Orth}}{\alpha_{Orth}} \chi''_{N-Orth}(\omega, B_{NV}) + \chi''_{Orth}(\omega, B_{NV})$.

5.4 Active Reset of the Spins

NV centers having transition frequency close to 3 GHz are mainly polarized in the spin ground state at mK temperatures. Once excited however, they relax extremely slowly in the spin ground state due to their long relaxation time [5, 6]. In the experiments of Chap. 4, we worked at the single-photon level so that the amount of excited spins was always negligible compared to the total number of spins. In the experiments which follow instead, we apply strong refocusing pulses that aim to invert the whole spin ensemble: at the end of the experimental sequence, the amount of excited spins is of order the total numbers of spins. Repeating this experimental sequence at a reasonable rate thus requests to implement an active reset of the spins. For that, we use the optical repumping property of NV centers described in Sect. 2.2.2.2 and implement it in a setup compatible with superconducting qubit technology. Optical irradiation is uncommon in cQED and the effect of shining light on superconducting circuits is not well known. In the following we thus first study the effect of light irradiation on the superconducting resonator. We then measure the dependence of the spin polarization on the optical power for continuous light irradiation and finally determine the spin reset efficiency of optical pulses.

5.4.1 Effect of Light Irradiation on the Superconducting Resonator

5.4.1.1 Protocol and Setup for Light Effects Measurement

The effects of light irradiation on the superconducting resonator are studied with the sample described in Sect. 5.2.1.3 with the diamond already on top of the superconducting resonator. In this experiment, we want to measure the effects on the resonator without being disturbed by the dynamics of spins under light irradiation. For that, we can take advantage of the difference in timescale between the two processes. We will see in the next sections that in our optical setup configuration, the active reset by optical pumping of the spin ensemble takes a time of order one second, whereas the effects of light irradiation on the resonator are expected to occur on a millisecond timescale. Spins can thus be saturated and the resonator measured shortly afterwards under light irradiation within a time window sufficiently short for the spins to remain saturated. The protocol is illustrated in Fig. 5.18. The spins are first saturated with a 20 µs strong microwave pulse and the reflected amplitude of an applied weak 2 ms measurement pulse is measured by homodyne detection. During this measurement pulse, a 1 ms optical pulse with power P_L is applied. To minimize the leakage of the strong ($P_{sat} = -24\,\text{dBm}$) saturation pulse at the position of the weak ($P_{meas} = -132\,\text{dBm}$) measurement pulse, the saturation pulse is shaped with 160 dB on/off ratio by two microwave switches in series. The first switch is the one of the Agilent E8267 microwave source, the second a Miteq microwave switch. The microwave and optical setup at room temperature for this measurement is shown on the bottom panel of Fig. 5.18.

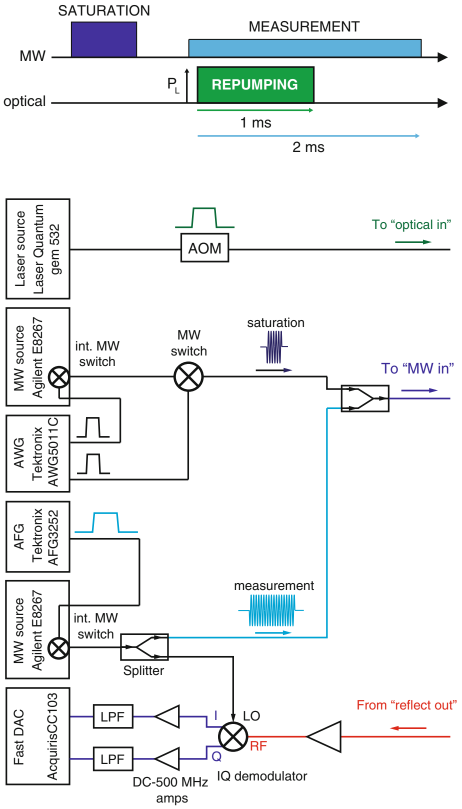
SATURATION
MEASUREMENT
MW
optical
P_L
REPUMPING
1 ms
2 ms
Laser source
Laser Quantum gem 532
AOM
To “optical in”
MW source
Agilent E8267
int. MW switch
MW switch
saturation
To “MW in”
AWG
Tektronix AWG5011C
AFG
Tektronix AFG3252
measurement
MW source
Agilent E8267
int. MW switch
Splitter
Fast DAC
AcquirisCC103
LPF
LPF
I
LO
Q
RF
From “reflect out”
DC-500 MHz amps
IQ demodulator

Fig. 5.18 Protocol and setup for light irradiation effects measurement

5.4.1.2 Experimental Characterization of the Modified Resonators Parameters

We extract the resonator parameters from measurements under continuous optical irradiation. We show in Fig. 5.19 a time domain measurement with 20 ns resolution of the reflected amplitude and phase of the measurement pulse at 2.88 GHz for a 1.6 mW optical pulse, with averaging over 500 identical sequences. At the position of the optical pulse, we observe that the reflected phase of the measurement pulse undergoes a phase shift and its amplitude is reduced. The optical pulse extends from point I (107.5 μs after the beginning of the measurement pulse) to point F. The beginning and the end of the optical pulse is followed by a transient during which the effects of the laser irradiation respectively appear and relax (see inset). In both cases, the steady state regime is reached within ∼15 μs. We denote $S_{11,A}$ (respectively $S_{11,B}$) the average over the region A (B) in which the resonator field is in the steady state regime with (without) laser irradiation. The top panel of Fig. 5.20 compares the resonator spectrum $S_{11,B}(\omega)$ to its counterpart $S_{11,A}(\omega)$ with 1.6 mW optical irradiation. Compared to $S_{11,B}$, a dip is visible in the amplitude of $S_{11,A}$ showing that the resonator is no longer in the over-coupled regime but is closer to the critical coupling regime seen in Sect. 2.1.1.2. This indicates that optical irradiation induces additional internal losses for the resonator. To go further we extract the modified resonator parameters $\left(\omega_{c,las}, \kappa_{las}, \kappa_{L,las}\right)$ from $S_{11,A}$. To do so, we need again to get

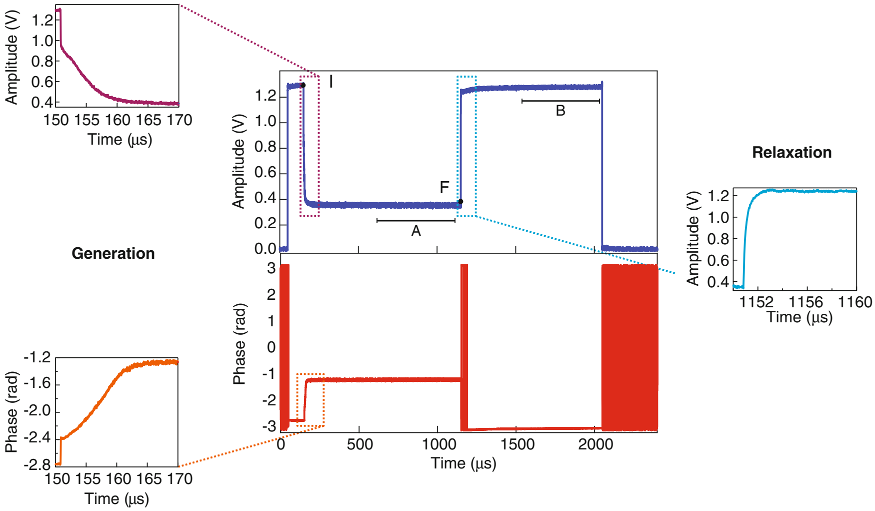

Fig. 5.19 Time-domain measurement during an applied optical pulse of power $P_L = 1.6$ mW, with the spins saturated. (*Main panel*) Reflected amplitude and phase of the measurement pulse at 2.88 GHz during the application of the 1 ms optical pulse at $P_L = 1.6$ mW. The spins remains saturated along the measurement. *Left* and *right* are zooms on the transients which appears at the beginning and the end of the optical pulse

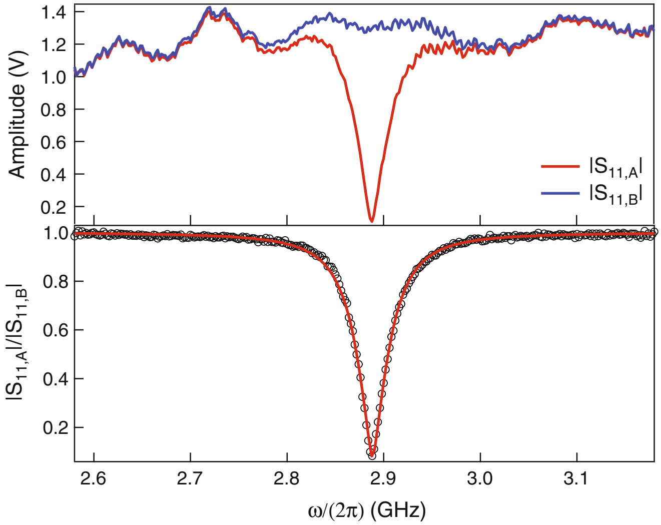

Fig. 5.20 Reflected amplitude $|r|$ under optical irradiation at P_L= 1.6 mW, with the spins saturated. (*top*) The resonator spectrum is probed under laser irradiation ON (*red*) and OFF (*blue*). Under laser irradiation, the reflected amplitude reaches almost 0 indicating that the internal losses κ_L are on the same order than the external damping rate κ (see Sect. 2.1.1.2). The additional internal losses are attributed to the effect of the optical irradiation on the resonator. (*Bottom*) Measured (*dots*) and fit (*red line*) of the corresponding calibrated reflected amplitude. The fit with Eq. 5.10 yields $\omega_{c,las}/2\pi = 2.888\,\text{GHz}$, $\kappa_{las} = 191.6 \pm 1.2 \cdot 10^6\,\text{s}^{-1}$ and $\kappa_{L,las} = 164 \pm 1.9 \cdot 10^6\,\text{s}^{-1}$

rid of the complex frequency-dependent transmission coefficient $G(\omega)$ which links reflected signals S_{11} to reflection coefficients r by renormalizing $|S_{11,A}|^2$ by $|S_{11,B}|^2$. In absence of optical irradiation, the internal losses rate κ_L of the resonator is much smaller than the external damping rate κ. The steady-state value of the reflected signal with spins saturated $|S_{11,B}|^2$ gives thus approximately $|G(\omega)|^2$:

$$|S_{11,B}|^2 = |r_{th}(\omega)G(\omega)|^2 = \frac{(\kappa - \kappa_L)^2 + 4(\omega - \omega_r)^2}{(\kappa + \kappa_L)^2 + 4(\omega - \omega_r)^2} \cdot |G(\omega)|^2 \approx |G(\omega)|^2 \quad (5.9)$$

so that the quantity $|S_{11,A}|^2/|S_{11,B}|^2$ rewrites:

$$\frac{|S_{11,A}|^2}{|S_{11,B}|^2} = \frac{(\kappa_{las} - \kappa_{L,las})^2 + 4(\omega - \omega_{c,las})^2}{(\kappa_{las} + \kappa_{L,las})^2 + 4(\omega - \omega_{c,las})^2} \quad (5.10)$$

This allows us to fit the 3 parameters with good accuracy. The fit of $|S_{11,A}|^2/|S_{11,B}|^2$ with Eq. 5.10 for 1.6 mW optical irradiation yields $\omega_{c,las}/2\pi = 2.888\,\text{GHz}$, $\kappa_{las} = 191.6 \pm 1.2 \cdot 10^6\,\text{s}^{-1}$ and $\kappa_{L,las} = 164 \pm 1.9 \cdot 10^6\,\text{s}^{-1}$ as shown on the bottom panel. The same measurement has been performed for different optical power. The dependence of the resonator parameters on the optical power P_L is shown in Fig. 5.21.

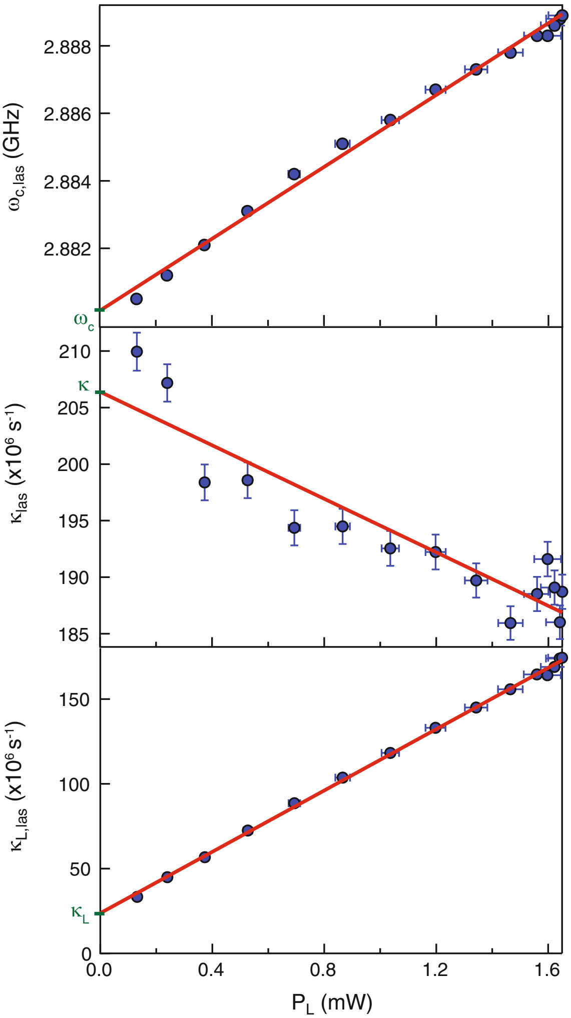

Fig. 5.21 Parameters of the resonator under optical irradiation. Resonator frequency $\omega_{r,las}$ (*top*), damping rate κ_{las} (*middle*) and internal losses $\kappa_{L,las}$ (*bottom*) as a function of the optical power P_L. The origin of the linear fit (*red lines*) gives a precise measurement of the resonator parameters without optical irradiation

The error bars in the y-axis are set by the precision of the fit, in the x-axis by the 3 % percentage error on P_L. We observe that all resonator parameters vary linearly with the optical power and can be fitted using $y = a + bP_L$ (with good approximation for κ_{las}. The origins a of the fits give the values ($\omega_c, \kappa, \kappa_L$) that corresponds to the resonator without optical irradiation. In this way, we obtain $\omega_r/2\pi = 2.8801 \pm 0.0001\,\text{GHz}$, $\kappa = 206.7 \pm 1.9 \cdot 10^6\,\text{s}^{-1}$ and $\kappa_L = 23.9 \pm 0.6 \cdot 10^6\,\text{s}^{-1}$. This set constitutes a more precise measurement of the resonators parameters than the direct spectroscopic measurement we have done in Sect. 5.3.1 and we use these values in the following.

5.4.1.3 Interpretation

We have seen in the previous section that the superconducting resonator is affected by laser irradiations. This is attributed to two effects: first, the laser beam heats up the circuit locally inducing the generation of quasiparticles in the superconductor, second since the frequency of the optical light is above the Silicon bandgap, it generates carriers in the Silicon. These effects take place in few tens of microseconds as evidenced by the transients observed in Fig. 5.19, and relax with similar time constants. In the steady state regime, both effects contribute to increase κ_L and their relative contributions are difficult to separate. They however have opposite effects on the resonator frequency: on the one hand, the generation of quasiparticles in the superconducting film increases the kinetic inductance which lowers the resonator frequency; while on the other hand, the carriers generated in the substrate reduce its dielectric constant (according to a Drude model description [7]), and thus reduces both the resonator capacitance C and the coupling capacitance C_c, which leads to an increase of the resonator frequency and a decrease of the resonator external damping rate. As seen in the top panel of Fig. 5.21, we observe that the resonator frequency increases with P_L, which shows that the relative decrease in capacitance induced by the carriers in the silicon is larger than the relative increase of the inductance induced by the quasiparticles in the Niobium film. It is however difficult to identify more precisely the separate contributions of these two effects. In the same way, the increase of κ_L observed in the middle panel can be attributed both to the carriers in silicon and to the quasiparticles in the film. The measured 10 % decrease of κ for $P_L = 1.47\,\mathrm{mW}$ can however to our knowledge only be explained by a decrease in the dielectric constant of silicon due to carrier generation.

An interesting question is then whether the resonator capacitance C and the coupling capacitance C_c are changed by the same amount, as would be the case if the light was homogeneously distributed over the chip area, or if the carriers generated by the laser absorption were able to diffuse over millimetric distances in the substrate (which seems very unlikely). We note that the coupling rate κ is given by the formula (Eq. 2.12 in Sect. 2.1.1.1) $\kappa = \omega_r^3 C_c^2 Z_0 Z_r$, which can be rewritten as $\kappa = (C_c/C)^2 Z_0/L$. According to this expression, if the dielectric constant change was the same in C and C_c, we shouldn't observe any change in κ contrary to our measurements. We are thus led to the conclusion that probably the laser light was more intense in the region of the coupling capacitor than in the region of the resonator capacitor. This is somewhat in contradiction to our attempts to align the laser spot with the resonator inductance, which is closer to C than to C_c, which could indicate a bad alignment of the laser spot. As discussed below, this is nevertheless indirectly confirmed by measurements of the spin repumping efficiency.

5.4.2 Continuous Irradiation: Dependence of the Spin Polarization on the Optical Power

We investigate here the spin polarization as a function of the optical power by measuring the reflection spectrum of the resonator under continuous laser irradiation and continuous microwave probing. We find a slight dependence of the steady-state polarization on the applied optical power.

5.4.2.1 Measuring the Spin Susceptibility Under Continuous Laser Irradiation

The hybrid circuit under optical irradiation is characterized again by microwave reflection measurement. The reflected spectrum is obtained with the VNA using probe power corresponding to $n \approx 20$ photons in the resonator, sufficiently low to avoid changing the spin polarization with the microwave. In this condition, the Holstein-Primakoff approximation is valid and the method developed in Sect. 2.3.3.2 to express the spin susceptibility can be used. The reflected amplitude $|S_{11}|$ under continuous irradiation with 0.2, 0.69 and 1.63 mW optical power is shown in Fig. 5.22. Compared to the data without optical irradiation (black curve), the curves are distorted around the resonator frequency and an additional broad dip at resonance is even visible at large optical power. This broad dip is caused by the resonator losses under optical irradiation that we have evidenced in Sect. 5.4.1, an effect that we need to deconvolve from the spin contribution to determine the spin polarization. To do so, we first get rid of the complex transmission coefficient $G(\omega)$ by renormalizing S_{11} with $S_{11,sat}$

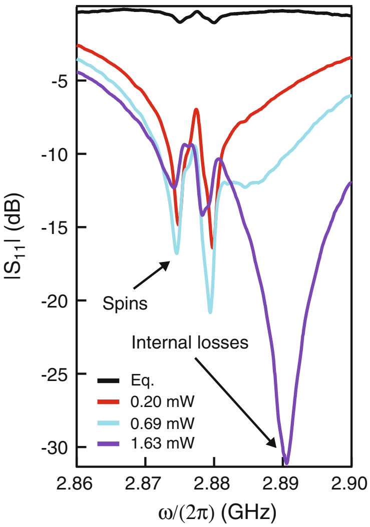

Fig. 5.22 Reflected amplitude $|S_{11}|$ under continuous optical irradiation. The absorption of the spins under optical irradiation with 0.2 (*red*), 0.69 (*light blue*) and 1.63 mW (*blue*) is compared to the one at equilibrium (*black line*). The *curves* show the $|0\rangle \rightarrow |\pm\rangle$ spectroscopic transitions of the spins, with a spin absorption that increases with P_L because of increasing spin polarisation. The additional broad peak at ω_r that increases with P_L corresponds to the internal losses induced by the optical irradiation

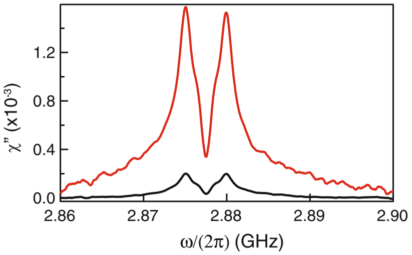

Fig. 5.23 Spin susceptibility χ'' under continuous optical irradiation at $P_L = 0.2$ mW. The measured reflected amplitude $|S_{11}|$ has been calibrated for the measurement lines ($G(\omega)$), and $|r|$ further converted in spin susceptibility χ''. The spin susceptibility under continuous optical irradiation at $P_L = 0.2$ mW (*red*) is larger than at equilibrium (*black*) by a factor 6.7

to access the reflection coefficient r and then use the modified resonator parameter values that we have measured in the previous section to convert with Eqs. 2.111 and 2.112 the reflected field into spin susceptibility χ''. The spin susceptibility for 0.2 mW continuous irradiation is shown in Fig. 5.23.

The spin susceptibility varies with frequency as the one measured at equilibrium (black curve). However, the spin susceptibility in the case of continuous irradiation with 0.2 mW optical power is larger than the one measured at equilibrium by a factor 6.7. Since the spin susceptibility is proportional to the spin polarization, it means that the spins under irradiation are polarized at a lower effective temperature than at thermal equilibrium. We conclude from this measurement that we are able to polarize the spins by optical pumping.

To analyze the evolution of the spin polarization with the optical power, it is desirable to estimate the accuracy we have on the frequency-dependent spin susceptibility curve as obtained with the above method. First, the finite uncertainty on the bare resonator parameters (ω_c, κ) introduces uncertainty in the conversion

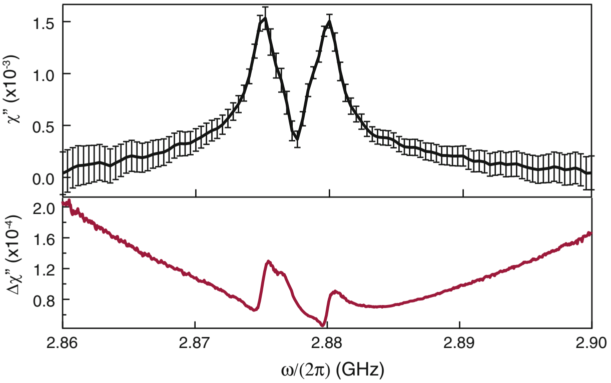

Fig. 5.24 Imprecisions on the conversion from $|S_{11}|$ to χ''. (*Top*) The spin susceptibility χ'' under continuous optical irradiation at $P_L = 0.2$ mW with its error bars and (*bottom*) the one-standard deviation. The imprecisions increase when getting far from resonance, suggesting that the spin susceptibility is not reliable in the wings

from reflected field S_{11} to reflection coefficient r, which induces uncertainty on the scaling of $\chi''(\omega)$. Second, the finite accuracy on the modified resonator parameters $\left(\omega_{c,las}, \kappa_{las}, \kappa_{L,las}\right)$ introduces uncertainty in the conversion from reflection coefficient r to spin susceptibility r which induce uncertainty on the symmetry of $\chi''(\omega)$. We have estimated in the previous sections $\Delta\omega_r/2\pi = 0.1\,\text{MHz}$, $\Delta\kappa = 1.9\cdot 10^6\,\text{s}^{-1}$, $\Delta\omega_{c,las}/2\pi = 0.01\,\text{MHz}$, $\Delta\kappa_{las} = 1.9\cdot 10^6\,\text{s}^{-1}$ and $\Delta\kappa_{L,las} = 1.2\cdot 10^6\,\text{s}^{-1}$. We show in Fig. 5.24 the spin susceptibility under continuous 0.2 mW irradiation together with its standard deviation. We see in particular that the uncertainty on the spin susceptibility increases as expected far from the resonator frequency.

5.4.2.2 Dependence on the Optical Power

We perform the same measurement than in the previous section for increasing optical power. We show in Fig. 5.25 a selection of these measurements. The spin susceptibility is obtained using Eqs. 2.111 and 2.112 with the modified resonator parameter values measured in Sect. 5.4.1.2. We observe that $\chi''(\omega)$ keeps the same shape but increases with increasing optical power which suggests an optical power dependence of the spin polarization.

In order to make this effect more visible, we have to get rid of the uncertainty on the scaling of $\chi''(\omega)$ discussed in the previous section. For that, we consider the difference $d = \chi''(\omega_e) - \chi''(\omega_0)$, with $\omega_e = 2\pi\cdot 2.8795\,\text{GHz}$ the point of maximum absorption and $\omega_0 = 2\pi\cdot 2.775\,\text{GHz}$ the zero-field splitting point. Its renormalization by the value at the optical power at which the spin susceptibility saturates defines the spin polarization:

$$p_{cont}(P_L) = \frac{d(P_L)}{d(P_{L,max})} \tag{5.11}$$

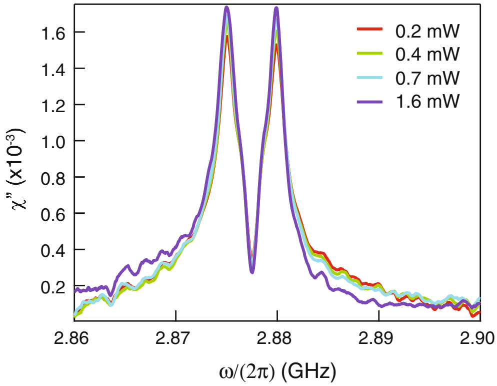

Fig. 5.25 Dependence of the spin susceptibility on the optical power $\chi''(P_L)$. The shape of the spin susceptibility is unchanged but its amplitude increases with the optical power P_L suggesting an increasing spin polarization. The slight asymmetry which appears at high optical power is attributed to the imprecisions on the conversion from $|S_{11}|$ to χ'', that increases with the optical power

The spin polarization $p_{cont}(P_L)$ as a function of the optical power for continuous irradiation is shown in Fig. 5.26. The spin polarization increases exponentially with P_L with characteristic power $P^{ch}_{L,cont} = 0.45\,\text{mW}$ and saturates around $P^{sat}_{L,cont} \sim 1\,\text{mW}$. This dependence suggests that two opposite effects contribute. On one hand, the spins are continuously polarized by optical cycling, on the other hand they are continuously slightly excited by thermal photons coming from the microwave measurement lines. The two effects have different timescales. For optical repumping, the timescale is set by the number of optical cycle which is proportional to the number of optical photons that participate in the process. The optical repumping is thus dependent on the optical power.

For a given optical power, the spin polarization reaches a steady state regime in which both effects compensate. The fact that the steady-state spin polarization saturates with increased optical power suggests that in our experiments we reach the maximum spin polarization reachable with optical pumping, 90 % according to [8]. In the following we apply optical pulses to reset the spin ensemble between experimental sequence, in contrast to the continuous irradiation investigated in this section. We will use the dependence $p_{cont}(P_L)$ obtained from Fig. 5.26 to renormalize to spin polarization.

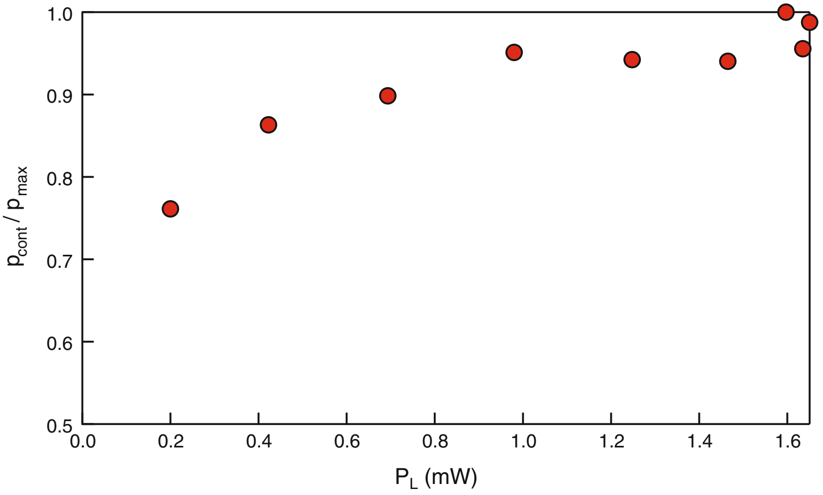

Fig. 5.26 Spin polarization under continuous optical irradiation $p_{cont}(P_L)/p_{max}$. The spin polarization increases exponentially with P_L with characteristic power $P_{L,cont} = 0.45\,\text{mW}$ and reaches the maximum allowed by optical repumping $p_{max} \sim 90\,\%$. The optical pumping is dependent on the optical power P_L due to a weak excitation by thermal photons that counteracts the repumping process

5.4.3 Pulsed Irradiation: Active Spin Polarization

5.4.3.1 Pulsed Spectroscopy with Optical Repumping

At this point, we switch from continuous to pulsed experiments. To demonstrate optical reset of the spins, we use the same microwave and optical setup at room temperature Fig. 5.18 as for the pulsed experiment of Sect. 5.4.1.1, but with a different synchronization sequence. The protocol is illustrated in Fig. 5.27. Microwave pulses are applied close to the bare frequency of the resonator at $\omega_d/2\pi = 2.884\,\text{GHz}$. The spins are first saturated by a $20\,\mu\text{s}$ long microwave pulse with frequency ω_d and applied power $-24\,\text{dBm}$ to start the experimental sequence from a reproducible spin polarization. They are then optically repumped with a laser pulse of power P_L and duration T_L. Finally the spin polarization is probed by measuring the reflected amplitude of an applied weak ($-132\,\text{dBm}$) $20\,\text{ms}$ long measurement pulse after the laser pulse. A delay of $300\,\mu\text{s}$ between optical and measurement pulses is introduced to let the effect of light irradiation on the resonator we have discussed in Sect. 5.4.1 to relax. At the time of probing, the resonator parameters are thus equal to their values without optical irradiation. To minimize frequency distortion, we keep the probe pulse frequency at resonance and sweep the external magnetic field B_{NV}.

Fig. 5.27 Protocol and setup for active spin polarization measurement

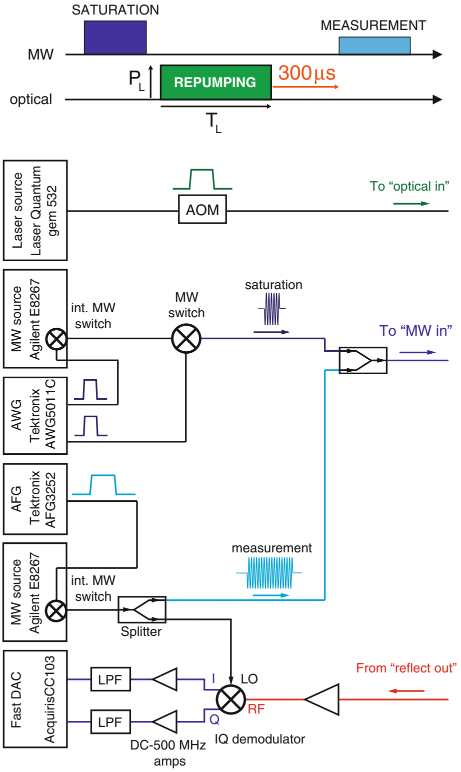
SATURATION
MEASUREMENT
MW
P_L
REPUMPING
300µs
optical
T_L
Laser source Laser Quantum gem 532
AOM
To "optical in"
MW source Agilent E8267
int. MW switch
MW switch
saturation
To "MW in"
AWG Tektronix AWG5011C
AFG Tektronix AFG3252
measurement
MW source Agilent E8267
int. MW switch
Splitter
Fast DAC AcquirisCC103
LPF
LPF
I
LO
Q
RF
From "reflect out"
DC-500 MHz amps
IQ demodulator

The results are shown in Fig. 5.28 for $P_L = 1.47\,\text{mW}$ and $T_L = 4\,\text{s}$. Without laser pulse, the reflected pulse amplitude is independent of B_{NV}, proving that the spins are efficiently saturated by the initial microwave pulse. With laser pulse, absorption peaks with the triplet shape characteristic of the NV hyperfine structure are observed, indicating a sizeable NV polarisation. To quantify the effect, we convert the absorption signal into the imaginary part of the spin susceptibility (using Eqs. 2.111 and 2.112 in Sect. 2.3.3) using the resonator parameters (ω_r, κ and κ_L). The spin susceptibilty after laser pulse (red curve) is compared to the spin susceptibility measured at thermal equilibrium (blue curve), that is without saturating and optical pulse. We measure a factor 6.3 between spins optically repumped and at equilibrium which suggests as already mentioned that the repumped spins are polarized at an effective temperature lower than the one of equilibrium. To link χ'' to spin polarization, we have to determine the optical pulse parameters that yield the maximum spin polarization.

Note that independently of the scaling that is proportional to the spin polarization, the shape of $\chi''(B_{NV})$ can be quantitatively understood from the distributions of Hamiltonian parameters we have determined in Sect. 5.3.2.2. The susceptibility $\chi''(\omega_d, B_{NV})$ computed without further adjustable parameters is plotted with a global scaling factor to match the experiment in Fig. 5.28 (dash-dotted line). All the features are reproduced but not exactly with the appropriate weight. These remaining discrepancies might be due to a spatial dependence of the strain distribution,

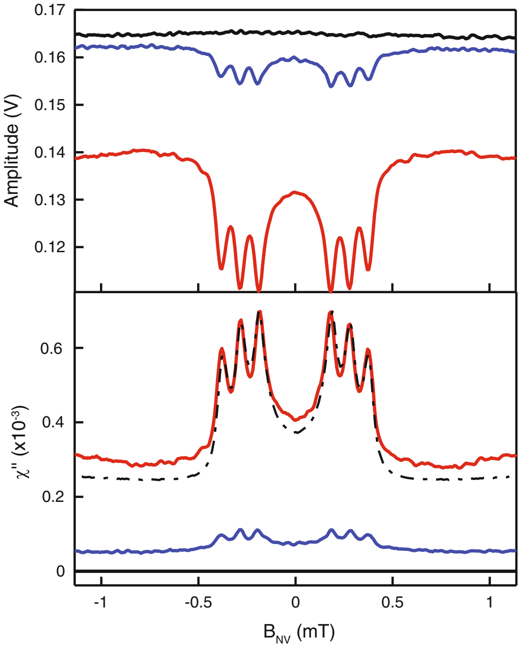

Fig. 5.28 Polarization of the spins with an optical pulse. The signal of the spins after an optical pulse of power $P_L = 1.47\,\text{mW}$ and duration $T_L = 4\,\text{s}$ (*red line*) is compared to the one at equilibrium (*blue line*) and saturated (*black line*). (*Top*) Reflected amplitude. The *curves* show the hyperfine split $m_S = 0$ to $m_S = \pm 1$ spectroscopic transitions of the *N-Orth* sub-ensemble. (*Bottom*) Corresponding imaginary part $\chi''(B_{NV})$ of the spin susceptibility. The calculated spin susceptibility (see Appendix B) and rescaled by a global factor to match the experimental spin polarization is shown (*dash-dotted line*)

in which case $\rho(E(r))$ would be correlated with the coupling constant distribution $\rho(g)$, making the method developed in Appendix B inaccurate.

5.4.3.2 Spin Susceptibility as a Function of the Optical Pulse Parameters

Dependence on the length of the optical pulse The results are shown in Fig. 5.29. The top panel shows the reflected amplitude $|S_{11}|$ and bottom the corresponding spin susceptibility at different T_L for $P_L = 1.5\,\text{mW}$. We observe that $\chi''(B_{NV})$ keeps the same triplet shape characteristic of the NV hyperfine structure but its amplitude increases with the optical pulse duration, indicating an increased spin polarization. The bottom panel shows the ratio $\chi''(T_L, B_{NV})/\chi''(T_{max}, B_{NV})$ as a function of

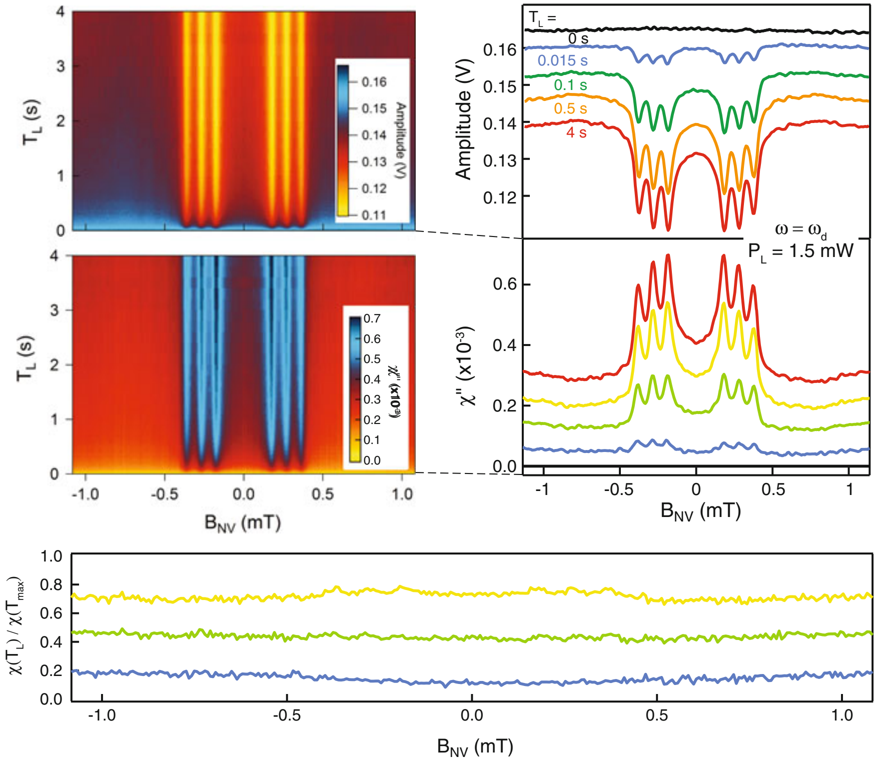

Fig. 5.29 Dependence of the spin susceptibility on the optical pulse duration T_L. (*Top*) Reflected amplitude and corresponding imaginary part of the spin susceptibility $\chi''(B_{NV})$ as a function of the optical pulse duration T_L for a fixed pulse power $P_L = 1.47\,\text{mW}$. The duration T_L is swept from $T_{min} = 0\,\text{s}$ to $T_{max} = 4\,\text{s}$. The *left panel* shows a selection. (*Bottom*) Ratio $\chi''(T_L, B_{NV})/\chi''(T_{max}, B_{NV})$ showing that the shape of the spin susceptibility $\chi''(B_{NV})$ is independent of the optical pulse duration

B_{NV}. This ratio is roughly independent of B_{NV}, which confirms that the optical pulse only induces spin polarization without distorting its susceptibility.

Dependence on the power of the optical pulse We show in Fig. 5.30 the results at different P_L for $T_L = 7\,\mathrm{s}$. The reflected amplitude $|S_{11}|$ and the corresponding spin susceptibility are shown on the top panel, and the ratio $\chi''(P_L, B_{NV})/\chi''(P_{max}, B_{NV})$ as a function of B_{NV} on the bottom. Again, the ratio is roughly independent of B_{NV} which confirms that the optical pulse only induces spin polarization without distorting its susceptibility. We analyze in the next section the spin reset efficiency as a function of the optical pulse parameters.

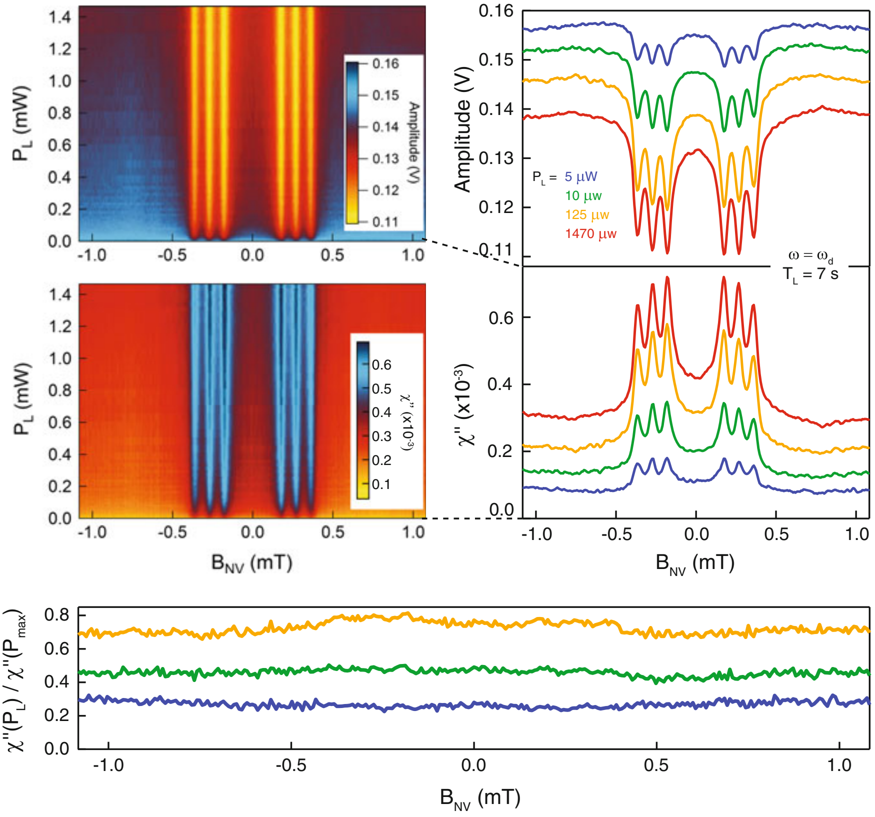

Fig. 5.30 Dependence of the spin susceptibility on the optical pulse power P_L. (*Top*) Reflected amplitude and corresponding imaginary part of the spin susceptibility $\chi''(B_{NV})$ as a function of the optical pulse power P_L for a fixed pulse duration $T_L = 7\,\mathrm{s}$. The power P_L is swept from $P_{min} = 0\,\mathrm{mW}$ to $P_{max} = 1.47\,\mathrm{mW}$. The *left panel* shows a selection. (*Bottom*) Ratio $\chi''(P_L, B_{NV})/\chi''(P_{max}, B_{NV})$ showing that the shape of the spin susceptibility $\chi''(B_{NV})$ is independent of the optical pulse duration

5.4.3.3 Spin Reset Efficiency

As evidenced in the previous section, the spin polarization increases with the energy contained in the optical pulse. To measure the spin polarization as a function of the optical pulse parameters, we choose a magnetic field $B_0 = 0.27\,\text{mT}$ at which we probe the spins and measure the spin susceptibility $\chi''(T_L, B_0)$ (respectively $\chi''(P_L, B_0)$). The relative spin polarization curves $p_{rel} = \chi''(P_L)/\chi''(P_{max})$ for an optical pulse duration $T_L = 6\,\text{s}$ is shown on the left panel of Fig. 5.31. We observe that the polarization increases with P_L and then saturates. This saturation is consistent with our observations of Sect. 5.4.2, demonstrating that the maximum spin polarization accessible using optical repumping is reached, corresponding to $p = 0.9$ according to [3]. From now, we use a laser power $P_L > P_{L,cont}^{sat} = 1\,\text{mW}$ to be as close as possible to this maximum spin polarization and express the spin polarization:

$$p = 0.9 \times p_{rel}(T_L) \times p_{cont}(P_L). \tag{5.12}$$

The dependence of the relative spin polarization with the optical pulse duration T_L for $P_L = 1.47\,\text{mW}$ is shown in the right panel of Fig. 5.31. The polarization increases with T_L and then saturates around $T_L^{sat} \sim 4\,\text{s}$. This suggests that the maximum polarization allowed by optical repumping is reached. The corresponding optical pulse energy is $\sim P_L \times T_L^{sat} = 6\,\text{mJ}$. The black point in Fig. 5.31 corresponds to the polarization level of the spins at equilibrium. We note that the polarization at equilibrium is[4] $p_{eq} = 0.14$, equivalent to an effective temperature $T_{eq} = 900\,\text{mK}$ significantly higher than the temperature of the sample stage (30 mK). This higher spin temperature is attributed to thermal excitation of the spin ensemble by thermal

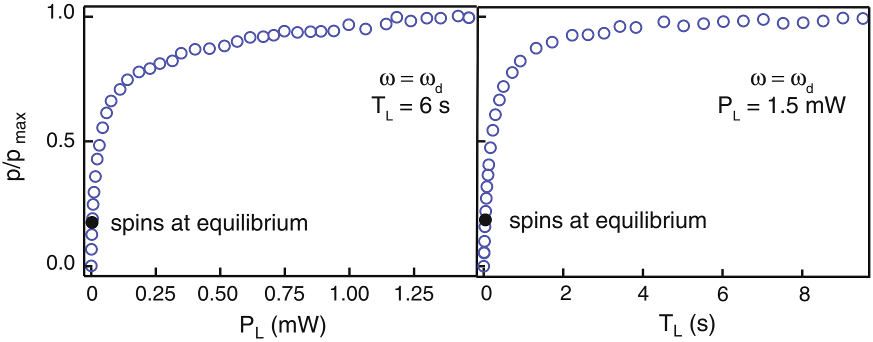

Fig. 5.31 Spin reset efficiency p/p_{max}. (*Left*) The relative spin polarization for $T_L = 6\,\text{s}$ as a function of P_L increases then saturates. This corresponds to our observation in Sect. 5.4.2, suggesting that the maximum polarization accessible by optical repumping is reached. (*Right*) The relative spin polarization for $P_L = 1.47\,\text{mW}$ as a function of T_L increases then saturates. Since $P_L > P_{L,max}$, the saturation corresponds to the maximum polarization accessible by optical repumping

photons coming from RT through the input microwave lines. Indeed, we have seen in Sect. 5.2.2.1 that the attenuation in the input line is not sufficient, implying thermal field with ∼5 photon in the resonator.

---

[4] $p_{eq} = 0.9 \times 0.16 \times 0.967$.

In the following experiments (except when noted), we use a 1 s optical pulse at 1.47 mW as *reset operation* which polarizes the spins at[5] $p = 0.72$. The experimental sequences are repeated at a rate close to 1 Hz with duty cycle close to 1. Note that with these parameters, the refrigerator cold stage is heated up to 400 mK. Such a high temperature would not be acceptable for a quantum memory experiment, and one can wonder whether it is possible to reduce it. Experiments with single NV centers, where the laser spot is well focussed with a spot size of 1 μm^2, polarize a NV center in 10 ns using 100 μW. The same power on a 100 × 100 μm area should thus achieve polarization in 100 μs, which is 5 orders of magnitude more efficient than our observations. We are thus led to the conclusion that our laser spot very likely is not well aligned with the resonator inductance. As explained in Chap. 6 we have indeed confirmed in a later experiment that more efficient repumping was indeed possible with less laser power, which will be crucial to implement the full quantum memory protocol.

5.4.4 Spin Relaxation Time Measurement

To measure the spin relaxation time, one can first excite the spins with a strong microwave pulse and measure their relaxation towards the thermal equilibrium. In our case however, the effective temperature of the spins is already quite high and this measurement technique provides insufficient signal. Instead, we polarize the spins by optical repumping and measure their relaxation towards equilibrium. For that, a series of 20 ms resonant microwave pulses separated by 10 s is applied following the optical reset of the spins. The average reflected amplitude of each pulse is plotted in Fig. 5.32. Note that the same measurement performed at different probe pulse rate yields no change in the relaxation time. This confirms that the probe microwave pulses have a weak enough power ($P_{probe} = -120$ dBm) not to create sizeable excitation during the relaxation process.

We observe a bi-exponential response with time constants $T_{1,a} = 35$ s and $T_{1,b} = 395$ s. The presence of two rates for the relaxation process has already been reported in [9] but its interpretation is not clear in our case. A possible explanation is that the resonator is coupled to two regions of the diamond with different nominal dipolar coupling strength between spins. The existence of two such regions is possible if the diamond have two regions with different spin density within the mode volume of the resonator.

Note finally that the two time constants are very long compared to the timescale of operation in superconducting circuit, which confirms the necessity of an active reset of the spins for the *read* experiment.

---

[5] $p = 0.9 \times 0.83 \times 0.964$.

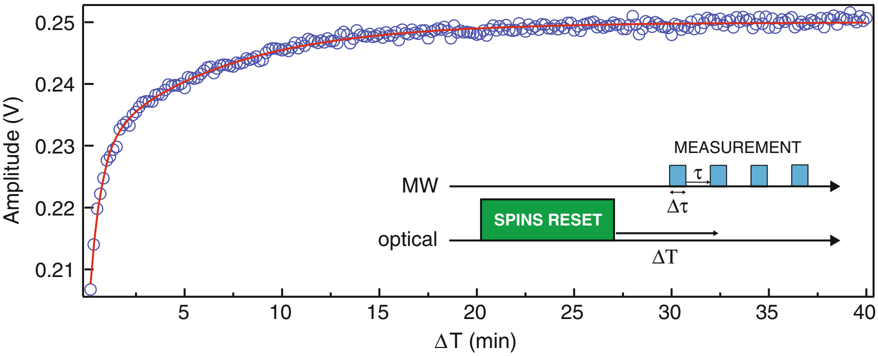

Fig. 5.32 **NV spin relaxation time.** *Blue dots* are the average reflected amplitude of each probe pulse. A bi-exponential fit (*red solid line*) yields $T_{1,a} = 35\,\mathrm{s}$ and $T_{1,b} = 395\,\mathrm{s}$, with respective weights $A_{1,a} = -0.022$ and $A_{1,b} = -0.020$

5.5 Multimode Retrieval of Few Photon Fields Stored in a Spin Ensemble

We now perform echo experiments, in the goal of making progress towards the implementation of the *read step* of our memory protocol. The experiment aims at storing classical microwave pulses with ultra-low power (corresponding to few photons in the resonator), and to retrieve them with a single refocusing pulse with as high fidelity as possible. In the following, we first present a Hahn echo at high power. We then demonstrate multimode storage and retrieval of few photons fields in the spin ensemble and finally discuss the factors limiting the retrieval efficiency.

5.5.1 Applying Hahn Echoes to the Spin Ensemble

The response of the spins to Hahn echo pulse sequences is presented in this section. The time-domain response to microwave pulses of different power is first investigated and the echo of high power stored microwave pulse analyzed. The experiments are performed at zero magnetic field, with a microwave frequency $\omega_e/2\pi = 2.8795\,\mathrm{GHz}$ corresponding to the maximum of the spin absorption (see Fig. 5.16).

5.5.1.1 Response of the Spins to an Incoming Square Microwave Pulse

Hahn echo sequences require to apply strong microwave pulses inducing spin rotations of angle π on the Bloch sphere, therefore bringing the spin ensemble well beyond the Holstein-Primakoff approximation. As a first step, we probe the spin dynamics by investigating the response of the spins to microwave pulses of increasing power [6]. The spins are first polarized at 72 % with an optical pulse of duration

Fig. 5.33 Protocol and setup for response of the spins measurement

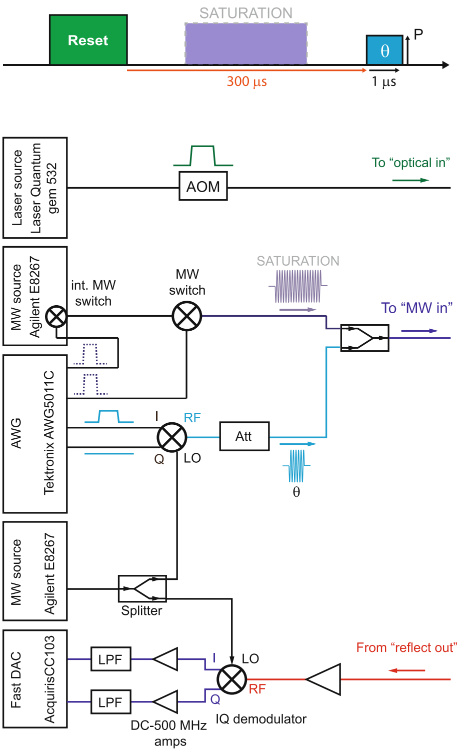
SATURATION
Reset
θ
P
300 µs
1 µs
Laser source
Laser Quantum gem 532
AOM
To "optical in"
MW source
Agilent E8267
int. MW switch
MW switch
SATURATION
To "MW in"
AWG
Tektronix AWG5011C
I
RF
Q
LO
Att
θ
MW source
Agilent E8267
Splitter
Fast DAC
AcquirisCC103
LPF
LPF
I
LO
RF
Q
From "reflect out"
DC-500 MHz amps
IQ demodulator

1 s and power 1.47 mW, and the reflected field of an applied 1 µs square microwave pulse of varying power P is measured by homodyne detection. A first experiment is performed with a saturation pulse applied before the pulse to obtain the resonator response alone and calibrate the signal-line and amplifier response. The microwave and optical setup at room temperature for this measurement is shown in Fig. 5.33, together with the protocol. We use two microwave switches in series to have a 160 dB on/off ratio on the saturation pulse, purposely to limit leakage to the measured pulse. The output demodulated signal is low-pass filtered with 200 MHz bandwidth, averaged over 200 identical sequences, and rescaled by $\sqrt{P}$ for easier comparison.

We start by discussing the data taken at low microwave power ($P_0 = -90$ dBm), for which the Holstein-Primakoff approximation (the linear regime) is valid. They are compared to the bare cavity response obtained by saturating the spins prior to the microwave pulse in Fig. 5.34. The pulse extends from 0.3 to 1.3 µs. We first note that the cavity response is dominantly on the in-phase quadrature. A small response on the other quadrature Q arises from the slight detuning between the microwave frequency ω_e, chosen at the maximum of the spin absorption, and the cavity frequency ω_r. Note also that the cavity field damping time $T_r = 1/\kappa \approx 5$ ns is barely visible on the scale of the figure and is anyway washed out by the detection bandwidth of 200 MHz; the slow increase of the cavity field on the saturated curve is thus not due to the cavity

Fig. 5.34 Response of the spins to an incoming weak microwave pulse. In-phase quadrature (*blue*) and out-of-phase (*green*) quadratures of the reflected field for an applied square microwave pulse of power $P_0 = -90\,\text{dBm}$. The *dashed lines* correspond to the same measurement with the spins saturated

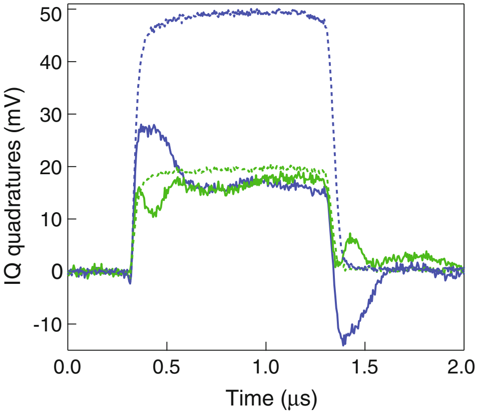

response but either to an imperfect profile of the AWG pulse, or to incomplete spin saturation. With the spins polarized, the in-phase quadrature of the reflected field first increases at the same rate as in the saturated case, before turning down when it reaches a certain value, and finally stabilizing at a lower value, after some oscillatory transient, corresponding to ≈33 % of the initial value.

This behavior is due to the progressive buildup of a steady-state transverse magnetization in the spins, whose radiated field interferes destructively with the intracavity field. After the pulse is switched off, a transient output microwave field is measured, which decays in ∼200 ns. It is radiated by the spin transverse magnetization, which decays in $T_2^* \approx 200\,\text{ns}$ from its steady-state value to 0. This microwave emission by the spins following an excitation pulse is a generic feature in Electron Spin Resonance, called "Free-Induction Decay" (FID). All the dynamics described in this paragraph is quantitatively reproduced by simulations performed by Brian Julsgaard along the lines described in Sect. 2.3.4, taking into account the distributions of spin frequencies (see Fig. 5.16) and coupling strengths (see Fig. 5.7) as seen in Fig. 5.35.

The same measurements performed at higher microwave powers show a progressively modified dynamics, because the spins undergo larger Rabi angles under the drive, leading to a breakdown of the linear approximation. This effect is easier to see on the reflected amplitude (see Fig. 5.36). At low power (the linear regime), after the initial transient where resonator and spins exchange energy, the reflected amplitude reaches half of the saturated value in steady state (region S), indicating that the spins absorb ≈75 % of the incoming power. This steady-state value of the reflected amplitude increases with incoming power, indicating reduced spin absorption caused by progressive saturation of the ensemble. This regime is precisely the regime of interest to apply refocusing pulses.

We note that no clear Rabi oscillations are observed, because of the spatial inhomogeneity of the microwave field generated by the planar resonator (see Fig. 5.7), which causes a spread of Rabi frequency within the ensemble. This inhomogeneity prevents the application of accurate π pulses to all the spins [10], which is an issue for Hahn echo sequences.

The temporal details in Figs. 5.35 and 5.36 are well reproduced, which confirms the validity of the calculations, both in the linear and non-linear regime. The ensemble is assumed of spin-$1/2$ particles, which is an approximation in the case of NV centers having a spin of 1. However, in the linear non-saturated regime, this description is exact, and for the non-linear saturated regime, we expect the approximation to be justified since the applied π-pulse has a narrow frequency bandwidth and is tuned predominantly to the $|0\rangle \rightarrow |+\rangle$ transition of the NV centers.

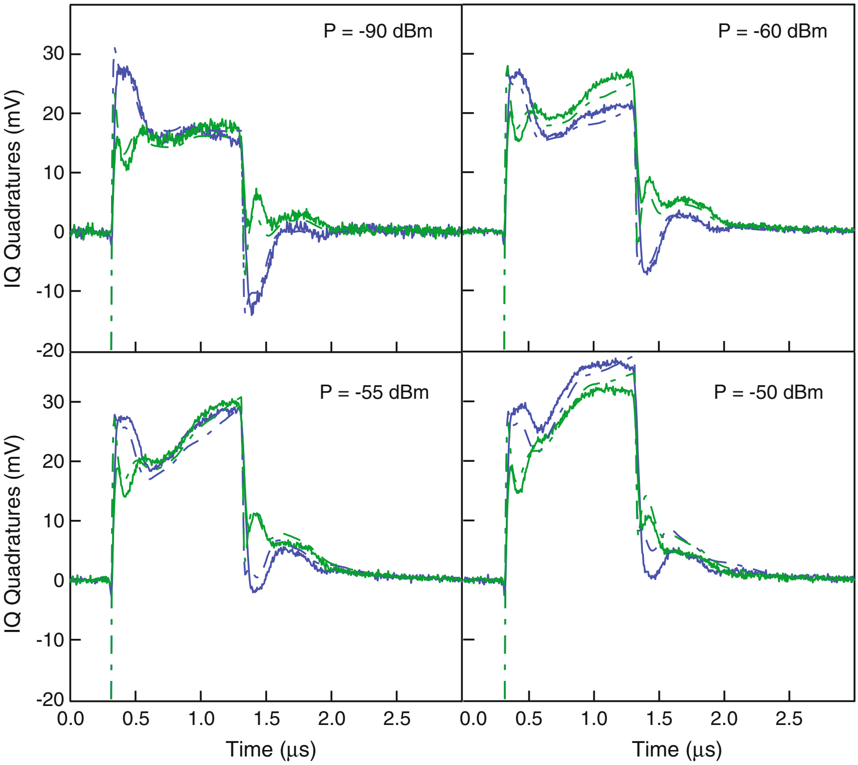

Fig. 5.35 Comparison to the result of numerical simulations. In-phase (*blue*) and out-of-phase (*green*) quadratures of the reflected field for $P = -90$, -60, -55, and -50 dBm. The *curves* have been rescaled by $\sqrt{P/P_0}$ for easier comparison, with $P_0 = -90$ dBm. *Dash-dotted lines* are simulations (see text)

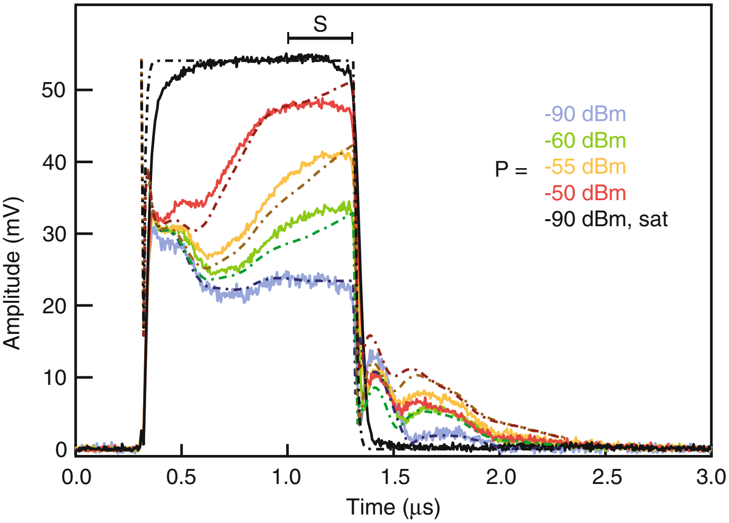

Fig. 5.36 Response of the spins to an incoming square pulse. Amplitude of the reflected field for $P = -90, -60, -55$, and -50 dBm. The curves have been rescaled by $\sqrt{P/P_0}$ for easier comparison, with $P_0 = -90$ dBm. The pulse extends from 0.3 to 1.3 μs, followed in the non-saturated case by the free induction decay signal of the spins. S denoted the steady state region. *Dash-dotted lines* are simulations (see text)

5.5.1.2 Hahn Echo Pulse Sequences

The two-pulse Hahn echo sequence described in Sect. 3.2.2.1 consists in storing a weak pulse θ into the spin ensemble at time t, and applying a strong refocusing pulse R at time τ which triggers the emission of an echo pulse at time $2\tau - t$. We present in the following first Hahn echo measurements, and study the dependence of the echo amplitude on the refocusing pulse parameters.

The microwave and optical setup at room temperature for this measurement is shown in Fig. 5.37, together with the protocol. At the beginning of the sequence, we first polarize the spins at 55 % with an optical pulse of duration 4 s and power 0.2 mW. A weak microwave pulse (θ) is then applied creating a transverse magnetization, followed after a delay τ by a strong refocusing pulse (R). As in the previous experiments, we use two different microwave sources for the weak and strong microwave pulses. Doing so makes it possible to use the internal switch of the microwave source used for the refocusing pulse as a second switch, and thus to reach large on/off ratio (160 dB ratio). Note that for all the echo experiments that follow, it is critical that the two sources conserve their relative phase constant since the phase of the echo ϕ_e is fixed by the respective phase of storage ϕ_θ and refocusing ϕ_R pulses (see Sect. 3.2.2.1). A 1 GHz phase synchronization chain is used purposely, instead of the standard 10 MHz, to phase-lock the two microwave generators and reduce the phase drift between them. The signal is measured by homodyne detection and low-pass filtered with 2 MHz bandwidth. The measurement are averaged over 40 identical sequences thanks to the active reset of the spins. We show in Fig. 5.38 the time evolution of

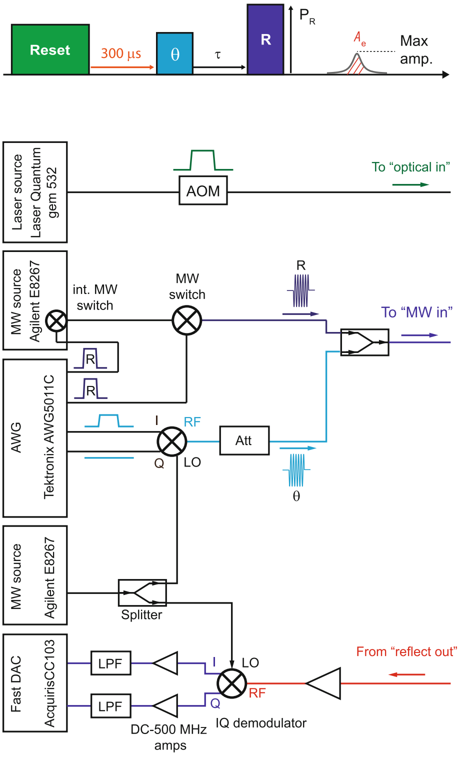
Reset
300 μs
θ
τ
R
P_R
A_e
Max amp.
Laser source Laser Quantum gem 532
AOM
To "optical in"
MW source Agilent E8267
int. MW switch
MW switch
R
To "MW in"
R
R
AWG Tektronix AWG5011C
I
RF
Att
Q
LO
θ
MW source Agilent E8267
Splitter
Fast DAC AcquirisCC103
LPF
LPF
I
LO
Q
RF
From "reflect out"
DC-500 MHz amps
IQ demodulator

Fig. 5.37 Protocol and setup for Hahn echo at high power

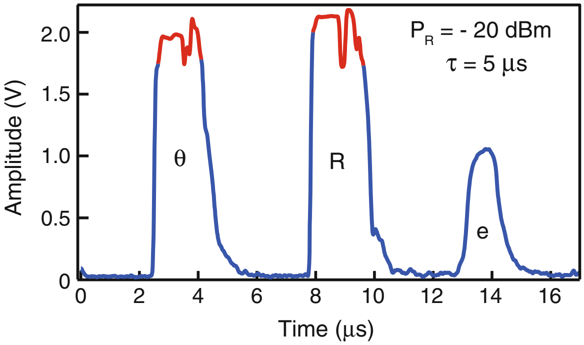

Fig. 5.38 Hahn echo at high power. The echo (*e*) is observed at time 2τ. Saturation of the amplifiers (shown in *red*) limits the measurable amplitude to about 1.8 V

the output signal obtained by applying a 1 μs θ-pulse with power -60 dB, followed $\tau = 5$ μs later by a 1 μs refocusing pulse with power $P_R = -20$ dBm. The expected spin-echo is observed at 2τ.

Hahn echo coherence time measurement To compare experiments to simulations in the rest of this chapter, we determine the Hahn echo coherence time T_2 of the spin ensemble. The sequence depicted in Fig. 5.37 is repeated with increasing duration τ

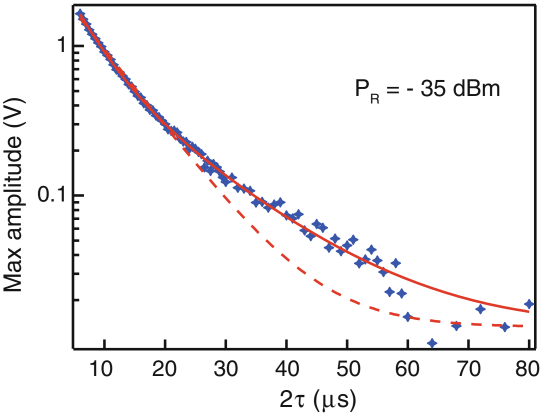

Fig. 5.39 Spin echo coherence time T_2 measurement. Measured (*crosses*) decay of the echo maximum amplitude as a function of τ. *Dashed* and *solid lines* are an exponential fit yielding a characteristic time $T_2 = 8.4\,\mu$s and a bi-exponential fit $f(\tau)$ yielding $T_{2A} = 4.7\,\mu$s and $T_{2B} = 14.3\,\mu$s, respectively

between the storage and refocusing pulses. The decay of the echo maximum amplitude as a function of the duration τ is shown in Fig. 5.39. As seen on the graph, this decay is better fitted by a bi-exponential than by a single exponential decay, with time constants $T_{2A} = 4.7\,\mu$s and $T_{2B} = 14.3\,\mu$s. The corresponding function writes

$$\begin{aligned} f(\tau) = A\ \exp\left(-2\tau/T_{2A}\right) \\ + B\ \exp\left(-2\tau/T_{2B}\right) \end{aligned} \tag{5.13}$$

with weights $A = 0.78$ and $B = 0.22$. This implies that two spin classes with different coherence times contribute to the echo signal. This effect is the object of Sect. 5.6.1; in the following we use the above weights and times constants at zero-magnetic field for the simulations.

Echo amplitude dependence on the refocusing pulse power We show in Fig. 5.40 a selection of measured spin echo signals for a $1\,\mu$s refocusing pulse with increasing power P_R. For each of these curves, a $1\,\mu$s θ-pulse with -60 dBm power is applied at the beginning, followed by a $5\,\mu$s waiting period. The power of the refocusing pulse ranges from -70 to -20 dBm, which corresponds to the non-linear regime of Fig. 5.36. We observe that the shape of the echoes depends on P_R and that their amplitude increases and then saturates. This saturation indicates that in average half of the spins are inverted. To go further, we perform a simulation as described in Chap. 2, using the coherence time corresponding to the single-exponential fit of Fig. 5.39. The results are superimposed on the measurements in Fig. 5.40. The details of the shape are captured by the simulations: (i) the echo pulse shape is well reproduced, (ii) the free-induction decay following both the θ and the π pulse is reproduced in a qualitative manner. If the amplitude of the echo is found to depend as expected on P_R, even the shape of the pulse varies from a rounded Gaussian-like pulse at low P_R up to a sharp rectangular pulse at higher P_R values. This striking shape dependence is well reproduced in the simulations as well. It can be qualitatively understood by reasoning in the frequency domain. Indeed, for the shape of the initial pulse to be

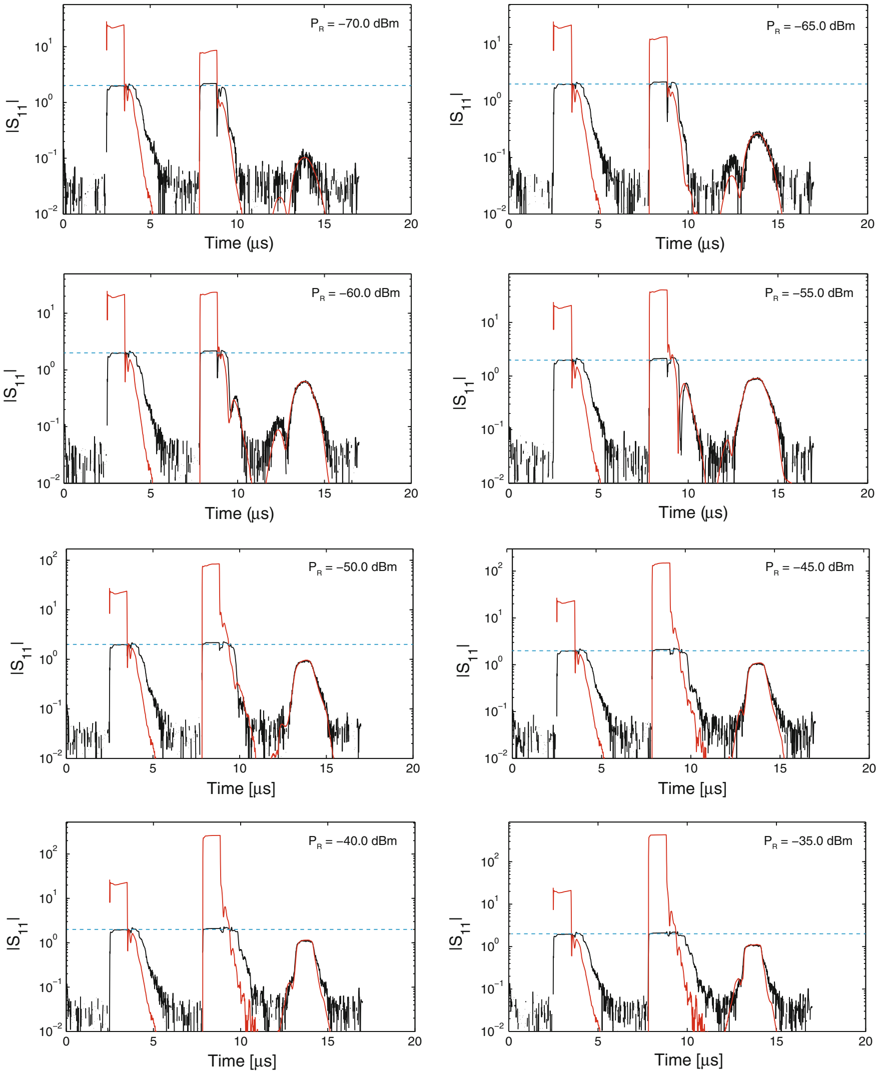

Fig. 5.40 Dependence of the echo shape on the refocusing pulse power. Measured (*black*) and simulated (*red*) Hahn echo for a selected refocusing pulse power P_R. The simulations are rescaled to match the area of the echo pulses. Saturation of the amplifiers (*blue dashed line*) limits the measurable amplitude to about 2 V

well reproduced as an echo, all the frequency components of the spin polarization profile generated by the θ pulse need to be refocused as efficiently. At large P_R, the large Rabi frequencies reached by the spins cause all spin frequency components generated by the θ to be equally rephased, but this is no longer the case at lower P_R. Then the echo results from the convolution of the two pulses, and gets more rounded.

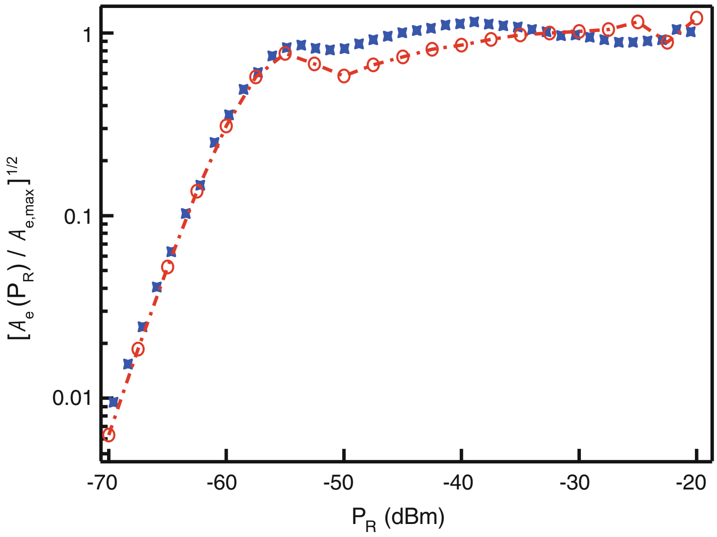

Fig. 5.41 Dependence of the echo amplitude on the refocusing pulse power. Experimental (*crosses*) and simulated and rescaled (*open circles*) area of the echo as a function of the refocusing pulse power P_R

To compare the dependence of the echo amplitude quantitatively, we plot the experimental and simulated area of the echo as a function of the refocusing pulse power P_R on the left of Fig. 5.41. The agreement is quantitative, and in particular the power $P_{R,sat} = -55$ dBm at which the echo amplitude saturates is well predicted by the simulations. This brings further evidence of the validity of calculated coupling strengths and of the spin-1/2 approximation. In the following, we keep the refocusing pulse power higher than the saturation power $P_{R,sat}$ to maximize the echo efficiency.

5.5.2 *Retrieval of Few-Photon Pulses Stored in the Spin Ensemble*

In the previous section, we have seen that applying Hahn echoes at high power in a hybrid quantum circuit is possible. Coming back to the perspective of developing a quantum memory, we now store and retrieve much weaker microwave pulses down to the few-photon level, and demonstrate the multimode ability of the spin ensemble.

5.5.2.1 Experimental Results

Since our chip does not include a superconducting qubit, we use a train of weak microwave pulses with varying phase to quantify the retrieval efficiency. The protocol and experimental setup are shown in Fig. 5.42. At the beginning of the sequence, spins are polarized at 72 % with an optical pulse of duration 1 s and power 1.47 mW. Six consecutive microwave pulses θ_i $(i = 1, ..., 6)$ with different phase and identical amplitude corresponding to $\approx 10^4$ photons in the resonator are applied to the spin ensemble, followed 10 µs later by a refocusing pulse R to trigger their retrieval. The pulses θ_i are Gaussian pulses of duration 1.2 µs with peak power −89.7 dBm and phases $\varphi_{1,2,4} = -\pi/4$ and $\varphi_{3,5,6} = \pi/4$. The refocusing pulse is a 1 µs squared pulse at −40.6 dBm with phase $\varphi_R = 0.1$ rad. As in the previous section, the strong refocusing pulse has a 160 dB on/off ratio obtained by using two microwave switches in series, and the storage pulse is obtained using an IQ mixer driven by an AWG. The output microwave signal is low-pass filtered with 5 MHz bandwidth and measured by homodyne detection. The sequence is repeated 10^4 times at 1 Hz rate, which is made possible by the active reset of the spins. The resulting averaged amplitude and IQ quadratures of the reflected field are shown in Fig. 5.43. In the inset of this figure, we also show the energy of the reflected θ_i pulses with the spins saturated and reset in their ground state, showing that about 75% of the incident power is absorbed by the spins, in agreement with the measurements shown in Fig. 5.36.

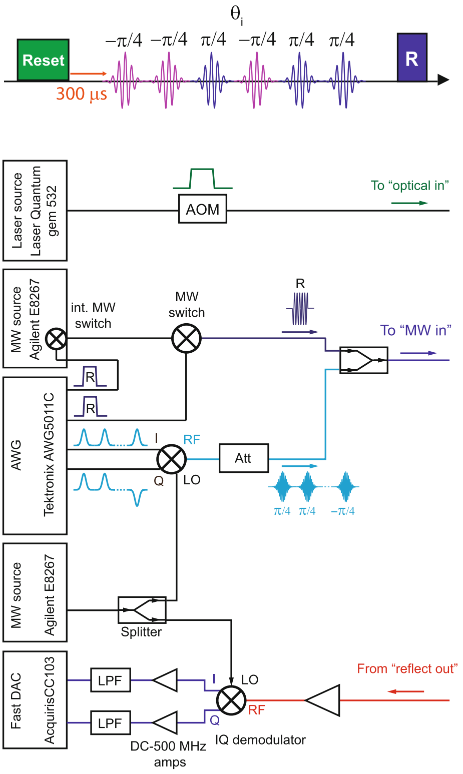
θ_i
−π/4 −π/4 π/4 −π/4 π/4 π/4
Reset
300 µs
R
Laser source
Laser Quantum gem 532
AOM
To “optical in”
MW source
Agilent E8267
int. MW switch
MW switch
R
To “MW in”
R
R
AWG
Tektronix AWG5011C
I
RF
Q
LO
Att
π/4 π/4 −π/4
MW source
Agilent E8267
Splitter
Fast DAC
AcquirisCC103
LPF
LPF
I
LO
Q
RF
From “reflect out”
DC-500 MHz amps
IQ demodulator

Fig. 5.42 Protocol and setup for multimode storage and retrieval. Experimental sequence including a spin reset pulse, a train of six microwave pulses θ_i $(i = 1, \ldots, 6)$ with an identical amplitude (corresponding to $\sim 10^4$ photons in the resonator) and different phases $\varphi_{i=1,2,4} = -\pi/4$ and $\varphi_{i=3,5,6} = \pi/4$, and a 50 dB stronger refocusing pulse R with phase $\varphi_r = 0.1$ rad

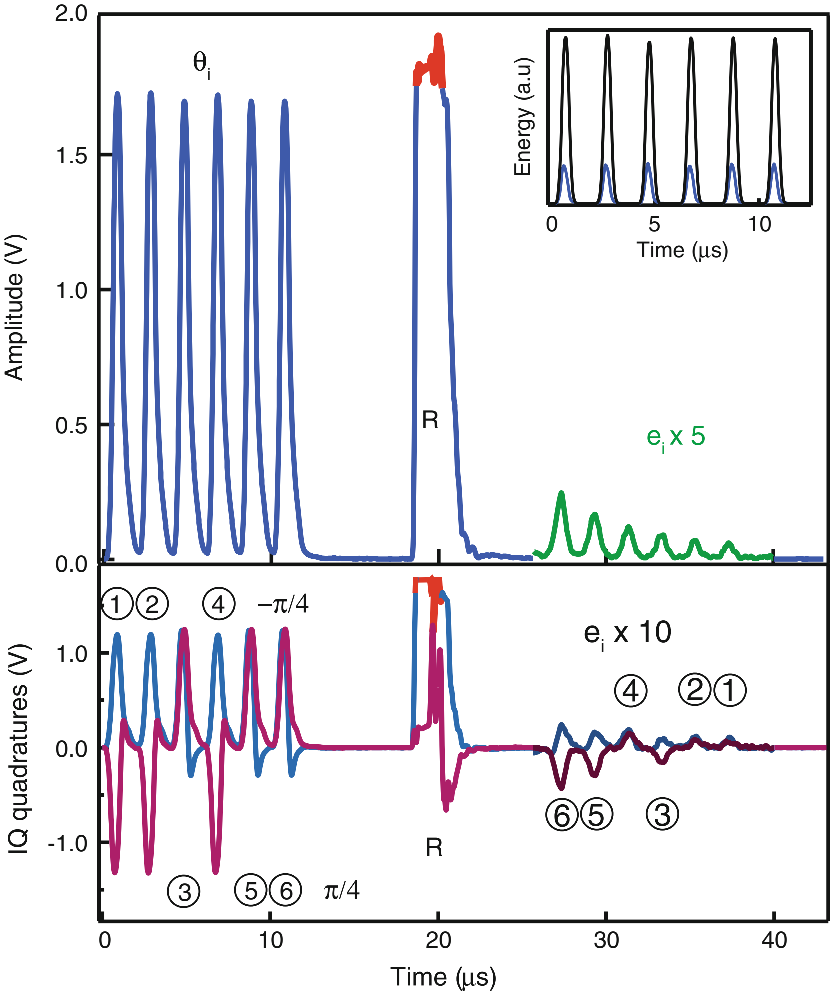

Fig. 5.43 **Retrieval of multiple weak microwave pulses initially stored in the spin ensemble.** (*Top*) Amplitude of the measured output signal showing the reflected pulses θ_i (after partial absorption by the spins) and R (its amplitude being trimmed by amplifier saturation, shown in *red*), as well as the six re-emitted echoes e_i (magnified by a factor 5). *Inset* the comparison between the energies of the reflected θ_i pulses with the spins saturated (*black line*) or reset in their ground state (*blue line*) shows that about 75 % of the incident power is absorbed by the spins. (*Bottom*) IQ quadratures of the output signal, showing that the e_i pulses (magnified by 10) are recovered with phase $-(\varphi_i - \varphi_r)$, as expected

The reflected amplitude shows the pulses θ_i after partial absorption by the spins, the refocusing pulse R (with its amplitude trimmed by amplifier saturation), as well as the six re-emitted echoes e_i (magnified by a factor 5). The six pulses are recovered up to 35 μs after their storage, with an amplitude reduced by $\sim 10^2$ compared to the incoming pulse, corresponding to ~ 1 photon in the resonator. The in-phase and out-of-phase quadratures (bottom panel) shows that the pulses are re-emitted in reverse order, as explained in Chap. 3, with phase $-(\varphi_i - \varphi_R)$. We conclude from these observations that the strong refocusing pulse ($\sim 10^9$ photons in the cavity) does not prevent detection of fields at the single-photon level few microseconds later, a prerequisite for the implementation of the full quantum memory protocol. Note that, as discussed in [1], the multimode storage and retrieval only works because of the low power used for the θ_i pulses, otherwise each pulse would act as a refocusing pulse for the previous ones, which would generate a wealth of spurious echoes.

We were able to detect a measurable spin-echo signal with a reasonable measurement time for pulses containing up to 100 times lower energy than in Fig. 5.43, thus populating the resonator with $\bar{n} \approx 100$ photons on average. We performed this experiment with a single storage microwave pulse because of the reduced bandwidth of the detection (1 MHz). The setup (see Fig. 5.44) differs from the one of the previous experiment in order to reach the sensibility required. An additional amplifier after the IQ demodulator is added. To avoid saturation of its saturation, the local oscillator of the IQ demodulator is pulsed to suppress the refocusing pulse from the reflected signal. The protocol is shown on the top of Fig. 5.44. As in the previous measurements, at the beginning of the sequence the spins are first polarized at 72 % with an optical pulse of duration 1 s and power 1.47 mW. The storage pulse is a square pulse of duration $2\,\mu$s with peak power -110 dBm, the refocusing pulse identical to the

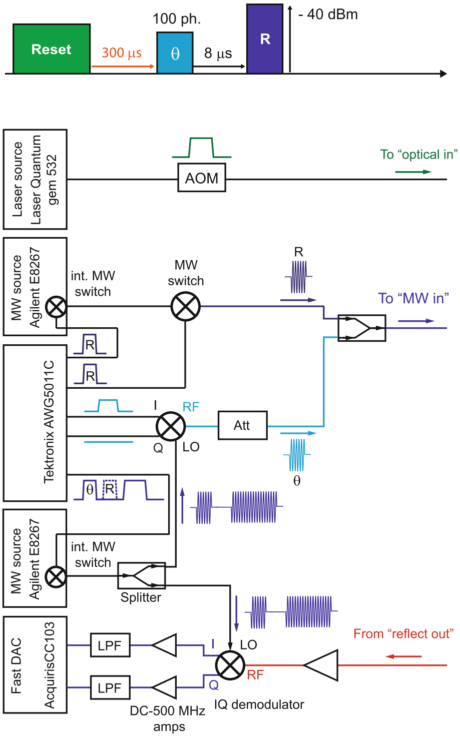
100 ph.
- 40 dBm
Reset
300 μs
θ
8 μs
R
Laser source
Laser Quantum
gem 532
AOM
To "optical in"
MW source
Agilent E8267
int. MW
switch
MW
switch
R
To "MW in"
R
R
Tektronix AWG5011C
I
RF
Att
Q
LO
θ
θ
R
MW source
Agilent E8267
int. MW
switch
Splitter
Fast DAC
AcquirisCC103
LPF
LPF
I
LO
Q
RF
From "reflect out"
DC-500 MHz
amps
IQ demodulator

Fig. 5.44 Protocol and setup for few photon pulse storage and retrieval. The local oscillator of the IQ demodulator is pulsed to suppress the refocusing pulse from the reflected signal

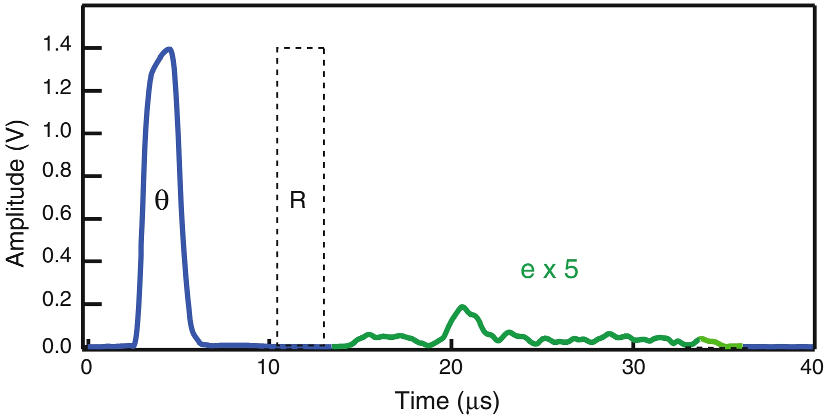

Fig. 5.45 Retrieval of a few-photon field initially stored in the spin ensemble. The echo e with $\sim$0.02 photons in the resonator is obtained for a θ pulse populating the resonator with only $\sim$100 photons. The refocusing pulse (*dashed line*) was suppressed in the room-temperature detection chain by a microwave switch to avoid saturating the follow-up amplifiers

one of Fig. 5.43. The experiment is averaged over more than 10^6 identical sequences to increase the signal to noise ratio.

The measured reflected amplitude is shown in Fig. 5.45. A spin-echo e of $\sim$0.02 photons in the resonator is observed. Coming back to the figures of merit defined at the beginning of this chapter, these measurements reach $n_{MW} \approx 3$, $n_{sp} \approx 0.1$, $\bar{n} \approx 100$, and $E \approx 2 \cdot 10^{-4}$.

5.5.2.2 Analysis

RETRIEVAL EFFICIENCY

An important figure of merit for this experiment is the field retrieval efficiency E, that we defined at the beginning of this chapter as the ratio between the energy recovered during the echo and the energy of the incoming pulse. The amplitude of the echo is seen to decrease with τ due to spin decoherence following the function $f(\tau)$ fitted in Fig. 5.39. Accordingly the experimental retrieval efficiency E_e follows approximately the relation $E_e = 0.03|f(\tau)|^2$, reaching $E_e = 2.4 \cdot 10^{-4}$ for $2\tau = 17\,\mu\text{s}$ (see Fig. 5.46). Reaching the quantum regime however requires a recovery efficiency E close to 1, and therefore calls for a quantitative understanding of our measurements imperfections. In this aim, we compare our experimental findings to the results of the numerical simulations performed by Brian Julsgaard at Aarhus University. Compared to what is described in Sect. 2.3, it is necessary to consider the two spin classes with different coherence time $T_{2,A}$ and $T_{2,B}$ (see Fig. 5.39). This was achieved by running the simulations twice with a single coherence time T_{2A} (respectively T_{2B}) and combining the results[6] according to the spin class weights A

---

[6] Further simulations have shown that this approximation is well justified.

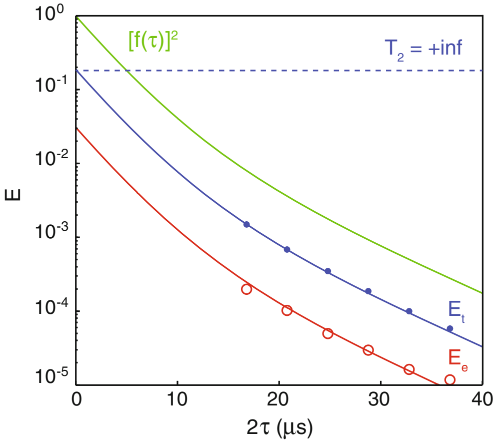

Fig. 5.46 The retrieval efficiency. The field recovery efficiency of the experimental (*red*) and simulated (*blue*) echo pulses versus the delay 2τ. The function $[f(\tau)]^2$ (*green*) is scaled such that $f(\tau = 0) = 1$ and shown for comparison. The experimental and simulated retrieval efficiencies follow the function $[f(\tau)]^2$ as $E_e = 0.03|f(\tau)|^2$ and $E_t = 0.21|f(\tau)|^2$, respectively. The *dash-dotted line* corresponds to the retrieval efficiency with infinite T_2

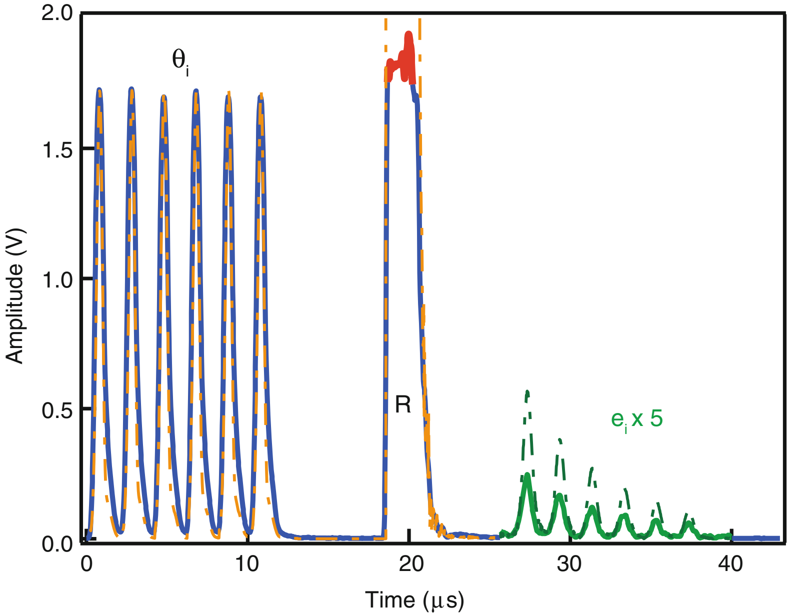

Fig. 5.47 Retrieval of multiple weak microwave pulses initially stored in the spin ensemble: the comparison with numerical simulations

and B. The simulations and experimental data are compared in Figs. 5.46 and 5.47. The measurements are quantitatively reproduced, although with a discrepancy in the amplitude of the echo by a factor 2.5.

We attribute this discrepancy to the imperfect modeling of decoherence. Indeed, our simulations treat spin decoherence in the Markov approximation, which is not adequate for a spin bath environment which displays strong memory effects. In particular this Markov approximation describes improperly the dynamics of a spin under the action of a microwave drive, as happens during the refocusing pulse. This non-Markovian bath causes the Rabi oscillation of a single spin to decay faster than the spin-echo damping time T_2 as was observed in [11] for instance. This effect is not included in our simulations and might explain the remaining discrepancy between the simulations and experimental data.

FACTORS LIMITING THE RETRIEVAL EFFICIENCY

We can extract from the simulations an interesting figure of merit, which is the efficiency that would be obtained if the NVs had infinite T_2. Indeed, the simulated retrieval efficiency in Fig. 5.46 is well fitted by the relation $E_t = 0.21|f(\tau)|^2$. This indicates that E_t would reach 0.21 if the coherence time was infinite. The finite spin coherence causes a $\sim 10^3$ reduction of the retrieval efficiency, thus appearing as the main limitation to the retrieval efficiency in this hybrid circuit.

The second limiting factor to the retrieval efficiency is the finite spins coupling to the cavity. When repumped, spins absorbed only 75 % of the incoming microwave pulses in the present experiment (see inset in Fig. 5.43), and inversely, they re-emit in the cavity with the same efficiency. The finite spin absorption and re-emission in the cavity thus causes a $\sim 0.75^2$ reduction of the retrieval efficiency. This effect depends only on the cooperativity, which is a parameter adjustable by the choice of the resonator quality factor. With a cooperativity superior to 1 (as in the experiment reported in Chap. 4), the absorption and re-emission would be perfect.

The remaining ~ 0.43 reduction of the retrieval efficiency is attributed to the imperfection of the refocusing pulse. We inferred in Sect. 5.2.1.3 and confirm experimentally in Sect. 5.5.1.1 that precise π-pulses cannot be applied to all the spins due to the strong field spatial inhomogeneity of the microwave field generated by the planar resonator. This means that only the fraction of the spins which are inverted by the refocusing pulse participate to the emission of the echo. To summarize, the efficiency budget is:

$$2.4\cdot 10^{-4} = \underbrace{10^{-3}}_{\text{finite coherence time}} \times \underbrace{0.75^2}_{\text{finite coupling to the cavity}} \times \underbrace{0.43}_{\text{imperfections of the refocusing pulse}}$$

The progress margins are discussed in Chap. 6.

5.6 NV Clock Transitions for Long Coherent Storage

The previous experiments demonstrate that the storage and retrieval in a spin ensemble is possible, paving the way towards the development of an operational quantum memory for superconducting qubits. A quantum memory, however, is only useful if it has long enough memory times. In our experiments, the storage time was limited to few microseconds due to the relatively short coherence time of the spin ensemble. This decoherence was caused by the magnetic environment of the spin ensemble, mainly due to the large concentration of P1 centers in our samples, which interact with the NVs by dipolar interactions. If the NV frequency was stationary with respect to magnetic field, they would become insensitive to first order to the P1 centers and hence should have an enhanced coherence time. The spin mixing caused by the strain that we described in Sect. 2.2.2.1 induces such sweet spots: they are called clock transitions (CTs) because of their high-finesse that can be used in the context of frequency standards. An enhancement of the echo coherence time at the CTs has been reported by Wolfowicz et al. [12] with bismuth donors in silicon. In the following, we investigate the echo coherence times at the CTs with NV center.

5.6.1 Atomic Clock Transitions in NV Centers in Diamond

To understand the origin of the clock transitions, we have to take a closer look to the NV Hamiltonian. As explained in Sect. 2.2.2.1, the degeneracy at zero magnetic field is lifted due to the effect of strain and local electric fields. The NV eigenstates are shown for a typical value of the strain parameter E in Fig. 5.48 as a function of B the

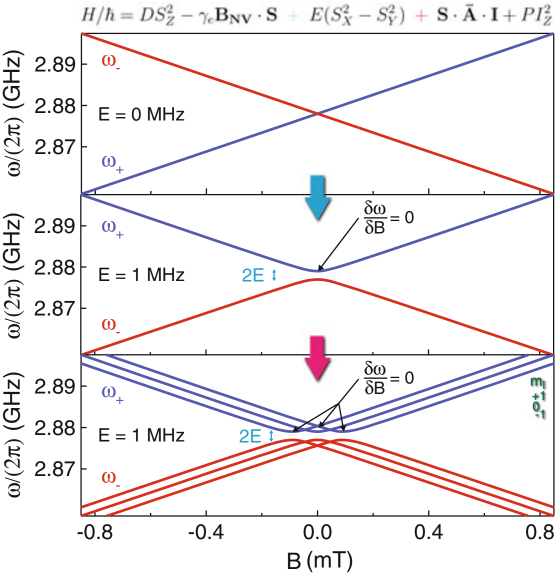

Fig. 5.48 **Origin.** The NV eigenstates present sweet spots $d\omega_{NV}/dB = 0$, at which the NV energy is insensitive to first order magnetic field fluctuations. These points originate from an effect of strain and are m_I-dependent

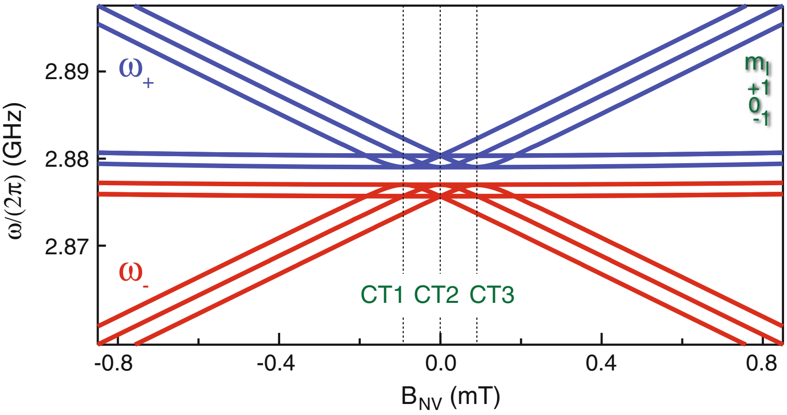

Fig. 5.49 **The three atomic clock transitions in NV center spins.** The clock transitions are positioned at $B = -B_{hf}$ for $m_I = -1$ (CT1), $B = 0$ for $m_I = 0$ (CT2) and $B = +B_{hf}$ for $m_I = +1$ (CT2)

magnetic field along the NV axis. At zero-magnetic field, the frequency is stationary, which yields a first order insensitivity to magnetic field fluctuations. This point $B = 0$ corresponds to a clock transition. Additionally, in our sample the hyperfine coupling with the $I = 1$ nuclear spin of the ^{14}N nitrogen atom causes the two transition frequencies between $m_S = 0$ and $|\pm\rangle$ to become m_I-dependent, resulting in 6 different possible transition frequencies $\omega_{m_I,\pm}(B)$. As a result, $d\omega_{m_I,\pm}/dB = 0$ at $B = m_I B_{hf}$ with $B_{hf} = A_{\parallel}/|\gamma_e|$, defining three m_I-dependent points where the NV energy is insensitive to first order magnetic field fluctuations. These three clock transitions are positioned at $B = -B_{hf}$ for $m_I = -1$ (CT1), $B = 0$ for $m_I = 0$ (CT2) and $B = +B_{hf}$ for $m_I = +1$ (CT3) as shown in Fig. 5.49. At the CTs, the contribution of the magnetic field fluctuations to the NV linewidth is reduced to second order and the strain and electric field fluctuations become dominant.

We have seen in Fig. 5.17 that in our sample the strain E increases approaching the zero-field splitting, which broadens the NV linewidth. This means that contrary to the isolated NV center case where the free induction decay time T_2^* becomes longer at the CTs (as evidenced in [13]), T_2^* decreases in our case. Strain fluctuations, however, are expected to be mainly static implying that their effect can be refocused. As a result, at the CTs we thus expect to see an enhancement of the echo coherence time T_2.

5.6.2 Full System Spectroscopy

In this section, we extend the spectroscopy performed in Sect. 5.3.2.2 to different magnetic field to identify experimentally the three clock transitions points. We then verify that the spectrum can be quantitatively understood at all magnetic fields with the distributions of NV Hamiltonian parameters we have extracted at zero field.

5.6.2.1 Magnetic Field Dependent Spin Susceptibility

The linear resonator was designed purposely to have a large linewidth (see Sect. 5.2.1.2). This makes it possible to probe the spins within a relatively large magnetic field span around the zero-field splitting. The NV spectrum is probed as in Sect. 5.3.2 by measuring the complex reflection coefficient S_{11} of a continuous microwave signal with frequency ω for various applied magnetic field B_{NV}. A continuous optical irradiation at $P_L = 0.2\,\mathrm{mW}$ is applied to polarize the spins at $p = 0.68$. The probe power corresponds to $n \approx 20$ photons in the resonator, sufficiently low to avoid changing the spin polarization, and for the Holstein-Primakoff approximation to remain valid. We show in Fig. 5.50 the corresponding spin susceptibility calculated using the formulas Eqs. 2.111 and 2.112 in Sect. 2.3.3, taking into account the losses induced in the resonator by the laser irradiation.

Noteworthy the energy levels are well resolved. At large $|B_{NV}|$, one identifies the two spin groups: the first one shows a linear B_{NV} dependence which originates from the *N-Orth* group, the other has a quadratic dependence with the magnetic field coming from the *Orth* group. The contributions from the two groups overlap, the lines broaden, and a complicated pattern emerges at magnetic fields closer

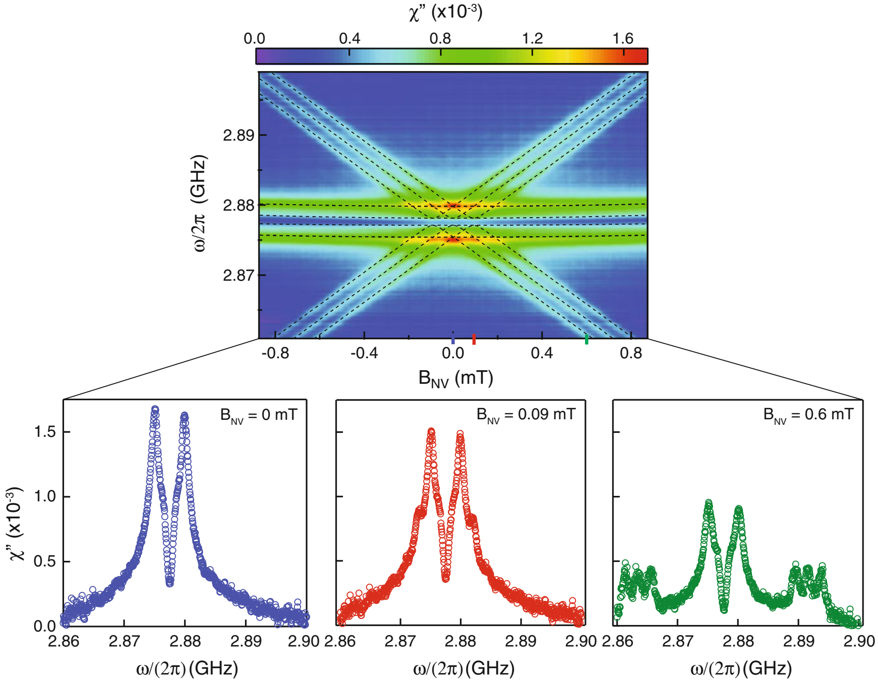

Fig. 5.50 Full NV spectroscopy. The spin susceptibility is measured as a function of the magnetic field B_{NV} by microwave reflection measurement. The spin signal is increased by polarizing the spins by a continuous 0.2 mW optical irradiation. *Blue*, *red* and *green curves* are cut at $B_{NV} = 0, 0.09, 0.6\,\mathrm{mT}$

to 0. We distinguish the three CTs for the *N-Orth* group at $B_{CT1}, B_{CT2}, B_{CT3} = -0.09, 0, +0.09\,\mathrm{mT}$.

5.6.2.2 Comparison to the Results of Numerical Simulations

In Sect. 5.3.2.2, we have extracted the m_I-dependent distributions of NV Hamiltonian parameters for the two spin groups (*Orth* and *N-Orth*). These distributions can be used to quantitatively understand the spin susceptibility at any magnetic field of Fig. 5.50. In this aim, the susceptibility is computed for B_{NV} without further adjustable parameters and rescaled to match the spin polarization of the experiment. The comparison between the experimental and computed susceptibilities is shown in Fig. 5.51. The m_I contributions to the susceptibility are also shown (sum of the hyperfine components of two spin groups *Orth* and *N-Orth*). One observes that the agreement is semi

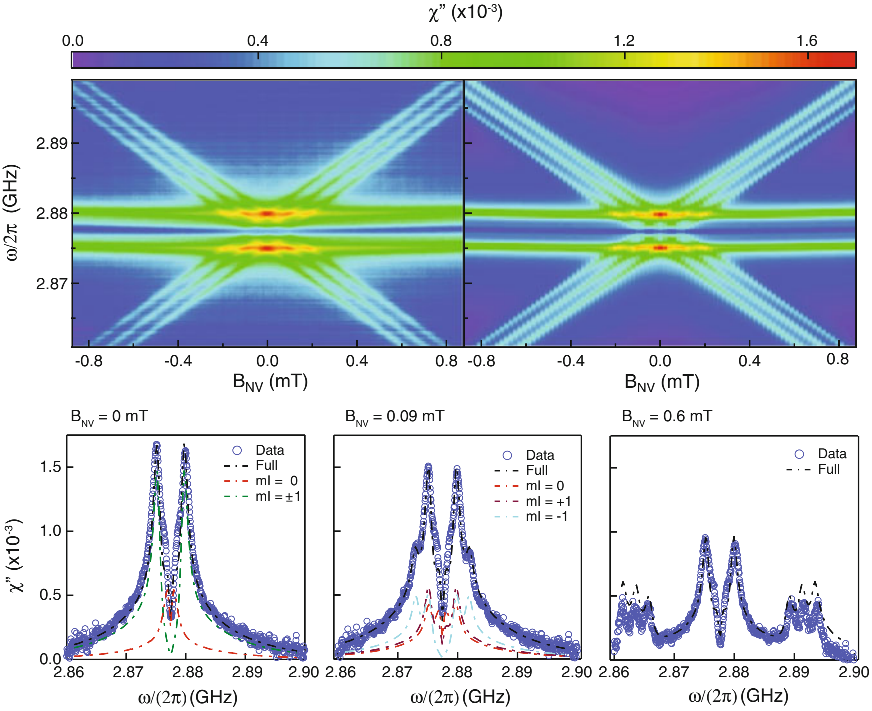

Fig. 5.51 Comparison of the measured spin susceptibility with the results of numerical simulations. Measured (*top left*) and computed (*top right*) two-dimensional plots of the spin susceptibility. The *bottom panel* shows the spin susceptibility at $B_{NV} = 0, 0.09, 0.6\,\mathrm{mT}$. The *dash-dotted line* is the computed spin susceptibility, rescaled to match the experimental spin polarization. The computed m_I contributions to the spin susceptibility are also shown (*red*, *purple* and *light blue dash-dotted lines*). At $B_{NV} = 0\,\mathrm{mT}$, the contributions from $m_I = -1$ and $m_I = +1$ add up (*green dash-dotted line*)

quantitative with some discrepancies visible at high magnetic fields. The contributions of the six spin classes ($m_I = 0, \pm 1$ for the two spin groups *Orth* and *N-Orth*) to the spin susceptibility provide information on the relative weight of the spins that are at the CT (IN CT) and not (OUT CT), for a fixed magnetic field. For the *N-Orth* group, at $B_{NV} = B_{CT2}$, spins $m_I = 0$ are IN CT while spins $m_I = \pm 1$ are OUT CT. At $B_{NV} = B_{CT1}$ (respectively $B_{NV} = B_{CT3}$), spins $m_I = -1$ (respectively $m_I = +1$) are IN CT while spins $m_I = 0$ and $m_I = +1$ (respectively $m_I = -1$) are OUT CT. For the *Orth* group, this is different due to its quadratic dependence on the magnetic field. The hyperfine component $m_I = 0$ is IN CT and the two others $m_I = \pm 1$ are OUT CT independently of the magnetic field (true at low magnetic field).

Two spin contributions (IN and OUT CT) are thus expected for the echo, summarized in the Table. This suggests an echo decay with two time constants $T_{2,IN}$ and $T_{2,OUT}$ and relative weight A_{IN}/A_{OUT} corresponding to the relative weight of the IN and OUT CT computed spin classes contributions to the spin susceptibility.

	$B_{NV} = B_{CT1}$	$B_{NV} = B_{CT2}$	$B_{NV} = B_{CT3}$
IN CT	$m_I = 0$ *Orth*	$m_I = 0$ *Orth*	$m_I = 0$ *Orth*
	$m_I = -1$ *N-Orth*	$m_I = 0$ *N-Orth*	$m_I = +1$ *N-Orth*
OUT CT	$m_I = \pm 1$ *Orth*	$m_I = \pm 1$ *Orth*	$m_I = \pm 1$ *Orth*
	$m_I = 0, +1$ *N-Orth*	$m_I = \pm 1$ *N-Orth*	$m_I = -1, 0$ *N-Orth*

For CT2, this model is not approximate, since the slopes $\frac{\delta\omega}{\delta B_{NV}}$ of the spin classes within IN CT (respectively OUT CT) are identical. For CT1 and CT3, this is an approximation: the six spin classes involve strictly speaking six time constants since the slope $\frac{\delta\omega}{\delta B_{NV}}$ of the spin classes energies levels are different. Within IN CT (respectively OUT CT) the slope $\frac{\delta\omega}{\delta B_{NV}}$ of the spin classes are close, which justify for CT1 and CT3 the dissociation in two time constants at the CTs rather than six. In the following, we measure the echo coherence times for various magnetic fields and use the predicted relative weight to deconvolve the contribution to the echo decay of the spins which are IN and OUT CT.

5.6.3 Dependence of the Echo Coherence Time on the Magnetic Field

5.6.3.1 Protocol and Setup for Coherence Time Measurement

The protocol and setup for this measurement are identical to Fig. 5.37 of Sect. 5.5.1.2. The spins are first polarized at 55 % with an optical pulse of duration 4 s and power 0.2 mW. A 2 μs storage pulse with power −60 dBm is then applied, followed by a 1 μs refocusing pulse after a variable delay τ. The echo signal of amplitude A is

Fig. 5.52 Variation of the probe frequency with B_{NV}. The echo coherence time dependence on the magnetic field B_{NV} is measured on resonance with the $m_I = 0$ component of the NV

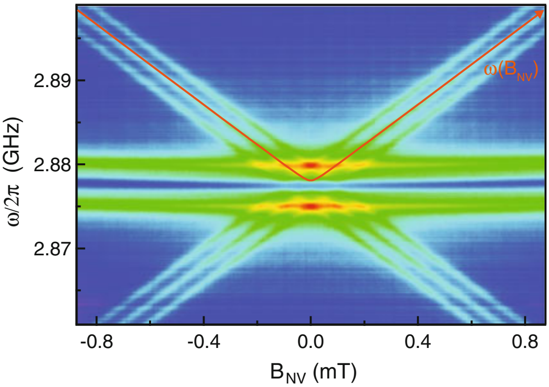

detected at time 2τ by homodyne detection. Note that the duration of the microwave pulses and of the subsequent free induction decay signal makes it possible to properly measure A only for $\tau \geq \tau_0$ with $\tau_0 = 3\,\mu$s. This restriction will be a constraint for the determination of the echo decay in the following because it implies that we miss the beginning of the curve, which is important to determine the shape of the echo. The echo coherence time dependence on the magnetic field is measured at the central NVs resonance. To do so, the probe frequency is varied with B_{NV} according to the function $\omega(B_{NV}) = A + \sqrt{E^2 + (g_e \mu_B B_{NV} \cos(\beta))^2}$, an approximation of the NV Hamiltonian with $D = 2.8775$ MHz and $E = 1$ MHz. We show in Fig. 5.52 the function $\omega(B_{NV})$ superimposed on the NV spectrum.

5.6.3.2 Experimental Result and Analysis

The resulting $A(B_{NV}, \tau)$ is shown in the *left* panel of Fig. 5.53. The echo is seen to decay slower in the region around zero-field and longer decay tails are observed at the three magnetic field values $B = -0.09, 0, +0.09$ mT corresponding precisely to the CTs positions. This is shown more quantitatively in the *right* panel of Fig. 5.53 where the time τ_1 at which $A(2\tau 1)/A(2\tau_0)$ reaches 0.1 is plotted.

To verify that the enhancement at the CTs is indeed linked to the magnetic field bias and not to the frequency for instance, we repeat these measurements for different frequencies ω. To do so, both the magnetic field and the probe frequency are swept linearly and the echo signal detected. The resulting $T_{dec}(B_{NV}, \omega)$ is shown in Fig. 5.54. We observe that the coherence time enhancement at the CTs is verified at all frequencies that lift the ambiguities on the effect of the frequency adjustment $\omega(B_{NV})$.

We return to Fig. 5.53. The three hyperfine components $m_I = -1, 0, +1$ of the *N-Orth* group contribute successively to the echo decay with a long coherence time resulting in $T_{dec,CT=1,2,3} = 13.5, 13, 14\,\mu$s at the three clock transitions respectively; outside these three points, T_{dec} is shorter. The overall effect in the region

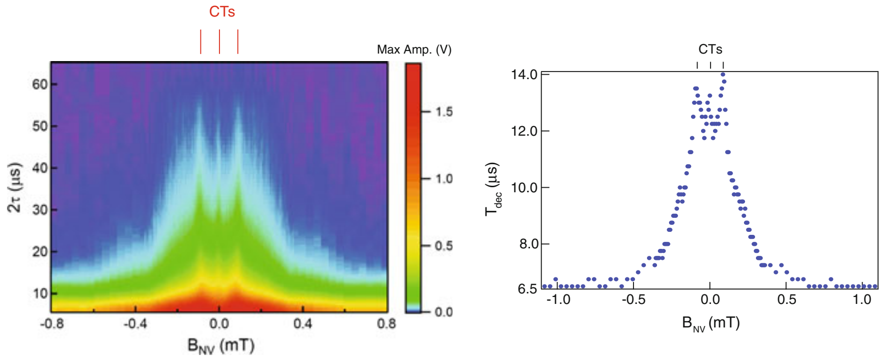

Fig. 5.53 Dependence of the echo decay on the magnetic field B_{NV}. (*Left*) Two-dimensional plot of the echo amplitude $A(B_{NV}, \tau)$. The spins of the *N-Orth* group contribute induce longer decay tails at the three magnetic field values $B_{NV} = -0.09, 0, +0.09\,\text{mT}$ corresponding to the clock transitions. The overall effect in the zero-field region arises from the $m_I = 0$ spins of the *N-Orth* group contribution. (*Right*) Corresponding time T_{dec} at which the amplitude of the echo is reduced by 10. At the CTs, the characteristic decay time T_{dec} shows an enhancement by a factor ~2

around zero-field is attributed to the *Orth* group: for low magnetic fields, the frequency of the $m_I = 0$ component of the *Orth* group stays stationary with B_{NV} to a good approximation, which results in a stable long coherence time contribution from this group to the echo decay all along the scan. When the magnetic field increases however, the probe frequency $\omega(B_{NV})$ departs from the *Orth* group resonance and its long coherence time contribution to the echo signal vanishes.

To quantify the enhancement in term of coherence time, the difficulty is to deconvolve the contribution to the echo decay of the spins that are in and out the clock transitions. Indeed, at all magnetic field, the contribution to the echo decay of the three hyperfine components $m_I = 0, \pm 1$ of the two groups *Orth* and *N-Orth* add up,

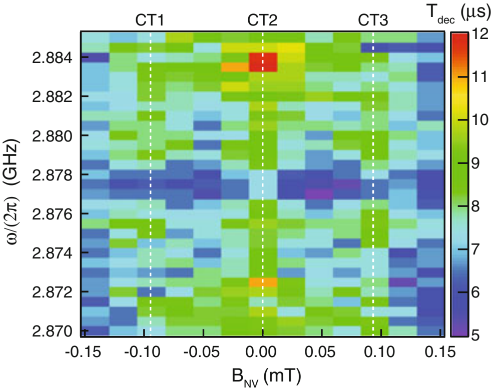

Fig. 5.54 Two-dimensional plot of the characteristic decay time $T_{dec}(\omega, B_{NV})$. At $B_{NV} = B_{CT1}, B_{CT2}, B_{CT3}$, the measured characteristic decay time is long independently of the probe frequency, confirming the absence of spurious effect

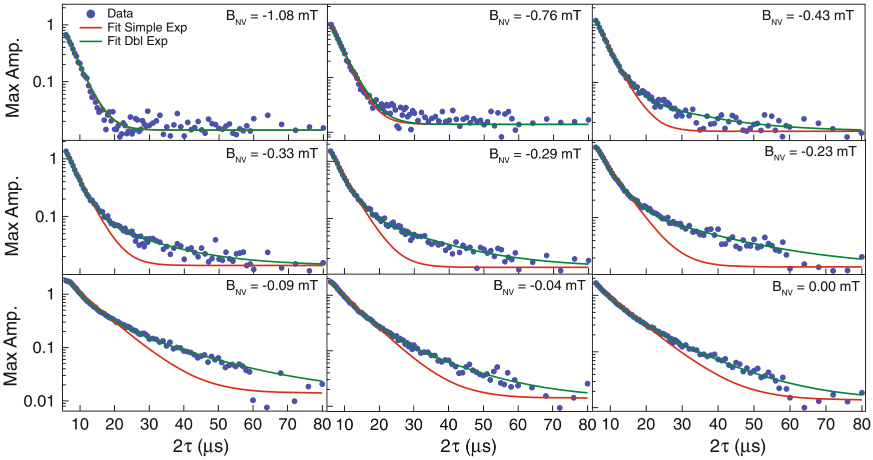

Fig. 5.55 Convergence from double to single exponential decay at large field. Measured (*dots*) decay of the echo maximum amplitude as a function of τ. *Green* and *red lines* are respectively an exponential and bi-exponential fit. At large field, the single exponential fit becomes reasonable

which make it difficult to identify respective spin classes coherence times. The solution is to dissociate the IN and OUT CT contributions as introduced in Sect. 5.6.2.2. This suggests to fit the decay with two time constants $T_{2,IN}$ and $T_{2,OUT}$ with weight A_{IN} and A_{OUT}.

We show in Fig. 5.55 in log scale a double exponential fit of the echo decay at various magnetic fields together with an exponential fit (in red) for comparison. The fit with two time constants yields a good agreement, which validates the interpretations. At large fields however, the single exponential fit becomes reasonable which suggests that we approach a single spin contribution. This can be understood coming back to the m_I-dependent susceptibility of Fig. 5.51: at large magnetic field the contribution to the echo signal of the *Orth* group which is IN CT vanishes because the probe frequency $\omega(B_{NV})$ get far from their resonance and the only left contribution to the echo decay comes from the *N-Orth* group which is OUT CT. This results in a single exponential decay at large field in Figs. 5.53 and 5.55.

We show in the *top* panel of Fig. 5.56 the echo decay together with single and double exponential fits at the three clock transitions. One sees that the fit with two time constants is well justified at these magnetic field points. We attribute the long time constant of the double exponential fit to the spins which are IN CT and find $T_{2,CT1} = 19.5\,\mu\text{s}$, $T_{2,CT2} = 14.1\,\mu\text{s}$ and $T_{2,CT3} = 19.8\,\mu\text{s}$.

To quantify the enhancement, we need to compare to the coherence time value out of the clock transitions $T_{2,oCT}$. The shortest time constant $T_{2,OUT}$ fitted here however is not a good estimation of $T_{2,oCT}$ because at the CTs the energy levels slopes of the spin classes which are OUT CT are slightly different. Instead, at large magnetic field we have mentioned above that there is a single contribution form the *N-Orth* group which are OUT CT with a slope identical for the three hyperfine

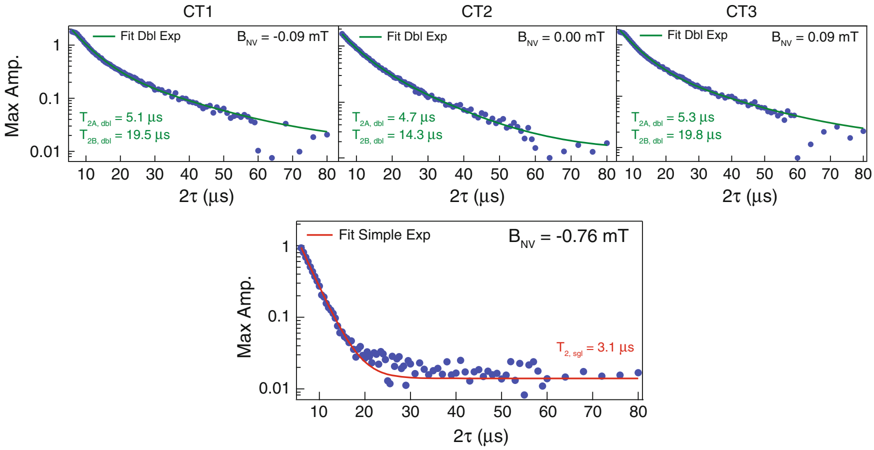

Fig. 5.56 Measurement of the coherence times IN and OUT CT. (*Top*) The coherence time of the spins IN CT corresponds to the long coherence time of the bi exponential fit of the echo decay at the three CTs. (*Bottom*) The single exponential fit at large field gives the coherence time of the spins IN CT

components. We show in the *bottom* panel of Fig. 5.56 a single exponential fit of the echo decay at large magnetic field ($B_{NV} = -0.76\,\text{mT}$) and find $T_{2,oCT} = 3.1\,\mu\text{s}$. The Hahn-echo time T_2 thus shows an enhancement by a factor $T_{2,CT}/T_{2,oCT} \sim 5$ at each of the three clock transitions. The limitation of the coherence time at the CTs is attributed to dynamical fluctuations of the charge (i.e. strain E) around the NVs.

5.6.4 Advanced Analysis: Spin Classes Contributions to the Echo Decay

As discussed above, it is difficult to measure the coherence times of the spins which are IN and OUT the CTs with the echo signals because we only measure the sum of the echoes from all the spins. This calls for a deconvolution of the spin classes contributions if possible. One way to do this is to look at the frequency dependence of the echo decay curves. Indeed, our model predicts a non-trivial frequency dependence of the ratio between spin classes IN and OUT CT. A difficulty arises from our lack of knowledge of the shape (exponential, Gaussian,...) of the decay curves. In this section, we focus on the clock transition at zero magnetic field (CT2), for which the model with two spin contributions IN and OUT CT is exact and investigate the echo as a function of the probe frequency.

5.6.4.1 Theoretical Predictions

We compare the experimental weights to the weights of the IN and OUT CT spin contributions predicted by numerical simulations. The predicted spin susceptibility is shown in Fig. 5.57, together with the IN and OUT CT spin contributions at CT2 (see Sect. 5.6.2.2). To be compared to the experimental weights, we further renormalize the two spin contributions to 1. One observes that the contributions from the spins which are OUT CT dominate far from the zero field splitting, as expected from the energy levels. Close to it, an inversion of the spin contributions with a major contribution from spins IN CT while minor one from the OUT CT appears. This inversion is smooth because of the spin frequency distribution induced by strain. There is a second effect of the strain distribution which appears far from the zero field splitting: spins IN CT are still present. In the following, we measure the echo decay at $B_{NV} = B_{CT2}$ as a function of the probe frequency and perform fit with various functions to compare the experimental weights to these predictions.

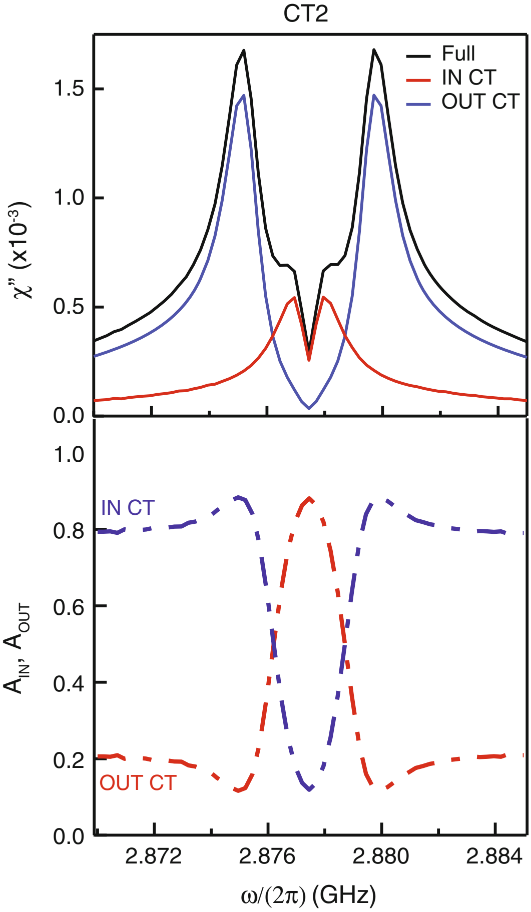

Fig. 5.57 Theoretical predictions at CT2. (*Top*) IN and OUT CT contributions to the spin susceptibility. (*Bottom*) Corresponding A_{IN} and A_{OUT} weights

5.6.4.2 At Zero Magnetic Field (CT2)

Echo measurements are performed in the same conditions as in Sect. 5.6.3. The measured echo decay as a function of the probe frequency is shown in Fig. 5.58. In the middle, one distinguishes the zero field splitting where there is almost no spins. The $|0\rangle \rightarrow |-\rangle$ transition is visible below this freq, and the $|0\rangle \rightarrow |+\rangle$ above. The two transitions are broadened by the strain distribution as explained above. In the following, we fit the echo decay with various fit functions with a short τ_1 and long τ_2 components and compare the experimental weights A_1 and A_2 to the predictions A_{OUT} and A_{IN} of Fig. 5.57.

We show in Fig. 5.59 the results of the fit with a double exponential $f_1(2\tau) = A_1 \exp(-2\tau/\tau_1) + A_2 \exp(-2\tau/\tau_2)$ together with few fit examples. The quality of the fit is good (*top* panel of Fig. 5.59), justifying further analysis. In the *bottom* panel of Fig. 5.59, one observes a long time constants τ_2 with weight A_2, and a shorter one τ_1 with weight A_1. The long component is attributed to the spins which are IN CT, the short to the spins OUT CT. One sees that τ_1 is almost independent of the probe frequency, which confirms that the magnetic field fluctuations is the main limitation to coherence for these spins. The long time constant, however, presents symmetrical peaks at 6 MHz from the zero field splitting. This symmetry suggests that this is not an artifact of our measurements. One possible explanation is an effect of the strain distribution. We note that the further from the zero-field splitting, the larger the strain splitting, and the more protected the spins against first order magnetic field fluctuations, implying longer T_2.

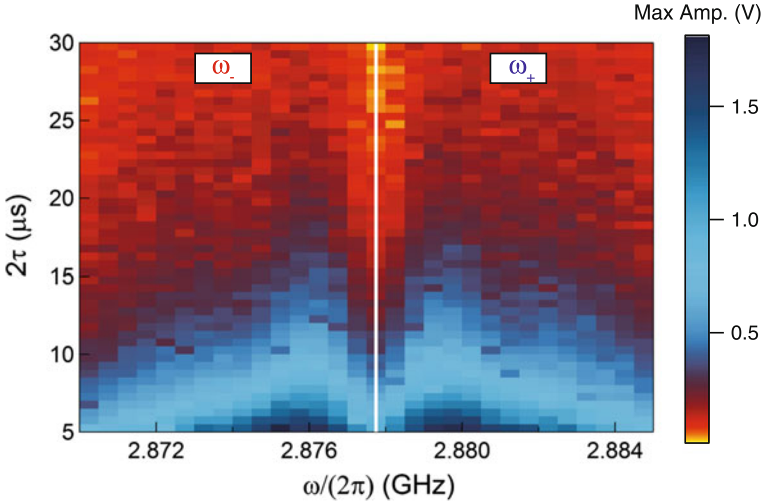

Fig. 5.58 Dependence of the echo decay on the probe frequency at B_{CT2}. Two peaks are visible, corresponding to the spin transitions $|0\rangle \rightarrow |\pm\rangle$

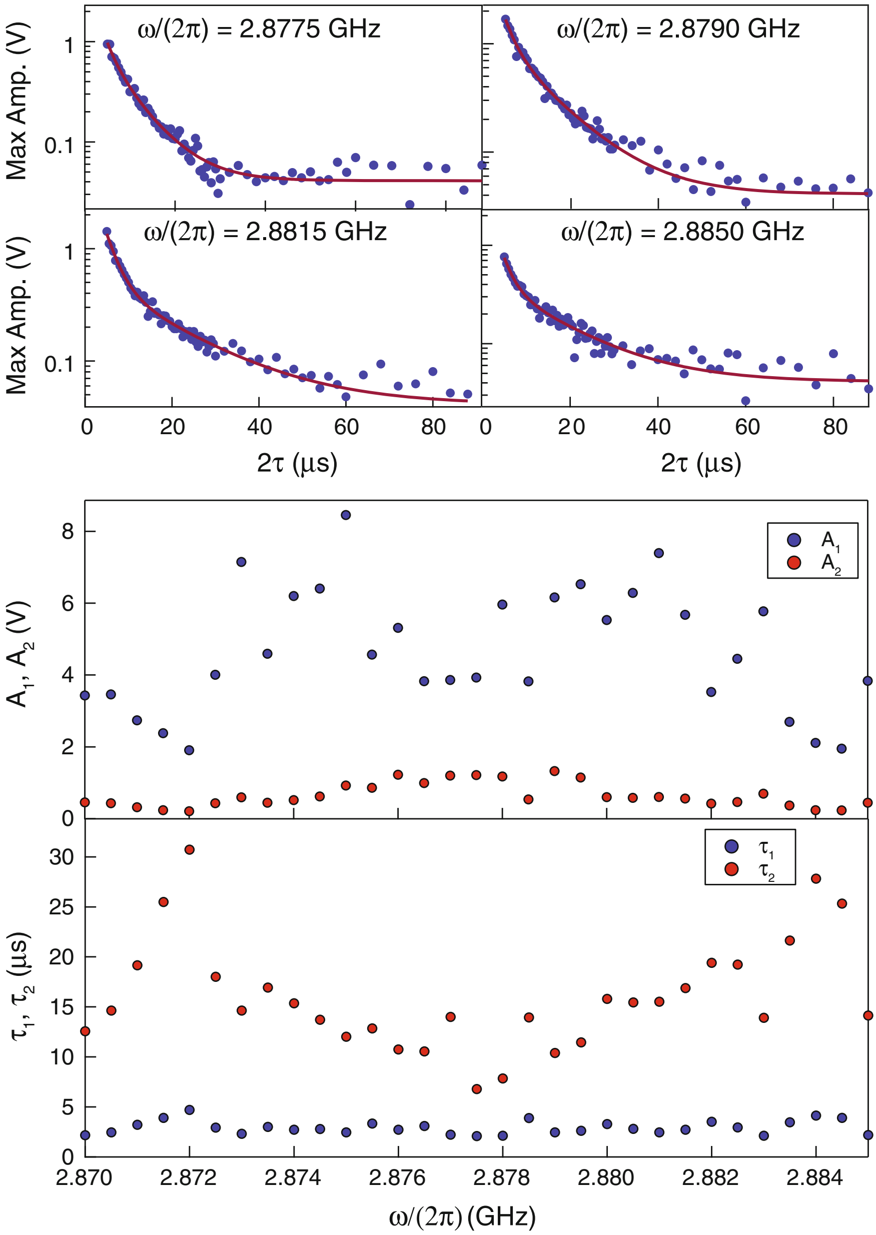

Fig. 5.59 **Double exponential fit of the echo decay.** (*Top*) Measured (*dots*) and fitted (*red line*) echo decay for a selection of probe frequency. (*Bottom*) Corresponding fitted $A_{1,2}$ and decay times $\tau_{1,2}$ as a function of the probe frequency

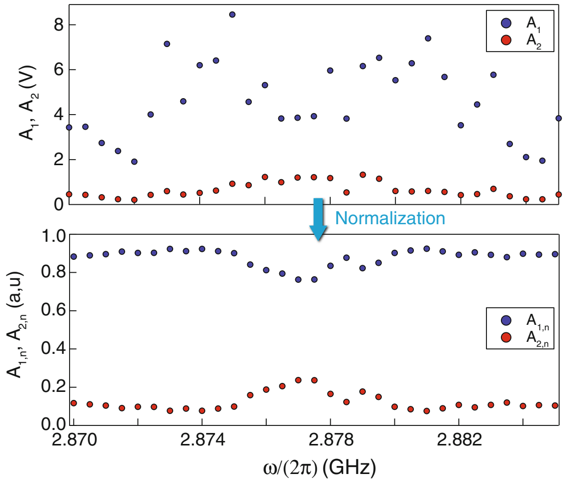

Fig. 5.60 Renormalization for comparison to the theory. The fitted $A_{i=1,2}$ (*top*) are renormalized to 1 (*bottom*) as $A_{i,n} = A_i/(\sum_i A_i)$ for $i = 1, 2$

Far from the zero-field splitting, there are two spin classes: those having large zero field splitting (more protected) and those having small zero field splitting (less protected) but being coupled to neighboring ^{13}C that shift their resonance frequencies (on the order of 1–100 MHz). The opposite contributions to coherence from the two spin classes might explain the peaks. Note that this long time constant dependence on the probe frequency will be found in all the following fits.

To estimate the pertinence of the fit, we compare the experimental weights to the predicted one. For that, A_1 and A_2 are first renormalized to 1 (see Fig. 5.60) and superimposed to the theoretical predictions in Fig. 5.61. Far from the zero field splitting (out of the central region), the experimental weighs are in reasonable agreement with the predictions. In the central region however the agreement is not satisfying. We attribute part of this discrepancy to an artifact of the fit. In the central region, $\tau_2 \rightarrow \tau_1$ suggesting a single exponential fit: it becomes difficult to dissociate A_1 from A_2. As a result, the 5 central points are irrelevant in the plot shown in Fig. 5.61.

A double exponential fit is a natural shape to try, but we can improve it. Indeed, it is known that decoherence due to dipolar interactions with a spin bath should rather lead to a Gaussian or cubic Gaussian shape for the echo [14]. Since on the other hand the long-term decay seems to be well fitted by an exponential (Fig. 5.62), we also fit our data in the following by a sum of an exponential decay (for the IN CT spins) and of a Gaussian and cubic Gaussian ($n = 2, 3$) for the OUT CT spins. The result is shown in Figs. 5.63 and 5.64, with good fit quality.

There is a qualitative resemblance of the fitted weights with the predictions of the model, with in particular the inversion between the two contributions IN and OUT CT which is reproduced.

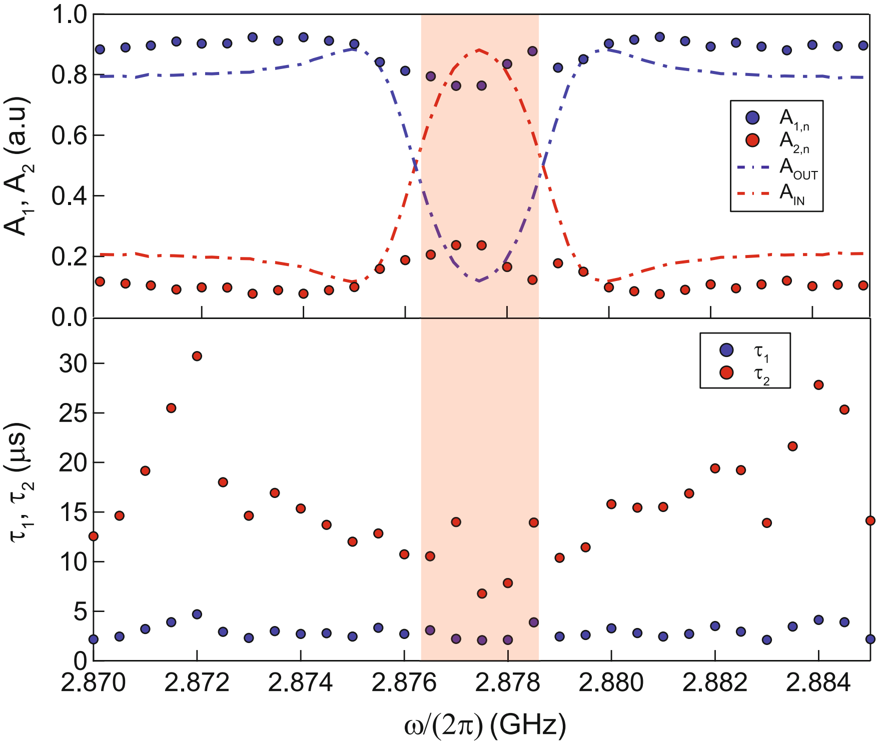

Fig. 5.61 Comparison of the double exponential weights to the theory. The red area corresponds to the region in which the fit are irrelevant

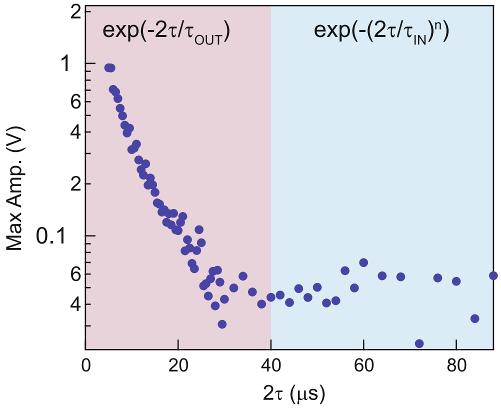

Fig. 5.62 Exp+*n* fit. The spins OUT CT (respectively IN CT) contributes to the rapid (*slow*) echo decay at short (*long*) time as $\exp(-2\tau/\tau_{OUT})$ (respectively $\exp(-2\tau/\tau_{IN})^n)$)

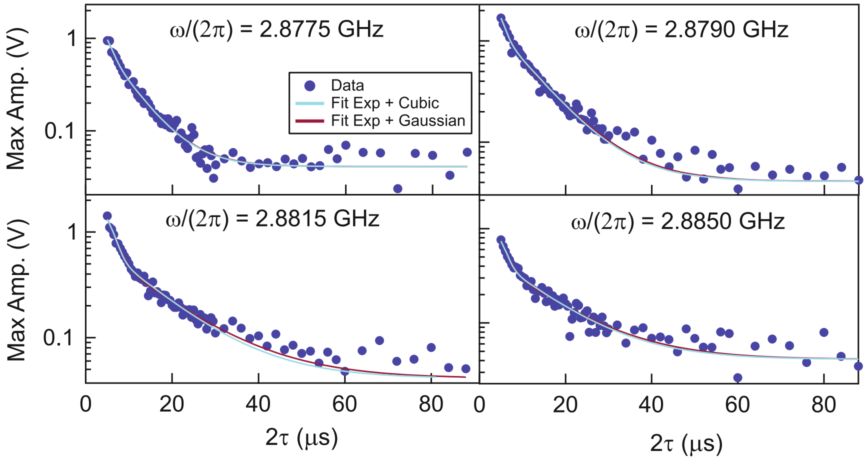

Fig. 5.63 **Gaussian ($n = 2$) and cubic ($n = 3$).** Measured (*dots*) and fitted (*red line*) echo decay for a selection of probe frequency

In conclusion, the fit above suggests an echo decay sum of an exponential decay and a higher order one ($n > 2$). Our predictions are semi quantitatively validated. The omission of the first echo decay points in our measurements however, does not make it possible to determine this higher order echo decay type with sufficient accuracy.

5.7 Conclusion on Experiment 2: The Read Step

We have demonstrated the multi-mode retrieval of few-photons microwave pulses initially stored in the spin ensemble, with active reset by optical pumping and refocusing by a strong microwave pulse. Coming back to the figures of merit defined in the introduction, the experiment reaches $n_{MW} \approx 3$, $n_{sp} \approx 0.1$, $\bar{n} \approx 100$, and $E \approx 2 \cdot 10^{-4}$, many orders of magnitude closer to the quantum regime than previous state-of-the-art experiments [1].

Reaching the quantum regime however requires a recovery efficiency E close to 1. The factors limiting the efficiency in this experiment were identified with the help of the numerical simulations, showing that a one order of magnitude increase of the coherence time would be necessary to reach the quantum regime. A sample with better coherence properties was provided to us after this experiment, with which preliminary experiments were performed. This is the object of the next Chapter.

Beside this result, we have identified 3 magnetic field values, for which the echo coherence time is enhanced. Put back in the perspective of the development of a quantum memory for microwave quantum field, those points have potential interest for memory operation.

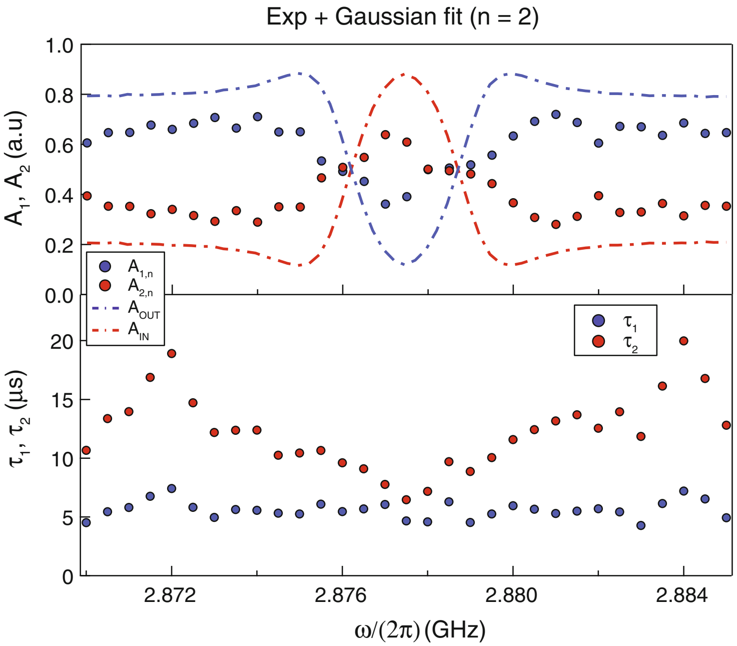

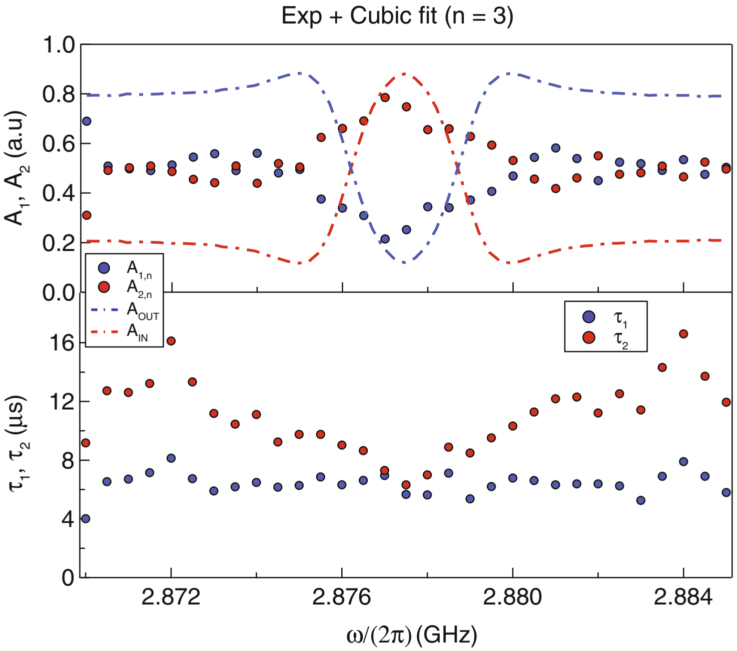

Fig. 5.64 Comparison of the cases $n = 2, 3$ to the theory

References

1. H. Wu, R.E. George, J.H. Wesenberg, K. Mølmer, D.I. Schuster, R.J. Schoelkopf, K.M. Itoh, A. Ardavan, J.J.L. Morton, G.A.D. Briggs, Storage of multiple coherent microwave excitations in an electron spin ensemble. Phys. Rev. Lett. **105**, 140503 (2010)
2. J. Morton. Private communication
3. R. Hanson. Private communication
4. E.R.I. Abraham, E.A. Cornell, Teflon feedthrough for coupling optical fibers into ultrahigh vacuum systems. Appl. Opt. **37**, 1762–1763 (1998)
5. A. Jarmola, V.M. Acosta, K. Jensen, S. Chemerisov, D. Budker, Temperature and magnetic field dependent longitudinal spin relaxation in nitrogen-vacancy ensembles in diamond. Phys. Rev. Lett. **108**, 197601 (2012)
6. C. Grezes, B. Julsgaard, Y. Kubo, M. Stern, T. Umeda, J. Isoya, H. Sumiya, S. Abe, S. Onoda, T. Ohshima, V. Jacques, J. Esteve, D. Vion, D. Esteve, K. Moelmer, P. Bertet, Multimode storage and retrieval of microwave fields in a spin ensemble. Phys. Rev. X **4**, 021049 (2014)
7. H. Engstrom, Infrared reflectivity and transmissivity of boron-implanted, laser-annealed silicon. J. Appl. Phys. **51**, 5245 (1980)
8. L. Robledo, L. Childress, H. Bernien, B. Hensen, P.F.A. Alkemade, R. Hanson, High-fidelity projective read-out of a solid-state spin quantum register. Nature **477**, 574 (2011)
9. V. Ranjan, G. de Lange, R. Schutjens, T. Debelhoir, J.P. Groen, D. Szombati, D.J. Thoen, T.M. Klapwijk, R. Hanson, L. DiCarlo, Probing dynamics of an electron-spin ensemble via a superconducting resonator. Phys. Rev. Lett. **110**, 067004 (2013)
10. H. Malissa, D.I. Schuster, A.M. Tyryshkin, A.A. Houck, S.A. Lyon, Superconducting coplanar waveguide resonators for low temperature pulsed electron spin resonance spectroscopy. Rev. Sci. Instrum. **84**, 025116 (2013)
11. R. Hanson, O. Gywat, D.D. Awschalom, Room-temperature manipulation and decoherence of a single spin in diamond. Phys. Rev. B **74**, 161203 (2006)
12. G. Wolfowicz, A.M. Tyryshkin, R.E. George, H. Riemann, N.V. Abrosimov, P. Becker, H. Pohl, M. Thewalt, S.A. Lyon, J. Morton, Atomic clock transitions in silicon-based spin qubits. Nat. Nanotechnol. **8**(6), 561–564 (2013)
13. F. Dolde, H. Fedder, M.W. Doherty, T. Nöbauer, F. Rempp, G. Balasubramanian, T. Wolf, F. Reinhard, L.C.L. Hollenberg, F. Jelezko, Electric-field sensing using single diamond spins. Nat. Phys. **7**(6), 459–463 (2011)
14. Z. Wang, G. de Lange, D. Ristè, R. Hanson, V.V. Dobrovitski, Comparison of dynamical decoupling protocols for a nitrogen-vacancy center in diamond. Phys. Rev. B **85**, 155204 (2012)

Chapter 6
Towards an Operational Quantum Memory

This chapter concludes the work we have made towards a spin ensemble quantum memory. It gathers a selection of experiments and realizations initiated at the end of this thesis work that illustrate the next steps to reach the operational level.

6.1 Reaching Efficient Memory Operations

In order to reach the operational level, the fidelity of the *write* and *read* steps of the memory protocol must be close to 1 and the *reset* operation compatible with the timescale of operation of superconducting circuits. The experiment reported in Chap. 4 suggests that the fidelity of the *write step* required to operate the quantum memory is within reach. The limiting factors for the *reset* and *read* steps have been well identified; it remains to address them experimentally. In the following, we present a first experiment showing significant improvement of the *read* and *reset* efficiency and propose solutions for bringing it up to the operational level.

6.1.1 Storage and Retrieval of Photon Fields at the Single Photon Level with Improved Efficiencies

In the experiment of Chap. 5, the main limitation to the retrieval and reset efficiencies were respectively the short echo coherence time of the spins and the poor alignment of the laser beam. Here we reproduce the same experiment, but with a new diamond crystal with longer NV coherence times and in a setup compatible with alignment optimization. These combined improvements make it possible to store and retrieve microwave pulses at the single photon level, a prerequisite to reach the operational level.

© Springer International Publishing Switzerland 2016
C. Grèzes, *Towards a Spin-Ensemble Quantum Memory for Superconducting Qubits*, Springer Theses,
DOI 10.1007/978-3-319-21572-3_6

6.1.1.1 Experimental Realization

The experiment The hybrid circuit we developed for this experiment follows the same design strategies we employed for the experiment described in Chap. 5. In particular we keep the same geometry, perform optical repumping of the spins and ensure that the resonator and the spins are in the low cooperativity regime for stabilizing the spins after refocusing. The diamond sample we use for this experiment however is enriched isotopically in ^{12}C and has lower P1 concentration yielding longer coherence times (picture on Fig. 6.1). It was prepared by our collaborator Pr. Isoya at Tsukuba University, with a concentration $\rho_{NV} \sim 1.76 \times 10^5\,\mu\text{m}^{-3}$ (1 ppm) of NV centers and nitrogen impurities of the same order. The spin linewidth is estimated to be $w/2\pi \sim 300$ kHz for each peak, and the echo coherence time $T_2 \sim 100\,\mu$s (using the relations in Sect. 2.2.3). The resonator parameters are designed accordingly with a frequency $\omega_r/2\pi = 2.93$ GHz and quality factor $Q \sim 10^3$, in order to satisfy $C < 1$ while still keeping sufficient signal.

The diamond crystal is placed on top of the resonator inductance and oriented such that the applied magnetic field B_{NV} is parallel to the [1, 1, 0] crystalline axis. As in the experiment described in Chap. 5, half of the spins (group *N-Orth*) make an angle $\beta = 35.5°$ with B_{NV} and the other ones (group *Orth*) are orthogonal to it. The estimate of the coupling strengths for the two spin groups yields $g_{ens,Orth}/2\pi = 3.18$ MHz and $g_{ens,N-Orth}/2\pi = 2.47$ MHz. The use of a sample with better coherence properties is not the only difference with the experiment described in Chap. 5. We also performed the experiment in a new dilution refrigerator, which contrary to the previous one offers optical access to the low temperature stage. This makes it possible to optimize the laser spot position with the sample already cold. The laser beam is sent from the outside through an optical window (see the picture on Fig. 6.2), and aligned using a setup at room temperature. A convergent lens is associated to the alignment stage to focus on the small diamond region above the inductance only.

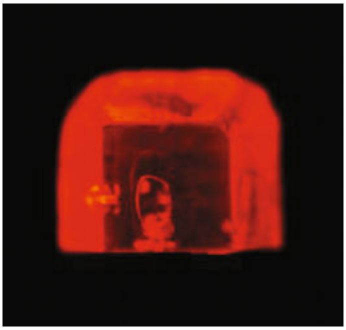

Fig. 6.1 The diamond sample. The picture of the diamond is taken under continuous irradiation at 532 nm. The *red* color corresponds to the photoluminescence of the NVs. An inclusion is visible on the top face

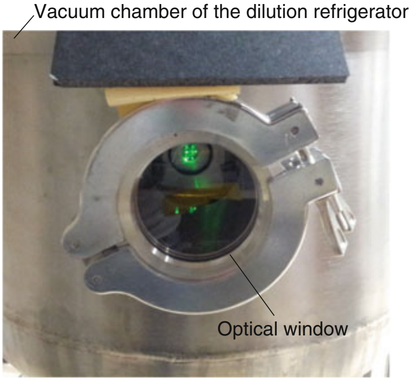

Fig. 6.2 The optical access. The laser beam enters in the vacuum chamber of the dilution refrigerator via an optical window, and is aligned to hit the diamond region above the inductance of the resonator

Spectroscopy of the system The resonator reflection spectrum S_{11} is measured with a vector network analyzer, with microwave power corresponding to ~100 photons, sufficiently low to avoid altering the equilibrium spin polarization. The complex resonator reflection coefficient $r(\omega)$ at zero magnetic field is shown on the left panel of Fig. 6.3, yielding $\omega_r/2\pi = 2.915\,\text{GHz}$ and $Q = 650 \pm 100$, corresponding to a damping rate $\kappa = 2.8 \cdot 10^7\,\text{s}^{-1}$. The spins are not visible at zero field since the resonator frequency is far from the NV resonance at ~2.88 GHz.

The NV characteristic 3-dips response is obtained for $B_{NV} \approx 1.74\,\text{mT}$ (right panel of Fig. 6.3), corresponding to the spin group *N-Orth*. The fit yields $\approx 200\,\text{kHz}$[1] spin linewidth for each line of the triplet, much narrower than in previous work due to the

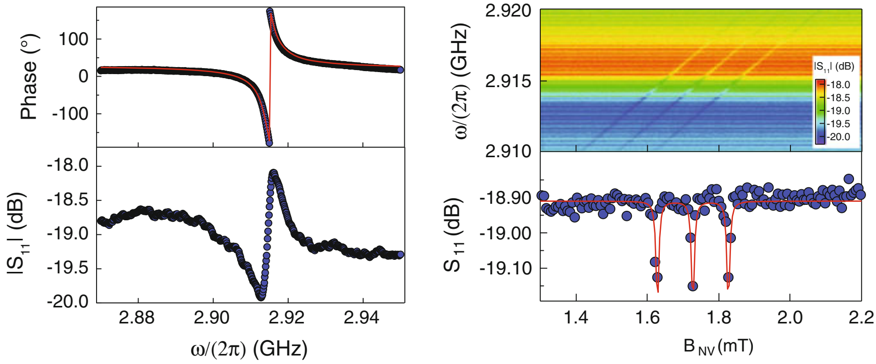

Fig. 6.3 Spectroscopy of the system. (*left*) Reflection spectrum S_{11} of the resonator. The fit of the phase response (*red line*) yields resonator frequency $\omega_r/2\pi = 2.915\,\text{GHz}$ and quality factor $Q = 650 \pm 100$. (*top right*) Reflected amplitude $|S_{11}|$ as a function of the applied magnetic field B_{NV}. The three dips characteristic of the NV hyperfine structure are observed. On the *bottom*, the measured (*dots*) and computed (*line*) reflection spectrum at the resonator frequency ω_r

---

[1] Upper estimate for the spin linewidth. The resolution of this measurement is 200 kHz, which makes it impossible to measure narrower linewidth.

lower P_1 center concentration and to the isotopic enrichment in ^{12}C. We keep this magnetic field B_{NV} unchanged throughout the experiments reported in the following.

6.1.1.2 Reset Efficiency

The spin reset efficiency is measured as described in Sect. 5.4. The spin polarization was first probed under continuous irradiation (data not shown) to determine the power $P_{L,sat} = 280\,\mu\text{W}$ at which the spins reach the maximum spin polarization ~90 % achievable by optical repumping. The relative spin polarization after repumping with an optical pulse of increasing length T_L was then measured with a 20 ms resonant probe pulse with microwave power corresponding to $\bar{n} \sim 1$ in the resonator. The result of this measurement is shown in Fig. 6.4. The relative spin polarization increases with a characteristic time $T_{L,wp} = 0.150\,\text{s}$ and then saturates around $T_{L,sat} = 1\,\text{s}$ suggesting that the maximum polarization is reached. This result can be compared to those reported in Chap. 5 in term of energy contained in the optical pulse. Here the complete spin polarization is obtained for an optical pulse of energy $\sim P_{L,sat} \times T_{L,sat} = 0.280\,\text{mJ}$ instead of ~6 mJ, thus with an improvement on the *reset* efficiency of more than one order of magnitude. This demonstrates that the physical limit on the optical pulse energy needed is not reached yet. Note again that, for technical reasons, the alignment was not optimized in this experiment, suggesting that the time needed to repump the spins can be further reduced.

In the experiments which follow (except where specified), the spins are polarized at $p = 75\,\%$ with an optical pulse of duration 200 ms and power 280 μW. The experimental sequence is repeated at 4 Hz and the refrigerator cold stage heated up at 95 mK, an improvement by a factor 4 on the temperature compared to the experiment described in Chap. 5.

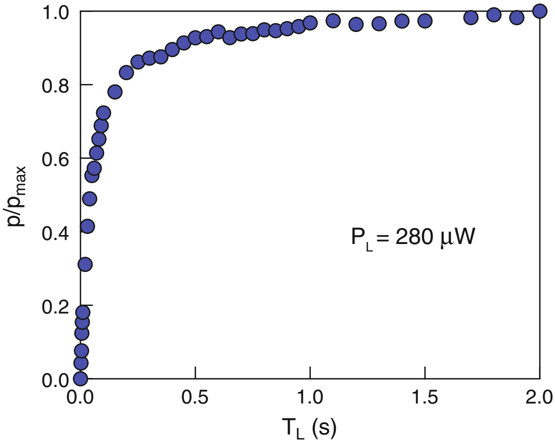

Fig. 6.4 Active reset of the spins. The relative spin polarization for $P_L = 280\,\mu\text{W}$ as a function of T_L increases then saturates around $T_L^{sat} = 1\,\text{s}$. Since $P_L > P_{L,max}$, the saturation corresponds to the maximum polarization allowed by optical repumping

6.1.1.3 Read efficiency

The storage and retrieval of microwave pulses are performed as in the experiments described in Sect. 5.5. Hahn echoes at high power were first obtained to determine the refocusing power $P_{R,sat} = -20\,\text{dBm}$ at which the echo amplitude saturates. The echo coherence time T_2 was then measured by applying a microwave pulse (θ) with power $-71\,\text{dBm}$ followed by a $1\,\mu\text{s}$ refocusing pulse (R) with power $P_{R,sat}$ (see Fig. 6.5). The exponential fit yields[2] $T_2 = 84\,\mu\text{s}$, confirming that the spin ensemble has ten times longer echo coherence time than the one used in the experiment reported in Chap. 5.

Decoherence occurs due to dipolar interactions with the bath of paramagnetic species present in the sample (^{13}C nuclei, P_1 centers, and NV centers), whose dynamical evolution causes a randomization of the phase acquired by NV centers during the two halves of the spin-echo sequence. The ^{13}C nuclei bath precesses at the Larmor frequency $\gamma_n B_{NV} = 2\pi \cdot 130\,\text{kHz}$ (γ_n being the ^{13}C gyromagnetic ratio), giving rise to a characteristic oscillation pattern [1–3] in the spin-echo amplitude, visible in the data on the right panel of Fig. 6.5. The dynamics due to flip-flop events within the P_1 center bath is responsible for a decoherence process known as spectral diffusion [4]. Finally, the bath consisting of NV centers at frequency ω_r (only half of the total NV concentration) unavoidably undergoes spin flips due to the refocusing pulse itself, which constitutes an efficient decoherence process called instantaneous diffusion [5]. The various contributions of each bath were calculated using the cluster-correlation expansion method [6], with concentrations $[P_1] = 0.6\,\text{ppm}$, $[NV^-] = 0.4/2 = 0.2$ ppm, and $[^{13}C] = 213\,\text{ppm}$, compatible with the sample parameters. Good agreement with the data is obtained. Overall, dipolar interactions between NV centers appear to be the dominant source of decoherence in our experiment.

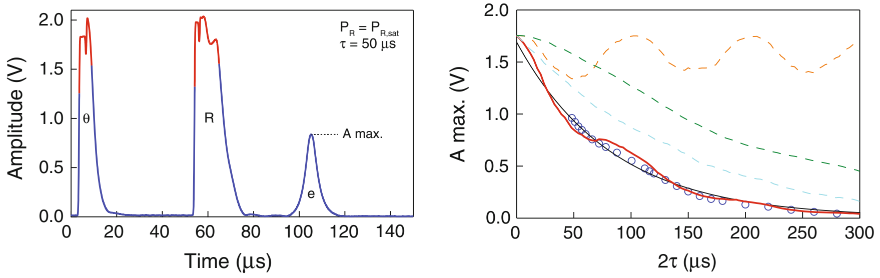

Fig. 6.5 Hahn echo sequences and spin coherence times. (*left*) The echo (*e*) is observed at time $2\tau = 100\,\mu\text{s}$. Saturation of the amplifiers (shown in *red*) limits the measurable amplitude to about 1.5 V. (*right*) Measured (*dots*) and calculated (*red solid line*) decays of the echo maximum amplitude as a function of τ. The calculated decay is a combination of the decays due to the bath of 213 ppm of ^{13}C (*dashed orange curve*), 0.6 ppm of P_1 centers causing spectral diffusion (*dashed green line*) and 0.2 ppm of NV centers causing instantaneous diffusion (*dashed blue line*). An exponential fit (*black solid line*) yields a coherence time $T_2 = 84\,\mu\text{s}$

---

[2] Note that there is only one time constant here since we operate at large magnetic field (see Sect. 5.6).

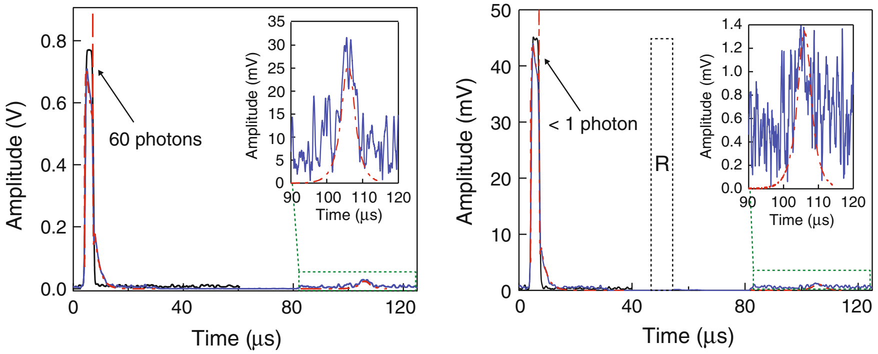

Fig. 6.6 Retrieval of few-photon fields initially stored in the spin ensemble with 0.3 % efficiency after 100 μs. The echo e is obtained for a low power incoming θ pulse populating the resonator with only $\sim$60 photons (*left*) and $<$1 photon (*right*). The refocusing pulse was suppressed in the room-temperature detection chain by a microwave switch to avoid saturating the follow-up amplifiers. The results of numerical simulations performed by Brian Julsgaard are superimposed on the graphs (*dash-dotted red lines*)

Since the echo efficiency was limited by the finite spin coherence time in the experiment of Chap. 5, a significant improvement is expected with this new sample. For the experiments at the few photons level, we keep the refocusing pulse power $P_{R,sat}$ and delay time $\tau = 50\,\mu$s. The storage and retrieval of a microwave pulse corresponding to $\sim$60 photons in the resonator is shown in the left panel of Fig. 6.6. By comparison with the reflected θ pulse with the spin saturated (black curve), we determine that 29 % of the photons contained in the microwave pulse are absorbed by the spins. The efficiency of the *read step* of the memory protocol described in Chap. 3, defined as the ratio $E_{READ} = E_e/E_{abs}$ between the energy recovered during the echo and the energy absorbed by the spins, reached $E_{READ} = 0.3\,\%$ after $100\,\mu$s storage. The storage and retrieval of a microwave pulse corresponding to $<$1 photon in the resonator is shown on the left panel of Fig. 6.6. Note that for this experiment, the spins are polarized at $p = 51\,\%$ with an optical pulse of duration 100 ms to reduce the acquisition time, and subsequently absorbed only 20 % of the incoming pulse. The echo is observed, demonstrating that when the retrieval efficiency is sufficient, we can indeed retrieve an echo out of a single photon field.

These measurements are accurately reproduced (dash-dotted red lines) by numerical simulations performed by Brian Julsgaard at Aarhus University. The simulations use a 130 kHz spin linewidth and a collective coupling constant $g_{ens}/2\pi = 410\,$kHz (when all spins are polarized) for each HF peak, in agreement with the experimentally determined parameters. Noteworthy, the discrepancy between the simulations and experiments is negligible in this new experiment in which the coherence time is ten times longer compared to the previous experiment (see Sect. 5.6.2.2), which strengthens the hypothesis that the discrepancy observed in Chap. 5 is due to the imperfect modeling of the decoherence during the refocusing pulse. These simulations confirm that finite T_2 and the imperfection of π pulse are the main factors limiting the efficiency, while the finite cooperativity $C = 0.22$ limits both the absorption and the echo emission out of the cavity.

6.1.1.4 Conclusions

We obtain an improvement of the reset efficiency by more than one order of magnitude compared to the experiment reported in Chap. 5, thanks to a better alignment of the laser beam. This demonstrates that the physical limit on the optical pulse energy needed for reset is not reached yet, opening the way for further optimization. Note in addition that the refrigerator cold stage was stabilized below 100 mK, a pre requisite for the operation of complex superconducting circuits, that was not reached in the experiment reported in Chap. 5.

Furthermore, thanks to the better coherence properties of the spin ensemble, we were able to demonstrate the retrieval of few photon field after 100 μs with $E_{READ} = 0.3\,\%$ efficiency, again a one order of magnitude improvement in both storage time and retrieval efficiency compared to the experiment reported in Chap. 5 ($E_{READ} = E/0.75 = 2.6 \cdot 10^{-4}$ after 17 μs storage). In this new experiment, the purposely designed low cooperativity is the main limiting factor to the retrieval efficiency with a factor 0.29^2 for absorption and re-emission, followed by the finite coherence time with a factor $|f(\tau)|^2 = |exp(-2\tau/T_2)|^2 = 0.1$ and the imperfection of the refocusing pulse with a factor 0.43 identical for this resonator geometry. This confirms that better fidelity can be obtained with experimental progress. Finally, the experiment with <1 photon demonstrates that when the efficiency of retrieval is sufficient, we can achieve storage and retrieval out of a single photon field, as required to reach the quantum level.

6.1.2 Reaching the Operational Level

At present, the coherence of the NV spin ensemble is at a level sufficient to not remain a prohibitive limitation to the retrieval efficiency. To reach efficient memory operation [7] however, a technical limitation must be addressed: the imperfection of the refocusing pulse. As explained in Chap. 5, it is indeed impossible to apply well-defined π-pulses in our hybrid circuits because of the large inhomogeneity of coupling strength within the ensemble. This inhomogeneity arises from that of the magnetic field sustained by the superconducting resonator. There are several approaches to overcome this issue. Two of them have been studied and partially developed during this thesis work: the adiabatic inversion of the spin ensemble and the control of the spatial distribution of the spins. These two strategies constitute interesting future directions of this project.

Performing an adiabatic inversion of the spins The adiabatic inversion of a spin proceeds along the same line as the adiabatic transfer of population we made in Chap. 4 between the qubit and the resonator. In the latter, we made use of a crossing of the qubit and the resonator states to transfer the population instead of using a

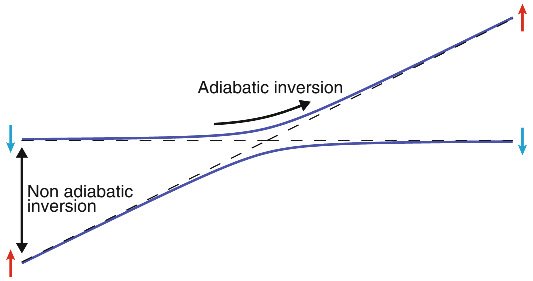

Fig. 6.7 Adiabatic versus non-adiabatic inversion. The resonant inversion makes use of the Rabi oscillations of the populations, for which inversion from the initial state $|\downarrow\rangle$ to the other state $|\uparrow\rangle$ occurs whenever the pulse area (i.e. the time-integrated Rabi frequency) equals an odd multiple of π, while the population returns to $|\downarrow\rangle$ when the pulse area equals an even multiple of π. The adiabatic passage is based upon adiabatic following of an eigenstate of the full Hamiltonian (an adiabatic state), which links the bare states $|\downarrow\rangle$ and $|\uparrow\rangle$

resonant transfer. Similarly, there are two possibilities to invert the spins: either applying a resonant π-pulse at the spin transition frequency or bringing adiabatically the spin from one state to the other. These two techniques are illustrated in Fig. 6.7. To perform an adiabatic inversion, the spin is submitted to a drive with time-dependent frequency and amplitude, the conditions for an adiabatic flip from spin down to spin up. Whereas the resonant π-pulse requires a precise pulse area, the adiabatic passage is robust against small-to-moderate variations of the interaction parameters, i.e. against variations of the spin coupling strength, reducing the refocusing pulse imperfections. This technique borrowed from NMR [8] is used for echo experiments with ensemble in the optical domain [9] and was recently adapted for the manipulation of a spin ensemble in a superconducting resonator [10].

Tailoring the spin spatial distribution The second approach is to confine the spin ensemble in a region where the magnetic field sustained by the resonator is uniform. A possible way to achieve this is to use NV centers created by implantation of Nitrogen atoms through a resist mask, patterned to fill a region of the substrate on which is

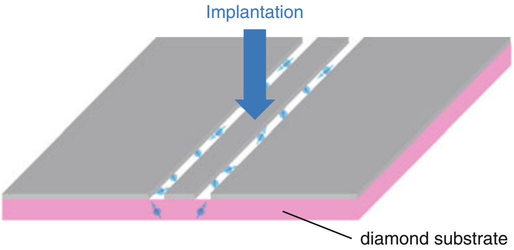

Fig. 6.8 The diamond as a substrate for the superconducting circuit. The circuit is patterned on the diamond substrate and the Nitrogen atoms implanted at posteriori. A mask is placed on the superconducting layer, such that the region in which the spins are implanted is restricted to the gap between the central conductor and the ground planes

fabricated the superconducting resonator (see Fig. 6.8). The difficulty is to obtain a large enough spin concentration to reach the strong coupling regime. Implantation as a method of nanopositioning NV centers has been used in several experiments, i.e. in [11].

6.2 Running the Full Quantum Memory Protocol

Running the full quantum memory protocol we proposed in Chap. 3 requires the development of a physical setup made of a resonator with both frequency and quality factor tunable. This task is challenging compared to what was developed up to now in microwave circuit engineering [12, 13]: when strong refocusing pulses are applied, usual ways of tuning the resonator parameters by inserting a SQUID (as used in Chap. 4) are not allowed because the resonator current would be above the junction critical current. We have worked on the development of alternative solutions which are compatible with the refocusing sequence. In the following, we present an experimental demonstration of one of the two functionalities required, the frequency tunability, and propose solutions for the implementation of the full physical setup.

6.2.1 Step 1/2: Realization of a Frequency Tunable Resonator Compatible with Refocusing Pulse Applications

In the memory protocol (summarized in Fig. 6.9), the requirement for the frequency tunability arises for two reasons: (i) to carry the information from the external processor to the spin ensemble (demonstrated in Chap. 4), (ii) to silence the primary echo. This experiment aims to demonstrate the second point. The design relies on the fact that in the protocol, strong refocusing microwave pulses need to be applied only

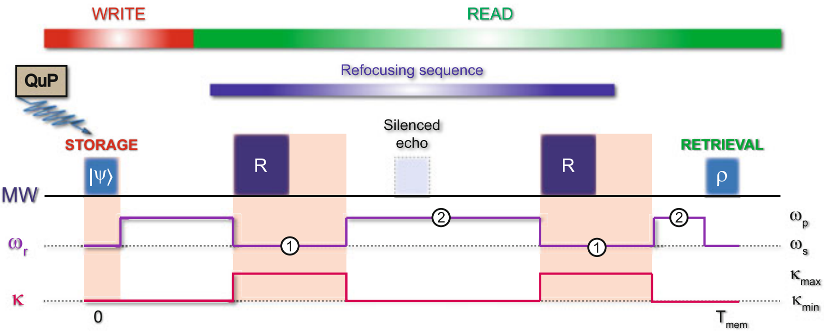

Fig. 6.9 Dynamical tuning of the resonator along the memory protocol. The periods of resonance with the spins are marked in *red*. In 1, the resonator is on resonance with the spins and contains a large intracavity field due to the applications of the refocusing pulses. In 2, the resonator is detuned and contains low intracavity field

when the cavity frequency is resonant with the spins (called “1”), and not when it is detuned (called “2”). This implies essentially that we can design a frequency tunable resonator which does not conserve its functionality during the refocusing pulse applications but remains stable in frequency and quality factor at these times.

6.2.1.1 Experimental Realization

Design The approach consists in coupling the resonator (B) to a second resonator (TF) itself made tunable in frequency by inserting a SQUID loop (see Fig. 6.10). In this scheme, the resonator B is a linear resonator designed at the frequency of operation (ω_B), the resonator TF a frequency tunable resonator designed at higher frequency (ω_{TF}) and both are strongly electrically coupled (g_{B-TF}). When TF is far detuned from B, the resonator B is at ω_B, while when approaching the B resonance, a normal mode splitting manifested by the apparition of two resonances separated by $2g_{B-TF}$ appears. As a result, when TF is tuned exactly on resonance with B, the spectral region $\omega_B \pm g_{B-TF}$ becomes exempt of resonance. This effect can be used to realize a frequency tunable resonator compatible with the refocusing sequence with TF made tunable in frequency by an embedded SQUID loop:

- When $|\omega_{TF} - \omega_B| \gg g_{B-TF}$, the exchange between both are negligible and current in B cannot pass through the Josephson junction embedded in TF: B is stable at its bare resonance frequency ω_B and refocusing pulses can be applied, satisfying the requirements for the region 1 of the protocol.
- When $|\omega_{TF} - \omega_B| \ll g_{B-TF}$, the spectral region $\omega_B \pm g_{B-TF}$ is exempt of resonance: B is not anymore at ω_B, satisfying the requirements for the region 2 of the protocol.

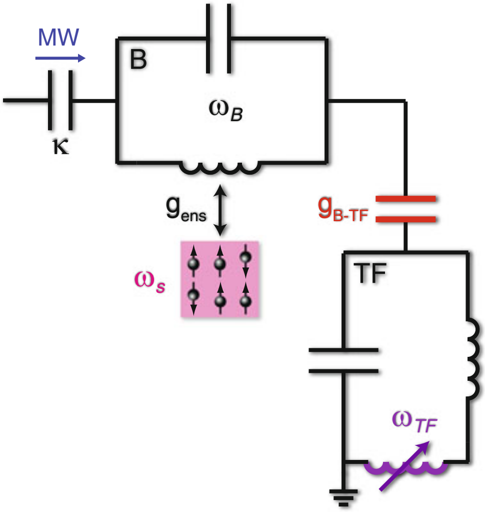

Fig. 6.10 Schematic of the circuit. The main resonator, with frequency ω_B and damping rate κ, is coupled to the spin ensemble (frequency ω_s) with a coupling constant g_{ens}. It is strongly coupled with strength g_{B-TF} to a second resonator with frequency ω_{TF}

The hybrid circuit The superconducting circuit that we developed to demonstrate the compatibility of this design with refocusing pulse applications is shown in Fig. 6.11. The resonator B which is coupled to the spins is a CPW resonator and TF a lumped element resonator. B is coupled at both ends to measuring lines through coupling capacitances. The design parameters are $\omega_B/2\pi = 2.93\,\text{GHz}$, $\omega_{TF}/2\pi = 3.4\,\text{GHz}$, $g_{B-TF}/2\pi = 40\,\text{MHz}$, $\kappa_1 = 75.4 \times 10^6\,\text{s}^{-1}$ and $\kappa_2 = 1.9 \times 10^6\,\text{s}^{-1}$.

The diamond used for this experiment is the same as the one used in the experiment reported in Chap. 5 with parameters $\rho_{NV} \approx 3.52 \times 10^5\,\mu\text{m}^{-3}$ (2 ppm), $w/2\pi = 1\,\text{MHz}$ and $T_2 = 8.4\,\mu\text{s}$. It is placed on top of the resonator B and positioned in the middle of the resonator mode. As in the experiment described in Chap. 5, there are two spins groups with respect to the applied magnetic field B_{NV}, *Orth* and *N-Orth*, resulting in two different ESR frequencies $\omega_{Orth,\pm}$ and $\omega_{N-Orth,\pm}$. The cooperativity with the *N-Orth* spin group is estimated to $C = 0.92$, bringing theoretically the experiment in the low cooperativity regime.

The circuit is cooled in the same dilution refrigerator as the one used for the experiment reported in Chap. 5 with identical microwave setup (see Fig. 5.8), plus an additional transmission line to tune the frequency of the resonator TF. Note that the fiber was not attached to the sample for repumping the spins in this experiment. The active reset is however not crucial since we perform Hahn echoes at high power and subsequently there is no need to repeat for averaging.[3]

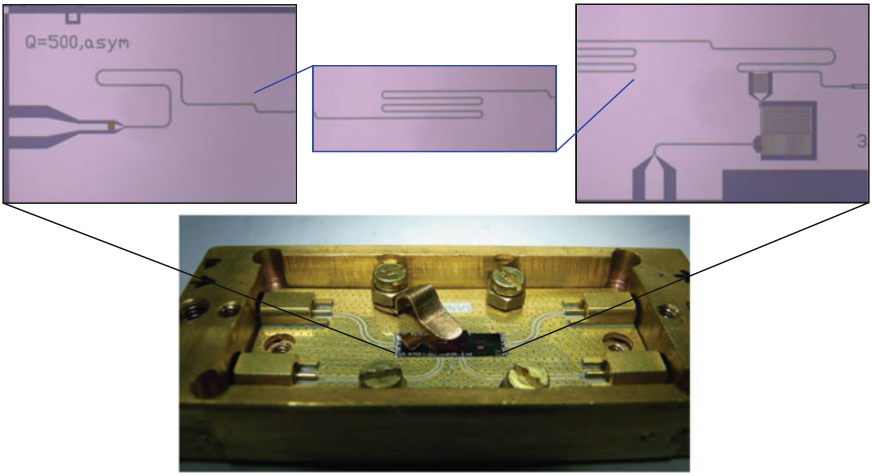

Fig. 6.11 The fabricated circuit with panels zooming on its most important features. The resonator B of CPW type extends from the *left* to the *right* panels. It is designed in meanders in the *middle* where the diamond crystal is positioned. The resonator TF of lumped element type is visible on the *right* panel, with the current line used for tuning its frequency. The circuit is made in Niobium on a silicon substrate using the process described in the Appendix A. The SQUID is fabricated on top by double-angle evaporation of aluminum through a shadow mask patterned using e-beam lithography

---

[3] We wait 20 min between each Hahn echo sequence for the spins to relax in the ground state.

6.2.1.2 Tuning the Resonator frequency

We first study the circuit at $B_{NV} = 0\,\mathrm{mT}$, that is with the spins out of resonance (at 2.88 GHz). For that, a vector network analyzer is used to measure the reflection spectrum S_{11}, with probe power corresponding to $\bar{n} \sim 1000$ photons in resonator B. The result is shown in Fig. 6.12, as a function of the flux $f = \Phi/\Phi_0$ applied to the SQUID loop embedded in TF.

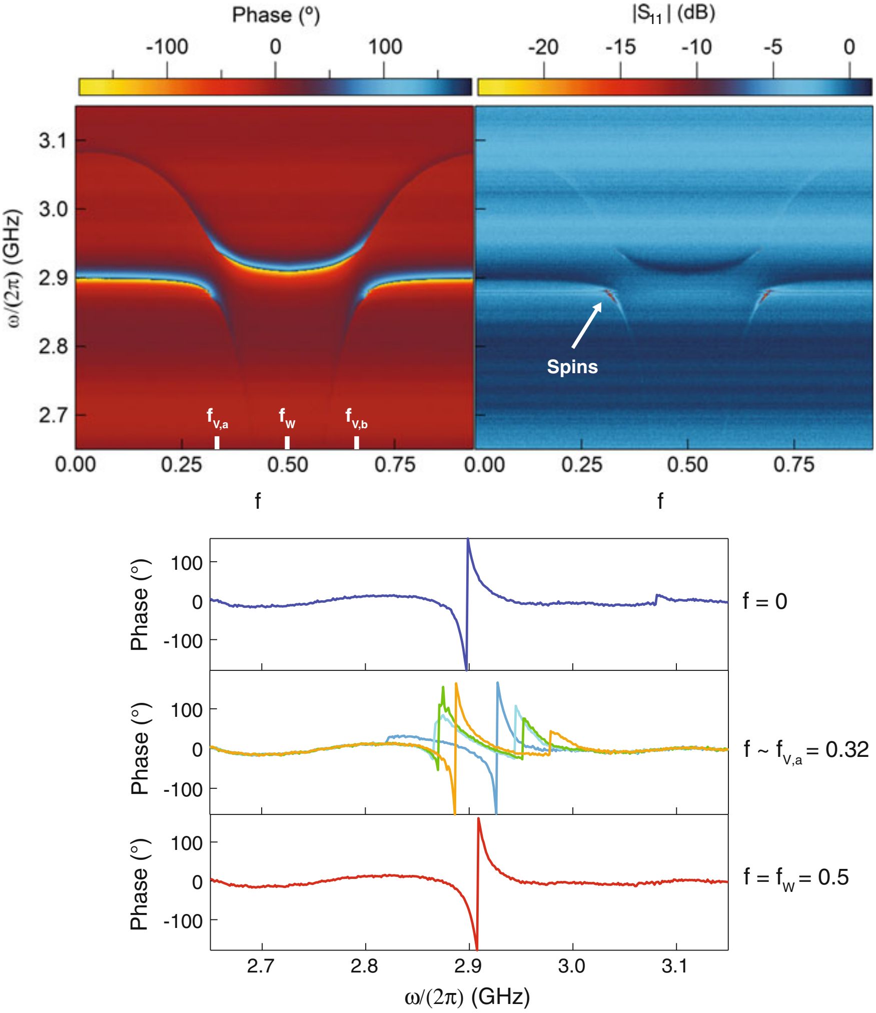

Fig. 6.12 Reflection spectrum S_{11} of the circuit. Reflected phase (*top left*) and amplitude (*top right*) as a function of the applied flux $f = \Phi/\Phi_0$, at $B_{NV} = 0\,\mathrm{mT}$. Two f-dependent resonances are visible, showing successive anticrossings at $f_{V,a} = 0.32$ and $f_{V,b} = 0.67$. The reflected phase at $f = 0$, $f_{V,a}$, f_W is plotted in the *bottom* panel

Two resonances are visible in the resonator spectrum. They are both f-dependent, showing two successive anticrossings at $f_{V,a} = 0.32$ and $f_{V,b} = 0.67$. These anticrossings correspond to a normal mode splitting between the two eigenmodes of the coupled B-TF system, confirming that both resonators are in the strong coupling regime. Note that far from resonance, we can distinguish the TF resonance from the one of B. At this probe power indeed, the resonator TF with a SQUID embedded is slightly non linear (see the bottom panels of Fig. 6.12). At $f = 0$, the linear resonance at 2.90 GHz corresponds to the B resonance and the second at 3.08 GHz, which shows a slight non linearity, corresponds to the TF resonance.

The spectrum around the anticrossing at $f_{V,a}$ is shown in Fig. 6.13. The fit of the eigenmodes (using Eq. 2.56 in Sect. 2.1.3.1) yields $g_{B-TF}/2\pi = 37$ MHz. Note that the spins are visible at 2.88 GHz. At $f_W = 1/2$, the resonator TF is far detuned and only the resonator B response is visible (see Fig. 6.14). The fit of the reflected

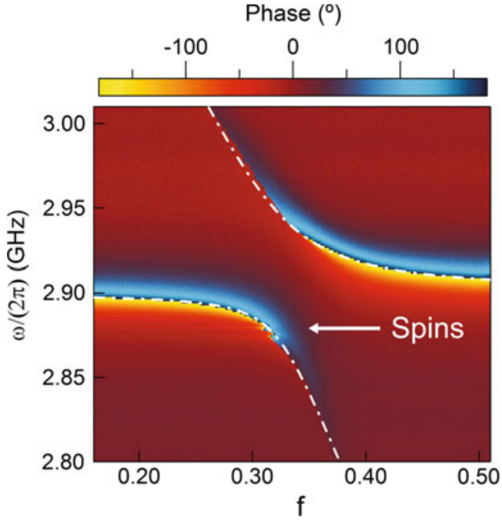

Fig. 6.13 **The anticrossing at $f = f_{V,a}$.** The *red line* is a fit with the model described in Sect. 2.1.3.1, yielding $g_{B-TF}/2\pi = 37$ MHz

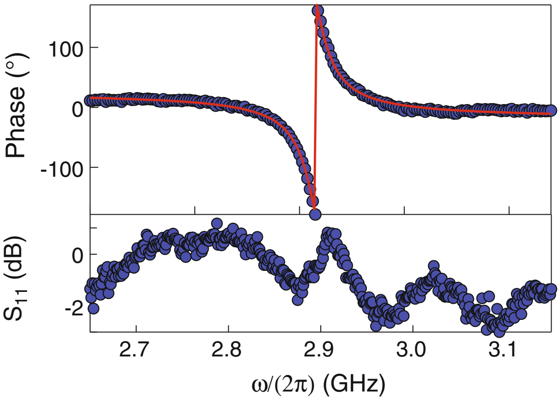

Fig. 6.14 **Spectrum of the resonator B at f_W.** The fit of the phase response (*red line*) yields resonator frequency $\omega_B/2\pi = 2.907$ GHz and quality factor $Q = 195 \pm 5$. The effect of spurious resonance in the measurement setup is visible in amplitude

phase yields resonance frequency $\omega_B/2\pi = 2.907\,\text{GHz}$ and quality factor $Q \sim 195$, corresponding to a resonator linewidth $\kappa = 93 \times 10^6\,\text{s}^{-1}$. In the next section, we study this point f_W, to determine if the photon exchange with the resonator TF is sufficiently small to allow for the application of strong refocusing pulses in B.

6.2.1.3 Applying Refocusing Pulses to the Spins

We bring the spin group *N-Orth* on resonance with the resonator B frequency at f_W by applying an external magnetic field $B_{NV} = 1.26\,\text{mT}$. The NV absorption is visible at 2.907 GHz on the reflected amplitude (see Fig. 6.15). In these conditions we apply a typical spin-echo sequence as used in Chap. 5. The recovered echo is shown in Fig. 6.16, which proves that it is indeed possible to refocus the spins in

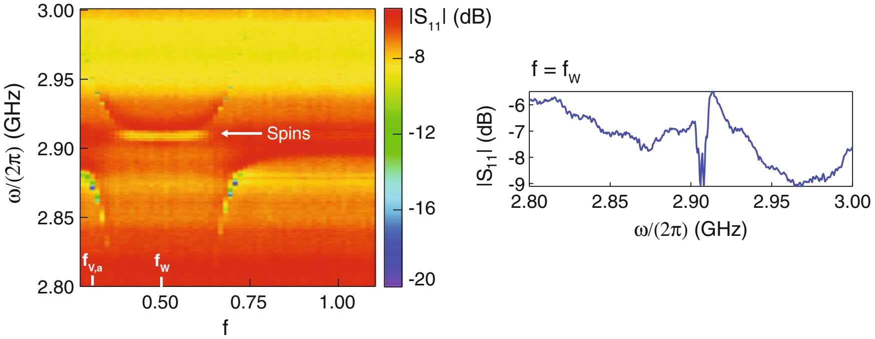

Fig. 6.15 Reflection spectrum $|S_{11}|$ at $B_{NV} = 1.26\,\text{mT}$. The spin absorption is visible on the reflected amplitude at $\omega_B/2\pi = 2.907\,\text{GHz}$. At $f = f_W$, the spins are on resonance with the resonator and refocusing pulse can be applied. At $f = f_{V,a}$, the spins are out of resonance

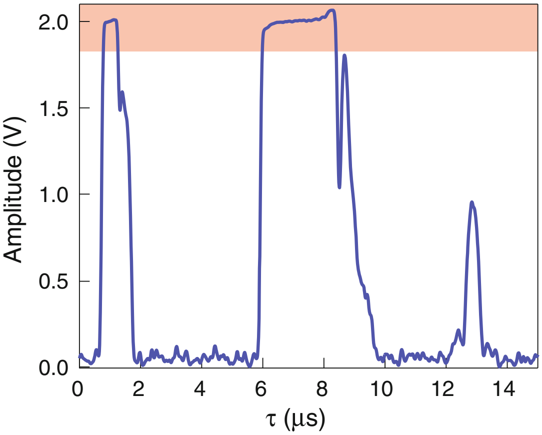

Fig. 6.16 Hahn echo at f_W. A 0.5 µs microwave pulse (θ) with power −68.5 dBm is applied creating a transverse magnetization in the spin ensemble, followed 6 µs later by a 2 µs refocusing pulse (R) with power −30.5 dBm. The echo (e) is observed at time 2τ, confirming that the circuit is not affected by the application of strong refocusing pulses. Saturation of the amplifiers (shown in *red*) limits the measurable amplitude to about 1.8 V

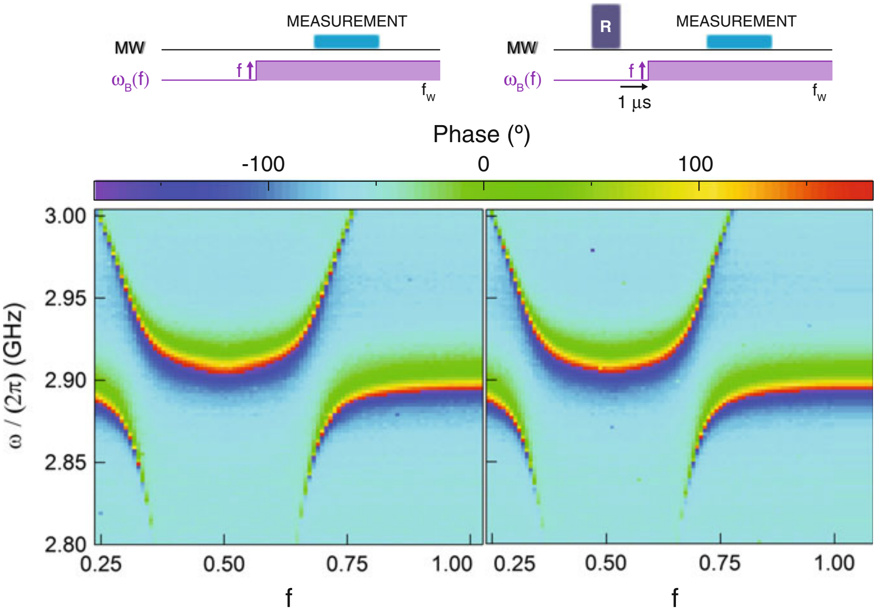

Fig. 6.17 Demonstration of dynamical tuning of the resonator frequency after the refocusing pulse. (*top*) Experimental sequence. A strong refocusing pulse (R) is applied on resonance with B at $\omega_B(f_W)$, followed after a 1 µs delay by a fast tuning of the resonator frequency at $\omega_B(f)$. The circuit is measured afterwards by homodyne detection. The sequence is repeated for increasing f. (*bottom*) Measured reflected phase after the dynamical frequency tuning without (*left*) and with (*right*) the initial application of a strong refocusing pulse. The spectra are identical, confirming that the circuit can be detuned after the application of strong refocusing pulses

this circuit. As a next step towards the echo silencing described in Chap. 3, we test that the application of the strong refocusing pulse still makes it possible to detune dynamically the resonator a few microseconds later. To do so, as described on the top of Fig. 6.17, we measure the reflection coefficient during a detuning pulse, and compare the results with and without an initial strong refocusing pulse applied to the spins. The sequence is repeated for increasing flux f and the circuit measured with probe power of -128 dBm, corresponding to $\bar{n} \sim 5$ photons in the resonator B. The spectra obtained with and without the initial application of refocusing pulse are compared in Fig. 6.17. They are identical, demonstrating that it is indeed possible to detune the resonator after the application of a refocusing pulse. This validates the compatibility of the hybrid circuit with the full quantum memory protocol.

6.2.1.4 Silencing the Echo by Detuning the Cavity

To demonstrate this part of the protocol, we apply on resonance the same microwave pulse θ and R than in the previous section and compare the echo obtained on resonance to the one obtained after detuning the cavity at $\omega(f_{V,b})$ 1 µs after the application of

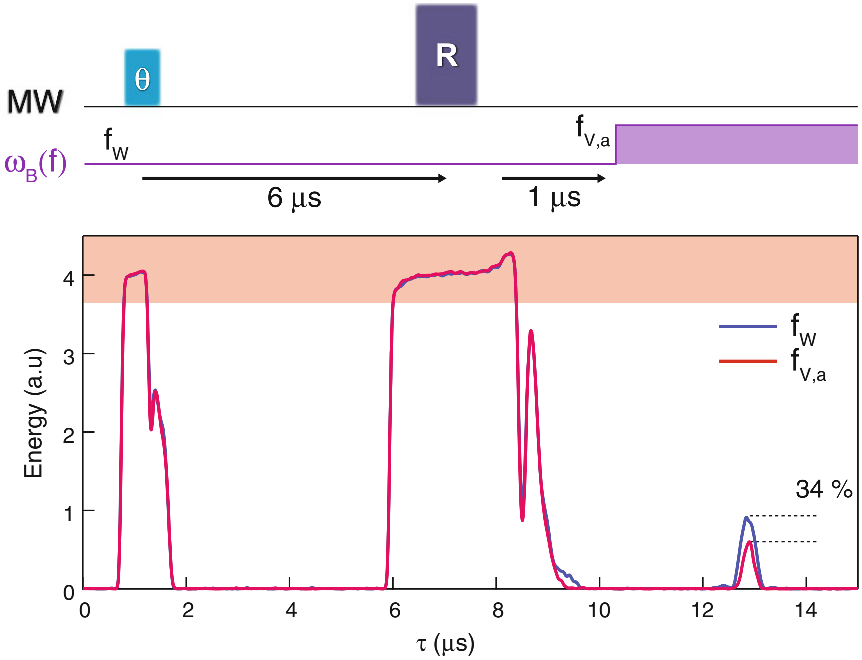

Fig. 6.18 **Partial silencing of the echo by dynamical detuning of the resonator.** (*top*) Protocol. The Hahn echo sequence at $f = f_W$ of Fig. 6.16 is applied, followed 1 μs after the application of the refocusing pulse by a detuning of the cavity at $\omega_B(f_{V,a})$. The sequence is repeated without detuning for comparison. (*bottom*) Measured reflected amplitude with (*red*) and without (*blue*) detuning after the refocusing pulse. The echo obtained when the resonator is at $\omega_B(f_{V,a})$ is reduced by 34 % in energy

the refocusing pulse. The results are shown in Fig. 6.18, with in blue the echo obtained on resonance, and in red the echo obtained with the cavity detuned. We observe that the echo is reduced by 34 % in energy compared to the echo obtained in normal condition, validating an effect of the detuning of the resonator on the spin emission. The silencing of the echo by detuning is however partial. This remaining emission by the spins is attributed to the insufficient detuning of $|\Delta_B| = 40\,\text{MHz}$ given the coupling constant between the two resonators.

6.2.1.5 Conclusions

This experiment demonstrates the operation of a frequency tunable resonator in which refocusing of the spins can be performed. One of the two requirements of the physical setup is thus met to run the full quantum memory protocol. The silencing of the echo was also tested and showed a partial reduction of the echo amplitude by 34 % in energy, bringing a proof of concept of this part of the protocol. The achievement of full echo silencing calls however for the implementation of the same

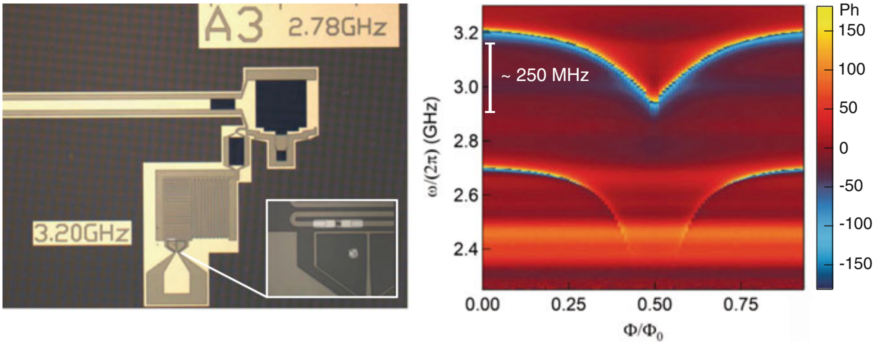

Fig. 6.19 **Towards a complete silencing of the echo.** (*left*) Fabricated circuit showing the resonators B and TF. The resonator B, to which the spins are coupled, is made in a geometry compatible with the reset operation. It is coupled to the frequency tunable resonator TF by a large coupling capacitance ($C_{B-TF} \sim 300$ fF). (*right*) Reflected phase onto the circuit. A detuning $\Delta_B \sim 2\pi \times 250$ MHz is achieved at $f = 0$

circuit with larger coupling strength g_{B-TF}. Such a circuit has been realized at the end of this thesis work and in a geometry compatible with the *reset* operation. We characterized this circuit with no diamond on top (see Fig. 6.19). The detuning $|\Delta_B|$ observed is $\sim 2\pi \times 250$ MHz, a result promising for the full silencing of the echo in a next experiment.

6.2.2 *Realizing a Hybrid Circuit Able to Run the Full Memory Protocol*

In the quantum memory protocol described in Chap. 3, we need not only the resonator frequency to be tunable, but also its quality factor. Here we simply want to indicate two possible approaches to achieve this goal, which we unfortunately had no time to test experimentally.

Coupling through a tunable resonator The first approaches consists in replacing the coupling capacitor that couples the resonator B to the external measurement lines by an auxiliary frequency tunable resonator (RQ), which can be tuned IN and OUT resonance with B (see Fig. 6.20). When RQ is resonant with B, photons can easily leak out of B and the quality factor of B is low, while when RQ is detuned, the leak of photons through RQ is reduced and the quality factor of B is high. Since the circuit must enable the application of refocusing pulses, the dynamical detuning of RQ is obtained as explained previously, by coupling Q to a fourth resonator (TQ), itself made tunable in frequency by inserting a SQUID loop. At total:

- When $|\omega_{TQ} - \omega_{RQ}| \gg g_{RQ-TQ}$, the resonator B has a low quality factor.
- When $|\omega_{TQ} - \omega_{RQ}| \ll g_{RQ-TQ}$, the resonator B has a high quality factor.

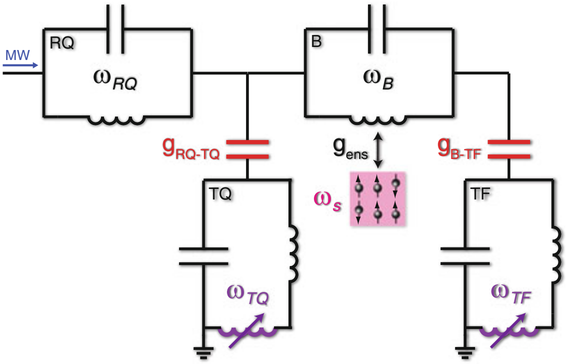

Fig. 6.20 Schematic of the circuit. The circuit B-TF is coupled to the external measurement lines via a resonator RQ, that can be detuned dynamically

Note that this implementation makes it necessary to carefully design the resonator Q, B and the coupling capacitances C_c, g_{RQ-B} to obtain $\omega_{RQ} = \omega_B$ when TQ and TF are far detuned.

Using destructive interference at the input of the resonator This approach is inspired by the work of Lehnert and coworkers on coherent feedback network [14]. It relies on 3 elements (see Fig. 6.21): the resonator B which is coupled to the spin

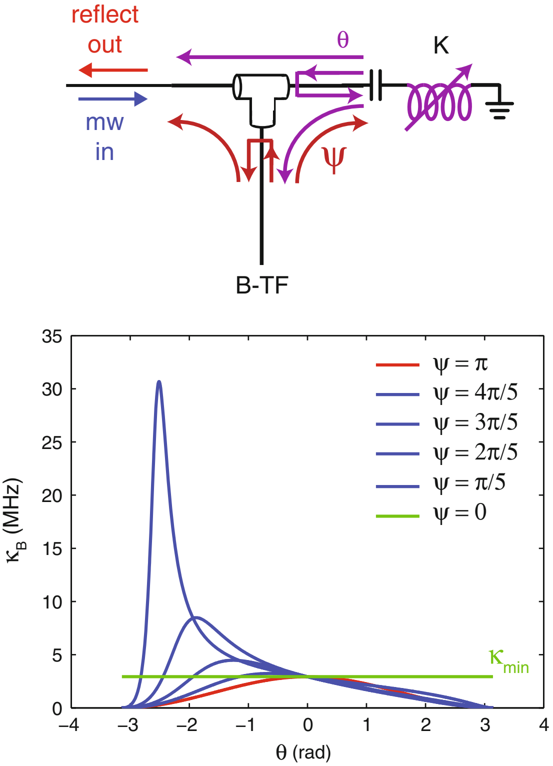

Fig. 6.21 Schematic of the circuit and simulations. The microwave tee can be either a commercial tee connected to the circuit K and B-TF (placed in separated sample box) via microwave cables, or patterned directly together with K and B-TF on a single circuit. The simulations of this circuit relies on the formulas in [14]

ensemble, a frequency tunable resonator K and a microwave tee connecting the two first elements to the external measurement channel. In this scheme, microwave signals leaving B and carrying information on the spins are split at the tee, with most of the amplitude evenly between the external measurement lines and the tunable resonator K input, and a small fraction reflected back to B. K reflects the signal with a frequency phase shift, further split by the tee with a portion which interferes with the B-to-external signal, enhancing or diminishing the rate of information leaving B. This interference enhances or diminishes the effective microwave damping rate κ_B of B, as seen by the microwave input port. This effective tuning of the damping rate κ_B is controlled by the resonator K center frequency, which is made tunable in frequency with pulsed local magnetic flux through an embedded SQUID loop. The length of the transmission lines between the tee and both elements is designed to obtain an effective high damping rate $\kappa_{B,max}$ when K is tuned on resonance with B, while recovering the intrinsic low damping rate $\kappa_{B,0}$ when K is far detuned from B. Note that this implementation does not impose strict conditions on the parameters of the resonator K.

We simulated, designed and fabricated two circuits along these design strategies, which should be measured in a future experiment (see Fig. 6.22).

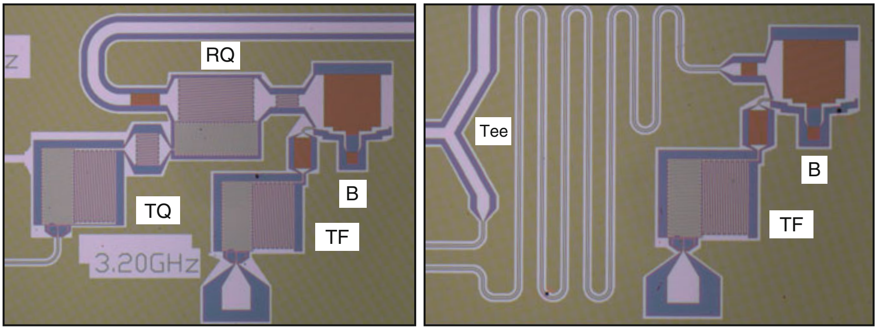

Fig. 6.22 Two realizations towards a circuit able to run the full memory protocol. (*left*) A realization using the first approach. The design parameters are $\omega_B/2\pi = \omega_{RQ}/2\pi = 2.88$ GHz, $\omega_{TF}/2\pi = \omega_{TQ}/2\pi = 3.20$ GHz and $g_{B-TF}/2\pi = g_{RQ-TQ}/2\pi = 300$ MHz. A coupling capacitance $C_c = 200$ fF to the external measurement lines was added to set the lower limit of the quality factor of B at $\sim$100. (*right*) A realization using the second approach. The circuit B-TF, the tunable resonator K and the tee are patterned on a single circuit (K not shown on this picture). The design parameters are $\omega_B/2\pi = 2.88$ GHz, $\omega_{TF}/2\pi = \omega_K/2\pi = 3.20$ GHz and $g_{B-TF} = 300$ MHz. The coupling capacitance of B to the external measurement lines is designed to set the lower limit of the quality factor of B at $\sim$200

References

1. J.R. Maze, J.M. Taylor, M.D. Lukin, Electron spin decoherence of single nitrogen-vacancy defects in diamond. Phys. Rev. B **78**, 094303 (2008)
2. N. Zhao, S.-W. Ho, R.-B. Liu, Decoherence and dynamical decoupling control of nitrogen vacancy center electron spins in nuclear spin baths. Phys. Rev. B **85**, 115303 (2012)
3. P.L. Stanwix, L.M. Pham, J.R. Maze, D. Le Sage, T.K. Yeung, P. Cappellaro, P.R. Hemmer, A. Yacoby, M.D. Lukin, R.L. Walsworth, Coherence of nitrogen-vacancy electronic spin ensembles in diamond. Phys. Rev. B **82**, 201201 (2010)
4. G. de Lange, Z.H. Wang, D. RistÃš, V.V. Dobrovitski, R. Hanson, Universal dynamical decoupling of a single solid-state spin from a spin bath. Science **330**(6000), 60–63 (2010)
5. A.M. Tyryshkin, S. Tojo, J.L. Morton, H. Riemann, N.V. Abrosimov, P. Becker, H.-J. Pohl, T. Schenkel, M.L.W. Thewalt, K.M. Itoh, S.A. Lyon, Electron spin coherence exceeding seconds in high-purity silicon. Nat. Mater. **11**(2), 143–147 (2012)
6. W. Yang, R.-B. Liu, Quantum many-body theory of qubit decoherence in a finite-size spin bath. Phys. Rev. B **78**, 085315 (2008)
7. B. Julsgaard, K. Mølmer, Fundamental limitations in spin-ensemble quantum memories for cavity fields. Phys. Rev. A **88**, 062324 (2013)
8. E. Kupce, R. Freeman, Stretched adiabatic pulses for broadband spin inversion. J. Magn. Reson. **117**, 246–256 (1995)
9. V. Damon, M. Bonarota, A. Louchet-Chauvet, T. Chanelière, J.-L. Le Gouët, Revival of silenced echo and quantum memory for light. New J. Phys. **13**, 093031 (2011)
10. A.J. Sigillito, H. Malissa, A.M. Tyryshkin, H. Riemann, N.V. Abrosimov, P. Becker, H.-J. Pohl, M.L.W. Thewalt, K.M. Itoh, J.J.L. Morton, A.A. Houck, D.I. Schuster, S.A. Lyon, Fast, low-power manipulation of spin ensembles in superconducting microresonators. Appl. Phys. Lett. **104**(22) (2014)
11. D.M. Toyli, C.D. Weis, G.D. Fuchs, T. Schenkel, D. Awschalom, Chip-scale nanofabrication of single spins and spin arrays in diamond. Nano Lett. **10**(8), 3168–3172 (2010)
12. A. Palacios-Laloy, F. Nguyen, F. Mallet, P. Bertet, D. Vion, D. Esteve, Tunable resonators for quantum circuits. J. Low Temp. Phys. **151**, 1034 (2008)
13. Y. Chen, C. Neill, P. Roushan, N. Leung, M. Fang, R. Barends, J. Kelly, B. Campbell, Z. Chen, B. Chiaro, A. Dunsworth, E. Jeffrey, A. Megrant, J.Y. Mutus, P.J.J. O'Malley, C.M. Quintana, D. Sank, A. Vainsencher, J. Wenner, T.C. White, M.R. Geller, A.N. Cleland, J.M. Martinis, Qubit architecture with high coherence and fast tunable coupling. arXiv, pp. 1402–7367 (2014)
14. J. Kerckhoff, R.W. Andrews, H.S. Ku, W.F. Kindel, K. Cicak, R.W. Simmonds, K.W. Lehnert, Tunable coupling to a mechanical oscillator circuit using a coherent feedback network. Phys. Rev. X **3**, 021013 (2013)

Chapter 7
Conclusions and Perspectives

In this thesis work, we designed a memory protocol able to store and retrieve on-demand the state of a large number of qubits in a spin ensemble and we demonstrated building blocks of its implementation with NV centers in diamond. The protocol requires a challenging combination of advanced techniques of superconducting quantum circuits and pulsed electron spin resonance. The experimental results we obtained are summarized in Fig. 7.1. The first step, the coherent storage of a qubit state into the spin ensemble, was achieved in a first experiment with $\sim$95 % efficiency. The second step, the retrieval using refocusing techniques of a single photon stored in the spin ensemble, was obtained in the classical regime in a second experiment with $\sim$0.5 % efficiency after 100 μs memory time. The third step, the reset of the spin memory by optical repumping, was adapted in a dilution refrigerator and achieved with $\sim$90 % efficiency in 1 s. Finally the multi-mode character of the NV spin ensemble memory was evidenced in a multiple microwave pulses storage and retrieval experiment.

These results bring a proof of concept of a spin-based quantum memory for superconducting qubits. In this perspective, the efficiency of the *write step* required to operate the memory is almost reached. The *read step* efficiency however must be enhanced by two orders of magnitude. The simulations [1, 2] and experiments we made in the first part of Chap. 5 indicate that the physical limits are not reached yet, suggesting that the implementation up to the operational level still requires new experimental developments. On the memory side, the coherence time of the NV spin ensemble we used in our experiments was improved by two orders of magnitude since the beginning of this thesis work thanks to the rapid progress on highly-doped diamond fabrication made in Tsukuba University. At present, the memory time is around $\sim$100 μs and should probably be further extended up to seconds by including dynamical decoupling [3, 4] in the protocol.

The realization in the near future of a quantum memory able to store tens of qubits states for milliseconds and retrieve them on demand seems not an impossible task. The next challenges is to combine the building blocks demonstrated in this thesis work in a single experiment, in which the retrieve state would be reconstructed by

© Springer International Publishing Switzerland 2016
C. Grèzes, *Towards a Spin-Ensemble Quantum Memory for Superconducting Qubits*, Springer Theses,
DOI 10.1007/978-3-319-21572-3_7

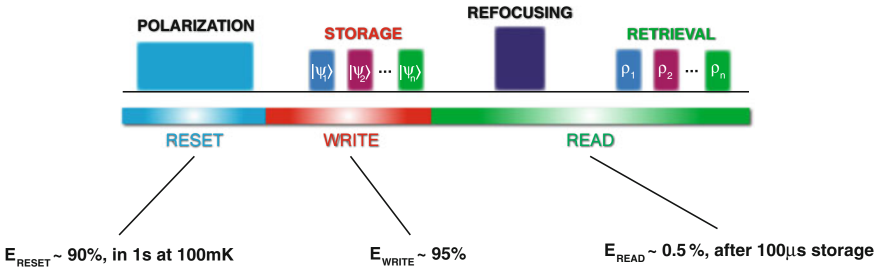
POLARIZATION
STORAGE
REFOCUSING
RETRIEVAL
$|\psi_1\rangle$ $|\psi_2\rangle$ ... $|\psi_n\rangle$
ρ_1 ρ_2 ... ρ_n
RESET
WRITE
READ
E_{RESET} ~ 90%, in 1s at 100mK
E_{WRITE} ~ 95%
E_{READ} ~ 0.5 %, after 100μs storage

Fig. 7.1 **Summary of the experimental results**

quantum state tomography to be compared to the encoded one. This requires the development of a circuit made of a resonator with both frequency and quality factor tunable that is compatible with refocusing of the spins. By developing an alternative approach for the frequency tunability in the second part of Chap. 6, we made one of the two steps towards the implementation of this physical setup.

The work presented in this thesis also opens the way towards new directions for a spin-ensemble quantum memory, which might be explored in future projects in the group. A first interesting possibility would be to harness the hyperfine interaction of each NV center with the nuclear spin of the nitrogen atom to transfer quantum information from the electron spin degree of freedom into the nuclear spin ensemble, in order to benefit from the much longer coherence times of nuclear spins. A prerequisite would be to polarize the nitrogen nuclear spins into a well-defined quantum state, which could be possible by adapting techniques demonstrated for single NVs at room-temperature, based on optical pumping [5], to NV ensembles at millikelvin temperatures. The optical NV reset demonstrated in this work is a first step in that direction. Another path is to use other types of electron spins, with potentially interesting properties. An outstanding system is the bismuth dopant in silicon, which has been shown to possess prominent clock transitions at which remarkably long Hahn-echo coherence times of several seconds were reported in isotopically purified silicon [6], which makes it an ideal system for a quantum memory. In collaboration with J. Morton's group at UCLondon, a project led by J. Pla is presently making efforts in that direction.

Besides realizing a quantum memory at microwave frequencies, spin-based hybrid quantum circuits as studied in this thesis have other potential applications as an emergent quantum technology. A first one would be the coherent conversion of a microwave photon into the optical domain, which should be feasible as discussed in two recent proposals [7, 8]. Alternatively, spin-based hybrid circuits are ideal playgrounds to investigate magnetic resonance detection with ultimate sensitivity. In that spirit, the sample described in Chap. 4 was also used to demonstrate qubit-based microwave detection of the NV centers spin resonance, with a gain of several orders of magnitude compared to more traditional ESR spectrometers [9].

References

1. B. Julsgaard, C. Grezes, P. Bertet, K. Mølmer, Quantum memory for microwave photons in an inhomogeneously broadened spin ensemble. Phys. Rev. Lett. **110**, 250503 (2013)
2. B. Julsgaard, K. Mølmer, Fundamental limitations in spin-ensemble quantum memories for cavity fields. Phys. Rev. A **88**, 062324 (2013)
3. G. de Lange, Z.H. Wang, D. Ristè, V.V. Dobrovitski, R. Hanson, Universal dynamical decoupling of a single solid-state spin from a spin bath. Science **330**(6000), 60–63 (2010)
4. N. Bar-Gill, L. Pham, A. Jarmola, D. Budker, R. Walsworth, Solid-state electronic spin coherence time approaching one second. Nat. Commun. **4**, 1743 (2013)
5. V. Jacques, P. Neumann, J. Beck, M. Markham, D. Twitchen, J. Meijer, F. Kaiser, G. Balasubramanian, F. Jelezko, J. Wrachtrup, Dynamic polarization of single nuclear spins by optical pumping of nitrogen-vacancy color centers in diamond at room temperature. Phys. Rev. Lett. **102**, 057403 (2009)
6. G. Wolfowicz, A.M. Tyryshkin, R.E. George, H. Riemann, N.V. Abrosimov, P. Becker, H. Pohl, M. Thewalt, S.A. Lyon, J. Morton, Atomic clock transitions in silicon-based spin qubits. Nat. Nanotechnol. **8**(6), 561–564 (2013)
7. C. O'Brien, N. Lauk, S. Blum, G. Morigi, M. Fleischhauer, Interfacing superconducting qubits and telecom photons via a rare-earth-doped crystal. Phys. Rev. Lett. **113**, 063603 (2014)
8. L.A. Williamson, Y.H. Chen, J.J. Longdell. arXiv:1403.1608v1 (2014)
9. Y. Kubo, I. Diniz, C. Grezes, T. Umeda, J. Isoya, H. Sumiya, T. Yamamoto, H. Abe, S. Onoda, T. Ohshima, V. Jacques, A. Dréau, J.-F. Roch, A. Auffeves, D. Vion, D. Esteve, P. Bertet, Electron spin resonance detected by a superconducting qubit. Phys. Rev. B **86**, 064514 (2012)

Appendix A
Fabrication

The resonators, transmission lines and flux lines are fabricated by optical lithography on a niobium thin-film. The substrate used is a 2-inch high resistivity ($>1000\,\Omega$cm) silicon wafer, covered with 50 nm of thermally grown SiO_2. The lithography consists in five steps (Fig. A.1):

1. Sputtering of a niobium thin-film by a DC electric discharge in a low density (10^{-2} mbar) argon plasma, that bombards a niobium target. The duration of the process determines the thickness of the film: 200–300 nm in our case to support the application of strong microwave pulses.
2. A layer of photosensitive resist (Shipley S1805) is spun on the wafer and baked.
3. The wafer is UV-exposed through a chromium on quartz mask and developed to dissolve the exposed resist.
4. Etching of the uncovered niobium, by Reactive-ion etching (RIE) with a SF_6 plasma at a pressure of 0.3 mbar.
5. Dissolution of the remaining resist.

This process is performed with wafers containing 45 chips, which are then diced on $3 \times 10\,\text{mm}^2$ chips, containing various resonators for hybrid circuit experiments. The Josephson junctions are fabricated afterwards, by double-angle evaporation of Aluminium through a resist mask patterned by e-beam lithography.

© Springer International Publishing Switzerland 2016
C. Grèzes, *Towards a Spin-Ensemble Quantum Memory for Superconducting Qubits*, Springer Theses,
DOI 10.1007/978-3-319-21572-3

Fig. A.1 Optical litography process

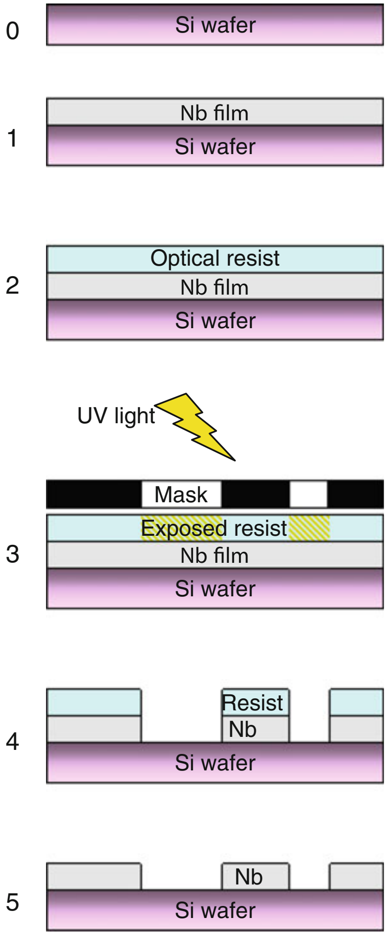
0
Si wafer
1
Nb film
Si wafer
2
Optical resist
Nb film
Si wafer
UV light
3
Mask
Exposed resist
Nb film
Si wafer
4
Resist
Nb
Si wafer
5
Nb
Si wafer

Appendix B
NV Center Distribution

The method which follows is used to extract the distribution of NV Hamiltonian parameters in Sect. 5.3.2.2. It reminds us that the NV center Hamiltonian (for ^{14}N nucleus) in the secular approximation is

$$H/\hbar = DS_Z^2 + E(S_X^2 - S_Y^2) + QI_Z^2 + AI_Z S_Z + g_e\mu_B(S_X B_X + S_Y B_Y + S_Z B_Z)$$

with $D \simeq 2\pi \times 2.8775$ GHz the zero-field splitting, E the strain splitting, $Q = 2\pi \times -5\,\mathrm{MHz}$ the nuclear quadrupole momentum, $A = 2\pi \times -2.14\,\mathrm{MHz}$ the hyperfine coupling of the NV to the ^{14}N nucleus, and $\mathbf{B}$ the magnetic field felt by the NV. Our ensemble of NV centers has a certain frequency distribution because the Hamiltonian parameters have a distribution, that we assume to be static. We consider in the following that both A and Q are fixed for all NVs. On the other hand, B_Z has evidently a certain distribution characterized by a function $\rho_B(B_Z)$ such that the number of spins seeing a certain magnetic field between B_Z and $B_Z + dB_Z$ is given by $N(B_Z) = \rho_B(B_Z)dB_Z$. This distribution originates from the different magnetic environments due to the local random distribution of $P1$ centers and ^{13}C nuclei. Note that although one can safely assume that B_X, B_Y and B_Z have the same distribution, we will only consider the B_Z distribution because it is the one that couples most strongly to the NV center, a good approximation when $D \gg E, |g_e\mu_B B|$ as is the case here. In the following we write $B \equiv B_Z$, and we note that $B = B_{NV}\cos\alpha + b$, B_{NV} being the applied magnetic field at an angle α from the NV axis and b the z component of the field due to the local environment of each NV. What is constant in the problem is the distribution of b, $\rho_b(b)$ The strain parameter E has another distribution $\rho_E(E)$. And finally, the zero-field splitting D is distributed with density $\rho_D(D)$, which is validated by recent work [1].

The Hamiltonian diagonalization leads to 9 states, corresponding to the 3 nuclear spin states $I_Z = +1, 0, -1$, and the 3 NV center states due to their spin $S = 1$. This gives 6 transition frequencies $\omega_{m_I,\pm}[E, B, D]$. Our goal is now to express $\tilde{\rho}(\omega)$ as a function of ρ_b, ρ_D,ρ_E. We write

© Springer International Publishing Switzerland 2016
C. Grèzes, *Towards a Spin-Ensemble Quantum Memory for Superconducting Qubits*, Springer Theses,
DOI 10.1007/978-3-319-21572-3

$$\tilde{\rho}(\omega, B_{NV}) = \sum_{m_I,\pm} \int\int\int dbdEdD\rho_b(b)\rho_E(E)\rho_D(D) \\ \times \delta\left(\omega - \omega_{m_I,\pm}[E, B_{NV}, D, b]\right)$$

For ρ_b and ρ_D we will assume a Lorentzian shape, which at least for ρ_b has a physical justification (the linewidth of a dipolar broadened spin ensemble is usually Lorentzian), with a width that will be "guessed" or adapted to fit the data. For ρ_E we use the $B_{NV} = 0$ dataset (see Fig. 5.16 of Chap. 5) to find an appropriate distribution.

The formula above is in principle sufficient to compute $\tilde{\rho}(\omega)$ numerically given ρ_b, ρ_D, ρ_E; however it would lead to very long calculation times and we need to simplify it. The first simplification is that instead of explicitly diagonalizing the Hamiltonian to obtain $\omega_{m_I,\pm}[E, B_{NV}, D, b]$ we use approximate formulas:

$$\omega_{0,\pm}[E, B_{NV}, D, b] = D \pm \sqrt{E^2 + (g_e\mu_B)^2(B_{NV}\cos\alpha + b)^2}$$
$$\omega_{+1,\pm}[E, B_{NV}, D, b] = D \pm \sqrt{E^2 + (g_e\mu_B)^2(B_{NV}\cos\alpha - B_{hf} + b)^2}$$
$$\omega_{-1,\pm}[E, B_{NV}, D, b] = D \pm \sqrt{E^2 + (g_e\mu_B)^2(B_{NV}\cos\alpha + B_{hf} + b)^2}$$

with $B_{hf} = |A/(g_e\mu_B)|$, considering the hyperfine interaction with the nuclear spin as a nuclear-spin-state dependent effective magnetic field of modulus B_{hf}. These formulas are valid when $D \gg E, |g_e\mu_B B|$, a very good approximation in our case. This allows to very easily invert the formula yielding, for given frequency ω, strain E and zero-field splitting D, the local magnetic field $b_{m_I,\pm}$ needed so that $\omega_{m_I,\pm}[E, B_{NV}, D, b] = \omega$. This equation has either zero or two solutions depending on ω. For the $0 \rightarrow +$ transitions there are two solutions if $\omega \geq D + E$, and zero else; for the $0 \rightarrow -$ transitions there are two solutions if $\omega \leq D - E$, and zero elsewhere. For the $0 \rightarrow +$ transitions:

$$b^{(1)}_{0,+}[\omega, E, B_{NV}, D] = \sqrt{(\omega - D)^2 - E^2}/g_e\mu_B - B_{NV}\cos\alpha$$
$$b^{(2)}_{0,+}[\omega, E, B_{NV}, D] = -\sqrt{(\omega - D)^2 - E^2}/g_e\mu_B - B_{NV}\cos\alpha$$
$$b^{(1)}_{+1,+}[\omega, E, B_{NV}, D] = \sqrt{(\omega - D)^2 - E^2}/g_e\mu_B - B_{NV}\cos\alpha + B_{hf}$$
$$b^{(2)}_{+1,+}[\omega, E, B_{NV}, D] = -\sqrt{(\omega - D)^2 - E^2}/g_e\mu_B - B_{NV}\cos\alpha + B_{hf}$$
$$b^{(1)}_{-1,+}[\omega, E, B_{NV}, D] = \sqrt{(\omega - D)^2 - E^2}/g_e\mu_B - B_{NV}\cos\alpha - B_{hf}$$
$$b^{(2)}_{-1,+}[\omega, E, B_{NV}, D] = -\sqrt{(\omega - D)^2 - E^2}/g_e\mu_B - B_{NV}\cos\alpha - B_{hf}$$

Identical equations apply for the $0 \rightarrow -$. Using that for any function $g(x)$ which has roots x_i the equality $\delta(g(x)) = \sum_i \delta(x - x_i)/|g'(x_i)|$ holds, we can rewrite

$$\tilde{\rho}(\omega, B_{NV}) = \sum_{m_I,\pm} \iiint dbdEdD\rho_b(b)\rho_E(E)\rho_D(D)\delta\left(\omega - \omega_{m_I,\pm}[E, B_{NV}, D, b]\right) \\ = \sum_{m_I,\pm,i} \iint dEdD\rho_E(E)\rho_D(D)\frac{\rho_b\left(b_{m_I,\pm^{(i)}}[\omega, E, B_{NV}, D]\right)}{\left|\frac{\partial\omega_{m_I,\pm}}{\partial b}(b_{m_I,\pm}[\omega, E, B_{NV}, D])\right|}.$$

Note that from the previous formulas it is clear that the density of NV centers at a given frequency ω can have a strong dependence on the nuclear spin state. This might explain in particular why the relative contributions of the $m_I = \pm 1$ and $m_I = 0$ to the spin echo signal at $\omega_e/2\pi = 2.8795\,\text{GHz}$ were found to be slightly different from the expected 0.66 and 0.33 by fitting the decoherence signal (see Fig. 5.39 in Chap. 5).

A difficulty arises when $\frac{\partial \omega_{m_I,\pm}}{\partial b}$ vanishes, giving rise to a divergence. To smoothen this out, we discretize the problem: we choose some small frequency scale $d\omega_0$ and we solve the equation $\omega_{m_I,+}[E, B_{NV}, D, b + db] - \omega_{m_I,+}[E, B_{NV}, D, b] = d\omega_0$. This equation has always two solutions, we take the Min of the two yielding the quantity $db[E, B_{NV}, D, b]$. The new formula is

$$\tilde{\rho}(\omega, B_{NV}) = \sum_{m_I,\pm,i} \iint dE dD \rho_E(E) \rho_D(D) \rho_b \left(b_{m_I,\pm^{(i)}}[\omega, E, B_{NV}, D] \right) \\ \times db[E, B_{NV}, D, b_{m_I,\pm}[\omega, E, B_{NV}, D]]/d\omega_0.$$

Reference

1. V. Acosta, Private communication

Curriculum Vitae

Cécile Grèzes
Born on December 27, 1988
Nantua, France

Springer Theses Series

Education

2014	**Ph.D. Physics, CEA Saclay/Université Pierre et Marie Curie, Paris**
2011	**M.Sc. Physics, Ecole Normale Supérieure, Paris** With honors
2008	**B.Sc. Physics and Mathematics, Université Joseph Fourier, Grenoble** Ranked first among all Bachelors students in Physics-Mathematics
2006	**Baccalauréat série S, Lycée Charles Poncet, Cluses**

Research Experience

2014	**Postdoctoral Research Scholar, Electrical Engineering department, University of California Los Angeles, Los Angeles** (Advisor Pr. Kang Wang) Nonvolatile magnetic memory and logic
2011–2014	**Graduate Research Assistant, Service de Physique de l'Etat Condensé, CEA Saclay, Gif sur Yvette** (Advisor Pr. Daniel Esteve) Quantum physics and quantum information experiments with Josephson qubits and NV centers in diamond
2010–2011	**Undergraduate Research Assistant, School of Engineering and Applied Sciences, Harvard University, Cambridge** (Advisor Pr. Federico Capasso) Nonlinear light generation and multiwavelength operation in heterogeneous mid-infrared quantum cascade lasers

© Springer International Publishing Switzerland 2016
C. Grèzes, *Towards a Spin-Ensemble Quantum Memory for Superconducting Qubits*, Springer Theses,
DOI 10.1007/978-3-319-21572-3

Honors and Awards

- **Madeleine Lecoq Price,** 2015, awarded by the French Academy of Science for one of the best Ph.D. thesis of the year in France
- **Springer Thesis Price,** 2015, awarded by Springer for outstanding Ph.D. research
- **PRL Editors' Suggestion of the American Physical Society,** 2011, for the publication "Hybrid quantum circuit with a superconducting qubit coupled to a spin ensemble"
- **Selected based on academic excellence to enter at the Ecole Normale Superieure (French Grande Ecole)**

Publications Related to This Thesis

- Y. Kubo, **C. Grezes**, A. Dewes, T. Umeda, J. Isoya, H. Sumiya, N. Morishita, H. Abe, S. Onoda, T. Ohshima, V. Jacques, A. Dréau, J.-F. Roch, I. Diniz, A. Aueves, D. Vion, D. Esteve, and P. Bertet, *Hybrid quantum circuit with a superconducting qubit coupled to a spin ensemble*, Phys. Rev. Lett. 107, 220501 (2011)—Marked as Editor Suggestion.
- Y. Kubo, I. Diniz, **C. Grezes**, T. Umeda, J. Isoya, H. Sumiya, N. Morishita, H. Abe, S. Onoda, T. Ohshima, V. Jacques, A. Dréau, J.-F. Roch, A. Aueves, D. Vion, D. Esteve, and P. Bertet, *Electron spin resonance detected by a superconducting qubit*, Phys. Rev. B 86, 064514 (2012).
- B. Julsgaard, **C. Grezes**, P. Bertet, and K. Mølmer, *Quantum memory for microwave photons in an inhomoge- neously broadened spin ensemble*, Phys. Rev. Lett. 110, 250503 (2013).
- M. Stern, G. Catelani, Y. Kubo, **C. Grezes**, A. Bienfait, D. Vion, D. Esteve, and P. Bertet, *Flux Qubits with Long Coherence Times for Hybrid Quantum Circuits*, Phys. Rev. Lett. 113, 123601 (2014).
- **C. Grezes**, B. Julsgaard, Y. Kubo, M. Stern, T. Umeda, J. Isoya, H. Sumiya, H. Abe, S.Onoda, T. Ohshima, V. Jacques, J. Esteve, D. Vion, D. Esteve, K. Mølmer, and P. Bertet, *Multi-mode storage and retrieval of microwave fields in a spin ensemble*, Phys. Rev. X 4, 021049 (2014).
- **C. Grezes**, Y. Kubo, M. Stern, B. Julsgaard, T. Umeda, J. Isoya, V. Jacques, K. Mølmer, D. Vion, D. Esteve, and P. Bertet, *Clock transitions in NV centers in diamond*, to appear in 2015.
- **C. Grezes**, B. Julsgaard, Y. Kubo, W. L. Ma, M. Stern, A. Bienfait, K. Nakamura, J. Isoya, S. Onoda, T. Ohshima, V. Jacques, D. Vion, D. Esteve, R. B. Liu, K. Mølmer, and P. Bertet, *Storage and retrieval of microwave fields at the single-photon level in a spin ensemble*, to appear in 2015.
- **C. Grezes**, Y. Kubo, B. Julsgaard, T. Umeda, J. Isoya, H. Sumiya, H. Abe, S. Onoda, T. Ohshima, I. Diniz, A. Aueves, V. Jacques, J.-F. Roch, D. Vion, D. Esteve, K. Mølmer, P. Bertet, *Towards a spin-ensemble quantum memory for superconducting qubits*, to appear in 2015.

Conference Contributions

Invited Speaker

- **C. Grezes**, Y. Kubo, D. Vion, D. Esteve, and P. Bertet, *Towards a spin-ensemble quantum memory for superconducting qubits*, Circuit and Cavity Quantum Electrodynamics Conference, Munich, Germany, September 2013.
- **C. Grezes**, Y. Kubo, D. Vion, D. Esteve, and P. Bertet, *Towards a spin-ensemble quantum memory for superconducting qubits*, Coherent Control of Complex Quantum Systems Workshop, Okinawa, Japan, April 2014.
- **C. Grezes**, *Towards hybrid quantum devices combining superconducting qubits to a spin-ensemble multi-qubit register*, APS March meeting, San Antonio, USA, March 2015.

Contributed Speaker

- **C. Grezes**, Y. Kubo, D. Vion, D. Esteve, and P. Bertet, *Refocusing spins by photon echo protocol*, Spins in Aarhus workshop, Aarhus, Denmark, April 2012.

- **C. Grezes**, D. Esteve, and P. Bertet, *Towards a spin ensemble quantum memory for superconducting qubits*, European project CHIST-ERA review meeting, Brussels, Belgium, March 2013.
- **C. Grezes**, Y. Kubo, D. Vion, D. Esteve, and P. Bertet, *Towards a spin ensemble quantum memory for superconducting qubits*, Spins in Saclay workshop, Aarhus, Denmark, April 2013.
- **C. Grezes**, Y. Kubo, D. Vion, D. Esteve, and P. Bertet, *Spin ensemble quantum memory for superconducting qubits*, CIFAR Quantum cavities workshop, Montreal, Canada, Mai 2013.
- **C. Grezes**, Y. Kubo, D. Vion, D. Esteve, and P. Bertet, *Atomic clock transitions in NV centers in diamond*, APS March meeting, Denver, USA, March 2014.

Seminars and Invited Talks

- CEA Saclay, February 2013, Saclay, France
- New York University, March 2014, New York, USA
- University of California Irvine, March 2014, Irvine, USA
- University of California Los Angeles, March 2014, Los Angeles, USA
- Berkeley University, March 2014, Berkeley, USA
- Qualcomm, March 2014, San Diego, USA
- HGST, March 2014, San Jose, USA
- IBM, March 2014, San Jose, USA